Advances in Sustainability Science and Technology

Dharmendra Tripathi
Ravi Kumar Sharma
Hakan F. Öztop *Editors*

Advancements in Nanotechnology for Energy and Environment

KES International

Springer

Advances in Sustainability Science and Technology

The book series aims at bringing together valuable and novel scientific contributions that address the critical issues of renewable energy, sustainable building, sustainable manufacturing, and other sustainability science and technology topics that have an impact in this diverse and fast-changing research community in academia and industry.

The areas to be covered are

- Climate change and mitigation, atmospheric carbon reduction, global warming
- Sustainability science, sustainability technologies
- Sustainable building technologies
- Intelligent buildings
- Sustainable energy generation
- Combined heat and power and district heating systems
- Control and optimization of renewable energy systems
- Smart grids and micro grids, local energy markets
- Smart cities, smart buildings, smart districts, smart countryside
- Energy and environmental assessment in buildings and cities
- Sustainable design, innovation and services
- Sustainable manufacturing processes and technology
- Sustainable manufacturing systems and enterprises
- Decision support for sustainability
- Micro/nanomachining, microelectromechanical machines (MEMS)
- Sustainable transport, smart vehicles and smart roads
- Information technology and artificial intelligence applied to sustainability
- Big data and data analytics applied to sustainability
- Sustainable food production, sustainable horticulture and agriculture
- Sustainability of air, water and other natural resources
- Sustainability policy, shaping the future, the triple bottom line, the circular economy

High quality content is an essential feature for all book proposals accepted for the series. It is expected that editors of all accepted volumes will ensure that contributions are subjected to an appropriate level of reviewing process and adhere to KES quality principles.

The series will include monographs, edited volumes, and selected proceedings.

Dharmendra Tripathi · Ravi Kumar Sharma ·
Hakan F. Öztop
Editors

Advancements in Nanotechnology for Energy and Environment

Springer

Editors
Dharmendra Tripathi
Department of Mathematics
National Institute of Technology
Uttarakhand, India

Ravi Kumar Sharma
Department of Mechanical Engineering
Manipal University Jaipur
Jaipur, India

Hakan F. Öztop
Department of Mechanical Engineering
Fırat University
Elazig, Turkey

ISSN 2662-6829 ISSN 2662-6837 (electronic)
Advances in Sustainability Science and Technology
ISBN 978-981-19-5200-5 ISBN 978-981-19-5201-2 (eBook)
https://doi.org/10.1007/978-981-19-5201-2

This Springer imprint is published by the registered company Springer Nature Singapore Pte Ltd.
The registered company address is: 152 Beach Road, #21-01/04 Gateway East, Singapore 189721, Singapore

Preface

Energy and environment are the two key assets as well as challenges for the survival of human beings in the universe. Nowadays, environmental and energy-related issues are prominent and challenging which are facing humanity. Modern technologies are enough capable of encountering problems related to renewable energies and conducting environmental remediation. Therefore, it is important to acknowledge the interactions among energy, environment, and technology to drive society moving and forward to civilization. The sustainability of the environment is directly linked with global climate change and pollutions, such as air, soil, and water. Climate change is still a controversial and even complicated aspect in most developed countries.

Along with the remit of technology, direct evidence from research, awareness of people, and government initiatives should also play a collaborative role in encountering issues and challenges of climate and ecology. Meanwhile, the existing technological setups can offer to eliminate/minimize the environmental pollutions from its various sources like heavy metals, organic compounds, biological or radiation hazards, oil spills, and microplastics, etc. Recent advancement in technologies for environmental applications, for instance, sensing and remediation, has been vividly improved by the use of nanomaterials and nanoparticles, which are proved to be the emerging and evolving of environmental nanotechnology.

This book presents a very useful and readable/valuable collection of chapters associated with recent developments in energy, environment, and nanotechnology including modelling and simulation of nanofluids dynamics. This will help to throw light on cutting-edge research and will be a ready reference for the researchers working in this arena of academia. This book mainly emphasizes technical expansions linked with energy, nanotechnology applications, energy storage, solar photovoltaic, and various other related areas. Readers will find this book useful for research contribution as well as it can also refer to as a reference book for courses for graduate and undergraduate students. This book will provide insights related to various forms of nanotechnological applications in green buildings, environmental and electrochemical, solar distillation systems, green energy, storage tank of the SWH system, solar concentrator system's receiver, solar adsorption refrigeration system, and CFD

simulations of various aspects of nanofluids/hybrid nanofluids, which are particularly useful and valuable for the betterment of society, culture, and ultimately human beings in the universe.

The early chapters of the book focus on the environmental impact in India and abroad along with the techniques to preserve it. They discuss how to improve carbon footprints and development of energy-efficient buildings. Mediocre chapters of the book discuss the energy materials' development and their uses for the Sustainable Development Goals. They primarily discuss the use of different materials including nanomaterials for energy efficiency. Various applications such as food drying and water heating using energy storage materials have also been highlighted in these chapters. Later chapters of this book emphasize on the use of nanofluids/nanoparticles/composite nanoparticles for various applications in energy systems and nanotechnologies. Some of these studies highlight the computational modelling and simulation-based findings which are very important to predict/estimate the dynamical behaviour of a system to be designed. Lastly, the chapters report the physical and chemical behaviours of hybrid nanofluids flow driven by emerging pumping mechanisms through the complex geometries which are applicable in various nanotechnology-based systems. The chapters included in this book cover various environmental aspects, renewable energy and energy storage-based systems, and nanofluids/hybrid nanofluids-based analysis for the development of nanotechnologies which will be very much useful and ready information for future applications of engineers, industrialists, and researchers.

Uttarakhand, India — Dharmendra Tripathi
Jaipur, India — Ravi Kumar Sharma
Elazig, Turkey — Hakan F. Öztop

Contents

Editors and Contributors

About the Editors

Dharmendra Tripathi has been working as Associate Professor in Department of Mathematics, National Institute of Technology, Uttarakhand. Prior to joining NIT Uttarakhand, he has worked more than 11 years as Faculty Member (Associate Professor, Assistant Professor) in various reputed institutions like Manipal University Jaipur, NIT Delhi, IIT Ropar, and BITS Pilani, Hyderabad. He has completed his Ph.D. in Applied Mathematics (Mathematical Modelling of Physiological flows) in 2009 from Indian Institute of Technology BHU and M.Sc. in Mathematics from Banaras Hindu University. He has supervised 06 Ph.D. students and 03 are working under his supervision. He has also guided 20 B.Tech. projects. He has published more than 160 papers in reputed international journals, 01 edited Book in Springer, 01 edited Book in CRC, 10 book chapters and presented more than 40 papers in International and National Conferences. He has delivered more than 100 lectures as Invited Speaker, Keynote Speaker, and Resource Person in various conferences, workshops, FDP, STTP, STC, refresher courses, etc. His research h-index is 41 and i-10 index is 127, and his papers have more than 5300 citations. He has been listed in top 2% researchers/scientist across the world as per updated science-wide author databases of standardized citation indicators in year 2020 and year 2021. He has received President Award in 2017 by the Manipal University Jaipur for outstanding contribution, Prof PR Sharma Memorial award from International Academy for Physical Sciences (IAPS) in 2021 and also become Associate Fellow of IAPS in 2022. He has been recognized by the Head of Institution for excellent work and contribution for the NIT Uttarakhand and also recognized by various reputed journals for reviewing the articles and editing the special issues for the journals. He was awarded some prestigious fellowships INAE fellowship in 2015 and 2016, 2017, and 2018, post-doctoral fellowships (NBHM, Dr. D. S. Kothari and Indo-EU) in 2010, etc. He has also organized various events like National and International conferences/STC/STTP /FDP/Workshops/Winter Schools on various emerging topics. He is Life Time Member of various professional bodies, Member of editorial board of two journals,

and Reviewer of more than 50 International Journals. His research work is focused on the mathematical modelling and simulation of biological flows in deformable domains, peristaltic flow of Newtonian and non-Newtonian fluids, membrane-based pumping flow models; dynamics of various infectious diseases; microfluidics; CFD, biomechanics; heat transfer; nanofluids; energy systems; numerical methods; etc.

Ravi Kumar Sharma has been working with Manipal University Jaipur as Professor and Director of Entrepreneurship cell at Manipal University Jaipur. He has total of 15 years of teaching and research experience in various reputed Indian and foreign universities. He earned his Ph.D. in Thermal Engineering from the University of Malaya, Malaysia, in 2016, and Master from BITS Pilani, India. He has published 50 research papers in international journals of repute and presented his research work in many international conferences in India and abroad. He has also written 5 book chapters and one edited book published by Springer and reviewer of many international journals. He has also delivered numerous invited/keynote speeches in FDP/STTP/Workshop, and conferences. His current area of research is renewable energy and thermal energy storage, in particular solar energy. His primary research is focused on the development of phase change materials or rapid heat transfer by enhancing their thermal conductivity. Dr. Sharma has supervised 3 Ph.Ds. successfully and currently supervising 04 Ph.Ds. He is also working on the development of carbon-based materials. His research is being cited globally, and one of his papers has been in the top downloaded articles and most cited in the journal for more than a year.

Hakan F. Öztop has been working as Full Professor in Department of Mechanical Engineering, Technology Faculty, Fırat University, Elazig, Turkey. He got his Master and Ph.D. degrees on Computational Fluid Dynamics (CFD) in the same university. He had been in Universite De Montreal, Canada during his Ph.D. studies. And, he worked as a postdoc student in the Department of Mechanical Engineering, Auburn University, Alabama, USA. He has supervised 4 Ph.D. students and 13 Master student under his supervision. His research h-index is 80 and i-10 index is 334, and his papers have more than 22000 citations. He is in Highly Citation Researchers (HCR) list since 2018. His research areas are nanofluids, CFD, energy storage, drying applications, solar energy and natural, and mixed convection heat transfer and combustion.

Contributors

Abu-Hamdeh Nidal H. Department of Mechanical Engineering, Faculty of Engineering, King Abdulaziz University, Jeddah, Saudi Arabia;
K. A. CARE Energy Research and Innovation Center, King Abdulaziz University, Jeddah, Saudi Arabia;
Energy Efficiency Group/Center of Research Excellence in Renewable Energy and Power Systems, King Abdulaziz University, Jeddah, Saudi Arabia

Anand Abhishek Non-Conventional Energy Laboratory, Rajiv Gandhi Institute of Petroleum Technology, Jais, Amethi, India

Anand S. School of Energy Management, Shri Mata Vaishno Devi University, Katra, J&K, India

Anand Y. School of Mechanical Engineering, Shri Mata Vaishno Devi University, Katra, J&K, India

Balaji R. Department of Mathematics, Panimalar Engineering College, Chennai, Tamil Nadu, India

Basavarajappa Mahanthesh School of Mathematical and Statistical Sciences, University of Texas Rio Grande Valley, Edinburg, TX, USA

Bruno F. Future Industries Institute, University of South Australia, Mawson Lakes, Australia

Buddhi D. UIT, Uttaranchal University, Dehradun, India

Chaubey Ajay K. Department of English, Jananayak Chandrashekhar University, Uttar Pradesh, Ballia, India

Firdose Heena Department of Mathematics, Centre for Mathematical Needs, CHRIST (Deemed to be University), Bengaluru, India

Idris Ruwaidiah Special Interest Group Modelling and Data Analytics, Faculty of Ocean Engineering Technology and Informatics, Universiti Malaysia Terengganu, Kuala Nerus, Terengganu, Malaysia

Kothari Richa Department of Environmental Sciences, Central University of Jammu, Jammu, India

Malik Prashant Centre of Excellence in Energy Science & Technology, Shoolini University, Solan, Himachal Pradesh, India

Nandal Reena Department of Mathematics, Centre for Mathematical Needs, CHRIST (Deemed to be University), Bengaluru, India

Okulu Damla Department of Mechanical Engineering, Manisa Celal Bayar University, Manisa, Turkey

Othmani Amina Faculty of Sciences of Monastir, University of Monastir, Monastir, Tunisia

Öztop Hakan F. Department of Mechanical Engineering, Technology Faculty, Fırat University, Elazığ, Turkey

Prakash J. Department of Mathematics, Avvaiyar Government College for Women, Karaikal, Puducherry-U.T., India

Raina Gautam Centre for Energy and Environment, Malaviya National Institute of Technology, Jaipur, Rajasthan, India

Raza Jawad Department of Mathematics, The COMSATS University Islamabad, Vehari Campus, Pakistan

Saleem Khalid Department of Mathematics, National College of Business Administration & Economics Multan, Multan, Pakistan

Sawhney A. Department of Physics, GGM Science College, Jammu, J&K, India

Selimefendigil Fatih Department of Mechanical Engineering, Manisa Celal Bayar University, Manisa, Turkey

Sharma Atul Non-Conventional Energy Laboratory, Rajiv Gandhi Institute of Petroleum Technology, Jais, Amethi, India

Sharma Dilip Malaviya National Institute of Technology Jaipur, Jaipur, Rajasthan, India

Sharma Manu Department of History, School of Social Sciences & Language, Lovely Professional University, Phagwara, Punjab, India

Sharma R. K. Department of Mechanical Engineering, Manipal University Jaipur, Rajasthan, India

Sharma Shubham Centre for Energy and Environment, Malaviya National Institute of Technology, Jaipur, Rajasthan, India

Sharma Vikrant National Institute of Solar Energy, Gurugram, Haryana, India

Shukla Amritanshu Non-Conventional Energy Laboratory, Rajiv Gandhi Institute of Petroleum Technology, Jais, Amethi, India;
Department of Physics, University of Lucknow, Lucknow, India

Siddheshwar P. G. Department of Mathematics, Centre for Mathematical Needs, CHRIST (Deemed to be University), Bengaluru, India

Singh Hemant Raj Manipal University Jaipur, Jaipur, Rajasthan, India

Singh Shailendra Non-Conventional Energy Laboratory, Rajiv Gandhi Institute of Petroleum Technology, Jais, Amethi, India

Sinha Sunanda Centre for Energy and Environment, Malaviya National Institute of Technology, Jaipur, Rajasthan, India

Soibam Davita Devi Centre for Mathematical Needs, Mathematics Department, CHRIST (Deemed to be University), Bengaluru, India

Srivastava Ankit Non-Conventional Energy Laboratory, Rajiv Gandhi Institute of Petroleum Technology, Jais, Amethi, India

Thappa Sahil School of Energy Management, Shri Mata Vaishno Devi University, Katra, J&K, India

Tiwari Abhishek Kumar Department of Applied Mechanics, Motilal Nehru National Institute of Technology Allahabad, Prayagraj, India

Tripathi Dharmendra Department of Mathematics, National Institute of Technology, Uttarakhand, Srinagar, India

Verma Shubham Kumar School of Energy Management, Shri Mata Vaishno Devi University, Katra, J&K, India

Yadav Santosh Kumar Department of History, School of Social Sciences & Language, Lovely Professional University, Phagwara, Punjab, India

Chapter 1
Applications of Nanotechnology through the Ages: A Socio & Eco-critical Study for the Welfare of Humanity

Santosh Kumar Yadav, Ajay K. Chaubey, and Manu Sharma

Abstract Nanotechnology is the use of matter on an atomic, molecular, and supramolecular scale for several scientific and industrial purposes. Recent developments in nanoscience and nanotechnology intend new and innovative applications in the various aspects of human lives. The exclusive qualities of non-materials enhance the approach that it can be used in a wide range of fields. The basic innovations that come from nanotechnology have the potential to contribute to the betterment of human health and environmental safety in numerous ways. It involves developed techniques and methods for pollution reduction, treatment of water, sensing of environmental issues, remediation, and ensuring the availability of alternative sources of energy in a more cost-effective and sustainable way. It appears in ancient Indian society being used in the field of medical science, for making weapons related to warfare, tools for agriculture, and work of goldsmiths. Today, it also lowers costs, produces stronger and lighter wind turbines, and improves fuel efficiency which saves energy. This work is the attempt to capture the nanotechnological development in India through the ages by highlighting and critically analyzing its impact upon society and environment. It has also been discussed that how the understanding and pursuing the old-world knowledge in conjunction with modern technological advances yield greater scientific knowledge for the benefit of environment and mankind.

Keywords Nanotechnology · Bhasma · Nanoscience · Environment · Nanoelectronics · Wootz steel · Nanomedicine

S. K. Yadav (✉) · M. Sharma
Department of History, School of Social Sciences & Language, Lovely Professional University, Phagwara, Punjab, India
e-mail: skyadav.iitr@gmail.com

A. K. Chaubey
Department of English, Jananayak Chandrashekhar University, Uttar Pradesh, Ballia, India

D. Tripathi et al. (eds.), *Advancements in Nanotechnology for Energy and Environment*,
Advances in Sustainability Science and Technology,
https://doi.org/10.1007/978-981-19-5201-2_1

1 Introduction

Human dreams and imagination often give rise to new science and technology. Nanotechnology, a twenty-first century, was born out of such dreams. Besides, human exposure to nanoparticles has occurred throughout human history; it has dramatically increased during the industrial revolution. The study of nanoparticles is not new. Nanosciences and nanotechnologies are leading to a major turning point in our understanding of nature. Such a force has its consequences or in the words of a famous fictional character: every force has its dark side. Our future depends on how we use new discoveries and what risks they bring upon humanity and our natural environment. The ethical implications of this must therefore be discussed. The unique properties of nanomaterials encourage the belief that they can be applied in a wide range of fields, from medical applications to electronics, environmental sciences, information and communication, heavy industries like aerospace, refineries, automobile, consumer, and sports good, etc.

It is a difficult subject to write about since compiling knowledge about nature that has not been recorded in an easily decipherable form, coupled with the possibility of some natural records having been lost during the long periods of history either by nature or by us, makes most information unavailable to us. We realized that apart from nature, human beings have also knowingly or unknowingly fabricated and utilized nanoparticles for various reasons. Looking back through history and searching for the existence of nanoparticles, not visible to the eye, nanotechnology, not yet known to us but seen in nature, has been an interesting journey for us.

It is a novel idea to write about nanotechnology in ancient periods. Since I have been a student of ancient Indian history and culture, it is difficult for me to review science, especially nanotechnology and its effect in ancient times. They have very lucidly described its application in prehistoric times. In ancient India, unknowingly as well as knowingly people have used it in the field of medicine, cosmetics, metallurgy, etc. Nanotechnology flourished in the Indian Civilization, Maya Civilization of South America and also in Roman culture.

The concept of a "nanometer" was first proposed by Richard Zsigmondy, the 1925 Nobel Prize Laureate in chemistry. He coined the term nanometer explicitly for characterizing particle size, and he was the first to measure the size of particles such as gold colloids using a microscope. In 1959, the physicist Richard Feynman, Nobel Prize winner for Physics in 1965, came up with the brilliant concept of the nano when he said "there is plenty of room at the bottom" during a conference of the American Physical Society.

The term "nano" which is one-billionth of a meter, originated from Greek word, "nanos" which means dwarf [1]. Nanotechnology can be defined as the technology used for design and synthesis of materials which is having at least one spatial dimension in non-orange, i.e., 1–100 nm (10–9 to 10–7 m). As mentioned above, the concept of nanotechnology was first put forward by physicist Richard Feyman in 1959 in his talk entitled "There's plenty of room at the bottom" [2]. New properties

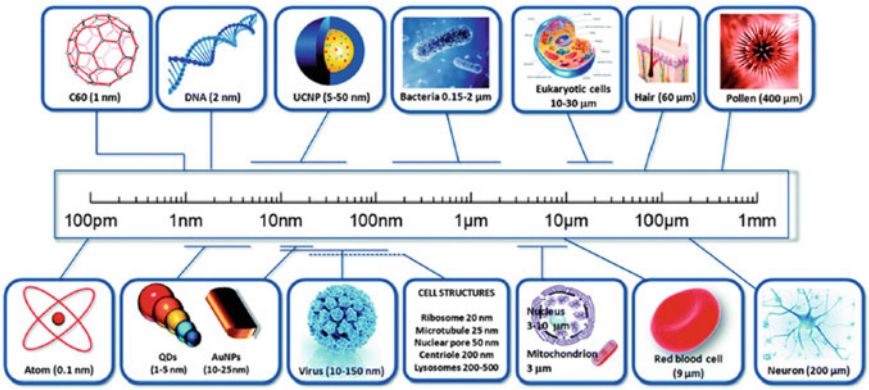

Fig. 1 Size of nanomaterial on scale

are incorporated to the matter at the nanoscale, which makes it suitable for the development of new products with new functions [3]. Nanotechnology may appear new in every aspects and a contemporary world's invention, but there are many historical references which claim that ancient India was well acquainted with this technology [4].

Nanotechnology is defined as the understanding and control of matter at dimensions between 1 and 100 nm, where unique phenomena enable novel applications. Nanoscience is the study of structures and molecules on the scales of nanometers ranging between 1 and 100 nm, and the technology that utilizes it in practical applications such as devices is called nanotechnology [5]. As a comparison, one must realize that a single human hair is 60,000 nm thickness and the DNA double helix has a radius of 1 nm [6] (Fig. 1).

The US National Nanotechnology Initiative defines the nanotechnology as: nanotechnology is the understanding and control of matter at dimensions of roughly 1–100 nm, where unique phenomena enable novel applications. Encompassing nanoscale science, engineering, and technology involves imaging, measuring, modeling, and manipulating matter at this length scale. According to the Japan: second Science and Technology Basic Plan (2001–2005) of Japan, nanotechnology is an interdisciplinary S&T that encompasses IT technology, the environmental sciences, life sciences, material sciences, etc. It is for controlling and handling atoms and molecules in the order of nanometer (1/1 000 000 000), enabling discovery of new functions by taking advantage of its material characteristics unique to nano-size, so that it can bring technological innovation in various fields.

2 Classification of Nanotechnology

Nanomaterials can be vastly classified as naturally occurring and man-made nanomaterials. Materials such as viruses, proteins, nucleic acids fall under the naturally occurring materials. The materials that are anthropogenic could be produced unintentionally from combustion of hydrocarbons or through a defined synthesis procedure. Nanotechnology basically deals with intentionally produced nanomaterials. "Moreover, nanomaterials are also present in nature in the form of various minerals produced by erosions and volcanic eruptions, in the multilayered nano- structures in the butterfly wings and feet of gecko, and the epicuticular wax crystal structures on lotus leaf surface" [7].

3 Evolution and Continuity of Nanotechnology

While nanosciences seem to be a new research field which appeared only in these past decades, it must be noted that chemical synthesis of metallic nanoparticles has been performed since a long time. Indeed, scientists have analyzed a lot of antiquities, for which the unusual colors have been attributed to the presence of metallic nanoparticles.

Though the development of electron microscopic techniques has been largely responsible for the dynamic growth in this sector, there have been records on the use of nanomaterials from the ancient times. Nanoparticles were primarily used as colorants in tumblers, ornamental glassware, and medieval paintings. "Thus, the use of metallic nanoparticles seems to have started with the beginning of glass-making in Egypt and Mesopotamia back in the fourteenth and thirteenth centuries BCE. Indeed, the red color of some glasses is explained by the presence either of metal copper nanoparticles or of cuprous oxide nanoparticles, as revealed by several chemical analyses performed on these ancient pieces" [8]. Antimony is almost always present: Generally used as opacifier, it could have also non-deliberately served as a reducing agent, allowing the formation of copper nanoparticles from cupric ions. Such pieces with copper nanoparticles have been found in this region until the sixth century BCE.

The most iconic example of the use of nanotechnology in ancient artifact is the Lycurgus Cup dating from the fourth century CE, showing a mythological frieze depicting the legend of Roman King Lycurgus and exposed in the British Museum in London (Fig. 2). "The most remarkable aspect of this cup relies on its dichroism: the cup resembles jade with an opaque greenish-yellow tone when it is illuminated from outside—reflected light—whereas the cup turns to a translucent ruby color when it is illuminated from inside—transmitted light" [9].

In India, the concept of reduction in particle size of precious metals has been prevalent since ancient times. It is clearly evident from the oldest classical text in

Fig. 2 Lycurgus Cup, illuminated from outside (left) or from inside (right) Trustees of the British Museum

Aryuveda, "Charak Samhita". "Bhasmas are unique herbo-metallic/mineral formulation, prescribed in very minute dosage for treatment of variety of chronic diseases since seventh century. These are nontoxic, easily digestible and absorbed in the body" [10]. Bhasmas, an ash, is claimed to be biologically produced nanomaterials. These are prepared by purification of starting material (process is known as shodhana) followed by the incorporation of mineral/herbal extracts in the next step, i.e., reaction phase [11]. The material prepared in pallet form is further subjected to incineration to obtain a nontoxic, lustureless ash, known as bhasma. Swarna ash (gold bhasma) has been characterized to contain particle size of 56–57 nm. "The bhasmas are useful in maintaining optimum alkalinity in body, stronger bones & teeth, maintaining mineral balance and metabolizing iron in body etc. Lauha bhasma (Iron) is documented to possess good potential as therapeutic agents" [12].

Chemistry's Noble Laureate Robert Floyd Curl Jr. (1996) explained that the concept of nanotechnology was utilized over 2000 years ago in India by the craftsmen in the manufacturing of **Wootz steels** and paintings. Carbon nanotubes and cementite nanowires have been found in a sample of Wootz steel with the aid of high-resolution microscopy. "Wootz steel was manufactured by unique smelting process, which led to nanotization, giving it a long-lasting edge. It also had 1.5% carbon, incorporated by wood and organic matter, during fabrication. The presence of these nanostructures has high impact upon mechanical properties" [13]. It can be clearly seen in the reference made to the sword of Tipu Sultan, an eighteenth-century king of Southern India, where the strength of sword can now be explained by nanotechnology [14]. Carbon nanotubes were also found in Ajanta paintings. These nanotubes are cylindrical fullerenes with extraordinary strength in terms of elastic modulus and tensile strength (Fig. 3).

Fig. 3 Wootz steel sword

According to Robert Floyd Curl Junior, Indian craftsman used nanotechnology in Wootz steel as well as in paintings. In 1952, Russian scientists told about carbon nanotubes, but they were present in sword of Tipu Sultan as well as in Ajanta paintings. Curl also claimed in 95th Indian Science Congress that Indian ancestors have been using this technology for over 2000 years and carbon nanotubes for about 500 years. Indian craftsman used unique smelting techniques to manufacture the Damascus blades which led to nanotization giving them a unique long-lasting edge. Wootz also had a high parentage of carbon, which was introduced by incorporating wood and other organic matter during fabrication. India, for ages, was a leading exporter of this steel which was used to make Persian daggers which were quite popular in Europe.

4 Nanomaterials in Medicine

Various nanomaterials were being used extensively by humans for several centuries, and they have been found in nature in inanimate as well as in various animals, insects, and plants. These natural nanostructured materials can help us understand their amazing properties and help us in gaining inspiration for designing and engineering high-performance materials. With the advent of electron microscopy and various synthetic approaches, nanotechnology is finding itself growing at a very fast rate [15].

Ayurveda, the science of life, was established and developed over thousands of years ago. Ayurveda works on the principle that mind and body are connected, and it is one of the most sophisticated and powerful holistic healing systems in the world. The Ayurvedic records can be traced back to 5000 BCE. It is considered to be an auxiliary knowledge in Vedic tradition. "The origin of Ayurveda is said to be found in Atharvaveda as well. It is also believed that Sage Agnivesha is the founder of Ayurveda and all his research is compiled in Agnivesa Samhita. Charaka, a physician in 300 BC, simplified Agnivesha's compilation and popularized it. Sushruta, an ancient Indian physician, also known as the father of surgery, authored a treatise titled Susruta Samhita. Susruta Samhita is considered to be the institutional text for Ayurveda" [16]. Very accurate and detailed surgical accounts have been be found in this epic treatise. Nagarjuna is credited with updating the Sushruta Samhita. Atreya Punarvasu, one of the great Hindu sages, was a renowned Ayurvedic scholar, and it is believed that the six branches of early Ayurveda are based on his teachings. He is credited as the author of Bhela Samhita [17]. The Charaka Samhita, the Sushruta Samhita, and the Bhela Samhita are the three principle early texts on Ayurvedic practice. Ayurveda burgeoned during the Middle Ages in India. The works of Charaka and Sushruta were translated into Chinese and Persian languages. These translational were found to have influenced various European schools of medicine as well [18].

Nanotechnology, in current state, is a revolutionary technology, so profound that it touches all parts of human society. The properties of nanomaterials differ significantly from bulk material. Nanoparticles possess enhanced structural integrity as well as unique optical, chemical, electronic, magnetic, and mechanical properties owing to which nanomaterials have become significant in recent years. Newly synthesized nanoproducts are coming to market rapidly for the betterment of our society, human health, and environment.

5 Nanoscience: Human Health

A fair assessment of the risks of any new technology must also consider positive contributions to increased safety. The basic innovations that come from nanotechnologies have the potential to contribute to human health and environmental safety in many ways. "They have the potential to contribute to solve urgent issues like the provision of clean drinking water or more efficient energy conversion and energy storage. The potential of nanotechnologies regarding economic benefits, the potential to create jobs, wealth and wellbeing is very high. At the moment, public awareness about nanotechnology is limited. What happens over the next few years will determine how the public comes to view it. A transparent discussion of benefits and risks will help people reach a considered, balanced view. This will enable a greater public acceptance, which, in turn, will enable society as a whole to profit from these fundamental technological developments while, at the same time, the risks are kept under control. Especially in the field of medicine there are quite a few technological developments that promise enhanced diagnostic possibilities, new ways to monitor

patients, new ways to treat diseases like cancer and to reduce side effects." To give a few examples:

- Nanoparticles can be used as carriers for targeted drug delivery. Their ability to penetrate certain protective membranes in the body, such as the blood brain barrier, can be beneficial for many drugs.
- This could open the way for new drugs from active substances that have not been able to pass clinical trials due to less precise delivery mechanisms.
- Nanosensors and lab-on-a-chip technologies will foster early recognition and identification of diseases and can be used for continuous monitoring of patients with chronic diseases.
- New therapeutic methods for the treatment of cancer with the help of nanoparticles are investigated.

Ultrasensitive detection of substances will have implications for safety in many other areas such as in the industrial medicine, environmental medicine, and food safety. To give one example: It has recently been shown that bacterial pathogens can be detected in very low concentrations with the help of nanoparticles. Quick and accurate testing is crucial for avoiding potential infections, but in order to be effective, many current tests require time-consuming amplification of samples.

6 Nanotechnology and the Environment

As nanotechnologies move into large-scale production in many industries, it is a just a matter of time before gradual as well as accidental releases of engineered nanoparticles into the environment occur. The possible routes for an exposure of the environment range over the whole life cycle of products and applications that contain engineered nanoparticles:

- Discharge/leakage during production/transport and storage of intermediate and finished products.
- Discharge/leakage from waste.
- Release of particles during use of the products.
- Diffusion, transport, and transformation in air, soil, and water.

Some applications like cosmetic products or food ingredients will be diffused sources of nanoparticles.

In addition, certain applications such as environmental remediation with the help of nanoparticles could lead to the deliberate introduction of nanoparticles into the environment. This is an area which will probably lead to the most significant releases in terms of quantity of nanoparticles in the coming years.

The main criteria used to assess the risks of chemicals for the environment and indirectly for human health are toxicity, persistence, and bioaccumulation. Substances that can cause direct damage to organisms (high toxicity) that decay in very slow

environment (high persistence) and that can concentrate in fatty tissues (high potential for bioaccumulation) are of particular concern. For engineered nanoparticles, the particular characteristics of nanomaterials will have to be considered for a specific risk assessment. The existing information about properties of the bulk material will not be sufficient to classify the environmental risk of the same material in the form of nanoparticles. "The possible environmental effect will therefore have to be assessed specifically for each type/class of nanomaterial. Only few studies on this very complex subject exist. From a scientific point of view, the results should be seen as indications rather than a sound basis for decision making".

"In the first study on the toxic effects of manufactured nanoparticles on aquatic organisms, fish (largemouth bass) were exposed to uncoated fullerene carbon-60 (C60) nanoparticles [19]. The fullerenes are one type of manufactured nanoparticle that is being produced by tons each year. Significant lipid peroxidation (oxidation of fats) was found in the brain of the animals after exposure to 0.5 ppm uncoated nC60. The study demonstrates that manufactured nanomaterials can have adverse effects on aquatic and possibly other organisms. Nanoscale iron particles have been investigated as a new generation of environmental remediation technology [20]. Due to their high surface reactivity and large surface area they can be used to transform and detoxify environmental contaminants like PCBs. Field tests in the US have shown that the nanoparticles remain reactive in soil and water for several weeks and that they can travel in groundwater as far as 20 m. The risks associated with free nanoparticles on ecosystems was not discussed in the original publication, but should be looked at in sufficient detail before environmental applications are brought to the market."

The Royal Society has called for the prohibition of the use of free nanoparticles in environmental applications until appropriate research has been undertaken. "A very specific environmental issue in the case of nanoparticles is their propensity to bind with other substances, possibly toxins in the environment such as Cadmium. Their high surface area can lead to adsorption of molecular contaminants. Colloids (natural micro- and nanoparticles) are known for their transport and holdings capacity of pollutants. The adsorbed pollutants could possibly be transported over longer distances/periods of time by nanoparticles. On the other hand, nanoparticles are less mobile than we intuitively might think. It seems that their movement is very case specific and that that are generally less mobile than larger particles. Here again their large surface area and their maximized chemical interaction comes into play. Their sticky nature considerably slows their transport through porous media like soil. In summary, the information about nanoparticles and the environment is only at an early stage. Among the research needs, there are topics like the effect of nanoparticles on species other than humans, about how they behave in the air, water or soil, or about their ability to accumulate in food chains." Taking into account the high number of parameters that characterize nanoparticles (like size, shape, specific surface treatment, chemical composition) as well as the variety of nanoparticles, it will need considerable research efforts to close the knowledge gaps. For cost-efficient and quicker results, harmonization of research is required that focuses on the most important materials and parameters and to concentrate on nanoparticles that are more likely to be produced.

By the summarizing the knowledge and awareness about nanotechnology, the evidences from past prove that ancient India was familiar with the manufacturing of nanomaterials, although they were unaware of the term nanotechnology. In this discussion, we can observe that the nanotechnological development in India through the ages was well established and profound. Its impact upon society and environment and the various initiatives are undertaken by the establishment from time to time to promote basic awareness and applications of nanotechnology in a sustainable approach and emphasizing the forthcoming opportunities for its application in the natural environmental systems. It has also been discussed that how the understanding and pursuing the old-world knowledge in conjunction with modern technological advances yield greater scientific knowledge for benefit of the environment and mankind. In today's world, nanotechnology is an emerging scientific field which has the potential to radically generate new products and processes by using nanomaterials and characterize the use of sophisticated instruments.

References

1. Gade A, Rai M, Yadav A (2008) Current [corrected] trends in photosynthesis of metal nanoparticles. Crit Rev Biotechnol 28(4):277–284
2. Feynman RP (1960) There's plenty of room at the bottom. Eng Sci 23(5):22–36
3. Sekhon BS (2014) Nanotechnology in agri-food production: an overview. Nanotechnol Sci Appl 7:31–53
4. Kumar A (2014) Nanotechnology development in India, an overview. RIS-DP # 193
5. Mansoori G, Fauzi Soelaiman T (2005) Nanotechnology—an introduction for the standards community. J ASTM Int 2:1–22
6. Gnach A, Lipinski T, Bednarkiewicz A, Rybka J, Capobianco JA (2015) Upconverting nanoparticles: assessing the toxicity. Chem Soc Rev 44:1561–1584
7. Schaming D, Remita H (2015) Nanotechnology: from ancient time to nowadays. Found Chem 17(3):187–205
8. Brill RH, Cahill ND (1988) A red opaque glass from Sardis and some thoughts on red opaques in general. J Glass Stud 30:16–27
9. Freestone I, Meeks N, Sax M, Higgitt C (2007) The Lycurgus cup—a roman nanotechnology. Gold Bull 40(4):270–277
10. Garg AN, Kumar AA, Nair GA, Reddy V (2006) Bhasmas: unique ayurvedic metallic-herbal preparations, chemical characterization. Biol Trace Elem Res 109(3):231–254
11. Haldar A, Pal DK, Sahu CK (2014) Bhasma: the ancient Indian nanomedicine. J Adv Pharm Technol Res 5(1):4–12
12. Dash MK, Dwivedi LK, Joshi N, Khilnani GD (2016) Toxicity study of Lauha Bhasma (calcined iron) in albino rats. Ancient Sci Life 35(3):159–166
13. Curl RF Jr (2006) Materials—carbon nanotubes in an ancient Damascus sabre. Nature 444(7117):286. Special lecture on Nanotechnology at 95th Indian science congress
14. Nair JK (2008) Nanotechnology in ancient India. History: Before 1 CE
15. Liu N, Lu Z, Zhao J, McDowell MT (2014) Pomegranate-inspired nanoscale design for large volume change lithium battery anodes. Nat Nanotechnol 9(3):187–192
16. Mukhopadhyaya G (1977) The surgical instrument of Hindus: with a comparative study of surgical instrument of the Greek, Roman, Arab, and the modern Eureopean Sergeons; RK Naahar, New Delhi, India
17. Bhishagrantna KL (1907) An English translation of the Sushrut Samhita based on original Sanskrit text, vol I. Wilkins Press Calcutta, India

18. Chattopdhyaaya D (1991) History of science & technology in ancient India: formation of the theoretical fundamentals of natural sciences. Firma KLM Private Limited, Kolkata, India
19. Oberholster E (2004) Manufactured nanomaterials (fullerenes, C60) induce oxidative stress in the brain of juvenile largemouth bass. Environ Health Perspect 112(10):1058–1062
20. Zhang W-X (2003) Nanoscale iron particles for environmental remediation: An overview. J Nanopart Res 5:323–332

Chapter 2
Electrodes Coated with Nanomaterials and Their Use for Environmental and Electrochemical Applications

Amina Othmani

Abstract The use of nanomaterials in electrochemical and environmental applications has gained a great attraction due to their excellent electrical, optical, thermal, catalytic properties, and strong mechanical strength. Electrodes modification with nanomaterials can offer high performance for the used electrodes for better performance in many electrochemical and environmental applications. Carbon nanotubes, gold nanoparticles, silicon nanowires, etc. have been considered as innovative electrode materials for environmental and electrochemical applications. In this context, we tried to discuss the importance of the coating of electrodes with various types of nanomaterials for the enhancement of their properties for environmental and electrochemical applications, especially for wastewater decontamination. An overview of the nanomaterials: Properties and applications were given. Also, we have described and discussed the methods used for the coating of electrodes with nanomaterials.

1 Introduction

Thanks to the development of manipulation and characterization techniques, which have opened up a way for the study and manipulation of matter on the scale of the atom, nanomaterials form the basis of several studies and research [1]. Many methods are developed to predict the physical properties and/or chemicals of nanomaterials which vary in particular according to their chemical composition, their size, and surface condition, which are completely different from the same materials in the massive state [2]. Nanomaterials represent an area of scientific research and growing technique for discovering properties or behaviors, physico-chemical particularities of interest at the atomic scale; these smooth out the creation of new materials currently

A. Othmani (✉)
Faculty of Sciences of Monastir, University of Monastir, Avenue of the Environment, 5019 Monastir, Tunisia
e-mail: othmaniamina@gmail.com

D. Tripathi et al. (eds.), *Advancements in Nanotechnology for Energy and Environment*, Advances in Sustainability Science and Technology,
https://doi.org/10.1007/978-981-19-5201-2_2

used in industry and new technologies in different fields (automotive, health, chemistry, packaging, cosmetology, energy, etc.). Therefore, thanks to the excellent electrical, optical, thermal, catalytic properties, and strong mechanical strength of nanomaterials, their use in electrochemical and environmental applications has gained a great attraction [3].

Electrodes modification with nanomaterials can offer high performance for the used electrodes for better performance in many electrochemical and environmental applications. Carbon nanotubes, gold nanoparticles, silicon nanowires, etc. have excellent properties that allowed them to be very effective for environmental and electrochemical applications [4]. The continuous increase in energy consumption and environmental pressure [5, 6] requires the development of sensitive, selective, rapid, cost effective, and miniature techniques for the detection of environmental pollutants [7]. Recently, nanomaterials-based technologies have offered good physical and chemical properties that allowed them to be used for environmental and electrochemical applications [8]. The material of electrodes and their properties define their effectiveness for the target applications. In many cases, the electrodes type limits the application [9]. Thus, searching solution for this problem is always required [10, 11]. Here, electrodes modification with nanomaterials presents an excellent choice to overcome the main drawbacks of their use at raw state. In this context, we tried in this chapter to review the main properties, classification, and application of nanomaterials. Furthermore, we tried to emphasize the importance of coupling nanomaterials with technology for better applications especially, in wastewater treatment, environmental issues, and electrochemical fields.

2 Nanomaterials: Properties and Applications

A nanomaterial is a material with at least one external dimensions that measures 100 nm (nm) or less, or with internal structures, measuring size is between 1 and 100 nm which have specific properties of the nanometric scale [12]. Thanks to nanotechnology, several environmental and human problems have been solved [13]. Nanomaterials can be nanoscale in one dimension (surface films), two dimensions (strands or fibers), or three dimensions (particles). They can exist in single, fused, and aggregated or agglomerated forms with spherical, tubular, and irregular shapes. Common types of nanomaterials include nanotubes, dendrimers, quantum dots, and fullerenes. Nanomaterials have applications in the field of nanotechnology and display different physical chemical characteristics from normal chemicals (i.e., silver nano, carbon nanotube, fullerene, photocatalyst, carbon nano, silica) [14]. Nanomaterials can be classified into four families according to their forms of use (Fig. 1): Materials of dimension 0: materials in dispersed, random, or organized form, as in colloidal crystals for optics or magnetic fluids.

Materials of dimension 1: materials in the form of nanowires or nanotubes.

Materials of dimension 2: materials in the form of a thin layer, as in the deposits of aggregates or thick coatings obtained by plasma spraying or electrochemical.

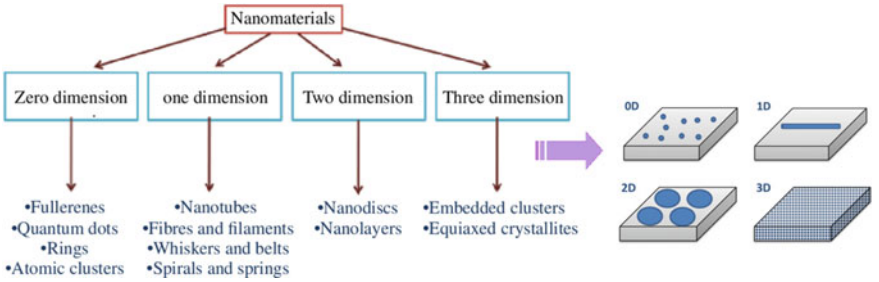

Fig. 1 Classification of nanomaterials according to ISO (Inspired from [15, 16])

Materials of dimension 3: materials in compact form as in the ceramics and nanostructured metals.

Based on the literature, and up to date, nanotechnology has been successfully used to facilitate our lives. Nanotechnologies and nano-objects bring together the techniques and tools of the world of the infinitely small: the millionth of a millimeter. Working on such a scale offers immense prospects in many fields like cosmetics, electronic, photonics, energy, pharmaceuticals, biomedicine, textile, etc. [17]. Often mentioned as part of the new technological revolution, nanosciences and nanotechnologies are booming, and their uses are conquering many aspects of our lives. Among them, health has a special place: Nanotechnologies not only promise to improve diagnosis and care in areas already encountered by current medicine and pharmacy, but also to open an infinity of possibilities in areas where science is only in its infancy, such as complex tissue regeneration, gene editing, or predictive diagnosis [18]. These innovations, scientific, and technological prowess allow the control of the matter in a dimension indistinguishable by the naked eye, arouse as much interest as questions, in terms of technique, safety, the environment, or even ethics and society. These uncertainties must find an echo, if not an answer, in the legal framework for nanosciences and nanotechnologies, which can guide the future of these innovations and the resulting societal changes [13, 18, 19].

Nanotechnology is one of the areas of materials science that specifically relates to material science, mechanical building, bioengineering, and chemical designing, where it shapes a run of disciplines that see fabric properties at the micro-level [20]. There are numerous applications of nanotechnology in numerous regions of life. There are moreover a few challenges concerning nanotechnology applications and are a few negative impacts of nanotechnology in our life [21]. For about half a century, new cooling techniques have appeared rapid, so-called soft chemistry, sol–gel techniques, for example, which provide access to much smaller grain sizes. Other production methods under the electric arc, laser, plasma, or microwaves have allowed to access very small particulate matter. It was thus possible to obtain grain sizes of dimensions of the order of the sizes, characteristics of defects that govern certain properties such as dislocations (mechanical properties), the Bloch walls (ferromagnetic properties), phenomena that occur only at the nanometer scale or below (tunnel

effect, "confinement" effects when the size of the particles is lower to the wavelength of the particles—electrons, photons—which intervene in the phenomenon studied). These dimensions, depending on the case, vary between a few nanometers and 100 nm. In parallel with this miniaturization approach, known as the "top-down", another approach, called "bottom-up", consists in building in a controlled way from atoms and molecules of new buildings and structures. The processes for producing these materials constitute a new field of investigation which remains to be developed.

The current processes allowing the elaboration of nano-objects are classified into three main categories: physical elaboration, chemical production, elaboration by mechanical method [22].

Given the complexity of applications and the rapid development of techniques, it seems difficult to give an exhaustive list of the processes used or under development.

Table 1 collects some advantages and disadvantages of the use of nanotechnology in many fields like biomedical applications, electronic, energy, etc.

3 Nanomaterials for Electrochemical Applications

Nanotechnology has shown an excellent potential to transform people's lives for the better. It facilitated the human lives in many fields start using cheap, lightweight solar plastics, which makes solar energy widely available [34]. Nanoparticles can clean up toxic chemical spills, as well as airborne pollutants. Thanks to nanotechnology, several environmental and human problems have been solved [35]. Based on the literature, and up to date, nanotechnology has been successfully used to facilitate our lives [36].

The attractive properties of nanoparticles have paved the way for the development of electroanalytical systems exhibiting promising analytical behaviors. Taking advantage of the special physical or chemical properties of nanoparticles, the electrochemical use of nanomaterials has gained a good interest in many fields of applications. For instance, electrodes coated with nanomaterials can be a good option for safe environmental and electrochemical applications [37, 38].

Nanomaterials can be divided into four types: inorganic-based nanomaterials; carbon-based nanomaterials; organic-based nanomaterials; and composite-based nanomaterials [39]. Inorganic-based nanomaterials include different metal and metal oxide nanomaterials: like silver (Ag), gold (Au), aluminum (Al), cadmium (Cd), copper (Cu), iron (Fe), zinc (Zn), and lead (Pb) nanomaterials. The examples of metal oxide-based inorganic nanomaterials are zinc oxide (ZnO), copper oxide (CuO), magnesium aluminum oxide ($MgAl_2O_4$), titanium dioxide (TiO_2), cerium oxide (CeO_2), iron oxide (Fe_2O_3), silica (SiO_2), and iron oxide (Fe_3O_4), etc. Carbon-based nanomaterials include graphene, fullerene, single-walled carbon nanotube, multi-walled carbon nanotube, carbon fiber, activated carbon, and carbon black. The organic-based nanomaterials are formed from organic materials excluding carbon materials, for instance, dendrimers, cyclodextrin, liposome, and micelle. The

Table 1 Application of nanotechnology: advantages

Applications	Offered advantages	References
Electronic device	Nanotechnology was the foremost important mechanical improvement within the twentieth century, which contributed to the make and innovation of silicon hardware or transistor and electronic research facilities and risen in so-called little sections that driven to a specialized transformation in all regions: communications, the computer, and pharmaceutical	[23]
Microelectronics	There are so-called semiconductors, which combine metallic and nonmetallic properties. This variation in physical and chemical behavior can be used for modern science Nanotechnology is here to make these semiconductors with electronic properties by extrusion of metal alloys of these elements—the silicon element—for example, fine elements of the accuracy of nanoparticles such as phosphorus, to form our so-called diodes and transistors, which are the chips used in the manufacture of computers, central processing units, and all electronic and electrical devices	[24]
Medical field	Scientists have made precision blood-size machines to treat many surgical conditions like arterial blockages and tumors. Electronic nose (e-nose) is invented with the help of nanotechnology, using carbon nanotubes to diagnose cancer diseases by analyzing the air that comes out of the lungs during the exhalation process	[20]
Aeronautical field	The National Aeronautics and Space Administration (NASA) has created precision nanotechnology machines to inject them into astronauts to monitor health conditions	[25]
Energy field	By using nanotechnology, many storage batteries are produced that store large amounts of energy and for long periods, thus producing clean, low-cost, non-oil-based cars. Nanotechnology is being used to reduce the cost of catalysts used in fuel cells. These catalysts produce hydrogen ions from fuel such as methanol. Nanotechnology is also being used to improve the efficiency of membranes used in fuel cells to separate hydrogen ions from other gases, such as oxygen	[26]
Manufacturing	Nanotechnology is used in the manufacture of a range of commodities, especially those that use nanoparticles of various kinds, such as aluminum and titanium, and therefore, they are present in cosmetics and anti-radiation ointments Nanoparticles are now widely used in sports clothing to eliminate unpleasant odors of sweat because they are antimicrobial	[27, 28]
Chemistry	The revolution of nanotechnology has created a common environment between chemists and other pros within the areas of material science, science, and designing until it comes to participation with realists, industry, and so that researchers and masters in each sort of science may development their science quickly. They get it the necessities of other sciences in arrange to reach at an instrument of effective participation among them. The nanoscience pros are presently working on natural chemistry, polymer chemistry, item union, and other fields	[29–31]

(continued)

Table 1 (continued)

Applications	Offered advantages	References
Industrial field	Nanotechnology is present in many industries, through the careful use of manufacturing technology, as well as trying to reduce the sizes of industries and make them achieve the fundamental goal and in smaller volumes and may also lead us to reduce the economic burden by finding solutions less expensive than it is now	[32, 33]

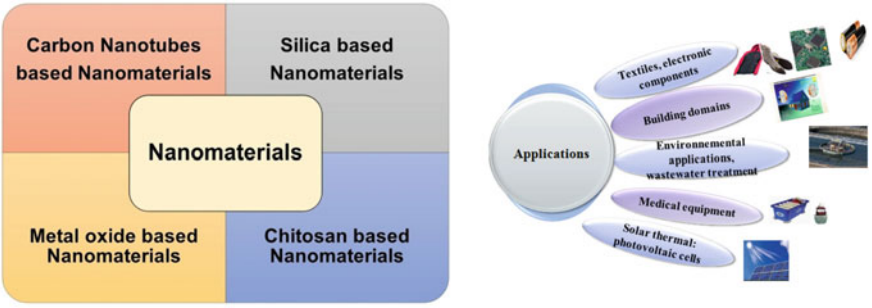

Fig. 2 Main types and applications of nanomaterials

composite nanomaterials are any combination of metal-based, metal oxide-based, carbon-based, and/or organic-based nanomaterials [39].

Figure 2 shows the main types and applications of nanomaterials. As seen, nanomaterials can be used in many applications including mechanical industries, medicine, environmental applications, sensors and biosensors for electronics, wastewater treatment, textile, energy harvesting, food, drugs and medications, and manufacturing materials, etc. [14, 40].

Many researchers have highlighted the importance of the use of nanomaterials employed for the detection of chemical contaminants [41]. Carbon-based nanomaterials include single-walled carbon nanotubes (SWNTs), multi-walled carbon nanotubes (MWNTs), single-walled carbon nanohorns (SWCNHs), fullerenes, and graphene, among many others, and have gained interest for electrode materials in electrochemical sensor applications [42]. Govindha et al. have discussed the ability of the developed electrochemical sensors to resolve a potentially large number of analytical problems and challenges across very diverse areas, such as defense, homeland security, agriculture, food safety, environmental monitoring, medicine, pharmacology, and industry [43]. Based on the literature, the application of electrochemical sensors for food analysis and the detection of specific analytes in environmental applications have gained interest. Nanomaterials-based electrochemical sensing platforms have been developed for the recognition and quantification of chemical contaminants in water and food [44].

Marín and Merkoçi have highlighted the merits offered by the use of nanomaterials-based sensing systems as a new class of rapid and low-cost detection alternatives with interest in the field of safety and security applications [45]. They have proved that nanomaterials are used either as modifiers of the electrochemical transducers or as labels to enhance the electrochemical signal, improve the stability, and in general the performance of the detection systems including their cost-efficiency.

Furthermore, Xu et al. have studied the critical advancement of the nano-electrochemical cytosensors based on metal nanoparticles and carbon nanomaterials. Within the past three years, there has been a part of sensors writing distributed where the cytosensors spoken to a quickly expanding course due to a few one of a kind preferences such as the quick response, uncomplicated instrumented, moo taken a toll, straightforward fabrication, great selectivity, tall specificity, and affectability. As mentioned previously, the nano-electrochemical cytosensors have the excellent possibility in therapeutic areas such as the recognition of cancer cells. Despite the fabulous merits of nano-electrochemical cytosensors in cancer cell acknowledgment, merely adding up cells seems not to offer extra points of interest required to prepare a vital clinical determination [46].

Thanks to their flexibility, stability, excellent conductivity, and compatibility, nanomaterials have empowered the electrochemical biosensors for better performance. Wang et al. have discussed their performance on the detection of pesticides. Also, they have detailed the main challenges and offered solutions to enhance their performance like the improvement of the electrochemical response of the electroactive analytes and the promotion of multiple detection and fabrication of portable on-site analytical sensors. Furthermore, the multiple metallic nanomaterials are optimized with excellent catalytic properties, by employing the appropriate functional organic or biomolecules and integrating micro- or nanoelectrodes [47].

To sum up, and based on the literature discussed by Wang et al. [47], nanomaterials-based electrochemical (bio)sensors have been made to obtain reliable, specific, sensitive, low cost, and portable electrochemical detection methods [48, 49].

Electrochemistry has provided a powerful and promising analytical tool for research purposes in various sectors such as medical, pharmaceutical, environmental, water, wastewater, and food contributing health, safety, and property of human life [50].

Voltammetry, amperometry, and potentiometry are the most prominent methods extensively used for the diverse analyses. Electrochemical (bio)sensors transform the electrochemical information to measurable electrical signals [51, 52].

The linear sweep voltammetry (LSV), cyclic voltammetry (CV), differential pulse voltammetry (DPV), and anodic stripping voltammetry (ASV) are the most commonly used techniques in electrochemical sensors [53].

Electrochemical sensors present the most versatile and highly developed chemical sensors [54]. They use ion-selective membranes that produce a voltage output in response to the activity of selected ions (H^+, K^+, NO_3^-, Na^+, etc.). They are divided into several types: potentiometric (measure voltage), amperometric (measure

current), and conductometric (measure conductivity). In all these sensors, special electrodes are used. Either a chemical reaction takes place or the charge transport is modulated by the reaction. Electrochemical sensing always requires a closed circuit. Current must flow to make a measurement. Since we need a closed loop, we need at least two electrodes. These sensors are often called electrochemical cells. How the cell is used depends heavily on the sensitivity, selectivity, and accuracy [55].

The application of the electrochemical sensors has attracted growing interest owing to their great sensitivity, low cost, short analysis time, and instrumental robustness [56].

The electrochemical sensors are capable of an accurate analysis of various organic and inorganic compounds in a wide linear concentration range with a detection limit of as low as nano, femtomolar, or even lower concentrations that make them powerful devices for various practical applications [57]. The low power consumption along with the possibility of miniaturization and integration of the electrochemical sensors in portable tools leads to "sample-to response" devices, which can allow rapid, reproducible, and reliable real-time field analysis [58].

Moreover, they do not need a specialist operator due to simplicity of working with the electrochemical devices and their operation [59].

The high sensitivity, low detection limit, wide dynamic range, reasonable selectivity, reliable and fast response, and durability are the requisite parameters of efficient analytical sensors.

However, the slow kinetics of the electron exchange process between some analytes and the bare electrode surface with restricted surface area sometimes leads to a poor and insensitive response, especially at low concentrations [60].

Moreover, the bare electrodes suffer from the fouling process and lack of selectivity when analyzing real complex samples that effectively restrict their performance [61].

The electrode modification process could overcome these problems and improve the sensitivity, selectivity, and longtime stability of the electrochemical sensing. Among the various electrode modifiers, nanomaterials have been in the focus of attention because of their ability to improve effectively the stability, selectivity, sensitivity, and detecting capabilities of the electrochemical sensors [52].

They have facilitated the high-performance analysis of trace level of various analytes in diverse real samples with high reliability and rapid testing capabilities [62].

In recent years, extensive studies have been conducted to develop efficient electrochemical sensors based on diverse nanomaterials such as MOFs, carbon nanostructures, MIPs, metals, and metal oxides.

The electrode modification process could overcome these problems and improve the sensitivity, selectivity, and longtime stability of the electrochemical sensing. Among the various electrode modifiers, nanomaterials have been the focus of attention because of their ability to improve effectively the stability, selectivity, sensitivity, and detecting capabilities of the electrochemical sensors [63]. They have facilitated the high-performance analysis of trace levels of various analytes in diverse real samples with high reliability and rapid testing capabilities [64]

4 Nanomaterials for Environmental Applications

The continuous and rapid growth of the world's population has resulted in a huge increase in energy consumption and environmental pressure [5, 6]. Thus, there is an urgent need to develop highly sensitive, selective, rapid, cost-effective, and miniature sensor systems for the detection of environmental pollutants [7]. During these last years, nanomaterials-based technologies have been successfully applied for the treatment of emerging contaminants in wastewater and environmental applications. New materials with good physical and chemical properties provide opportunities to overcome the main drawbacks of the conventional used method for environmental remediation [8]. In this context, noble metal nanomaterials (NMNs), namely gold, silver, and platinum, also feature many intriguing physical and chemical properties when their sizes are reduced to the nano- or even subnano-scale; such assets may significantly increase the values of the noble metals as functional materials for tackling important social issues related to human health, and the environment may provide promising solutions for many environmental issues [65].

The physical and chemical properties of NMNs have offered good platforms for a variety of environmental applications, such as sensor development for environmental pollutants and catalytic decomposition of pollutants [66].

According to Corsi et al., the use of engineered nanomaterials (ENMs) for environmental remediation, known as nanoremediation, has shown a challenging and innovative solution, ensuring a quick and efficient removal of pollutants from contaminated resources. Due to its large surface area and high surface energy, the nanoparticles have the ability to absorb large amount of pollutants or catalyze reactions at a much faster rate, thus reducing energy consumption during degradation or helps in preventing release of contaminants. They have shown that even good results were achieved; many drawbacks related to the full-scale application should be overcome. Therefore, huge efforts should be devoted to develop innovative, green, and sustainable (nano)solutions, which own eco-safe features such as limited mobility in environmental media and no toxicological effects for fauna and flora equilibrium [8].

Wang et al. have reviewed the plasmonic-based nanomaterials for environmental remediation. They have discussed their customized features, including optical, photothermal, conducive, and catalytic qualities, plasmonic nanoparticles which allowed them to be promising in this field. These features have been widely employed to improve the light absorption efficiency, redox reaction kinetic rates, and charge separation efficiency of materials for environmental applications. They have also reviewed the tailored properties of plasmonic nanomaterials and how they are used to design efficient environment-functional materials. They have shown deeply that the primary obstacles in using plasmonic nanoparticles for environmental applications are in some circumstances, the total mineralization of pollutants which is required due to the risk of contamination. Also, the cost of plasmonic nanoparticles and the treatment processes associated with them must be kept low. Then, the stability of plasmonic nanoparticles in real environmental matrices must be quickly improved.

Finally, the ecological safety of these nanomaterials should be thoroughly examined. However, it is envisaged that as this science advances, plasmonic nanotechnology will be used for a variety of environmental applications in a broader sense, in other word, the contaminant identification and remediation, as well as resource recovery during waste treatment operations [6].

Based on these discussed works, within the environment, nanotechnology can add big development by using providing their position in monitoring, pollutants prevention, and remediation methods [67]. There are several promising regions of applications, which include contaminated water and air remedy, self-cleaning substances, energy programs, novel functionalized adsorbents for environmental, business programs, and nanomaterials for sustainable strength production [68].

Singh and Naveen have introduced the molecular nanotechnology as a new alternative for the environment treatment. Also, they have discussed the potential risks of using molecular nanotechnology in remediation applications. They have shown that the utility of nanoparticles for soil remediation is currently under examination. Zero-valent iron and iron oxides, catalyzed through noble metals along with Pd, are the material that is under consideration. Permeable barriers with iron filings are already used to remediate groundwater. Similarly, research of iron nanoparticles is wanted of agglomeration/aggregation even though it represents a more value effective solution as they have got a far better reactivity according to unit mass. There are still extreme problems regarding the effect of nanoparticle launch on soil ecosystems. This is a large research challenge as there is constrained information to be had. Among fundamental necessities are physico-chemical equilibrium and kinetic records, records on outcomes on living organisms, and improvement of modeling strategies on a case using case basis. Other strategies for nanoparticle remediation with the aid of the use of micro-organisms and phytoremediation strategies are wanted to be covered. The complexity of systems worries way that there are numerous unknowns. It is far consequently essential to set up a device of defining applicable and unacceptable risks [69].

Figure 3 presents some environmental applications of nanotechnology.

As seen in Fig. 3, nanotechnology is able to improve the current environmental protection measures and the understanding of the environment. The current research could unveil new emission control schemes, develop new “green” technologies that minimize the production of undesirable by-products, and remediate existing waste sites and polluted water sources [70]. Nanotechnology has the potential to remove the smallest contaminants from the water we drink and from the air we breathe as well as to continuously measure and mitigate pollutants in the environment. It could also help reduce waste, improve energy efficiency, create environmentally benign composite structures, conserve energy reserves, and remediate current wastes. Knowledge concerning the complex physical process involving nanostructures is essential to understanding the impact nanotechnology will have on the environment [71]. The process at the interface between inorganic and biological systems is relevant to health and biochemical responses [72] (Table 2).

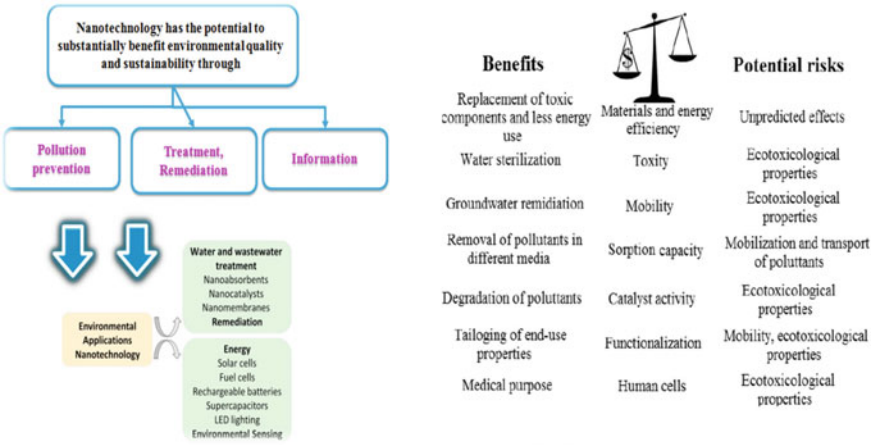

Fig. 3 Some environmental applications of nanotechnology: benefits and potential risks

Table 2 Nanocomposites for environmental applications

Nanocomposite	Application	Achievement	References
Modified CNC with succinic anhydride	Adsorption of Pb^{2+} and Cd^{2+}	High adsorption capacity of about tenfold more than raw CNC	[73]
Cellulose nanocrystals (CNC) prepared from rice straw by acid hydrolysis	Adsorption of Pb^{2+}, Ni^{2+}, and Cd^{2+}	The adsorption capacity of metal solution reached respectively 9.7, 9.42, and 8.55 mg g^{-1}	[74]
Polymer-based nanocomposites (PNCs): hydrated ferric oxide (HFO)	Adsorption of phosphate sulfonic resin As(III) and Arsenic	The use of PNCs in adsorption of pollutants, photo-/chem-catalysis degradation, and pollutant sensing and detection result in less pollution and benign products	[75, 76]
Porous calcium alginate/graphene oxide composite aerogel	Adsorption of copper, cadmium, and lead ions from water	The maximum adsorption capacities for Pb^{2+}, Cu^{2+}, and Cd^{2+} are 368.2, 98.1, and 183.6 mg g^{-1}, respectively. The removal rates for Pb^{2+}, Cu^{2+}, and Cd^{2+} were 95.4, 81.2, and 73.2%, respectively	[77]
Nanocellulose hybrids containing reactive polyhedral oligomeric silsesquioxanes	Adsorption of Cu^{2+} and Ni^{+} from wastewater	The results showed that the adsorption capacities of hybrids materials were higher than the raw one cellulose	[78]

5 Methods Used for the Coating of Electrodes with Nanomaterials

In 1970, it was discovered that electrodes might be modified for greater performance in electrochemical and environmental applications. Around 1975, the term "chemically modified electrode" was created to describe various sorts of electrode materials, with the first papers on electrodes made of explicitly "modified" graphite used in the electrosynthesis of optically active chemicals [79].

Initially, the word was used to describe any electrode that could be chemically modified. Chemically modified electrodes are electrodes that possess a certain chemical reactivity in addition to their ability to transfer electrons to or from the analyte, which also becomes possible in the presence of groups of substances that chemically reacts on their surface. Therefore, in addition to the electrochemical transformations, the analytes can undergo certain chemical reactions which mainly broaden the applicability of these electrodes [80]. The main reason for surface chemical modification of electrodes is to improve the mass transport and the limitations of electronic transfers at the surface of the electrode [81]. This can be achieved either by the generation or immobilization of electroactive species or reactants on or near the electrode-solution interface or transfer-enhancing compounds of electrons or functional groups. Chemical modification of electrodes also increases protection and stability of the surface of the electrode, as well as modifying the physical or physico-chemical properties in a favorable way to widen the field of applicability and the performances of these electrodes, or the exploitation of electrochemical and catalytic reactions that occur on the surface of the electrodes [82].

The electrodeposition presents a conventional surface modification method used to improve the surface characteristics, decorative, and functional, of a wide variety of materials. Recently, coated electrodes with nanomaterials have shown accepted versatile preparation techniques for environmental and electrochemical applications [81].

According to Zen et al., the chemical modification of electrodes offers high sensitivity and selectivity for analytical chemistry applications. The modification can be done by physisorption/chemisorption, covalently linked, homogenous (uniform) multilayer, and heterogeneous (non-uniform) multilayer chemical modified electrodes [83]. They have shown that the electrode itself can act as a reactant to pump (reduction)/withdraw (oxidation) electron in the reaction, which cannot be expected in spectroscopic characterization methods. By coupling the electrochemical methods with chemical modified electrodes, the electrodes can be able to be used in many applications in electrosynthesis, organic chemistry, and material characterization.

Furthermore, Jayankrishan, 2012, has confirmed the effectiveness of the electrochemical method for the synthesis of a wide range of nanostructured materials, like metal nanoparticles, nanowires, nanofilms, laminated composites, multilayered coatings, and nanoparticle reinforced composite coatings. He has shown that the electrodeposition of a pure metal, or codeposition of an alloy from an electrolyte, occurs on the cathode of the electrochemical system of the coating process. This

process happens by applying an external current (direct or pulsed) to the electrodeposition system. By this method, 2D and 3D nanostructures of metals, alloys, and nanocomposites have been deposited successfully. The 1D nanostructure crystallites can also be prepared using the electrodeposition method by utilizing the interference of one ion with the deposition of the other [84].

Ahmad et al. [85] have reviewed the methods used for the deposition of nanomaterials for biosensor fabrication. They have shown that the (nano)material deposition can provide a high surface area to improve the electroanalytical performance of biosensors by supporting the stable immobilization of enzymes in a more significant quantity as well as enhancing the catalytic or affinity features. They have discussed the coating-based methods like drop-casting, dip coating, spin coating, and blade coating which present the most commonly used methods for modifying electrodes with nanomaterials. The methods are effectives and not expensive for the biosensor fabrication. Figure 4 presents the main coating-based methods for nanomaterial deposition onto electrode surfaces.

Based on the literature, many researchers have worked on modifying the surface of the electrode with dispersed carbon nanomaterials [88, 89]. The first method consists of modifying the surface of the electrode in two stages, first with a quantity of well-dispersed carbon nanomaterials and then with the conductive polymer [90]. Electropolymerization is carried out in an appropriate solution, aqueous, organic, or even ionic liquid containing a suitable concentration of monomer and doping ion [88]. Cyclic voltammetry, galvanostatic, or potentiostat polarization is generally the electrochemical techniques used for polymer deposition. The second method is in a direct simultaneous combination of the polymer and the carbon nanomaterials on the surface of the electrode from a solution containing the monomer, the carbon nanomaterials, and the doping ion. Generally, electrochemical polymerization is easy and quick to carry out; it does not take minutes instead of hours for chemical curing, to form homogeneous and highly conductive nanocomposites [88]. The overall performance of the fabricated nanocomposites essentially depends on the dispersion of carbon nanomaterials in the polymer matrix [91]. In this regard, good dispersion and homogeneity of carbon nanomaterials are the key parameters of the successful preparation of these nanocomposites [92]. Up to date, a large number of research works have reported the use of nanocomposites conductive polymers/carbon nanomaterials in electrochemical sensor applications for the detection of a variety of metallic and organic pollutants [91]. The combination of conductive polymers with carbon nanomaterials (NMC) such as graphene (GR), carbon nanotubes (CNT), and carbon nanofibers (NFC) can give birth to new nanocomposites with unique physical and chemical properties and promising. Over the past decade, significant progress has been made in this direction which has opened up new fields of application for these nanocomposites. Several researchers have reported the synthesis of these nanocomposites, including the chemical and electrochemical that are the methods most often applied [93].

Table 3 collects some works dealing with the typical applications of conductive polymers/carbon nanomaterials nanocomposites as electrochemical sensors.

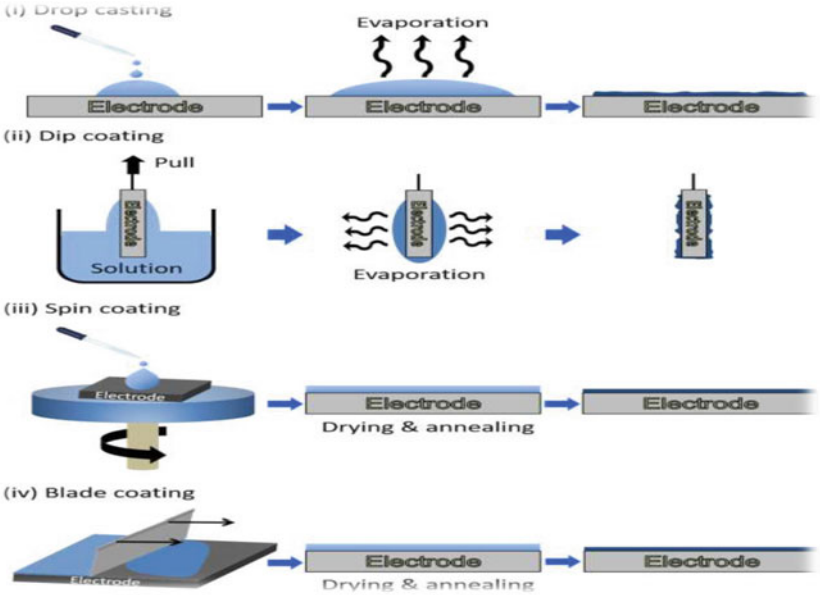

The influences factors in electrodeposition are:

- Current density
- Solution concentration
- Bath composition and temperature
- Nature of the anions and cations in the solution
- Power supply current waveform
- Presence of impurities
- Physical and chemical nature of substrate surface etc.

Advantages of electrodeposition over other liquid-phase and gas-phase deposition techniques are:

- They allow growing functional nanoparticles through complex 3D nano templates.
- This can be performed within a nanoporous membrane, which serves to act as a template for nanoparticle growth.
- Applicable at room temperature from water-based electrolytes.
- These methods are suitable to scale down to the deposition of a few atoms or up to large dimensions, film thickness could range from 1 nm to 10 microns, etc.

Fig. 4 **a** Description of the coating-based methods for nanomaterial deposition onto electrode surfaces. **b** Factors affecting the coating process and main offered benefits inspired by [85–87]

In recent years, many nanocomposites based on conductive polymers, carbon nanomaterials, metallic nanoparticles, and ionic liquids have been manufactured and widely used in the development of new electrochemical sensors [98].

A lot of researchers have been interested on the modification of electrodes with nanomaterials for electrochemical applications, in particular for biosensors fabrications [81]. Others have talked about the main offered benefits from the use of electrochemical deposition for electrodes coating, like Gurrappa and Binder who have shown that the obvious advantages of this method use the rapidity, low cost, free from porosity, high purity, industrial applicability, potential to overcome shape

Table 3 Overview of some applications of conductive polymers/carbon nanomaterials nanocomposites as electrochemical sensors

Nanocomposites	Application and limits of detection (LOD)	References
Graphene/polyaniline/polystyrene (G/PANI/PS)	This nanocomposite elaborated by electrospinning method was tested for the detection of Pb^{2+} and Cd^{2+} by using anodic stripping voltammetry (ASV) which reached respectively 3.30 and 4.43 µg/L	[94]
Nanorod-like nanocomposite of three-dimensional reduced graphene oxide and polyaniline (3D-rGO@PANI)	The nanorod-like nanocomposite of three-dimensional reduced graphene oxide and polyaniline by an in situ chemical oxidative polymerization method was prepared for the detection of mercury Hg^{2+} which reached about 0.035 nM	[95]
Platinum/oxide of graphene/polyaniline (Pt/GO-PANI)	This nanocomposite was prepared for the detection of carbaryl, carbofuran, and méthomyl which reached respectively 0.136, 0.145, and 0.203 mg/L	[96]
Poly (3,4- ethylenedioxythiophene) doped with graphene dioxide (PEDOT/GO)	The PEDOT/GO was prepared for the determination of the dopamine, where the limits of detection reached 39 nM	[88]
Molecularly imprinted polymer/graphene oxide (MIP/GO)	The molecularly imprinted polymer based on polypyrrole film with incorporated graphene oxide was fabricated and used for electrochemical determination of quercetin which reached 48 nmol/L	[97]

limitations or allow the production of free-standing parts with complex shapes, higher deposition rates, produce coatings on widely differing substrates, ability to produce structural features with sizes ranging from nm to µm, easy to control alloy composition, ability to produce compositions unattainable by other techniques, and the possibility of forming of simple low-cost multilayers in many different systems, like Cu/Ni, Ni/Ni–P etc. [99].

Genovese et al. have fabricated multi-walled carbon nanotube (MWCNT) electrodes modified with mixtures of $PMo_{12}O_{40}{}^{3-}$ (PMo_{12}) and $PW_{12}O_{40}{}^{3-}$ (PW_{12}). Keggin ions are investigated for electrochemical capacitor (EC) applications. They have shown that to engineer the modification of the electrode's surface by the polyoxometalate coatings represents a promising strategy for the development of high-performance pseudocapacitive electrodes [100].

Soldatkina et al. have fabricated a urea biosensor using nano-sized zeolites by spin coating method. The results showed that the nano-sized zeolite has offered a large surface area, which worked as an excellent matrix for the immobilization of different

enzymes. Spin coating method has been successfully applied for preparing films of polymers, also for making thin films/seed layers of metal oxides for solar cells, gas sensors, and light emitting diodes. However, one of its main drawbacks is the step of calcination at a higher temperature to transfer the sol–gel to stable metal oxide NP films; this step limits the use of flexible and polymer-based electrodes [101].

6 Conclusions

Nanotechnology has solved several environmental and human problems; it has been successfully used to facilitate our lives. Coupling nanotechnology with electrochemistry has enhanced the performance of the electrodes used in many applications especially environmental ones. This coupling has provided rapidity, purity of products as well as production of coatings on widely varying surfaces.

The coating has shown a powerful tool able to enhance the advantages of any nanoparticle materials. Electrodes modified or coated with nanomaterials have significantly improved the sensitivity of and the selectivity of the used techniques for the detection of a variety of pollutant.

Nanotechnology will have a profound impact on a wide run of applications and hence on numerous perspectives of human life, including natural decontamination, water decontamination, cheaper power, and better disease treatment modalities. One major challenge confronting industry and government is the need for data on the conceivable adverse health impacts caused by the introduction of different nanomaterials. Improvement of security guidelines by the government for the nanotechnology industries, counting fabricating, monitoring of specialist introduction, the surrounding discharge of NPs, and chance assessments is required to promote nanotechnology for its economic incentives and restorative applications.

References

1. Ghassan AA, Mijan N-A, Taufiq-Yap YH (2020) Nanomaterials: an overview of nanorods synthesis and optimization. Nanorods Nanocomposites 1–24. https://doi.org/10.5772/intechopen.84550
2. Mourdikoudis S, Pallares RM, Thanh NTK (2018) Characterization techniques for nanoparticles: comparison and complementarity upon studying nanoparticle properties. Nanoscale 10:12871–12934. https://doi.org/10.1039/c8nr02278j
3. Fritea L, Banica F, Costea TO et al (2021) Metal nanoparticles and carbon-based nanomaterials for improved performances of electrochemical (Bio)sensors with biomedical applications. Materials (Basel) 14. https://doi.org/10.3390/ma14216319
4. Tajik S, Beitollahi H, Nejad FG et al (2020) RSC Adv 10:21561–21581. https://doi.org/10.1039/d0ra03672b
5. Mas'ud NW (2013) 53:1689–1699

6. Wang D, Pillai SC, Ho SH et al (2018) Plasmonic-based nanomaterials for environmental remediation. Appl Catal B Environ 237:721–741. https://doi.org/10.1016/j.apcatb.2018.05.094
7. Li J, Zhao T, Chen T et al (2015) Engineering noble metal nanomaterials for environmental applications. Nanoscale 7:7502–7519. https://doi.org/10.1039/c5nr00857c
8. Corsi I, Winther-Nielsen M, Sethi R et al (2018) Ecofriendly nanotechnologies and nanomaterials for environmental applications: key issue and consensus recommendations for sustainable and ecosafe nanoremediation. Ecotoxicol Environ Saf 154:237–244. https://doi.org/10.1016/j.ecoenv.2018.02.037
9. Othmani A, Kesraoui A, Akrout H et al (2019) Use of alternating current for colored water purification by anodic oxidation with SS/PbO_2 and Pb/PbO_2 electrodes. Environ Sci Pollut Res 26:25969–25984. https://doi.org/10.1007/s11356-019-05722-w
10. Othmani A, Magdouli S, Kumar PS et al (2021) Agricultural waste materials for adsorptive removal of phenols, chromium (VI) and cadmium (II) from wastewater: a review Agricultural waste materials for adsorptive removal of phenols, chromium (VI) and cadmium (II) from wastewater: a review. Published Online First 2021. https://doi.org/10.1016/j.envres.2021.111916
11. Othmani A (2021) Use of agricultural materials for the anodic oxidation of Amaranth using SS/PbO_2 anodes. Chem Eng Technol 1–16. https://doi.org/10.1002/ceat.202100063
12. Chang J, Zhou G, Christensen ER et al (2014) Graphene-based sensors for detection of heavy metals in water: a review chemosensors and chemoreception. Anal Bioanal Chem 406:3957–3975. https://doi.org/10.1007/s00216-014-7804-x
13. Lamberti M, Zappavigna S, Sannolo N et al (2014) Advantages and risks of nanotechnologies in cancer patients and occupationally exposed workers. Expert Opin Drug Deliv 11:1087–1101. https://doi.org/10.1517/17425247.2014.913568
14. Ali AS (2020) Application of nanomaterials in environmental improvement. Nanotechnol Environ 1–20. https://doi.org/10.5772/intechopen.91438
15. Dolez PI (2015) Nanomaterials definitions, classifications, and applications. https://doi.org/10.1016/B978-0-444-62747-6.00001-4
16. Singh V, Yadav P, Mishra V (2020) Recent advances on classification, properties, synthesis, and characterization of nanomaterials. Green Synth Nanomater Bioenergy Appl 83–97. https://doi.org/10.1002/9781119576785.ch3
17. Von RA, Geurts P, Jansen M et al (2012) Influence of partner diversity on collaborative public R&D project outcomes: a study of application and commercialization of nanotechnologies in the Netherlands. Technovation 32:227–233. https://doi.org/10.1016/j.technovation.2011.12.001
18. Kandil MM, Nuclear E, Authority RR (2020) The role of nanotechnology in electronic properties of electronic properties of materials Dr. Magy Mohamed Kandil
19. Yokoyama H (2009) Nanotechnology: a breakthrough toward a resource and energy compatible society. Nanotechnology
20. Gayathri A, Satyanarayana T (2018) Applications of nanotechnology in electronics and communication engineering 1. Int J Adv Manag Technol Eng Sci 8:698–705. http://ijamtes.org/
21. Khan FH (2013) Chemical hazards of nanoparticles to human and environment (a review). Orient J Chem 29:1399–1408. https://doi.org/10.13005/ojc/290415
22. Modi S, Prajapati R, Inwati GK et al (2022) Recent trends in fascinating applications of nanotechnology in allied health sciences. Crystals 12. https://doi.org/10.3390/cryst12010039
23. Alok A, Kishore M, Panat S et al (2013) Nanotechnology: a boon in oral cancer diagnosis and therapeutics. SRM J Res Dent Sci 4:154. https://doi.org/10.4103/0976-433x.125591
24. Khoo KS, Chia WY, Tang DYY et al (2020) Nanomaterials utilization in biomass for biofuel and bioenergy production. Energies 13. https://doi.org/10.3390/en13040892
25. Allsopp M, Walters A, Santillo D (2007) Nanotechnologies and nanomaterials in electrical and electronic goods: a review of uses and health concerns. Greenpeace Res Lab 1–22. http://www.nanometer.ru/2007/12/26/nanomaterial_5521/PROP_FILE_files_1/nanotech_in_electronics_2007.pdf

26. Zhu W, Bartos PJM, Porro A (2004) Application of nanotechnology in construction summary of a state-of-the-art report. Mater Struct Constr 37:649–658. https://doi.org/10.1617/14234
27. Okoli JU, Briggs TA, Major IE (2013) Application of nanotechnology in the manufacturing sector: a review. Niger J Technol 32:379–385
28. Antonovič V, Pundiene I, Stonys R et al (2010) A review of the possible applications of nanotechnology in refractory concrete. J Civ Eng Manag 16:595–602. https://doi.org/10.3846/jcem.2010.66
29. Seery MK, McDonnell C (2013) The application of technology to enhance chemistry education. Chem Educ Res Pract 14:227–228. https://doi.org/10.1039/c3rp90006a
30. Wang L, Zhang Q, Chen B et al (2020) Some issues limiting photo(cata)lysis application in water pollutant control: a critical review from chemistry perspectives. Water Res 174. https://doi.org/10.1016/j.watres.2020.115605
31. Ilyas RA, Sapuan SM (2020) Biopolymers and biocomposites: chemistry and technology. Curr Anal Chem 16:500–503. https://doi.org/10.2174/1573411016052006030953 11
32. Giglou SM, Rashidi A, Manidari Z (2020) Investigating the application of technology acceptance model in smart schools. Interdiscip J Virtual Learn Med Sci 11. https://doi.org/10.30476/ijvlms.2020.85494.1022.perceived
33. Li X, Zhou Y, Xue L et al (2015) Integrating bibliometrics and roadmapping methods: a case of dye-sensitized solar cell technology-based industry in China. Technol Forecast Soc Change 97:205–222. https://doi.org/10.1016/j.techfore.2014.05.007
34. Sustainable nanotechnology for environmental remediation (2022). https://doi.org/10.1016/c2020-0-01522-7
35. Mohan VB, Lau K tak, Hui D et al (2018) Graphene-based materials and their composites: a review on production, applications and product limitations. Compos Part B Eng 142:200–220. https://doi.org/10.1016/j.compositesb.2018.01.013
36. CEDEFOF (2007) Skill needs in emerging technologies: nanotechnology. Cedefop, Thessaloniki, GR, p 65. http://scholar.google.com/scholar?hl=en&btnG=Search&q=intitle:Skill+needs+in+emerging+technologies:+nanotechnology#9
37. Ambaye AD, Kefeni KK, Mishra SB et al (2021) Recent developments in nanotechnology-based printing electrode systems for electrochemical sensors. Talanta 225:121951. https://doi.org/10.1016/j.talanta.2020.121951
38. de Dios AS, Díaz-García ME (2010) Multifunctional nanoparticles: analytical prospects. Anal Chim Acta 666:1–22. https://doi.org/10.1016/j.aca.2010.03.038
39. Baig N, Kammakakam I, Falath W et al (2021) Nanomaterials: a review of synthesis methods, properties, recent progress, and challenges. Mater Adv 2:1821–1871. https://doi.org/10.1039/d0ma00807a
40. Nanoparticles: properties, applications and toxicities. Arab J Chem 12:908–931. https://doi.org/10.1016/j.arabjc.2017.05.011
41. Yun Q, Li L, Hu Z et al (2020) Layered transition metal dichalcogenide-based nanomaterials for electrochemical energy storage. Adv Mater 32:1–29. https://doi.org/10.1002/adma.201903826
42. Kour R, Arya S, Young S-J et al (2020) Review—recent advances in carbon nanomaterials as electrochemical biosensors. J Electrochem Soc 167:037555. https://doi.org/10.1149/1945-7111/ab6bc4
43. He Y, Pei M, Du Y et al (2014) Synthesis, characterization and application of chitosan coated Fe_3O_4 particles as an adsorbent for the removal of furfural from aqueous solution. RSC Adv 4:30352–30357. https://doi.org/10.1039/c4ra04098h
44. Li Z, Mohamed MA, Vinu Mohan AM et al (2019) Application of electrochemical aptasensors toward clinical diagnostics, food, and environmental monitoring: review. Sensors (Switzerland) 19. https://doi.org/10.3390/s19245435
45. Marín S, Merkoçi A (2012) Nanomaterials based electrochemical sensing applications for safety and security. Electroanalysis 24:459–469. https://doi.org/10.1002/elan.201100576
46. Xu J, Hu Y, Wang S et al (2020) Nanomaterials in electrochemical cytosensors. Analyst 145:2058–2069. https://doi.org/10.1039/c9an01895f

47. Wang W, Wang X, Cheng N et al (2020) Recent advances in nanomaterials-based electrochemical (bio)sensors for pesticides detection. TrAC Trends Anal Chem 132:116041. https://doi.org/10.1016/j.trac.2020.116041
48. Guler M, Turkoglu V, Basi Z (2017) Determination of malation, methidathion, and chlorpyrifos ethyl pesticides using acetylcholinesterase biosensor based on Nafion/Ag@rGO-NH2 nanocomposites. Electrochim Acta 240:129–135. https://doi.org/10.1016/j.electacta.2017.04.069
49. Zhang P, Sun T, Rong S et al (2019) A sensitive amperometric AChE-biosensor for organophosphate pesticides detection based on conjugated polymer and Ag-rGO-NH 2 nanocomposite. Bioelectrochemistry 127:163–170. https://doi.org/10.1016/j.bioelechem.2019.02.003
50. Gila G (2021) Application of nanomaterials-based sensor for food analysis. Adv Food Anal Tools 213–235. https://doi.org/10.1016/b978-0-12-820591-4.00011-6
51. Choudhary M, Arora K, Advanced B (2022) Electrochemical biosensors electrochemical biosensors for early detection of cancer electrochemical medical biosensors for POC applications biosensing—drug delivery systems for in vivo applications
52. Grieshaber D, MacKenzie R, Vörös J et al (2008) Electrochemical biosensors—sensor principles and architectures. Sensors 8:1400–1458. https://doi.org/10.3390/s8031400
53. Ferrari AGM, Crapnell RD, Banks CE (2021) Electroanalytical overview: electrochemical sensing platforms for food and drink safety. Biosensors 11. https://doi.org/10.3390/bios11080291
54. Stradiotto NR, Yamanaka H, Zanoni MVB (2003) Electrochemical sensors: a powerful tool in analytical chemistry. J Braz Chem Soc 14:159–173. https://doi.org/10.1590/S0103-50532003000200003
55. Zhang K, Barhoum A, Xiaoqing C et al (2019) Handbook of nanofibers. https://doi.org/10.1007/978-3-319-53655-2
56. da Silva ETSG, Souto DEP, Barragan JTC et al (2017) Electrochemical biosensors in point-of-care devices: recent advances and future trends. ChemElectroChem 4:778–794. https://doi.org/10.1002/celc.201600758
57. Ng CP (2013) 基因的改变 NIH public access. Bone 23:1–7. https://doi.org/10.1021/la201801e.Antibacterial
58. Yuan X, Jiang Z, Wang Q et al (2020) Polychlorinated biphenyl electrochemical aptasensor based on a diamond-gold nanocomposite to realize a sub-femtomolar detection limit. ACS Omega 5:22402–22410. https://doi.org/10.1021/acsomega.0c02846
59. Azzouz A, Goud KY, Raza N et al (2019) Nanomaterial-based electrochemical sensors for the detection of neurochemicals in biological matrices. TrAC Trends Anal Chem 110:15–34. https://doi.org/10.1016/j.trac.2018.08.002
60. Lete C, López-iglesias D, García-guzmán JJ et al (2022) A sensitive electrochemical sensor based on sonogel-carbon material enriched with gold nanoparticles for melatonin determination. Sensors 22. https://doi.org/10.3390/s22010120
61. Abraham P, Renjini S, Vijayan P et al (2020) Review—review on the progress in electrochemical detection of morphine based on different modified electrodes. J Electrochem Soc 167:037559. https://doi.org/10.1149/1945-7111/ab6cf6
62. Naresh V, Lee N (2021) A review on biosensors and recent development of nanostructured materials-enabled biosensors. Sensors (Switzerland) 21:1–35. https://doi.org/10.3390/s21041109
63. Barek J (2021) How to improve the performance of electrochemical sensors via minimization of electrode passivation. Chemosensors 9:1–15. https://doi.org/10.3390/chemosensors9010012
64. Boumya W, Taoufik N, Achak M et al (2021) Chemically modified carbon-based electrodes for the determination of paracetamol in drugs and biological samples. J Pharm Anal 11:138–154. https://doi.org/10.1016/j.jpha.2020.11.003
65. Mauter MS, Elimelech M (2008) Environmental applications of carbon-based nanomaterials: critical review. Am Chem Soc 42:5843–5859

66. Guo S, Wang E (2011) Noble metal nanomaterials: controllable synthesis and application in fuel cells and analytical sensors. Nano Today 6:240–264. https://doi.org/10.1016/j.nantod.2011.04.007
67. Ibrahim RK, Hayyan M, AlSaadi MA et al (2016) Environmental application of nanotechnology: air, soil, and water. Environ Sci Pollut Res 23:13754–13788. https://doi.org/10.1007/s11356-016-6457-z
68. Aslam MMA, Kuo HW, Den W et al (2021) Functionalized carbon nanotubes (Cnts) for water and wastewater treatment: preparation to application. Sustain 13:1–54. https://doi.org/10.3390/su13105717
69. Singh M, Naveen BP (2014) Molecular nanotechnology: a new avenue for environment treatment. IOSR J Environ Sci Toxicol Food Technol 8:93–99. https://doi.org/10.9790/2402-08119399
70. Abdelbasir SM, McCourt KM, Lee CM et al (2020) Waste-derived nanoparticles: synthesis approaches, environmental applications, and sustainability considerations. Front Chem 8:1–18. https://doi.org/10.3389/fchem.2020.00782
71. John AC, Küpper M, Manders-Groot AMM et al (2017) Emissions and possible environmental Implication of engineered nanomaterials (ENMs) in the atmosphere. Atmosphere (Basel) 8:1–29. https://doi.org/10.3390/atmos8050084
72. Karn B (2005) Nanotechnology and the environment: applications and implications, p 391
73. Yu X, Tong S, Ge M et al (2013) Adsorption of heavy metal ions from aqueous solution by carboxylated cellulose nanocrystals. J Environ Sci (China) 25:933–943. https://doi.org/10.1016/S1001-0742(12)60145-4
74. Sun B, Zhang M, Hou Q et al (2016) Further characterization of cellulose nanocrystal (CNC) preparation from sulfuric acid hydrolysis of cotton fibers. Cellulose 23:439–450. https://doi.org/10.1007/s10570-015-0803-z
75. Sahoo BP, Tripathy DK (2017) Properties and applications of polymer nanocomposites: clay and carbon based polymer nanocomposites. Prop Appl Polym Nanocomposites Clay Carbon Based Polym Nanocomposites 1–222. https://doi.org/10.1007/978-3-662-53517-2
76. Blaney LM, Cinar S, SenGupta AK (2007) Hybrid anion exchanger for trace phosphate removal from water and wastewater. Water Res 41:1603–1613. https://doi.org/10.1016/j.watres.2007.01.008
77. Pan L, Wang Z, Yang Q et al (2018) Efficient removal of lead, copper and cadmium ions from water by a porous calcium alginate/graphene oxide composite aerogel. Nanomaterials 8. https://doi.org/10.3390/nano8110957
78. Xie K, Zhao W, He X (2011) Adsorption properties of nano-cellulose hybrid containing polyhedral oligomeric silsesquioxane and removal of reactive dyes from aqueous solution. Carbohydr Polym 83:1516–1520. https://doi.org/10.1016/j.carbpol.2010.09.064
79. Larbi OULARBI (2018) Etude de nanocomposites polypyrrole/nanoparticule de carbone par impédance électrochimique et Ac-électrogravimétrie: application aux capteurs électrochimiques
80. Kamyabi MA, Aghajanloo F (2008) Electrocatalytic oxidation and determination of nitrite on carbon paste electrode modified with oxovanadium(IV)-4-methyl salophen. J Electroanal Chem 614:157–165. https://doi.org/10.1016/j.jelechem.2007.11.026
81. Tonelli D, Scavetta E, Gualandi I (2019) Electrochemical deposition of nanomaterials for electrochemical sensing. Sensors (Switzerland) 19. https://doi.org/10.3390/s19051186
82. Royston E, Ghosh A, Kofinas P et al (2008) Self-assembly of virus-structured high surface area nanomaterials and their application as battery electrodes. Langmuir 24:906–912. https://doi.org/10.1021/la7016424
83. Zen JM, Kumar AS, Tsai DM (2003) Recent updates of chemically modified electrodes in analytical chemistry. Electroanalysis 15:1073–1087. https://doi.org/10.1002/elan.200390130
84. Sobha JD (2012) Electrodeposition: the versatile technique for nanomaterials. Woodhead Publishing Limited. https://doi.org/10.1533/9780857095800.1.86
85. Ahmad R, Wolfbeis OS, Hahn YB et al (2018) Deposition of nanomaterials: a crucial step in biosensor fabrication. https://doi.org/10.1016/j.mtcomm.2018.09.024

86. Maarof HI, Daud WMAW, Aroua MKD (2017) Recent trends in removal and recovery of heavy metals from wastewater by electrochemical technologies. Rev Chem Eng 33:359–386. https://doi.org/10.1515/revce-2016-0021
87. Chung PP, Wang J, Durandet Y (2019) Deposition processes and properties of coatings on steel fasteners—a review. Friction 7:389–416. https://doi.org/10.1007/s40544-019-0304-4
88. Wang W, Xu G, Cui XT et al (2014) Enhanced catalytic and dopamine sensing properties of electrochemically reduced conducting polymer nanocomposite doped with pure graphene oxide. Biosens Bioelectron 58:153–156. https://doi.org/10.1016/j.bios.2014.02.055
89. Saleh TA (2020) Nanomaterials: classification, properties, and environmental toxicities. Environ Technol Innov 20:101067. https://doi.org/10.1016/j.eti.2020.101067
90. Zhuang Z, Li J, Xu R et al (2011) Electrochemical detection of dopamine in the presence of ascorbic acid using overoxidized polypyrrole/graphene modified electrodes. Int J Electrochem Sci 6:2149–2161
91. Oularbi L, Turmine M, El Rhazi M (2017) Electrochemical determination of traces lead ions using a new nanocomposite of polypyrrole/carbon nanofibers. J Solid State Electrochem 21:3289–3300. https://doi.org/10.1007/s10008-017-3676-2
92. Peng C, Zhang S, Jewell D et al (2008) Carbon nanotube and conducting polymer composites for supercapacitors. Prog Nat Sci 18:777–788. https://doi.org/10.1016/j.pnsc.2008.03.002
93. Salavagione HJ, Díez-Pascual AM, Lázaro E et al (2014) Chemical sensors based on polymer composites with carbon nanotubes and graphene: the role of the polymer. J Mater Chem A 2:14289–14328. https://doi.org/10.1039/c4ta02159b
94. Promphet N, Rattanarat P, Rangkupan R et al (2015) An electrochemical sensor based on graphene/polyaniline/polystyrene nanoporous fibers modified electrode for simultaneous determination of lead and cadmium. Sens Actuators B Chem 526–534. https://doi.org/10.1016/j.snb.2014.10.126
95. Yang Y, Kang M, Fang S et al (2015) Electrochemical biosensor based on three-dimensional reduced graphene oxide and polyaniline nanocomposite for selective detection of mercury ions. Sens Actuators B Chem 214:63–69. https://doi.org/10.1016/j.snb.2015.02.127
96. Luzi-Thafeni L, Silwana B, Iwuoha E et al (2015) Graphene-polyaniline biosensor for carbamate pesticide determination in fruit samples. Biosens—Micro Nanoscale Appl. Published Online First 2015. https://doi.org/10.5772/61220
97. Sun S, Zhang M, Li Y et al (2013) A molecularly imprinted polymer with incorporated graphene oxide for electrochemical determination of quercetin. Sensors (Switzerland) 13:5493–5506. https://doi.org/10.3390/s130505493
98. Ramanavičius A, Ramanavičiene A, Malinauskas A (2006) Electrochemical sensors based on conducting polymer-polypyrrole. Electrochim Acta 51:6025–6037. https://doi.org/10.1016/j.electacta.2005.11.052
99. Gurrappa I, Binder L (2008) Electrodeposition of nanostructured coatings and their characterization—a review. Sci Technol Adv Mater 9. https://doi.org/10.1088/1468-6996/9/4/043001
100. Genovese M, Foong YW, Lian K (2015) Designing polyoxometalate based layer-by-layer thin films on carbon nanomaterials for pseudocapacitive electrodes. J Electrochem Soc 162:A5041–A5046. https://doi.org/10.1149/2.0071505jes
101. Soldatkina OV, Soldatkin OO, Kasap BO et al (2017) A novel amperometric glutamate biosensor based on glutamate oxidase adsorbed on silicalite. Nanoscale Res Lett 12. https://doi.org/10.1186/s11671-017-2026-8

Chapter 3
Nanotechnology: The Future for Green Buildings

Shubham Kumar Verma, Sahil Thappa, A. Sawhney, Y. Anand, and S. Anand

Abstract With the increasing population, demands for sustainability are also growing and hence can be closely related to the requirement for innovations in technology. Nanotechnology, a traditional and most rapidly growing science, can be regarded as a new technology for constructing sustainable buildings. They exhibit improved characteristics, distribution and morphology due to their size and are used in various scientific fields. Considering their good insulating abilities, better strength, and its ability to minimize carbon footprint and improve energy generation with photovoltaics, they can be considered as the future of building materials.

Keywords Nanotechnology · Green buildings · Sustainable buildings · Construction industry · Environmental implications

1 Introduction

The global population of the universe is growing at a very faster rate. The increasing population is causing an enhancement in the need for resources, and the need for shelter is one of the most prominent requirements of individuals. To accomplish the requirements of shelter, the construction rate is growing very swiftly and making the construction sector, one of the major consumers of energy. The buildings sector consumes more than one-third of global energy and results in an equivalent amount of carbon footprints [8]. This is impacting the environment and related phenomena

S. K. Verma · S. Thappa · S. Anand (✉)
School of Energy Management, Shri Mata Vaishno Devi University, Katra, J&K, India
e-mail: sanjeev.anand@smvdu.ac.in

Y. Anand (✉)
School of Mechanical Engineering, Shri Mata Vaishno Devi University, Katra, J&K, India
e-mail: y.anand@smvdu.ac.in

A. Sawhney
Department of Physics, GGM Science College, Jammu, J&K, India

D. Tripathi et al. (eds.), *Advancements in Nanotechnology for Energy and Environment*,
Advances in Sustainability Science and Technology,
https://doi.org/10.1007/978-981-19-5201-2_3

severely. The environmental problems can be directly related to energy production and consumption, climate change, inadequate air quality, water pollution, solid waste disposal, etc. Additionally, in comparison with other industries, the construction sector possesses the rare case that it generally experiences higher service life. Most of the developed structures remained there for more than a century with a typical service life between 80 and 100 years [19]. This implies that the building should be designed by keeping long-term performance outcomes in mind. However, in the present era, climate changes are observed more significantly and faster. These changes are impacting atmospheric temperature, rainy days, humidity level, etc., which on a longer perspective can deteriorate the indoor air quality, thus affecting the quality of lifestyle and energy resources significantly. To overcome these issues, many stakeholders are focusing on moving towards energy efficiency and sustainability which are considered as the future of the construction sector. This makes it important to shift the paradigm towards green/sustainable buildings from the very beginning of the project, i.e. design phase itself.

Green/sustainable building is a commonly used term that comprehensively addresses the environmental, ecological and social issues with respect to the community. The International Council for Research and Innovation in Building and Construction (ICRIBC) also elaborated on developing and operating a healthy building based on resource sufficiency, efficiency and ecological design as the basic requirements of sustainable construction [10]. The ICRIBC had also reported seven basic principles depicted in Fig. 1 as key to moving towards sustainability in the construction industry. These principles will also help in decision-making during the design and construction phases, thus impacting the life cycle of the buildings. Each of these principles/goals is having equal importance in making the buildings green/sustainable.

Further, Lechner [11], in their book stated that sustainability can be achieved by following the three-tier approach (Tiers 1–3). Tier 1 involves the reduction of loads

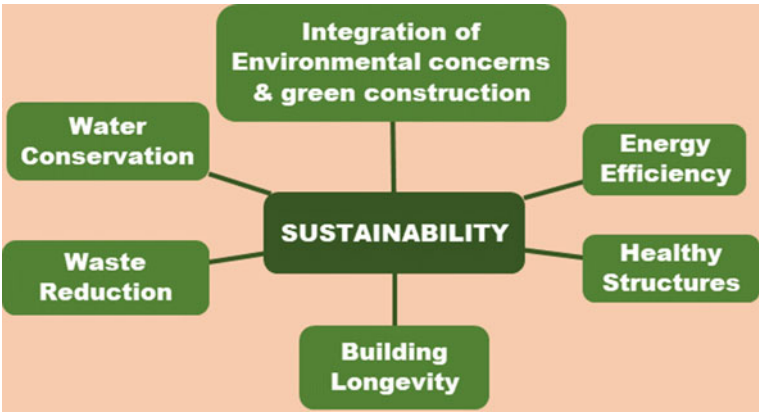

Fig. 1 Goals of sustainable development [10]

during the designing phase itself while utilization of passive means comes under Tier 2. Meanwhile, the third tier dictates the utilization of mechanical and electrical devices for substantiating the needs. They also reported that approximately 80–85% of the overall building's energy can be saved by adopting this tiered approach. Although, the adoption of renewable energy-based alternatives can generate the remaining energy and make the structures energy independent. Considering this, the international energy agency subsequently stated that there must be five-tier strategy for developing sustainable buildings [7]. They included Tier 0 and Tier 4 for site selection and renewable energy utilization as shown in Fig. 2. Further, they also stated that the incorporation of integrated technologies is the only way to find an optimal; however, it is required to link architect and engineer dominated societies together for finding sustainable/green solutions.

Further, green/sustainable buildings can be closely related to construction materials that how they are extracted, manipulated, manufactured and demolished. On average, approximately 15 billion tonnes of materials are being utilized in the building sector annually [6]. This material is equal to approximately half of the overall material flow. Also, it has been estimated that annually one-third of material gets wasted during construction activities. This makes the selection of materials extremely important for moving towards sustainable/green buildings [21]. In this context, the shift from traditional to high-performance and novel technologies in buildings will be possible only by bringing some novel aspects in terms of materials, coatings, insulations, adhesives, etc. The primary choice for developing innovative technologies could be nanotechnology. Earlier, its market applications have begun with small consumer devices, however, on a wider prospect, it can become the future of green buildings in the coming time [21].

Nanotechnology deals with studying and manipulating matter on an atomic and molecular scale as shown in Fig. 3. It is a science that involves developments in basic

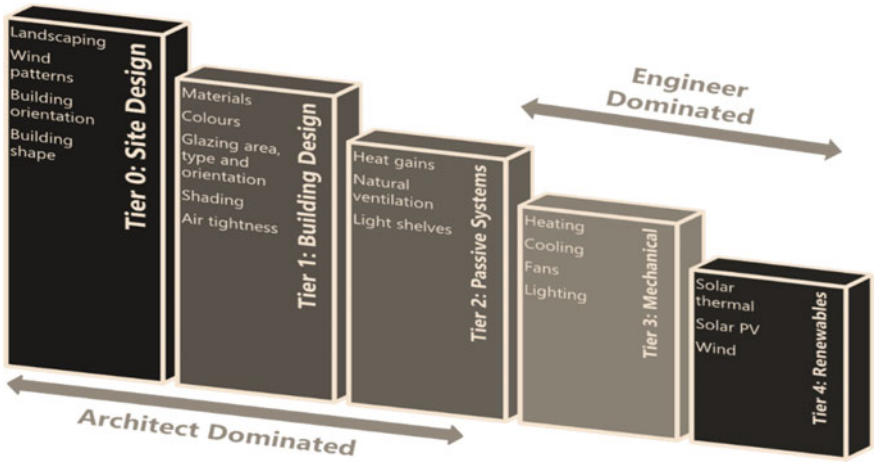

Fig. 2 Tiered approach for the integrated design process in buildings [7, 11]

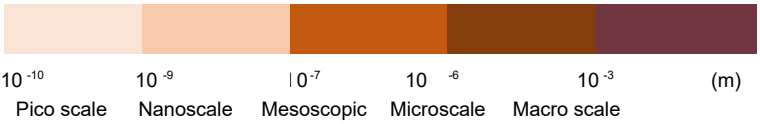

Fig. 3 Scale of measurement

physics and chemistry research. It is a recent and rapidly developing discipline that may be compared with the industrial revolution in terms of its impact on manufacturing, electronics, service industries, information technology, energy conservation, etc. Generally, nanotechnology is a field of science that deals with structures having a size smaller than 100 nm. It has been used across various industries for improving the environment and lifestyle on daily basis. In the building sector, nanotechnology offers several benefits by enhancing the properties of the material. Usually, traditional buildings are not much open to changes/innovations. Although, in the last few decades, demands for sustainability and green buildings are exaggerated, thus shifting the paradigm to applications of new materials and technologies.

The incorporation of the state-of-the-art technologies can be associated with nanocement, nanoparticle-based plasters/coatings, windows facets, etc. The addition of nanoparticles enhances the strength, durability, morphology and energy efficiency of the different materials. A futuristic energy-efficient house demonstrating nanotechnologies was presented in bluebook by Architecture, Engineering, Construction, Operations and Management [2] as shown in Fig. 4. They highlighted nanotechnology as an innovative way for transforming the construction industry into an energy-efficient sector. They reported that the incorporation of nanotechnology in houses can substantially increase the energy efficiency by 30% and hence can be observed as the future for moving towards sustainable/green buildings. Although, there exist certain limitations like its initial cost, manufacturing, etc., which resist its utilization. Considering all this, the present work is an attempt to showcase the selected representatives of nanotechnology along with their limitations/challenges in the construction sector. Further, this document is divided into three sections followed by an introduction. Section 2 outlines a few of the most common nanomaterials being used in the construction industry, while the selective major applications of nanomaterials were discussed in Sect. 3. Subsequently, Sect. 4 discussed the various challenges/issues faced by stakeholders in using nanomaterials in the construction industry. The purpose of this discussion is to highlight the importance of nanotechnology and showcase how nanotechnology can emerge as the future of green/sustainable buildings. Each of the prospects along with challenges for making the green buildings was elaborated in the subsequent sections.

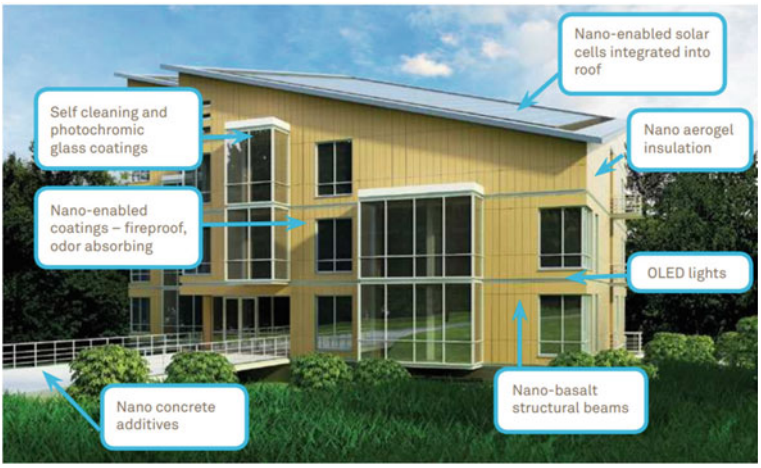

Fig. 4 Green/energy-efficient building of the future [2]

2 Types of Nanomaterials Used in the Construction Industry

Nanotechnology is a technique that works on a nanoscale (Fig. 3) and can produce a variety of products with improved properties. The products produced by nanotechnology are generally lighter and stronger due to their higher surface-to-volume ratio. Reduction from macroscale to nanoscale also asserts changes in optical absorption, electronic conductivity and mechanical properties. Also, it ascertains a remarkable increment in surface area, thus imparting improvement in surface morphology. This also impacts the chemical composition and properties of the structure. The improved properties cause improvement in tuneable wavelength-sensing ability, catalytic ability and result in better-designed pigments/paints with self-healing and self-cleaning properties. Further, there exists a variety of nanomaterials that are being used in different applications across the globe. However, a few of the most widely used materials in the construction industry are enlisted in Table 1.

3 Application of Nanotechnology for Developing Green Buildings

Green/sustainable buildings are considered as having the ability to maintain or improve the occupant's quality of life by ensuring comfort and energy efficiency in various constructional features. They minimize the consumption of resources and are considered as a key element for combating climate change. Also, the growth

Table 1 Most widely used nanomaterials in the construction industry [13]

S. No.	Material	Implementation	Health implications	Benefits
1	Titanium dioxide	Concrete	• Inflammation in lungs • Metabolic changes • Carcinogenesis	Enhances self-cleaning properties and degree of hydration
2	Carbon nanotubes	Concrete	• DNA damage • Inflammation • Oxidative stress	Prevents crack formation and improve durability
3	Aluminium oxide	Asphalt concrete Timber	Oxidative DNA damage	Good serviceability
4	Clay	Bricks mortar	Impacts the lungs on a wider scale	Increment in strength and surface roughness
5	Iron oxide	Concrete	Oxidative DNA damage	Increases compressive strength and make concreter abrasion resistant
6	Vanadium oxide	Glass	Headache, dizziness, nausea and vomiting	Reduces energy loads
7	Copper	Steel	DNA damage	Enhances formability, corrosion resistance and weldability
8	Silica	Concrete	Bronchoalveolar carcinoma-derived cells	Strengthened mechanical strength

in technology is having a major role in developing green buildings. The incorporation of nanotechnology is one of the most prominent options. Materials developed at nanoscale are having enhanced strength, durability and other characteristics which raise hygrothermal comfort and reduce energy consumption simultaneously. Further, there are clear opportunities for many firms which are commencing to work on nanomaterials. However, till now, nanotechnology is unable to make an impact on the construction industry as per its potential, due to its higher associated cost. Although, nanomaterials can be useful in a wide range of applications. It brings us a step forward with the material having higher performance and having a great impact on all the phases of the building. It adds on value to the construction by focusing on sustainability. Demirdoven [4], highlighted a value chain created by nanotechnologies in building design and construction as presented in Fig. 5. They reported that high-level integrative approaches are for all the phases of the buildings which is the need of the time. It has also been observed that the primary focus of the client is on comfort, durability, sustainability and aesthetics. The utilization of nanoscale materials fulfils all such requirements without affecting future needs much. Zhu et al. [23] also enlisted that the application of nanotechnology can bring revolution in the construction industry and can be the future of the industry. Further, a few of the most

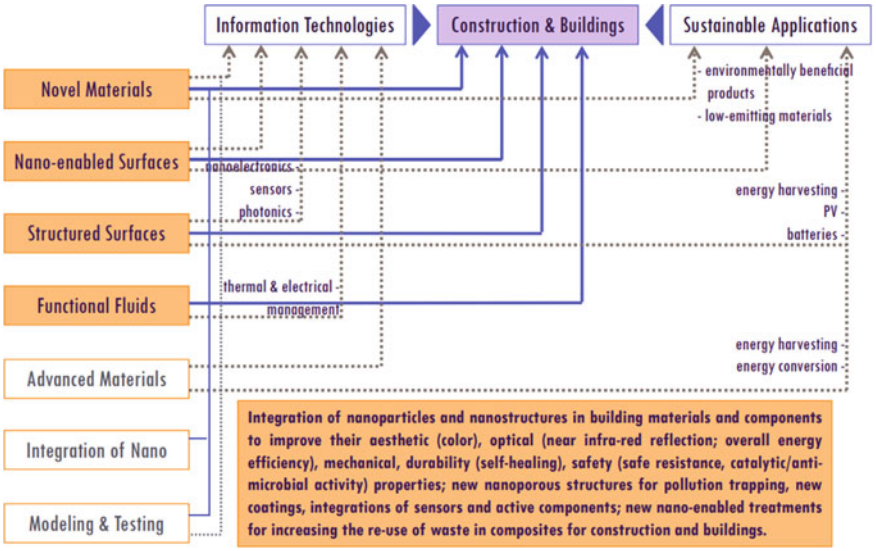

Fig. 5 Nanotechnology-enabled value chain for the construction industry [4]

common and widely used applications of nanomaterials in buildings are discussed in subsequent subheadings.

3.1 Nanomaterials-Based Cement

To ensure the longevity, durability and sustainability of the structure, strength and decomposition of structural elements are extremely important. One of the main requirements for maintaining the adequate strength of the structures is higher strength to weight ratio. This can be attained by ensuring a higher surface-to-volume ratio. Nanotechnology is one of the potential carriers which can enhance the strength, binding capabilities, durability and decomposability of such structures by increasing the surface-to-volume ratio. Nanotechnology enhances the material properties either by reinforcing the nanoparticles inside the existing materials or providing the structure developed by new materials. The majority of the structural member in buildings are developed with concrete. It is having the largest annual production among other materials. Cement is a major component used to develop concrete-based structures; however, the cement industry is alone responsible for 5% of the global anthropogenic carbon emissions [5]. Also, the production of cement is considered a highly emitting and energy-intensive process. Although, the cement industry is going through drastic improvements with the involvement of nanotechnology. In conventional concrete, SiO_2 is commonly used. However, in recent studies, it has been observed that the blending of cement with nanoparticles of silica, titania, and carbon nanotubes is

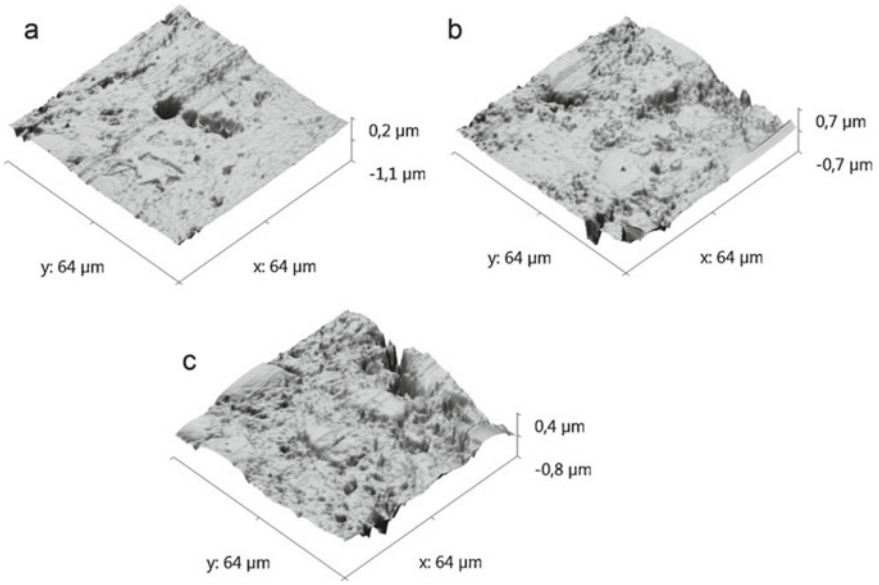

Fig. 6 Three-dimensional topology of cement slurry with **a** 0% nanoparticles, **b** 0.3% nanoparticles, and **c** 0.5% nanoparticles [24]

continuously used. It enhances the physical and mechanical properties of structures and results in enhanced durability of materials. A generalized influence showing the impact of the addition of nanoparticles on cement slurry is shown in Fig. 6.

3.2 Nanomaterial-Based Coatings

Blending nanomaterial with existing material or developing a material using new technologies is not the only applications of nanotechnology, although they can be used in buildings on a much wider scale. Thin-film coating (TFC) is one of the most valuable and developing technologies for moving towards energy efficiency [20]. A thin layer of nanoparticles can be imposed on traditional walls/windows to add to their performance along with their value. Not only this, although, it also enhances the comfort, energy efficiency, and most importantly aesthetics of the structures. Also, there are some coatings which are having wear-resistant, corrosion-resistant, antibacterial, fire-resistant and self-cleaning properties. Subsequently, the utilization of paints and spray in form of coating also add on the performance of the structures. Considering the wide spectrum of applications of coatings, it can be very useful in buildings. An illustration highlighting TiO_2 TFC-based self-cleaning glass system is shown in Fig. 7. This kind of coating cleans the various types of particles ranging from dust to rain on their own, thus can be very useful in construction industries.

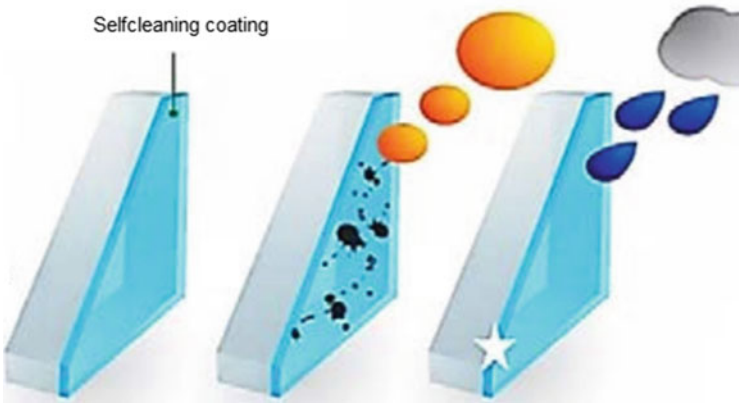

Fig. 7 Titanium oxide (TiO_2) coating-based self-cleaning glass system [3]

3.3 Nanomaterial-Based Thermal Insulations

The first and foremost important aspect of developing a green building is to reduce the heating/cooling load. Generally, buildings are developed to serve as a barrier between outdoor and indoor conditions which resist warm/cool air to penetrate inside the structure in respective seasons. However, improperly insulated buildings are unable to resist it adequately, thus making it important to use mechanical devices for heating/cooling and resulting in higher energy consumption. Although, as per the Kyoto Pyramid principles, the best way to achieve energy efficiency in the buildings is by providing better thermal insulation. There are a number of traditional insulations materials like glass wool, polyurethane foam, cellulose, polystyrene foam, cork, etc., available in the market. However, they need a thickness of approximately 250 mm to become efficient [1, 22]. However, availing of such high thickness insulation reduces the internal volume substantially while also resulting in higher costs. This makes it important to develop some high-performing insulation that is having a lower thickness and can able to work efficiently. Adopting nanotechnology-based thermal insulations can be quite a viable and promising solution for developing such low thickness and efficient insulations in comparison with conventional insulation panels [14]. Along with lower thickness, these insulations are 20–30% more efficient than conventional insulation. Also, Jelle [9], reported that nanotechnology can be futuristic technology for developing high-performing thermal insulation for buildings. In general, the majority of sectors focus on works on particles at an atomic and molecular scale, viz. 0.1–100 nm. Although, developing thermal insulations materials using nanotechnology requires dealing with pores rather than particles. Figure 8 highlights the various aspects of developing nanotechnology-based thermal insulation [9].

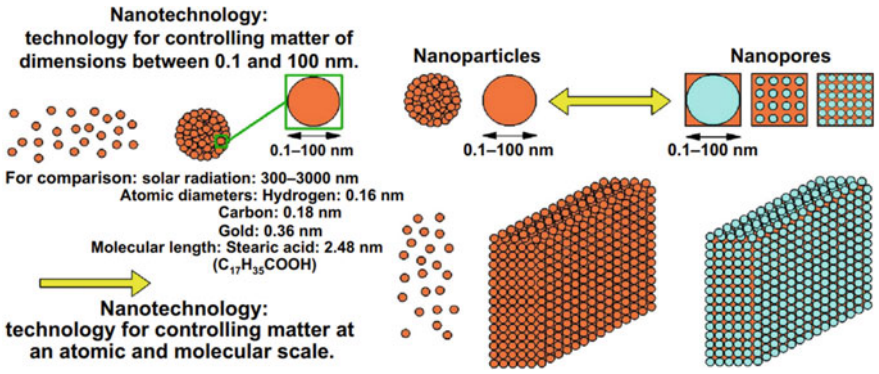

Fig. 8 Nanotechnology and its application to efficient thermal insulation materials [9]

3.4 Nanotechnology-Based Energy Savings/Generation

The building sector is one of the major consumers of energy and is responsible for an equivalent amount of carbon emissions. These consumptions, being unavoidable, are growing significantly due to climatic changes and hence the increased demand for indoor thermal comfort. However, the building sector is considered as having the maximum potential to minimize energy consumption, thus stressing the importance of moving towards energy-efficient buildings. This transition into energy-efficient buildings can be effectively achieved by adopting nanotechnology-based alternatives. There are several nano-based technologies for energy generation. Few among those are elaborated on below.

3.4.1 Smart Window-Based Technology

Windows are considered as one of the major sources of heat penetration inside the buildings. People generally use blinds, curtains, etc., to avoid this penetration up to some extent. However, using smart windows developed using nanoparticles of vanadium oxide (V_2O_5) can be one of the best alternatives for this. V_2O_5 is a nanotechnology-based material that belongs to the family of photochromic materials as shown in Fig. 9. It undergoes a transition from metal to an insulator when exposed over a temperature above 68 °C [16]. Windows are generally exposed to continuous solar radiation, and in peak summers glass temperature may be reached up to 68 °C [16]. The use of windows with vanadium coating under such conditions makes it enough capable of controlling internal temperature, thus resulting in an energy-efficient building.

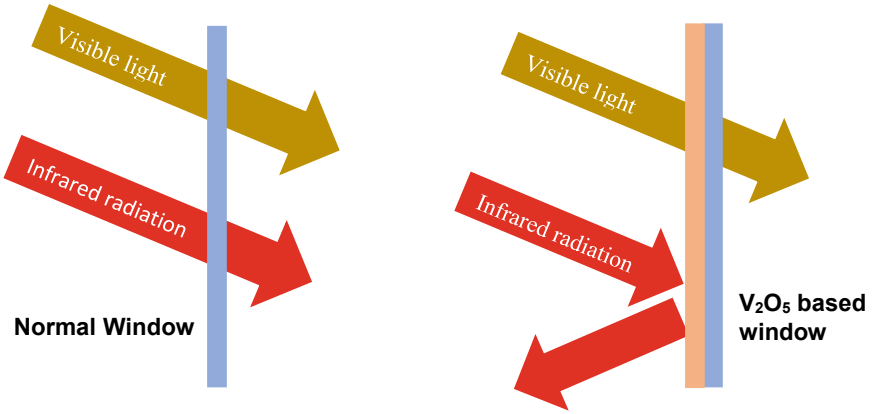

Fig. 9 Distinguishing major differences between normal and smart windows

3.4.2 PCM-Based Technology

Building material is another important source of heat gain in summers. Generally, the outer surface of buildings is exposed to solar radiation which heats the outer surface. This higher heat at the outer surface gets conducted and thus increases indoor temperature and results in the wastage of the heat energy. However, utilization of PCM based building elements can store this energy in day time which can be utilized in the night time as shown in Fig. 10. The primary purpose of PCM in building systems is to stock and discharge the energy as per the requirements. Redistributing the energy loads from on-peak to off-peak periods and vice versa would enable the latent thermal energy storage system to improve the heating/cooling efficacy. Phase change materials are the materials that are greatly favoured to attain the energy redistribution necessities in building by means of the latent thermal energy storage system. The addition of nanoparticle-based PCMs could further add on value to the system. They undergo a transition in the phase of material from solid to liquid during the daytime by absorbing the ambient energy. This heat gets released in the nighttime with the transition of a liquid to the solid phase, thus resulting in a lesser heat flow from indoors to outdoors and vice versa.

3.4.3 Third-Generation Photovoltaics

Requirements for producing low-cost renewable energy are essential with a view to eliminating the dependence on non-renewable sources of energy. Photovoltaic cell utilization is one of the ways to reduce dependence. However, their spectrum contains photons with energy spanning between 0.4 and 4.0 eV, thus substantiating the lower efficacy which is always a concern [18]. Although, the rise of a third-generation PV technology which is in starting phase can be seen as a blinking light in dark. Quantum

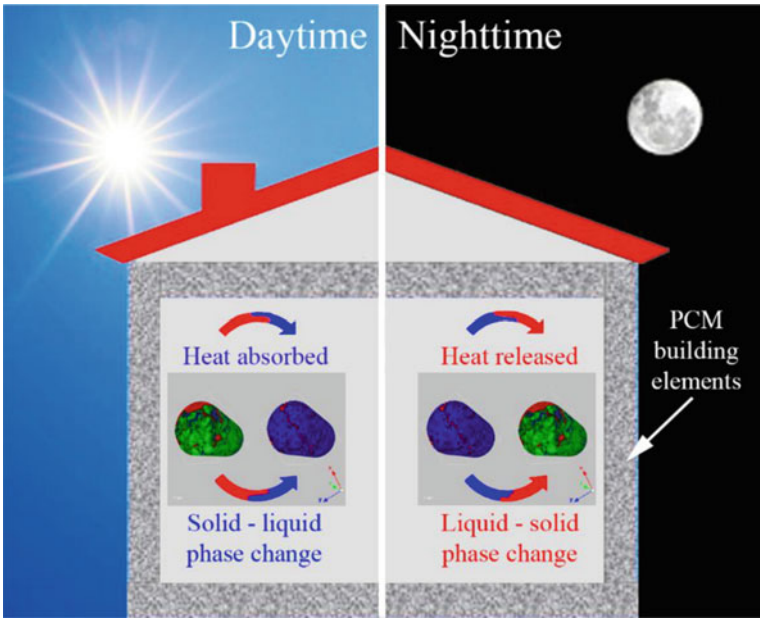

Fig. 10 Working process of PCMs in buildings [17]

dots, perovskites and solar cells sensitized by dyes are the three most widely used nanotechnologies based on the third-generation technological advancements. They are having the ability to develop high efficacy conversion devices that can convert photons into electricity at a lower cost. When semiconductor's charge carriers are confined by potential barriers to small regions of space, huge quantization of charge occurs. These regions are having confinement less than that de Broglie wavelength of the charge carriers. Later when the holes and electrons are limited by potential barriers in three spatial dimensions, this system is termed as a quantum dot. They are generally nano-dimensional structures which are having a narrow bandgap. They are generally not so expensive, thus can be integrated into devices with higher potential efficacy [15] and can be a very useful technology for solar energy generation in the building sector.

4 Challenges to Adopting Nanotechnology in Construction Industry

Nanotechnology is one of the fastest-growing industries globally. Its wider applicability and high-performing ability had made it one of the most demanding fields. From the perspective of the construction industry, nanotechnology is considered as

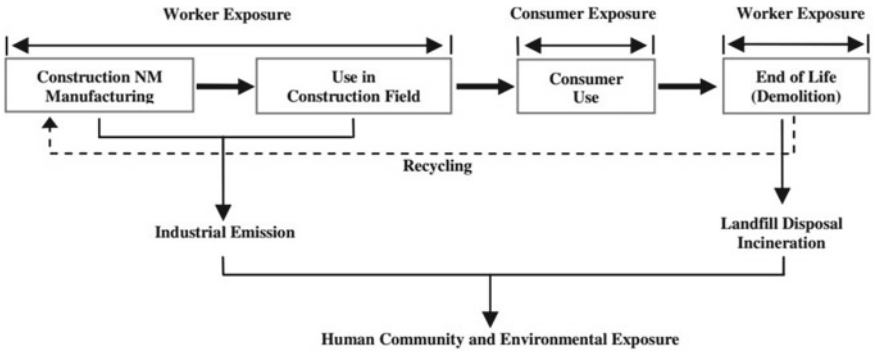

Fig. 11 Possible negative implications of nanomaterials in the construction industry [12]

to bring revolution in a particular sector. A significant hike in the utilization of nanostructures of concrete, bricks, timber, steel, wood, etc., has been substantially observed in the last decade. The incorporation of nanomaterials-based structures enhances the building's strength, durability, wear/tear resistance, makes it aesthetically pleasing, etc. Although withstanding the exceptional features of incorporating nanotechnology, there exist some limitations/challenges that various stakeholders face. A generalized schematic highlighting the main issue is showcased in Fig. 11. Starting from developing a nanomaterial to its demolition, some serious consequences impact the human body and environment significantly. Further few of the major challenges/issues faced by various stakeholders are detailed below.

4.1 Health Implications

Utilizing nanomaterials poses serious threats to the human body. Due to the nanoscale size of the particles, they generally travel in air, thus posing a serious threat of inhalation. Titanium oxide is one of the most commonly used nanomaterials in the construction industry. Although, it has been reported that inhalation of TiO_2 nanoparticles results in infiltration of inflammatory cells, tumorigenesis in mouse lung tissue and reduced body weight. Further, several studies reported dermal exposure as another important aspect that impacts human health. It has been observed that silver and gold-based nanoparticles can penetrate through the skin and cause serious threats, while nickel, cobalt, and palladium release ions in the body, thus considered more hazardous. So, it is extremely important to wear proper equipment while using such nanoparticles.

4.2 Environmental Implications

Nanomaterials being used in various applications are generally very small and can travel in the air, thus posing increased threats of air pollution. They are released by different channels which may be intentional/unintentional, thus causing threats to the environment. Further, a very high amount of energy is required for the synthesis of nanoparticle-based material. Also, they disseminate toxic gases and have lower recovery, thus harming the environment.

4.3 Associated Cost

Lastly, one of the major challenges of nanotechnology faced by researchers is its associated cost. They are generally having a high cost and are not being used by the common masses. It is required to develop some cost-effective nanomaterials which are sustainable in nature and can be used by common people. Also, this brings in the importance of the life cycle assessment of the material which is quite a critical parameter for developing any material.

5 Conclusion

In today's world, the construction sector is one among the most energy-intensive sector and is considered as having the most potential to save energy. This potential can be utilized by focusing on sustainability which is prospectively most important for moving towards green buildings. However, the incorporation of traditional strategies is not that much efficient, thus demanding some novel aspects to develop high-performing technologies. Nanotechnology is one of the most rapidly growing technologies which is seeking a lot much attention globally. It is having some unique characteristics which raise the bar of expectations to another level. Nanotechnology is having the potential to bring revolution to the construction industry by bringing novel materials. There are a variety of nanomaterials like titanium dioxide, carbon nanotubes, aluminium oxide, iron oxide, etc., available in the market. They are having a wider range of applications from reducing the heating/cooling load to the generation of electricity. However, there are some challenges like cost, environmental impact, health implications, etc., which restrict its utilization in the buildings sector. It is required to conduct the studies related to health implications and life cycle assessment on a wider scale. Considering the high-performing and energy-efficient behaviour of nanomaterials in the construction industry, their adoption in buildings can be confronted as a futuristic point for developing energy-efficient and sustainable buildings. Further, developing materials from the local climatic materials themselves might be a viable solution from a futuristic point of view.

References

1. Abdelrady A, Abdelhafez MHH, Ragab A (2021) Use of insulation based on nanomaterials to improve energy efficiency of residential buildings in a hot desert climate. Sustainability 13(9):5266
2. AECOM (2014) The blue book. Property and construction handbook international edition
3. Boostani H, Modirrousta S (2016) Review of nanocoatings for building application. Procedia Eng 145:1541–1548
4. Demirdoven J (2012) Nanotechnology enabling BIM for facility owners. In: Ecobuild America 2012 conference, Washington, DC
5. Durastanti C, Moretti L (2020) Environmental impacts of cement production: a statistical analysis. Appl Sci 10(22):8212
6. Huang B, Gao X, Xu X, Song J, Geng Y, Sarkis J, Nakatani J (2020) A life cycle thinking framework to mitigate the environmental impact of building materials. One Earth 3(5):564–573
7. IEA (2019) Energy efficiency in buildings. International Energy Agency
8. IEA (2021) World energy balances: overview, IEA, Paris. https://www.iea.org/reports/world-energy-balances-overview
9. Jelle BP (2016) Nano-based thermal insulation for energy-efficient buildings. In: Start-up creation. Woodhead Publishing, pp 129–181
10. Kibert CJ (2016) Sustainable construction: green building design and delivery. Wiley
11. Lechner N (2014) Heating, cooling, lighting: sustainable design methods for architects. Wiley
12. Lee J, Mahendra S, Alvarez PJJ (2009) Potential environmental and human health impacts of nanomaterials used in the construction industry. In: Nanotechnology in construction, vol 3. Springer, Berlin, Heidelberg, pp 1–14
13. Mohajerani A, Burnett L, Smith JV, Kurmus H, Milas J, Arulrajah A, Abdul Kadir A (2019) Nanoparticles in construction materials and other applications, and implications of nanoparticle use. Materials 12(19):3052
14. Nawar AH (2021) Nano-technologies and nano-materials for civil engineering construction works applications. Mater Today: Proc
15. Nozik AJ, Beard MC, Luther JM, Law M, Ellingson RJ, Johnson JC (2010) Semiconductor quantum dots and quantum dot arrays and applications of multiple exciton generation to third-generation photovoltaic solar cells. Chem Rev 110(11):6873–6890
16. Papadaki D, Kiriakidis G, Tsoutsos T (2018) Applications of nanotechnology in construction industry. In: Fundamentals of nanoparticles. Elsevier, pp 343–370
17. Podara CV, Kartsonakis IA, Charitidis CA (2021) Towards phase change materials for thermal energy storage: classification, improvements and applications in the building sector. Appl Sci 11(4):1490
18. Semonin OE, Luther JM, Beard MC (2012) Quantum dots for next-generation photovoltaics. Mater Today 15(11):508–515
19. Sev A, Ezel M (2014) Nanotechnology innovations for the sustainable buildings of the future. World Acad Sci Eng Technol Int J Civ Environ Struct Constr Archit Eng 8(8):886–896
20. Thappa S, Chauhan A, Sawhney A, Anand Y, Anand S (2020) Thermal selective coatings and its enhancement characteristics for efficient power generation through parabolic trough collector (PTC). Clean Technol Environ Policy 22(3):557–577
21. Verma SK, Anand Y, Gupta N, Jindal BB, Tyagi VV, Anand S (2022) Hygrothermal dynamics for developing energy-efficient buildings: building materials and ventilation system considerations. Energy Build 111932
22. Yang C, Li YJ, Gao X, Xu L (2012) A review of vacuum degradation research and the experimental outgassing research of the core material-PU foam on vacuum insulation panels. Phys Procedia 32:239–244

23. Zhu W, Bartos PJ, Porro A (2004) Application of nanotechnology in construction. Mater Struct 37(9):649–658
24. Zyganitidis I, Stefanidou M, Kalfagiannis N, Logothetidis S (2011) Nanomechanical characterization of cement-based pastes enriched with SiO_2 nanoparticles. Mater Sci Eng B 176(19):1580–1584

Chapter 4
Application of Green Energy for Drying of Food Products

Ankit Srivastava, Abhishek Anand, Amritanshu Shukla, Richa Kothari, D. Buddhi, F. Bruno, and Atul Sharma

Abstract Drying food products is the oldest and cheapest technique of preserving food for a long time. Since green energy is abundant and free, adopting green energy in the drying process is the best solution for food product drying. Drying involves reducing moisture content from food products, which aids in long-term food preservation and prevents food product deterioration. Several drying methods are developed utilizing green energy (solar, wind, biomass, geothermal energy, etc.) in the drying process. Solar energy can be used majorly for drying applications, and other sources of green energy can be used for enhancing the drying performance. The solar drying method includes direct, indirect, and mixed-mode drying processes. Products relating to food are placed in direct sunlight exposure for drying in the direct method, which may influence the color, fragrance, and nutrient value of the dried material after drying. In the indirect method, solar energy is typically employed to create warm air that is used to dry food goods, but in the mixed method, a combination of direct and indirect methods is used for drying. Several technical advancements in the field of food product drying have occurred in recent years, resulting in more efficient energy use and the production of high-quality dried products. Even though solar energy is irregular in nature, so there is a chance for reabsorption of moisture content in the surrounding environment to food products to be dried. So, energy storage is required to overcome this limitation. Green energy storage technology is used to facilitate

A. Srivastava · A. Anand · A. Shukla · A. Sharma (✉)
Non-Conventional Energy Laboratory, Rajiv Gandhi Institute of Petroleum Technology, Jais, Amethi, India
e-mail: asharma@rgipt.ac.in

A. Shukla
Department of Physics, University of Lucknow, Lucknow, India

R. Kothari
Department of Environmental Sciences, Central University of Jammu, Jammu, India

D. Buddhi
UIT, Uttaranchal University, Dehradun, India

F. Bruno
Future Industries Institute, University of South Australia, Mawson Lakes, Australia

D. Tripathi et al. (eds.), *Advancements in Nanotechnology for Energy and Environment*,
Advances in Sustainability Science and Technology,
https://doi.org/10.1007/978-981-19-5201-2_4

the drying process. The theory of food products drying, technological developments, and the economics of different drying techniques to dry food products are given and explored in this chapter. Finally, the most important problems and possibilities of drying technology are investigated.

Keywords Green energy · Solar dryers · Thermal energy storage · Phase change materials

1 Introduction

Food consumption is increasing as the world's population grows rapidly, and a lot of food is lost during the post-harvesting season in developing countries due to inadequate storage facilities. To satisfy future food demand, it is vital to limit food waste and store food after the harvesting season. As cold storage facilities in developing countries are limited, it is preferable to preserve food through the drying process so that future food demand may be met by dried food items. Drying is the most efficient and cost-effective means of extending the shelf life of most foods since the microbial activity is significantly decreased. Farmers have also acknowledged the necessity of improving the storage life of their products to maximize the return on their investment. Another well-known fact is that drying decreases total shipping costs while also increasing shelf life. In general, drying is now an essential component of the food processing [1].

Drying with conventional energy sources is very expensive and produces carbon emissions. As a result, using green sources of energy for the drying process is a better and more cost-effective option. The oldest and most cost-effective method of drying food products is to use solar energy. Although solar energy has been used for food drying in developing countries for decades as an open sun drying method, this method has several limitations, including over- and under-drying, a high manual labor requirement, dirt inclusion in the drying products, etc. These limitations of open sun drying can be eliminated with specially designed solar dryers, in which solar energy is properly utilized for the purpose of drying, and the problem of under- and over-drying is also removed [2].

In today's climate, current trends are toward higher oil expenses and uncertainty about future expenses and availability. Probably, the use of solar dryers will expand and be economically viable in the drying of agricultural products in the near future. By warming up the air to around 10–30 °C, solar dryer gives higher drying speeds, which enables faster air circulation, less moisture, and avoids bugs. Drying is an advanced method involving mass exchange and heat between the surface of the product and the medium around it [3].

Solar drying technology promotes a variety of products for preserving food in domestic as well as industrial sectors in a simpler way. It makes a certain product considerably more difficult, increases storage capacity, makes transport more cost-effective and easier, and regulates direct or indirect environmental gain. Therefore, a strong solar dryer system will help farmers increase their income [4].

The correct drying innovations using green energy can be used as options to boost product quality and minimize product losses. Solar drying is the best solution for enhancing product quality. Other green sources of energy also can be used with solar energy to make the drying process more efficient [5].

This book chapter focuses on green energy sources that may be used to dry food products. Solar energy is a fantastic green source of energy that may be employed directly in food drying activities. Other green energy resources can be used with solar energy to increase drying efficiency while maintaining product quality.

2 Fundamentals of Food Drying

Drying is simply a method of extracting moisture from a solid by evaporating it. Drying is not widely considered to be a mechanical method of insulating a liquid substance. A compact review of the necessary drying requirements for agricultural products shall be carried out in the appropriate region [6]. These criteria usually refer to traditional mechanical drying and relate mainly to solar drying. Either way, when it is finished, traditional drying norms and wonders are free energy used [7].

Product drying is an unpredictable process of heat and mass exchange that relies on external properties like temperature, humidity, and air speed and drying material properties such as surface attributes, composition, physical structure, and the physical dimension of the product [8]. The moisture transfer rate from the component to the external air from one object to the next depends on the content which is hygroscopic or non-hygroscopic [9]. It is possible to dry non-hygroscopic material to a humidity level of zero, while the residual moisture content of the hygroscopic material is constantly present. This moisture content in hygroscopic material might abound moisture content or unbound moisture content which stays in material because of surface tension of water [10].

3 Solar Energy-Based Drying System

The conventional technique of drying agricultural goods in developing nations is to disperse the material at an open to sun place in a fine layer. Natural drying does not require cash apart from some jobs, but because of no control over-drying rate, unhygienic, and food loss, it brings in low quality of goods. Solar energy can be used effectively for managed drying, thereby producing high-quality goods [11]. All things considered, controlled drying includes regulating the parameters of drying such as air temperature, humidity, drying rate, moisture content, and wind strength. In this way, the solar dryer should be designed with caution considering all of the drying parameters above and the dryer's properties. Since there are numerous choices in the solar dryer program, the design of solar dryers thus offers huge options [12].

3.1 Classification of Solar Dryer

Solar dryers were categorized from several viewpoints. However, as per the possible air movement within the drying chamber of the solar dryer, these may generally be categorized into two types: passive solar dryer (natural air circulation/convection-based solar dryer) and active solar dryer (forced air circulation/convection-based solar dryer) as illustrated in Fig. 1. These dryers may absorb solar energy in direct, indirect, or mixed-mode form. As per the requirement of solar dryers, various designs of solar dryers are possible.

Solar drying is one of the techniques used to save horticultural items. Experts suggest that drying is complicated process of heat and mass transmission between the product to be dried and the medium in which drying takes place [13]. Solar drying research so far shows that quick, modest, and effective solar dryers need to be built to meet the increased food conservation demand, particularly in developing countries like India [14]. A variety of solar dryer systems have been developed, and good work is still being conducted for various applications. The key combination of these devices is a flat plate collector (FPC) or the indirect application of solar energy. In the daytime hours, the solar flat plate group produces an immense range of hot air. Many farm commodities are dried at a consistent and mild temperature for a few days [15]. In some situations, the heat storage unit, which is coordinated with the solar drying system, is absorbed heat during peak daylight duration and is used when solar radiation is not present to supply hot air to the dryer product [16].

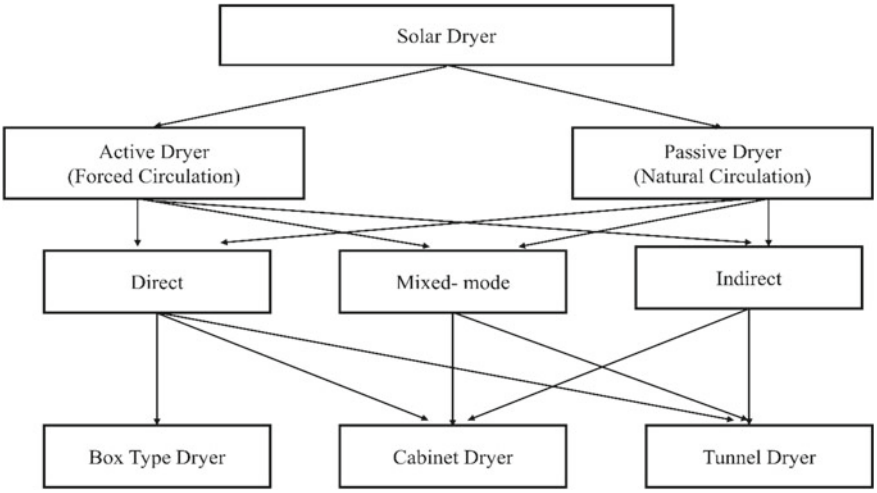

Fig. 1 Classification of solar dryer

3.2 Types of Solar Dryer

3.2.1 Passive Solar Dryer (Natural Air Circulation/Convection-Based Solar Dryer)

In a passive solar dryer, heated air is naturally transported throughout the solar dryer's drying chamber. To improve dryer air circulation, no extra equipment is attached to the solar dryer. The natural convection process removes the food product's moisture content. Passive solar dryers come in a variety of designs, including direct type, indirect type, and mixed-mode type solar dryers. In a passive direct solar dryer, the food absorbs solar radiation directly and moisture is removed from the food by naturally circulated air, whereas in an indirect solar dryer, the air absorbs solar radiation and is then naturally circulated within the drying chamber where food is stored [17]. The characteristics of a mixed-mode type solar dryer are a blend of direct type and indirect type solar dryers.

3.2.2 Active Solar Dryer (Forced Air Circulation/Convection-Based Solar Dryer)

In the active solar dryers, warm air is forcedly circulated throughout the solar dryer's drying chamber. For forced air circulation within the dryer, fan/blowers are attached to the solar dryer. Forced heated air absorbs the foodstuff moisture content in the drying chamber and escapes the dryer. This dryer shows better drying speed as compared with a passive solar dryer. Active solar dryer required some additional sources to run fan/blowers so that air is forced within the drying chamber. These dryers come in a variety of designs too, including direct type, indirect type, and mixed-mode type solar dryers. In an active direct solar dryer, the food absorbs solar radiation directly and moisture is removed from the food by forcefully circulated air, whereas in the active indirect type solar dryer, the air absorbs solar radiation and is then forcefully circulated within the drying chamber where food is stored. Active mixed-mode type solar dryer is a combination of the active direct and active indirect solar dryer. Food products directly absorb solar radiation, as well as heated air, which is forcefully circulated within the drying chamber [18].

3.3 Common Design of Solar Dryers

The solar dryer should be designed with caution considering all of the drying parameters above and the dryer's properties. Since there are numerous choices in the solar dryer system, the design of solar dryers thus offers huge options. These solar dryers were categorized from several viewpoints. However, given the operating modes and possibilities of dryers, these may generally be categorized into three types: dryers of the direct type, dryers of the mixed-mode type, and dryers of the indirect type.

3.3.1 Dryer of Direct Type

Such dryers have all the assignments to be most suitable for use in developing nations because they generally do not use a fan or blower to work with electrical methods [19]. These are also low in cost and easy to work. Anyway, the issue with such dryers is slow drying, less temperature, and humidity regulation, the limited amount can be dried, and because of direct exposure to the sun, certain items can alter shading and taste [20]. They contain a kind of enclosure and a transparent cover in its least complex form. Owing to the high temperature of the fenced-in area, the food products are heated due to direct heat absorption, and thus, the moisture of the product dissipates and flows into the natural or forced air circulation. There are a few structures of direct solar dryers, and these are produced taking into account either the accessibility of the local materials needed for their manufacturing or the drying of a particular product [21]. In various nations, a few dryers are made, tested, and analyzed. In passive dryer of direct type, air circulated naturally in the dryer while in active dryer of direct type uses fan/blower for forced circulation of air as seen in Fig. 2. The benefits of direct solar drying against open sun drying are as follows:

(a) Simpler in design and less expensive than the indirect type to build to a similar stacking limit.
(b) Food is sealed in a container such that food is protected from bird attacks and bugs.

Dryer of direct type has some issues regarding the quality of dried food products; generally, the color and aroma of the food product are affected because the food product is placed in direct exposure to solar radiation.

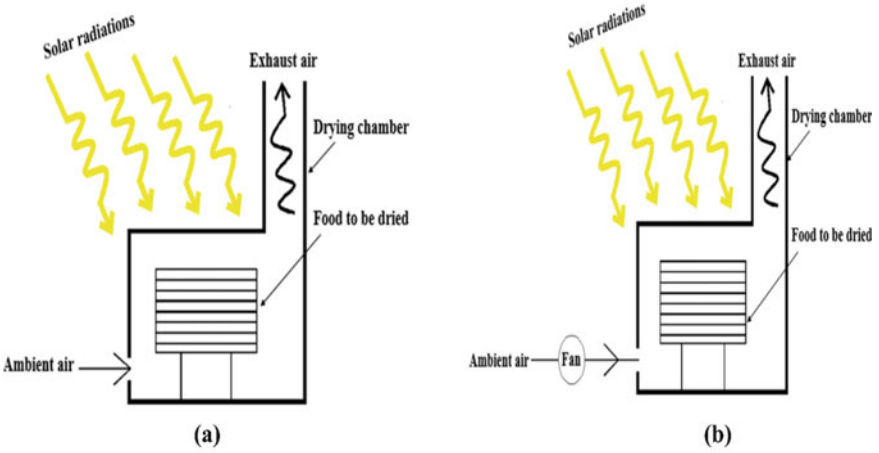

Fig. 2 (**a**) Passive dryer of direct type. (**b**) Active dryer of direct type [10]

3.3.2 Dryer of Indirect Type

Most of the dryers of indirect type are used to tackle the drawback of the dryers of direct type. Two distinct types of the indirect solar dryer are manufactured as per the natural or forced air circulation within the solar dryer [22]. Natural ventilation creates an air movement in passive kinds of the indirect solar dryer. Solar collectors receive heat through common convection and reach the dryer chamber. Food items kept in such dryers would get the heat out of this hot air [23]. Just because of the development of hot air over the food products, the moisture which is transferred and the free moisture present at a superficial level are evaporated and escape from the dryer by the natural circulation of hot air [24]. Figure 3 displays natural air circulation/convection solar dryer with a chimney, which is generally referred to as a passive solar dryer. This device features a solar collector-style flat plate collector to assimilate solar radiation. The drying chamber is attached directly to a solar collector, and there is a chimney on the top of the dryer. The solar collector is packed with a dark, colored, copper sheet. A transparent glass sheet with some air hole is placed on the head of this copper sheet, to render the wind stream portion. The collector's base is shielded from the base surface of the collector plate to reduce heat losses [25].

In the instance of an active indirect type solar dryer, the working fluid circulates forcefully from the inlet of collector to the dryer outlet throughout the system, as compared to the natural circulation/convection solar dryer as shown in Fig. 4. The air movement is carried through the device by a blower or fan which is managed either by a traditional or non-conventional source of energy [26]. The solar collector places

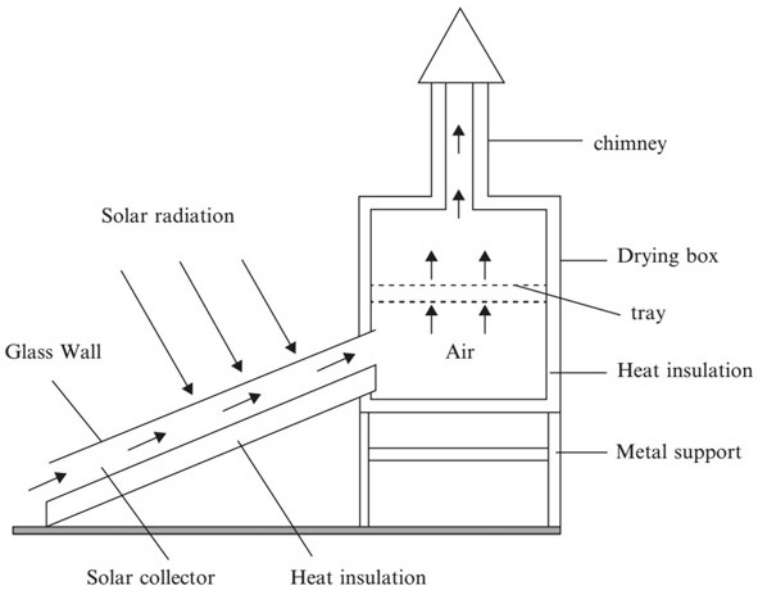

Fig. 3 Passive indirect solar dryer [25]

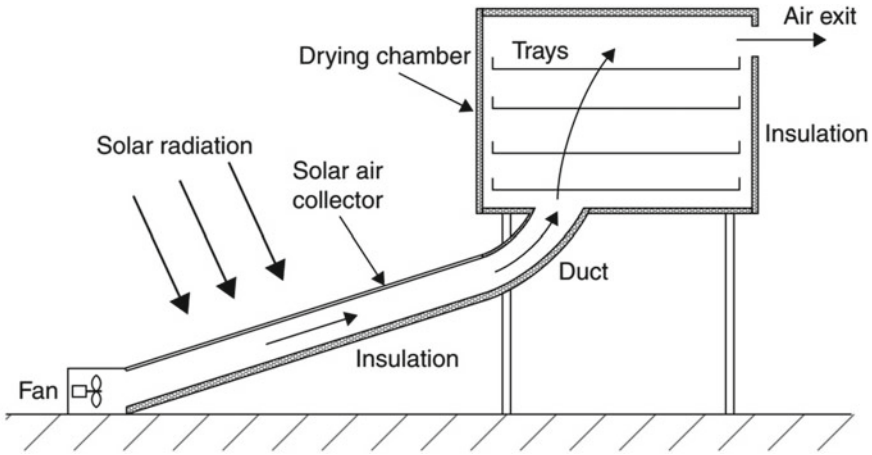

Fig. 4 Active indirect type solar dryer [27]

barriers in this type of system, and the air blower is used to turn the operating fluid into force convection. The device has a solar air flat plate, a chamber for drying, and a fan at the end of the drying chamber [27].

The upside of indirect type solar drying is:

(a) Provides superior over-drying control and the item obtained is of preferable quality over open-sun drying.
(b) The crispy texture and minimal heat damage do not occur because the yields are stable and opaque to direct radiation.
(c) May be worked at a higher temperature, recommended for drying deep layers.
(d) Highly suggested for cultures sensitive to appearance of dried product.
(e) Have a natural tendency to be more notable than direct solar drying capacity.

They are, however, moderately growing systems that require more capital investment in hardware and result in higher maintenance costs compared to direct type drying devices.

3.3.3 Dryer of Mixed-Mode Type

Mixed solar dryers blend the highlights of both direct type and indirect types of solar energy dryers. Here, the consolidated operation of the incident direct solar radiation on the substance being dried and the pre-heated air in the solar air collector heater produces the necessary heat needed for the purpose of drying [28]. Passive mixed-mode solar dryer absorbs radiation from sun directly; additionally heated air also circulates naturally within the solar dryer as illustrated in Fig. 5. In a passive mixed-mode dryer, the collector is used to warm the air and heated air naturally circulated inside the chamber containing the food product to be dried. Heated air absorbs the

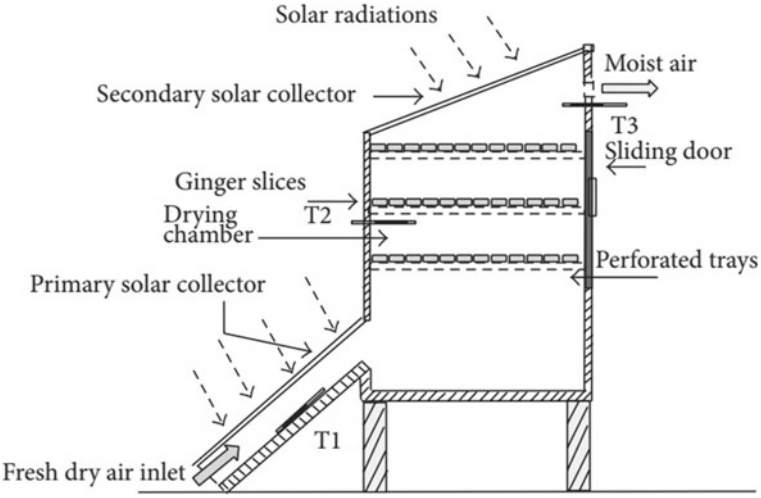

Fig. 5 Passive mixed-mode type solar dryer [29]

food product's moisture, and then, humid air escapes from the solar dryer through a vent available in the solar dryer [29].

Active mixed-mode type solar dryer also absorbs solar radiation directly as well as heated air within the solar dryer was vigorously circulated. A fan/blower is installed in mixed-mode design of dryer so that within the solar dryer, air is forced to circulate. Forceful circulation of air within the dryer improves the drying rate. The value of temperature within the solar dryer chamber is higher than the direct and indirect type solar dryer. Fan/blower can be installed in different locations, and the basic purpose is to provide force circulation of air. In Fig. 6, the blower is installed between the solar collector unit and the dryer's drying chamber. The input energy required to run the fan/blower is generally obtained from a renewable source of energy. Solar collector area and size of the drying chamber depend on the drying capacity of the solar dryer.

4 Various Aspects for Designing a Solar Drying System

The design of a solar drying system depends on the temperature required for food products to be dried, material availability, and the fund available for the fabrication of solar dryers. Direct type, indirect type, or mixed-mode type solar drying systems can be fabricated as per the requirement of the individual. Generally, the design of a solar dryer must consider several factors, including the design of solar collectors, the design of the drying cabinet, controls, and the right selection of other mechanical components such as ducting, air filters, and so on.

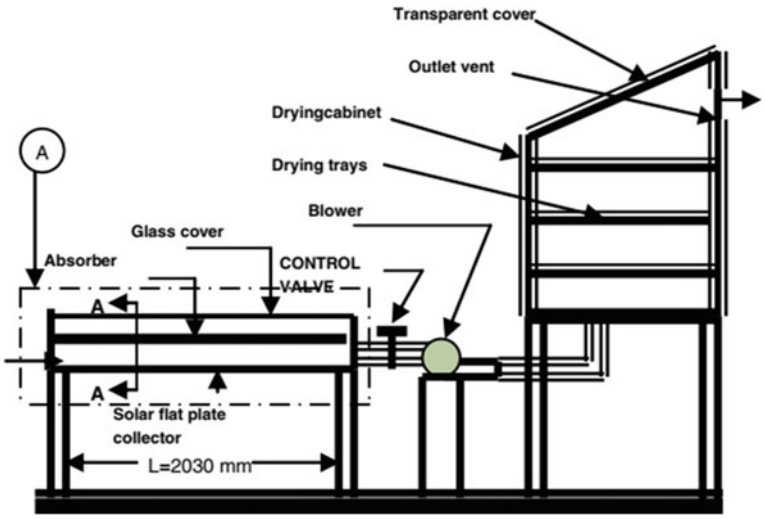

Fig. 6 Active mixed-mode type solar dryer [30]

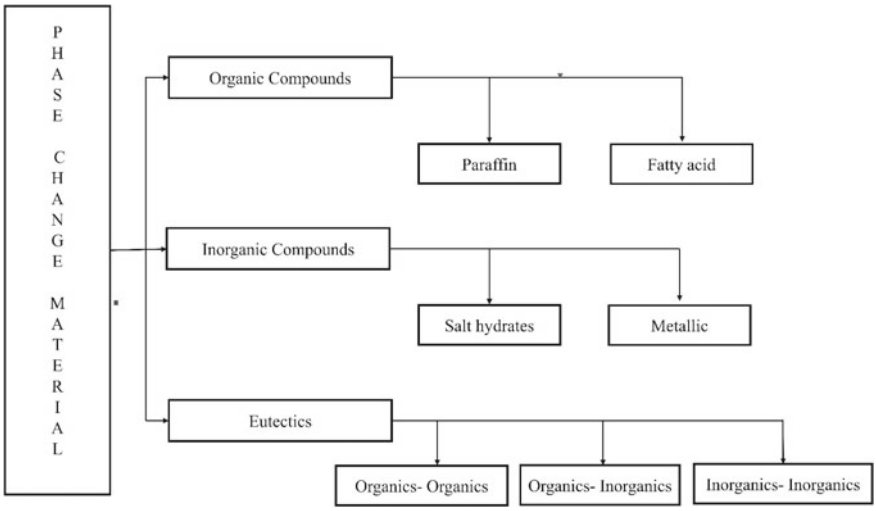

Fig. 7 Types of phase change materials

4.1 Solar Collector

The collector area is essential for properly absorbing solar energy and sufficiently heating the needed volume of air to be utilized in the dryer. The surface area required for solar dryer collectors may be calculated using the dryer's energy requirement. The drying needs and hence the drying properties of the material must be the starting

point for dimensioning the collectors. The drying requirements indicate the drying time and material temperature that can be used. The drying parameters determined by laboratory drying experiments aid in determining the input properties of drying air (the needed relative humidity and temperature) and the required air mass flow rate for optimal drying based on the cost of operation and end-product quality. The collector area may be calculated using an energy balance based on the needed drying air temperature. However, it is also vital to understand the efficiency of any collector because the area required determined using the aforementioned technique may not always offer the proper number, causing the design to fail. Although solar collectors come in a variety of designs, FPCs are the most commonly used for rising the temperature of air.

4.2 Design of Drying Chamber

A drying chamber's dimensions are determined by the greatest batch size that may be processed for a given application. In general, it is the amount of dried fresh product in a single batch of loading, measured in kg per batch. The number of trays to be placed in a drying cabinet is predetermined by the batch size and the density of the fresh product to be processed. The maximum sum of trays required may be computed after the capacity of a tray to be utilized is determined based on a single layer of the product. To ensure appropriate air circulation in the drying cabinet, keep a clear vertical space between the two trays. It should be noted that the number of vertical trays at a given location should not exceed 15; otherwise, the drying cabinet's height will be quite high, as a result of non-uniform the dried product's quality. Researchers have stated and empirically observed that the dryer design plays a critical role in ensuring consistent product quality. The design of the drying cabinet can have a major impact on the air dispersion in the solar cabinet dryer and, as a result, the moisture distribution. The product in specific areas of the cabinet may get overheated, resulting in over-drying and, eventually, casehardening. While the hot air may not reach some areas of the dryers (flow maldistribution), the anticipated moisture level may not be met. This can have a tremendous impact on the complete quality of the product and may result in the dried product being rejected. To prevent excessive-velocity/low-velocity zones, the drying air must be distributed evenly. This may be accomplished primarily by adjusting the drying chamber's size or altering the airflow directions.

4.3 Layout of Air Duct

Another crucial aspect of the solar cabinet dryer design is the ductwork. Even if it is not vital, poor duct design can result in significant fixed and operational costs. This has an impact on the flow characteristics of a system, particularly the pressure drops.

As a result, the ducts should be built so that the reduction in pressure in the air loop is as small as possible. A continuity equation based on the minimum air velocity required for drying is used to determine the size of the connecting duct between the collector panel and the cabinet. To reduce heat losses, all ducts must be correctly insulated using a suitable insulating material. The material used to manufacture the duct is also essential since it might impact the capital cost of a cabinet dryer. In order to minimize corrosion and other difficulties, stainless steel is commonly used for drying most food products.

4.4 Other Major Aspects

As previously said, there are several strategies to improve overall efficiency of a solar cabinet dryer. The two methods are to increase collector efficiency by novel design and sufficient insulation; however, proper microprocessor-based control systems may assure great energy efficiency while also delivering higher product quality. Because, a lot of the time, the air escaping from the dryer has not been saturated, partial air recycling can improve thermal efficiency. Another way to use renewable energy is to store extra solar radiation energy throughout the day and use it when solar radiation is not present. Another critical factor to consider when building a solar dryer is the presence of dust and microbiological pollutants in the atmospheric air that will be utilized for drying. If polluted air is utilized directly for drying, the product quality may suffer significantly. Microbe development can be rapid in the solar dryer under relatively warm circumstances. When solar energy is not present throughout the night, most drying processes are halted. In such a case, microbial growth might be quite high, causing harm to the food products. Before the air enters the dryer, high-efficiency particulate absorbing (HEPA) filters must be used. These filters are installed before the air is routed by the solar collectors and is heated for drying. This can provide a higher quality product with no fungal development throughout the post-drying storage period.

5 Solar Drying Advancements

Because of the sporadic pattern of solar irradiance and the seasonal change in radiation strength, operating solar dryers is more complex and expensive. It is critical to have a backup thermal energy supply during overcast periods and at night since sun drying is inefficient and may take one or more days to dry average agricultural goods. During times with low solar heat, it is critical to continue drying so that the drying item, notably meals and meats or marine goods, does not become microbially contaminated. Sugar-containing damp organic goods provide a perfect substrate for microorganisms to develop quickly and damage the product unless the water activity in the drying material is reduced to a suitably low value. As a result, backup heating

is required. The majority of recent developments in solar drying attempt to address these issues while also focusing on lowering overall energy consumed. This section goes through some of the advancements in solar drying that have occurred as a consequence of the ongoing study.

5.1 Solar Drying with Thermal Heat Storage Materials

Since solar energy is sporadic already discussed. When there is no solar radiation, the drying process stops, and the food product absorbs moisture from the environment. This will extend the drying period of the food. Thermal storage materials overcome this problem because they collect heat when there is solar radiation and release heat when there is no radiation. The incorporation of these materials into a solar dryer increases the system's effectiveness [31].

The two most basic forms of thermal energy storage systems are sensible heat storage, in which the temperature of the storage material fluctuates according to the quantity of energy stored, and latent heat storage, in which the energy stored is used when the content melts from phase to phase (as from ice to water) [32]. Table 1 contains typical data for comparing key associated features of heat storage materials used in thermal stores. The table's final row displays the relative volume of each storage medium with a heat storage capability of 106 kJ and a temperature rise of 15 K during heat storage [33].

The most efficient method for storing thermal energy is to employ phase change materials (PCMs) or latent heat storage materials. Energy per unit mass is transferred from solid to liquid during phase shifts and released after freezing at a steady temperature [35]. The energy consumed by the material helps the vibrational energy states of the constituent atoms or molecules to expand [36]. The atomic bonds weaken

Table 1 Thermal heat storage material comparison [34]

Thermal storage materials	Properties		Latent heat of fusion (kJ/kg)	Specific heat (kJ/kg)	Density (kg/m^3)	Storage mass for storing 10^6 kJ (kg)	Relative mass**	Storage volume for storing 10^6 kJ (m^3)
	Sensible heat storage	Rock	*	1.00	2240	67,000	15.00	30.00
		Water	*	4.20	1000	16,000	4.00	16.00
	Phase change material	Organic	190.0	2.00	800	5300	1.25	6.60
		Inorganic	230.0	2.00	1600	4350	1.00	2.70

* For sensible heat storage, latent heat of fusion is of little importance. ** Latent heat storage in inorganic phase transition materials is used to quantify mass and volume

Table 2 PCMs' advantages and disadvantages [45]

Phase change materials			
Types Of PCMs	Organic PCMs	Inorganic PCMs	Eutectics
Advantages	• A wide temperature range is available • There is no supercooling • The compatibility with other materials is higher • No separation • PCMs that are chemically stable • Safe to use • Nature is non-reactive • Easily recycled	• High volumetric latent heat • Cost-effective • Easily accessible • Thermal conductivity is high • These PCMs have a high thermal fusion rate • Reduced volumetric variation • Non-flammable PCMs	• These PCMs' melting points are sharp • Large volumetric storage density
Disadvantages	• Thermal conductivity is low • Substantial volume changes • Combustible • Except for technical grade paraffin wax, which is expensive	• Changed volume is exceptionally high • Corrosiveness • Supercooling	• Data on thermophysical characteristics is limited

during the melting process, and the substance transitions from solid to liquid [37]. However, during solidification, the material transfers energy and so the molecules lose energy and order themselves in a solid state. There are several different kinds of substances of phase change available but three main types are available: organic (paraffin and non-paraffin), inorganic (salt and metal alloys), and eutectic (mixing of two and more elements of PCMs: organic and inorganic and both) [38] (Fig. 7).

The researchers have highlighted PCMs in the last few decades, in which latent heat of fusion is used to keep the heat [40]. The heat storage unit volume (HSU) may be reduced greatly using the same PCM. However, limited fossil fuel reserves, the growth in emissions of greenhouse gas, and the speedy expansion in consumption of energy have brought to light the significance of efficient energy use. Low-temperature PCMs were prime research objects [41]. Most forms of work have centered on the production of new energy sources for these purposes [42]. A cost-effective and reliable energy storage device is the most useful way to improve energy production and thereby high peak demand and energy usage by using the PCMs for thermal energy storage. Thermal energy storage (TES) involves the storage of thermochemical heat and latent heat [43]. As a result of its low power density and the suitable design for thermal power discharge, responsive thermal storage necessitates huge volumes. However, latent heat storage techniques are less complicated to control than thermochemical heat storage systems [44] (Table 2).

Solar drying systems with thermal energy storage, i.e., PCMs, are capable and commonly used to solve the inconvenience of conventional solar dryers with a phase change material that absorbs heat during sunlight hours and releases the same stored heat during night hours [46]. Some of the PCMs which are used in solar drying application are listed in the following Table 3.

In the food and agriculture industry, the solar drying system has gained considerable attention because it makes the preservation process simpler. Furthermore, it offers tremendous ecological advantages. A 40–60 °C operating temperature is required to dry goods such as vegetables and fruits [65]. The moisture content and product consistency (e.g., nutritional value) can be regulated by the operating temperature levels and humidity. For various items, these parameters are varied.

Table 3 Thermophysical properties of major PCMs used for solar drying applications

PCMs	Type	Melting temperature (°C)	Latent heat of fusion (kJ/kg)	References
Lauric Acid	Organic	42.50	211.60	[47]
Myristic Acid	Organic	53.00	181.00	[48]
RT54	Organic	54.00	190.00	[49]
Stearic Acid	Organic	54.70	159.30	[50]
Paraffin 130/135	Organic	55.80	232.40	[51]
Paraffin wax 56	Organic	56.00	226.00	[52]
Palmitic Acid	Organic	61.30	179.90	[50]
Stearic Acid/Carbonized sunflower straw	Organic	66.40	186.10	[53]
Stearic Acid	Organic	67.00–69.00	–	[54]
Mg(NO3)·6H2O	Inorganic	89.00	162.00	[54]
MPCM-37D	Organic	37.00	166.50	[55]
PCMD-32SP	Organic	32.00	140.00–160.00	[56]
Paraffin 28	Organic	28.00	120.00	[57]
Delta®-Cool 28	Inorganic (salt hydrate)	26.00–30.00	188.00	[58]
48% CaCl + 4.3% NaCl + 0.4% 2 KCl + 47.3% H_2O	Inorganic (salt hydrate)	26.00–28.00	188.00	[59]
GR-25	Organic	23.20	45.30	[60]
RT-23	Organic	22.00–24.00	128.00	[61]
SP-22	Inorganic (salt hydrate)	21.50	154.70	[62]
n-heptadecane/graphite (92:8)	Organic	21.10	26.90	[63]
Capric Acid/Lauric Acid (65:35)	Organic	19.10	35.20	[64]

PCMs can store extra energy from the solar radiation and release stored energy when required. Various specifications, such as thermal transfer characteristics, outlet and inlet temperature, and the impact of air velocity, were investigated during loading and unloading [66].

Major findings using thermal energy storage-based solar dryers in various literature are compiled in Table 4.

5.2 Solar Drying with Hybrid System

A hybrid system is one in which a solar drying system is combined with conventional energy sources to increase the drying system's performance. On sunny days, the dryer is used as a solar dryer, and on gloomy days or at night, it was used as a hybrid solar dryer. To improve the efficiency of solar dryers, a variety of hybrid solar dryer designs have been developed. Amer et al. created a hybrid solar dryer by combining direct solar energy with a heat exchanger. As shown in Fig. 8, the dryer is made up of a solar collector, a heat exchanger, a reflector, and a heat storage drying chamber. The drying chamber was installed beneath the collector. Drying was also done at night using heat energy stored in the water acquired during sunshine and electrical heaters installed in the water tank [87].

Hatem Oueslati fabricated a solar-gas tunnel dryer that was hybrid in nature as shown in Fig. 9, and the author analyzed the performance of the fabricated hybrid solar dryer. This equipment was intended to dry off wet horticulture components (dates, carrots, bananas, tomatoes, grapes). The tunnel dryer had a south-facing chamber that includes a drying cabinet, a solar panel, and an auxiliary heating unit. The auxiliary heating unit had a backup heating system that runs in the solar panel when the main heating system fails. It was made up of two major components: a heat exchanger and a gas burner. According to the results of the conducted drying tests, the combined drying approach appeared to be excellent for drying food goods, which was a drying condition based on defined setpoints (drying air temperature and velocity) that were properly determined, depending on the quality required after drying. This approach reduced drying time, which had been demonstrated in a number of laboratory trials [88].

Daghigh et al. presented a multistate study of a solar dryer in conjunction with a photovoltaic thermal collector and an evacuated tube collector. In this analysis, using a evacuated tube (ET) collector and photovoltaic thermal (PV/T), an indirect type solar dryer was designed and manufactured. The PV and ET collectors were independently paired with the solar dryer in two modes in the built system. The first air was circulated into the ET collector or heat exchanger mounted behind the PV collector utilizing a blower to test the device, where it was heated by heat exchange and sent to the dryer. The PV/T solar dryer's overall performance was 13.7 percent and that of the ET solar dryer was 28.2%. In the ET solar dryer, the payback time was better than in the PV/T solar dryer in comparison with the number of sunshine days a year [89].

Table 4 Major research findings of solar dryer integrated with thermal energy storage

Type of solar dryer	Nature of work	Agriculture product to be dried	Thermal energy storage material	Auxiliary source of heat	Main findings	References
Indirect solar dryer	Experimental	Sweet potato	Paraffin	N.A	• Charging time reduced as ambient temperature and air speed improved	[67]
Natural convection solar dryer	Modeling and numerical analysis	Onions	Airstream	N.A	• Thermal power storage impacts drying in non-sunlight hours • Highly beneficial for minimizing temperature differences to dry	[68]
Passive solar dryer	Experimental	Mangoes, Litchi, Aonla, Jamun	Sodium Hydroxide (NaOH.H2O), Sodium Thiosulphate Penta Hydrate (Na2S2O3.5H2O)	N.A	• A mixture of high heat capacity material combined with PCMs will maintain the temperature within the desired range	[37]
Indirect solar dryer	Mathematical model	N.A	N.A	N.A	• The efficiency of systems that use storing materials in the solar collector is higher	[69]
Solar greenhouse dryer	Experimental	Coconuts	Rock bed	N.A	• Coconuts can be dried to an optimum moisture level of 52.3 percent (w.b.), 7 percent (w.b.) with and without heat storage in 54 and 60 h, respectively	[70]
Solar cabinet dryer	Experimental	Green chili	Gravel bed	N.A	• Solar cabinet dryer in combination with a gravel bed heat storage unit ideal for drying green chili	[71]
Forced convection solar dryer	Experimental	Garlic clove	Propylene glycol 60% and water 40% v/v	N.A	• For 8 h, garlic cloves were dried at a moisture level of 55.5 percent (wb) to 6.5 percent (wb) • During the analysis, energy generation without and with re-circulation of the air exiting the drying chamber varied from 43.06 to 83.73 percent and from 3.98 to 14.95 percent, respectively	[72]
Hybrid solar dryer	Experimental	Mushrooms	Paraffin wax	N. A	• The ultimate moisture quality was statistically affected by slice thickness and air recycling quantity • For the use of low-level air recycling suitable for thin and even slices	[73]

(continued)

Table 4 (continued)

Type of solar dryer	Nature of work	Agriculture product to be dried	Thermal energy storage material	Auxiliary source of heat	Main findings	References
Indirect solar dryer	Experimental	Pineapples	Rock pebbles	Biomass backup burner	• Both solar and biomass air heaters have been retained by the thermal mass • Moderate temperature variations in the drying chamber and minimizing energy wastage	[74]
Oven-drying method	Experimental	Potato slices	Paraffin wax	N.A	• Natural convection is primarily affected by heat transfer while charging • The melting rate is faster at the uppermost section • The heat transfer during discharge is primarily determined by the conduction and the heat rate due to the low thermal conductivity of the PCM • During discharge, the transmission is relatively poor	[36]
Indirect solar dryer	Experimental	Cocoa beans	Thermochemical energy released by the desiccant	N. A	• Thermal energy storage allows the drying with solar energy more efficient in terms of drying time and real energy usage	[75]
Flat plate collector solar dryer	Experimental	Selected crops	Paraffin wax	N.A	• The PCM dryer with the packed bed was able to store thermal energy throughout the day in latent heat • Release the same heat after hours of sunshine • This accumulated energy has helped to stabilize the drying temperature varied between 40 and 45° C • Thereby decreasing the drying time • The thermal efficiency of the dryer was found to be 28.2%	[66]
Indirect solar dryer	Experimental and numerical	Bitter gourds	Pebble bed (sensible heat storage)	N. A	• To achieve better device efficiency and good quality of the dried product, it is necessary to choose the acceptable air mass flow rate for the solar dryer	[76]
Mixed-mode solar dryer	Experimental and numerical	Apricot and plum	Paraffin	Heater integrated with photovoltaic and battery system	• Decrease of drying time by about 50% • The overall thermal efficiency and the pick-up efficiency of the solar dryer were enhanced	[77]

(continued)

Table 4 (continued)

Type of solar dryer	Nature of work	Agriculture product to be dried	Thermal energy storage material	Auxiliary source of heat	Main findings	References
Indirect solar dryer	Experimental	Valeriana jatamansi (medicinal herb)	Paraffin RT-42	N.A	• Phase change (paraffin RT-42) substance helped to constantly supply hot air of temperature 40° C • Indirect and isothermal dryers below an optimal temperature led to the healthy preservation of volatile compounds	[78]
Solar cabinet dryer	Experimental	No load	Paraffin (n-docosane)-kerosene composite	N.A	• Thermal absorption and storage vary with temperature gradient, air velocity, and solar intensity • One of the efficient materials ideal for low-cost thermal storage in a solar cabinet dryer is paraffin-based composite material	[31]
Indirect solar dryer	Experimental	No load	Paraffin	N.A	• The environmental conditions (relative humidity and temperature) in the drying chamber reach the ambient climatic condition during the night • The solar energy accumulator's daily energy efficiency was 33.9 percent, while its daily exergy efficiency was 8.5 percent • The relative humidity in the drying chamber should be 17–34.5 percent lower than the ambient relative humidity, and the drying chamber temperature should be 4–16 °C higher than the ambient temperature	[42]
Mixed-mode solar dryer	Experimental	Black turmeric	Paraffin wax (PCM)	N. A	• When compared to open sun drying, employing a mixed-mode solar dryer saved 60.7 percent of the time • The solar dryer's total efficiency was determined to be 12.0 percent	[79]

(continued)

Table 4 (continued)

Type of solar dryer	Nature of work	Agriculture product to be dried	Thermal energy storage material	Auxiliary source of heat	Main findings	References
Indirect and direct forced convection solar dryer	Experimental	Camel meat drying	Pebbles	N. A	• The sensible heat storage by a bed of pebbles improved the thermal efficiency of the direct drying chamber by 11.8% more than when no packed bed is used for the solar dryer. • maintained its efficiency by 28% for an hour after sunset	[18]
Indirect solar dryer	Numerical	Orange slices	Pebblestone	N.A	• Thermal energy storage medium reduced the moisture content of orange slices from 93.5% to 10.28% • The energy storage systems in drying processes will significantly increase the energy and exergy efficiency	[80]
Indirect solar cabinet dryer	CFD modeling and analysis	Apple slices	Paraffin RT50 (PCM)	N.A	• When compared to the other system without PCM, PCM inside the storage tank reduces drying time by around 9.37 percent, 9.67 percent, and 10.02 percent for airflow rates of 0.025, 0.05, and 0.09 kg/s, respectively • Using PCM increases the input thermal energy by roughly 1.72 percent and 5.12 percent, respectively, for airflow rates of 0.025 and 0.05 kg/s • Increased air flow rate (up to 0.09 kg/s) reduces input thermal energy • Increased air mass flow rate reduces overall drying efficiency • The system using PCM at a flow rate of 0.025 kg/s had the highest overall drying efficiency of 39.9%	[81]
Active solar dryer	Experimental	Potato	Glycerol	Wind-powered	• Solar dryers produced can shorten open sun drying time by 9–16 h • Using a wind-powered axial fan accelerated drying compared to using solely glycerol as thermal storage	[82]

(continued)

Table 4 (continued)

Type of solar dryer	Nature of work	Agriculture product to be dried	Thermal energy storage material	Auxiliary source of heat	Main findings	References
Indirect solar dryer	Experimental	Kiwifruit	α-AL_2O_3-PW nanocomposites	N.A	• The AL_2O_3-PW nanoparticles were injected into steel pipes and placed in the solar energy storage unit • Stored energy was increased by adding nanoparticles AL_2O_3-PW to pure paraffin • The highest absorbed thermal energy is related to nanocomposite with 1% nanoparticles of AL_2O_3	[83]
Passive flat plate collector solar dryer	Experimental	Mushroom	Paraffin wax (PW1)	N.A	• The FPC-solar dryer took 36.36 percent less time to dry button mushrooms than the open-sun drying	[17]
Indirect solar dryer	Experimental	Chili	Paraffin wax (PCM) and gravel mixed with iron scrap (SHS)	N.A	• By employing solar drying without thermal storage and in the natural sun, the moisture content of chilies is decreased to 4.85 percent from 86.50 percent (wet basis) in 21 h as opposed to 96 h and 150 h, respectively • The results of this study show that dehydration time is reduced by 78.12 percent and 86.00 percent, respectively, when compared to drying without the use of SHS and PCM and natural sun	[84]
Large-scale greenhouse solar dryer	Experimental	Chili	Paraffin wax	N.A	• Drying time in the solar greenhouse dryer is reduced considerably • The averaged exergy efficiencies of the drying room with a PCM thermal storage system are greater than that of the dryer without a PCM thermal storage system	[85]
Indirect mode solar dryer	Experimental	Banana slices	Paraffin wax	N.A	• Paraffin wax is used as PCM, which helps to maintain the higher temperature in the drying chamber for 5 h after sunset • The use of this type of drying system increases the operation time of the drying unit which is ultimately helpful in overall performance and minimization of drying time to achieve the final moisture content	[86]

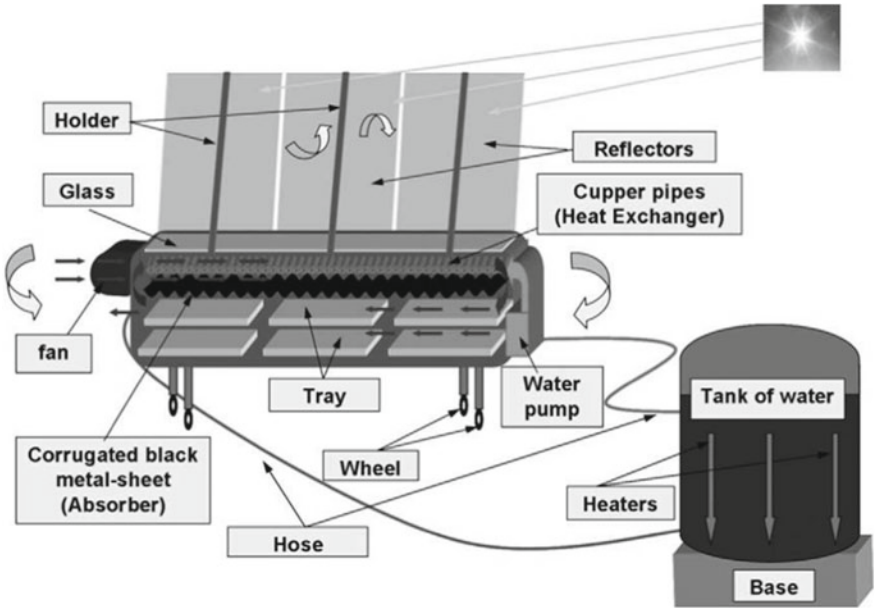

Fig. 8 Hybrid solar dryer design developed by Amer et al. [87]

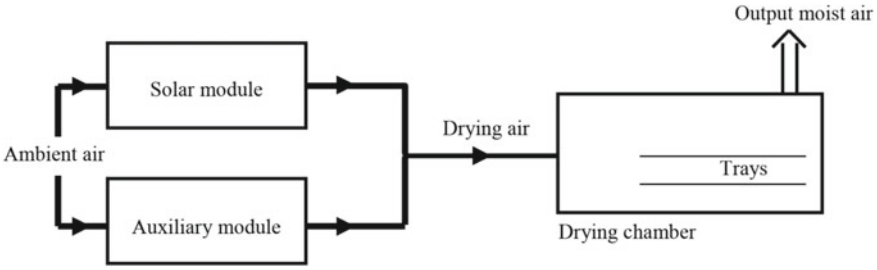

Fig. 9 Flow diagram of the drying process in a tunnel dryer [88]

6 Other Green Energy Sources Employed for Food Drying

Other green energy sources are employed to improve the solar dryer's performance. These green energy sources are not directly used as solar energy is used but these sources of green energy are employed to improve the solar dryer's efficiency and improve the performance of solar dryers.

6.1 Wind Energy

Wind energy is another sustainable energy source that may be utilized for drying. The use of wind energy and hydrothermal energy to generate power at drying sites is one option for making the process more cost-effective and environmentally pleasant. To the best of the authors' knowledge, this has not yet been tried in practice. Because renewable energy sources such as solar and wind are inherently intermittent and seasonal, as previously noted, it necessitates backup heating or storage devices, which raises the system's cost in some regions of the world. Bolaji et al. offered a performance study of a solar wind-ventilated cabinet dryer as shown in Fig. 10. Their research was an attempt to take advantage of the utilization of forced convection solar dryers by employing a rotating wind ventilator in remote locations where there was no electricity or other power sources. The data shows that the temperatures between the dryer and the air heater were higher than the ambient temperature throughout most hours of the day when drying food goods in the dryer versus drying identical items in the open air. In comparison with open-air drying, drying using the solar cabinet dryer produced superior results. The data also showed that the dryer's effectiveness was dependent on optimum air circulation throughout the system. As the airflow through the system grew, the system's dependability improved [90].

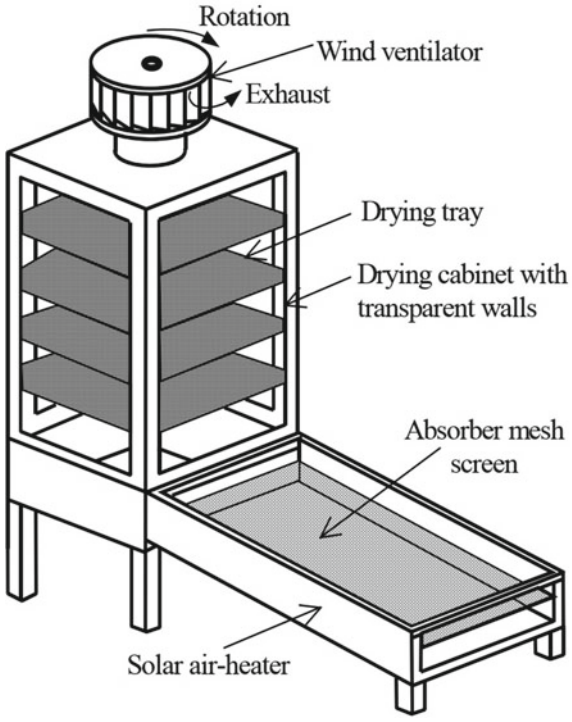

Fig. 10 Solar wind-ventilated cabinet dryer [90]

Wind energy is also used to generate electricity to facilitate the working of the solar dryer. Various designs of solar dryers are fabricated, in which wind energy is also utilized to enhance the performance of the solar dryer.

6.2 Biomass Energy

Biomass energy can be used with solar energy for heating air which circulated within the dryer. Generally, biomass energy is used as an auxiliary source of energy which provides energy in the absence of sunlight to the dryer. Madhlopa and Ngwalo developed and installed an indirect type natural air circulation/convection solar dryer integrated with solar collector-storage and biomass-backup heaters. Biomass burners (flue gas chimney, rectangular duct), collector mass thermal recovery, and drying chamber (conventional solar chamber) were the dryer's key components. The dryer was checked with fresh apples under diverse environmental conditions in three operation modes (solar, biomass, and solar-biomass). Results indicated that both solar and biomass air heaters maintained thermal weight, minimizing temperature variations in a drying chamber and energy loss; when the door to the biomass burner was left open during combustion, relatively high full temperatures were obtained. Solar activity mode was slowest when the samples were dried, and solar-biomass mode was quicker when the atmosphere prevailed. In solar-biomass activity mode, drying persisted successfully even under very poor conditions [74]. Ndukwu et al. presented a new hybrid solar-biomass dryer as shown in Fig. 11 and carry out an energy-based thermal analysis and exergy-sustainability analysis. In construction, an indirect type solar dryer was integrated with the biomass furnace. When solar radiation was available, the indirect dryer absorbed solar energy and the air temperature rose and then circulated within the drying chamber. When solar radiation was not present, the biomass furnace was used to generate flue gas, and flue gases within the copper tube were circulated around the drying chamber. So, the drying process continues even when the solar radiation was not present. Thermal analysis of this hybrid dryer showed improvement in performance [91].

6.3 Geothermal Energy

Several solar dryer design configurations created by various authors may be coupled with accessible temperatures provided by geothermal power plants. Direct usage of geothermal heat for drying may give economic benefits to local farmers if working finance is made available. Ananno et al. provided a systematic idea for a hybrid geothermal PCM flat plate solar collector as shown in Fig. 12, self-supporting clean energy food drying equipment, as well as thorough computational research. The computational analysis was done ensuring very effective and accurate near-null

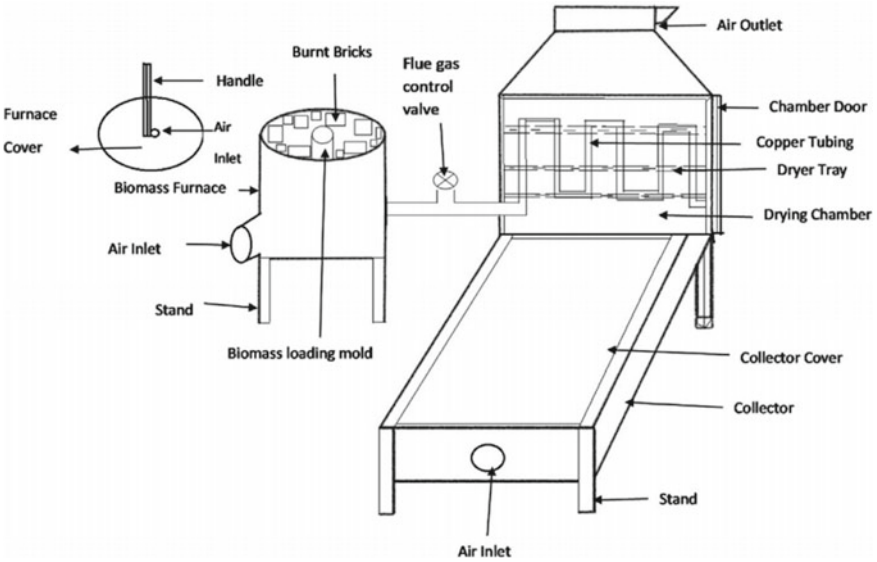

Fig. 11 Indirect solar dryer with biomass furnace [91]

hybrid energy technology. The intended test project computed functional parameters of the hybrid geothermal PCM solar collector dryer platform using the associated mathematical model. Two separate earth-to-air heating exchangers (EAHX) and PCM flat solar collector systems tested the proposed concept of a dryer. For the output condition of the geothermal component, the PCM solar plate collector employed an idealized input condition. The two systems were connected to the geothermal exhaust pipe by a soiled link between the pilot platforms. The PCM model was a rectangular cross-section channel. Solar radiation was absorbed by the top layer (glass plate) and the temperature increase. The resulting heat was transferred from geothermal EAHX by air convection. The solar flat plate collector for airflow was considered to have the same duration parts. Each section was heated by the previous section convection, conduction, and radiation. The research developed core efficiency parameters and proposed simple temperature equations based on mass flow rate, collector side ratios, and heat loss factors. The corresponding equation followed well-reported experimental findings. Theoretically, with 20.5% more energy than the conventional flat plate solar collector and 6% more energy than the v-corrugated solar air heater, the hybrid system could operate and dry food for 20 h a day [92].

7 Conclusion

The application of green energy for food product drying is price-effective. Solar drying is a better way to utilize green energy for obtaining a high-quality dried

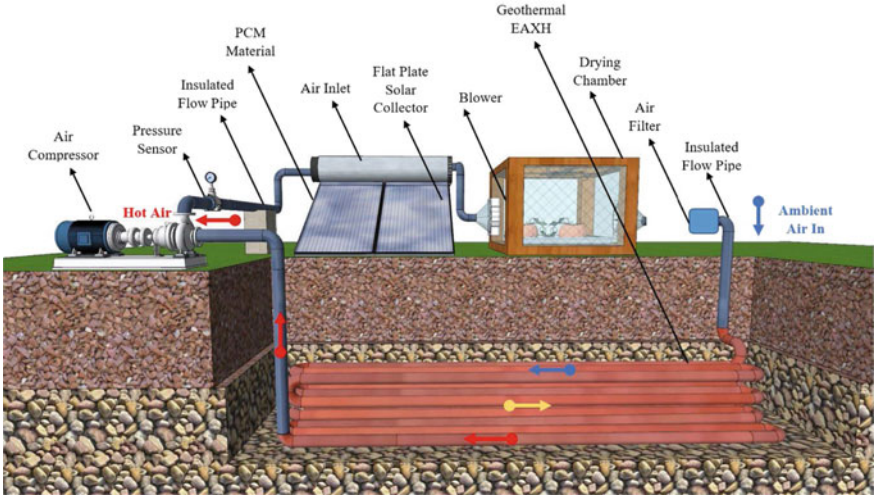

Fig. 12 Hybrid geothermal PCM flat plate solar collector concept design [92]

product. The sporadic presence of solar radiation constraints the continuous drying process inside the solar dryer. Efforts have been made to overcome this solar energy limitation in hybrid solar dryers by using other green energy sources, such as biomass, in addition to solar energy. However, combining solar dryers with thermal energy storage might assist to mitigate the problem, theoretically reducing the need for continuous fossil fuel drying and making it self-sustaining using solar energy. Among the available methods, using phase change material (PCM) is an ideal way to store thermal energy. A nearly constant drying temperature can be obtained by the use of PCMs. There are many resources available in the field of solar dryers. Researchers concentrate on designing solar dryers that demonstrate the highest performance and increased consistency of the dry product. Improving the characteristics of PCMs and improving the architecture of solar dryers to allow the proper use of solar radiation will make this possible. Since costs are the main factor in the production of solar dryers, it is important to quantify and encourage short-term and long-term costs and benefits. Finally, the growing technical rollout in developed countries often involves effective cooperation and coordination between key players in the agricultural research-producers-extension partnership.

Acknowledgements The author (Abhishek Anand) is highly obliged to the University Grants Commission (UGC) and Ministry of Education, Government of India, New Delhi, for providing the Senior Research Fellowship (SRF). Part of the research work has been conducted under Indo-Australian joint project entitled "Thermal Energy Storage for Food/Grain Drying with CST/RE to Lower Pollution" and thankfully acknowledged.

References

1. Srivastava A, Anand A, Shukla A, Kumar A, Buddhi D, Sharma A (2021) A comprehensive overview on solar grapes drying: Modeling, energy, environmental and economic analysis. Sustain Energy Technol Assess 47:101513. https://doi.org/10.1016/j.seta.2021.101513
2. Menon A, Stojceska V, Tassou SA (2020) A systematic review on the recent advances of the energy efficiency improvements in non-conventional food drying technologies. Trends Food Sci Technol 100:67–76. https://doi.org/10.1016/j.tifs.2020.03.014
3. Fudholi A, Othman MY, Ruslan MH, Sohif M, Sopian KB (2013) Prospect and future of solar dryer for agricultural and marine product : perspective Malaysia 141–149
4. Gorjian S, Calise F, Kant K, Ahamed MS, Copertaro B, Najafi G, et al. (2021) A review on opportunities for implementation of solar energy technologies in agricultural greenhouses. J Clean Prod 2021:124807. https://doi.org/10.1016/j.jclepro.2020.124807
5. Chauhan PS, Kumar A, Gupta B (2017) A review on thermal models for greenhouse dryers. Renew Sustain Energy Rev 75:548–558. https://doi.org/10.1016/j.rser.2016.11.023
6. Lhendup T (2005) Technical and financial feasibility of a solar dryer in Bhutan. Energy Sustain Dev 9:17–24. https://doi.org/10.1016/S0973-0826(08)60496-2
7. Shukla AK, Sudhakar K, Baredar P (2017) Renewable energy resources in South Asian countries: challenges, policy and recommendations. Resour Technol 3:342–346. https://doi.org/10.1016/j.reffit.2016.12.003
8. Joshi CB, Pradhan BD, Pathak TP (2000) Application of solar drying systems in Rural Nepal. World Renew Energy Congr VI 2000:2237–2240. https://doi.org/10.1016/b978-008043865-8/50483-9
9. Fudholi A, Sopian K, Bakhtyar B, Gabbasa M, Yusof M, Ha M (2015) Review of solar drying systems with air based solar collectors in Malaysia. 51:1191–204. https://doi.org/10.1016/j.rser.2015.07.026
10. El Hage H, Herez A, Ramadan M, Bazzi H, Khaled M (2018) An investigation on solar drying: a review with economic and environmental assessment. Energy 157:815–829. https://doi.org/10.1016/j.energy.2018.05.197
11. Moses JA, Norton T, Alagusundaram K, Tiwari BK (2014) Novel drying techniques for the food industry. Food Eng Rev 6:43–55. https://doi.org/10.1007/s12393-014-9078-7
12. Singh P, Vyas S, Yadav A (2019) Experimental comparison of open sun drying and solar drying based on evacuated tube collector. Int J Sustain Energy 38:348–367. https://doi.org/10.1080/14786451.2018.1505726
13. Masoom A, Kosmopoulos P, Bansal A, Kazadzis S (2020) Solar energy estimations in india using remote sensing technologies and validation with sun photometers in Urban Areas. Remote Sens 12:254. https://doi.org/10.3390/rs12020254
14. Pochont NR, Mohammad MN, Pradeep BT, Kumar PV (2020) A comparative study of drying kinetics and quality of Indian red chilli in solar hybrid greenhouse drying and open sun drying. Mater Today Proc 21:286–290. https://doi.org/10.1016/j.matpr.2019.05.433
15. Karim SA (2020) Solar dryers save time, increase income for Afghan farmers 2020:2015–2016
16. Belessiotis V, Delyannis E (2011) Solar drying. Sol Energy 85:1665–1691. https://doi.org/10.1016/j.solener.2009.10.001
17. Tarafdar A, Nema PK (2020) Design and performance evaluation of a passive flat plate collector solar dryer for agricultural products 2020. https://doi.org/10.1111/jfpe.13484
18. Braham W, Khellaf A, Mediani A, El M, Slimani A, Loumani A et al (2018) Experimental investigation of an active direct and indirect solar dryer with sensible heat storage for camel meat drying in Saharan environment. Sol Energy 174:328–341. https://doi.org/10.1016/j.solener.2018.09.037
19. Kumar A, Singh R, Prakash O, Ashutosh (2014) Review on global solar drying status. Agric Eng Int CIGR J 16:161–177
20. Tiwari A (2016) A review on solar drying of agricultural produce. J Food Process Technol 7. https://doi.org/10.4172/2157-7110.1000623

21. Lingayat AB, Chandramohan VP, Raju VRK, Meda V (2020) A review on indirect type solar dryers for agricultural crops—dryer setup, its performance, energy storage and important highlights. Appl Energy 258:114005. https://doi.org/10.1016/j.apenergy.2019.114005
22. Essalhi H, Tadili R, Bargach MN (2018) Comparison of thermal performance between two solar air collectors for an indirect solar dryer. J Phys Sci 29:55–65. https://doi.org/10.21315/jps2018.29.3.5
23. Hajar E, Rachid T, Najib BM (2017) Conception of a solar air collector for an indirect solar dryer. Pear drying test. Energy Procedia 141:29–33. https://doi.org/10.1016/j.egypro.2017.11.114
24. Castillo Téllez M, Pilatowsky Figueroa I, Castillo Téllez B, López Vidaña EC, López OA (2018) Solar drying of Stevia (Rebaudiana Bertoni) leaves using direct and indirect technologies. Sol Energy 159:898–907. https://doi.org/10.1016/j.solener.2017.11.031
25. Dincer I, Ozgur Colpan C, Akif Ezan M, Kizilkan O. Progress in clean energy, vol 2. Springer International Publishing, Cham. https://doi.org/10.1007/978-3-319-17031-2
26. Goud M, Vardhan Reddy MV, Chandramohan VP, Suresh S (2019) A novel indirect solar dryer with inlet fans powered by solar PV panels: drying kinetics of capsicum annum and Abelmoschus esculentus with dryer performance. Sol Energy 194:871–885. https://doi.org/10.1016/j.solener.2019.11.031
27. Kalogirou SA (2009) Industrial process heat, chemistry applications, and solar dryers. Sol Energy Eng, Elsevier 391–420. https://doi.org/10.1016/B978-0-12-374501-9.00007-8
28. Ayua E, Mugalavai V, Simon J, Weller S, Obura P, Nyabinda N (2017) Comparison of a mixed modes solar dryer to a direct mode solar dryer for African indigenous vegetable and chili processing. J Food Process Preserv 41:e13216. https://doi.org/10.1111/jfpp.13216
29. Deshmukh AW, Varma MN, Yoo CK, Wasewar KL (2014) Investigation of solar drying of ginger (Zingiber officinale): emprical modelling, drying characteristics, and quality study. Chinese J Eng 2014:1–7. https://doi.org/10.1155/2014/305823
30. Pardhi CB, Bhagoria JL (2013) Development and performance evaluation of mixed-mode solar dryer with forced convection. Int J Energy Environ Eng 4:23. https://doi.org/10.1186/2251-6832-4-23
31. Krishnan S, Sivaraman B (2017) Experimental investigations on thermal storage in a solar dryer 17:23–33
32. Lamidi RO, Jiang L, Pathare PB, Wang YD, Roskilly AP (2019) Recent advances in sustainable drying of agricultural produce: a review. Appl Energy 233–234:367–385. https://doi.org/10.1016/j.apenergy.2018.10.044
33. Abhat A (1981) Short term thermal energy storage. Energy Build 3:49–76. https://doi.org/10.1016/0378-7788(81)90005-0
34. Hasnain SM (1998) Review on sustainable thermal energy storage technologies, part I: heat storage materials and techniques. Energy Convers Manag 39:1127–1138
35. Sain P, Songara V, Karir R, Balan N (2014) Natural convection type solar dryer with latent heat storage. In: Proceedings 2013 International Conference Renewable Energy Sustainable Energy, ICRESE 2013 2014:9–14. https://doi.org/10.1109/ICRESE.2013.6927808
36. Agarwal A, Sarviya RM (2015) Solar dryer using paraffin wax as heat storage material. Eng Sci Technol Int J. https://doi.org/10.1016/j.jestch.2015.09.014
37. Paper R (2009) Temperature stabilization and value addition in solar drying of arid and high heat capacity materials 20:17–20
38. Dosapati C, Mandapati MJK (2019) Thermal performance of a packed bed double pass solar air heater with a latent heat storage system: an experimental investigation. World J Eng 17:203–213. https://doi.org/10.1108/WJE-08-2019-0221
39. Shukla A, Buddhi D, Sawhney RL (2009) Solar water heaters with phase change material thermal energy storage medium: a review. Renew Sustain Energy Rev 13:2119–2125. https://doi.org/10.1016/j.rser.2009.01.024
40. Senadeera W, Kalugalage IS (2004) Performance evaluation of an affordable solar dryer for drying crops. Bienn Conf Soc Eng Agric 2004, Dubbo, Aust 2004
41. Raponi F, Moscetti R, Monarca D, Colantoni A, Massantini R (2017) Monitoring and optimization of the process of drying fruits and vegetables using computer vision: a review. Sustainability 9. https://doi.org/10.3390/su9112009

42. El Khadraoui A, Bouadila S, Kooli S, Farhat A, Guizani A (2017) Thermal behavior of indirect solar dryer : nocturnal usage of solar air collector with PCM. J Clean Prod 148:37–48. https://doi.org/10.1016/j.jclepro.2017.01.149
43. Shanmugam V, Natarajan E (2007) Experimental study of regenerative desiccant integrated solar dryer with and without reflective mirror. Appl Therm Eng 27:1543–1551. https://doi.org/10.1016/j.applthermaleng.2006.09.018
44. Abu-Hamdeh NH, Alnefaie KA (2019) Assessment of thermal performance of PCM in latent heat storage system for different applications. Sol Energy 177:317–323. https://doi.org/10.1016/j.solener.2018.11.035
45. Nkwetta DN, Haghighat F (2014) Thermal energy storage with phase change material—a state-of-the art review. Sustain Cities Soc 10:87–100. https://doi.org/10.1016/j.scs.2013.05.007
46. Kant K, Shukla A, Sharma A, Kumar A, Jain A (2016) Thermal energy storage based solar drying systems: a review. Innov Food Sci Emerg Technol 34:86–99. https://doi.org/10.1016/j.ifset.2016.01.007
47. Sarı A, Kaygusuz K (2002) Thermal and heat transfer characteristics in a latent heat storage system using lauric acid. Energy Convers Manag 43:2493–2507. https://doi.org/10.1016/S0196-8904(01)00187-X
48. Sharma SD, Iwata T, Kitano H, Sagara K (2005) Thermal performance of a solar cooker based on an evacuated tube solar collector with a PCM storage unit. Sol Energy 78:416–426. https://doi.org/10.1016/j.solener.2004.08.001
49. Kabeel AE, Khalil A, Shalaby SM, Zayed ME (2016) Experimental investigation of thermal performance of flat and v-corrugated plate solar air heaters with and without PCM as thermal energy storage. Energy Convers Manag 113:264–272. https://doi.org/10.1016/j.enconman.2016.01.068
50. Sari A (2005) Eutectic mixtures of some fatty acids for low temperature solar heating applications: thermal properties and thermal reliability. Appl Therm Eng 25:2100–2107. https://doi.org/10.1016/j.applthermaleng.2005.01.010
51. Ismail KAR, Alves CLF, Modesto MS (2001) Numerical and experimental study on the solidification of PCM around a vertical axially finned isothermal cylinder. Appl Therm Eng 21:53–77. https://doi.org/10.1016/S1359-4311(00)00002-8
52. Kabeel AE, Abdelgaied M (2017) Observational study of modified solar still coupled with oil serpentine loop from cylindrical parabolic concentrator and phase changing material under basin. Sol Energy 144:71–78. https://doi.org/10.1016/j.solener.2017.01.007
53. Vinet L, Zhedanov A (2010) A "missing" family of classical orthogonal polynomials. J Chem Inf Model 53:1689–1699. https://doi.org/10.1088/1751-8113/44/8/085201
54. Domanski R, El-Sebaii AA, Jaworski M (1995) Cooking during off-sunshine hours using PCMs as storage media. Energy 20:607–616. https://doi.org/10.1016/0360-5442(95)00012-6
55. Wang SM, Matiašovský P, Mihálka P, Lai CM (2018) Experimental investigation of the daily thermal performance of a mPCM honeycomb wallboard. Energy Build 159:419–425. https://doi.org/10.1016/j.enbuild.2017.10.080
56. Tomizawa Y, Sasaki K, Kuroda A, Takeda R, Kaito Y (2016) Experimental and numerical study on phase change material (PCM) for thermal management of mobile devices. Appl Therm Eng 98:320–329. https://doi.org/10.1016/j.applthermaleng.2015.12.056
57. Devaux P, Farid MM (2017) Benefits of PCM underfloor heating with PCM wallboards for space heating in winter. Appl Energy 191:593–602. https://doi.org/10.1016/j.apenergy.2017.01.060
58. Weinlaeder H, Koerner W, Heidenfelder M (2011) Monitoring results of an interior sun protection system with integrated latent heat storage. Energy Build 43:2468–2475. https://doi.org/10.1016/j.enbuild.2011.06.007
59. Pasupathy A, Velraj R (2008) Effect of double layer phase change material in building roof for year round thermal management. Energy Build 40:193–203. https://doi.org/10.1016/j.enbuild.2007.02.016
60. Nagano K, Takeda S, Mochida T, Shimakura K (2004) Thermal characteristics of a direct heat exchange system between granules with phase change material and air. Appl Therm Eng 24:2131–2144. https://doi.org/10.1016/j.applthermaleng.2004.02.004

61. Weinläder H, Klinker F, Yasin M (2016) PCM cooling ceilings in the energy efficiency center—passive cooling potential of two different system designs. Energy Build 119:93–100. https://doi.org/10.1016/j.enbuild.2016.03.031
62. De Gracia A, Navarro L, Castell A, Cabeza LF (2013) Numerical study on the thermal performance of a ventilated facade with PCM. Appl Therm Eng 61:372–380. https://doi.org/10.1016/j.applthermaleng.2013.07.035
63. Biswas K. Chapter 9. Nano-based PCMs for building energy efficiency n.d.:1–32
64. Shilei L, Neng Z, Guohui F (2006) Eutectic mixtures of capric acid and lauric acid applied in building wallboards for heat energy storage. Energy Build 38:708–711. https://doi.org/10.1016/j.enbuild.2005.10.006
65. Manoj Kumar P, Mylsamy K, Saravanakumar PT (2020) Experimental investigations on thermal properties of nano-SiO 2/paraffin phase change material (PCM) for solar thermal energy storage applications. Energy Sources, Part A Recover Util Environ Eff 42:2420–2433. https://doi.org/10.1080/15567036.2019.1607942
66. Jain D, Tewari P (2015) Performance of indirect through pass natural convective solar crop dryer with phase change thermal energy storage. Renew Energy 80:244–250. https://doi.org/10.1016/j.renene.2015.02.012
67. Devahastin S, Pitaksuriyarat S (2006) Use of latent heat storage to conserve energy during drying and its effect on drying kinetics of a food product. Appl Therm Eng 26:1705–1713. https://doi.org/10.1016/j.applthermaleng.2005.11.007
68. Jain D (2007) Modeling the performance of the reversed absorber with packed bed thermal storage natural convection solar crop dryer. J Food Eng 78:637–647. https://doi.org/10.1016/j.jfoodeng.2005.10.035
69. Sami S, Rahimi A, Etesami N (2011) Dynamic modeling and a parametric study of an indirect solar cabinet dryer dynamic modeling and a parametric study of an indirect solar cabinet dryer 3937. https://doi.org/10.1080/07373937.2010.545159
70. Ayyappan S, Mayilsamy K (2012) Solar tunnel drier with thermal storage for drying of copra. Int J Energy Technol Policy 8:3–13. https://doi.org/10.1504/IJETP.2012.046017
71. Kamble AK, Pardeshi IL, Singh PL, Ade GS (2017) Drying of chilli using solar cabinet dryer coupled with gravel bed heat storage system. J Food Res Technol 1:87–94
72. Shringi V, Kothari S, Panwar NL (2014) Experimental investigation of drying of garlic clove in solar dryer using phase change material as energy storage. J Therm Anal Calorim 118:533–539. https://doi.org/10.1007/s10973-014-3991-0
73. Reyes A, Mahn A, Vásquez F (2016) Mushrooms dehydration in a hybrid-solar dryer, using a phase change material. Energy Convers Manag 83:241–248. https://doi.org/10.1016/j.enconman.2014.03.077
74. Madhlopa A, Ngwalo G (2007) Solar dryer with thermal storage and biomass-backup heater. Sol Energy 81:449–462. https://doi.org/10.1016/j.solener.2006.08.008
75. Farah S, Ambarita H, Napitupulu FH, Kawai H (2015) Case studies in thermal engineering study on effectiveness of continuous solar dryer integrated with desiccant thermal storage for drying cocoa beans. Case Stud Therm Eng 5:32–40. https://doi.org/10.1016/j.csite.2014.11.003
76. Vijayan S, Arjunan TV, Kumar A (2016) Mathematical modeling and performance analysis of thin layer drying of bitter gourd in sensible storage based indirect solar dryer. Innov Food Sci Emerg Technol 36:59–67. https://doi.org/10.1016/j.ifset.2016.05.014
77. Baniasadi E, Ranjbar S, Boostanipour O (2017) Experimental investigation of the performance of a mixed-mode solar dryer with thermal energy storage. Renew Energy. https://doi.org/10.1016/j.renene.2017.05.043
78. Bhardwaj AK, Chauhan R, Kumar R, Sethi M (2017) Author's accepted manuscript. Case Stud Therm Eng. https://doi.org/10.1016/j.csite.2017.07.009
79. Lakshmi DVN, Muthukumar P, Layek A, Nayak PK (2018) Drying kinetics and quality analysis of black turmeric (Curcuma caesia) drying in a mixed mode forced convection solar dryer integrated with thermal energy storage. Renew Energy 120:23–34. https://doi.org/10.1016/j.renene.2017.12.053

80. Atalay H (2019) Performance analysis of a solar dryer integrated with the packed bed thermal energy storage (TES) system. Energy 172:1037–1052. https://doi.org/10.1016/j.energy.2019.02.023
81. Iranmanesh M, Samimi Akhijahani H, Barghi Jahromi MS (2020) CFD modeling and evaluation the performance of a solar cabinet dryer equipped with evacuated tube solar collector and thermal storage system. Renew Energy 145:1192–1213. https://doi.org/10.1016/j.renene.2019.06.038
82. Ndukwu MC, Onyenwigwe D, Abam FI, Eke AB, Dirioha C (2020) Development of a low-cost wind-powered active solar dryer integrated with glycerol as thermal storage. Renew Energy 154:553–568. https://doi.org/10.1016/j.renene.2020.03.016
83. Bahari M, Naja B, Babapoor A (2020) Evaluation of α -AL 2 O 3 -PW nanocomposites for thermal energy storage in the agro-products solar dryer 28. https://doi.org/10.1016/j.est.2019.101181
84. Bhardwaj AK, Kumar R, Chauhan R, Kumar S (2020) Experimental investigation and performance evaluation of a novel solar dryer integrated with a combination of SHS and PCM for drying chilli in the Himalayan region. Therm Sci Eng Prog 20:100713. https://doi.org/10.1016/j.tsep.2020.100713
85. Pankaew P, Aumporn O, Janjai S, Pattarapanitchai S, Sangsan M, Bala BK (2020) Performance of a large-scale greenhouse solar dryer integrated with phase change material thermal storage system for drying of chili. Int J Green Energy 17:632–643. https://doi.org/10.1080/15435075.2020.1779074
86. Singh D, Mall P (2020) Experimental investigation of thermal performance of indirect mode solar dryer with phase change material for banana slices. Energy Sources, Part A Recover Util Environ Eff. https://doi.org/10.1080/15567036.2020.1810825
87. Lingayat A, Chandramohan VP, Raju VRK (2017) Design, development and performance of indirect type solar dryer for banana drying. Energy Procedia 109:409–416. https://doi.org/10.1016/j.egypro.2017.03.041
88. Oueslati H, Mabrouk SB, Marni A (2014) Design and installation of a solar-gas. Fift Int Renew Energy Congr IREC 2014:1–6
89. Daghigh R, Shahidian R, Oramipoor H (2020) A multistate investigation of a solar dryer coupled with photovoltaic thermal collector and evacuated tube collector. Sol Energy 199:694–703. https://doi.org/10.1016/j.solener.2020.02.069
90. Bolaji BO, Olayanju TMA, Falade TO (2011) Performance evaluation of a solar wind-ventilated cabinet dryer. West Indian J Eng 33:12–18
91. Ndukwu MC, Simo-Tagne M, Abam FI, Onwuka OS, Prince S, Bennamoun L (2020) Exergetic sustainability and economic analysis of hybrid solar-biomass dryer integrated with copper tubing as heat exchanger. Heliyon 6:e03401. https://doi.org/10.1016/j.heliyon.2020.e03401
92. Ananno AA, Masud MH, Dabnichki P, Ahmed A (2020) Design and numerical analysis of a hybrid geothermal PCM flat plate solar collector dryer for developing countries. Sol Energy 196:270–286. https://doi.org/10.1016/j.solener.2019.11.069

Chapter 5
Application of Latent Heat Storage Materials in the Storage Tank of the SWH System

Shailendra Singh, Abhishek Anand, Amritanshu Shukla, D. Buddhi, F. Bruno, and Atul Sharma

Abstract The demand for hot water in the domestic sector is increased rapidly in a few decades around the globe. As well the adverse effects of global warming due to the exploration of conventional coal-based technology are faced everywhere in this period. The technology of solar water heating (SWH) is the proven method for heating water from solar radiation for curbing greenhouse gas (GHG) emissions. But solar radiations are available in intermittent nature, so there is a need for the accumulation of solar energy in latent heat form in the storage tank of the SWH system. Many studies have revealed that storing latent heat, the phase change materials (PCMs) are the utmost eligible materials. It has been observed that PCMs are capable to improve the thermal efficiency as well as reducing the existing storage tank size of the SWH systems. Generally, it is found that the eligible PCMs are capable to store an appreciable amount of energy for more than 1500 thermal cycles without making corrosion for encapsulated container material. Even the biggest challenge for the commercialization of encapsulated PCMs in the storage tank is its associated cost. This study will provide a review of the benefits of applications of PCMs for the SWH storage tanks along with the potential eligible materials of PCMs.

Keywords Solar energy · Solar water heater · Phase change material

S. Singh · A. Anand · A. Shukla · A. Sharma (✉)
Non-Conventional Energy Laboratory, Rajiv Gandhi Institute of Petroleum Technology, Jais, Amethi, India
e-mail: asharma@rgipt.ac.in

A. Shukla
Department of Physics, University of Lucknow, Lucknow, India

D. Buddhi
UIT, Uttaranchal University, Dehradun, India

F. Bruno
Future Industries Institute, University of South Australia, Mawson Lakes, Australia

D. Tripathi et al. (eds.), *Advancements in Nanotechnology for Energy and Environment*,
Advances in Sustainability Science and Technology,
https://doi.org/10.1007/978-981-19-5201-2_5

Nomenclature

SWH	Solar water heating
PCM	Phase change material
GHG	Greenhouse gas
Q	Amount of heat stored (J)
m	Mass of PCM (kg)
C_p	Specific heat of PCM (J/kg K)
T_i	Initial temperature of PCM (°C)
T_f	Final temperature of PCM (°C)
T_c	Inlet cold water temperature (°C)
T_{max}	Maximum temperature of water without PCM (°C)
t_w	Time for storage of hot water in the storage tank without PCM (s)
$c_{P,PCM-s}$	Specific heat in solid-state of PCM (kJ/kg K)
Q_L	Latent heat of PCM storage tank (kJ)
ΔT_1	Temperature difference between the maximum hot water and melting temperature of PCM (K)
T_m	Melting temperature of PCM (°C)
C_{sp}	Specific heat of PCM in the solid phase (J/kg K)
C_{lp}	Specific heat of PCM in the liquid phase (J/kg K)
a_m	Fraction melted
Δh_m	Latent heat of fusion (J/kg)
$\dot{m}_w$	Mass flow rate of water (kg/s)
$\dot{m}_w$	Mass flow rate of water (kg/s)
$c_{p,w}$	Specific heat of water (kJ/kg K)
$c_{p,w}$	Specific heat of water (kJ/kg K)
T_h	Hot water temperature (°C)
m_w	Water mass in the heat storage tank without PCM (kg)
T_{mean}	Mean temperature of water without PCM (°C)
$c_{P,PCM-L}$	Specific heat in the liquid state of PCM (kJ/kg K)
Q_S	Sensible heat of PCM storage tank (kJ)
Q_{PCM}	Total heat for the PCM storage tank (kJ)
ΔT_2	Temperature difference between the hot water taken and melting temperature of PCM (K)

1 Introduction

It is well known that the SWH system is utilizing solar radiation for heating water through the collector, and then, the heated water is stored in the storage tank. But the availability of solar radiation for heating of water is from morning time of 6 am to till evening time of 6 pm. At the same time, the majorly of demand in the domestic application of hot water is taken place from 5 am to 8 pm in the late evening. The

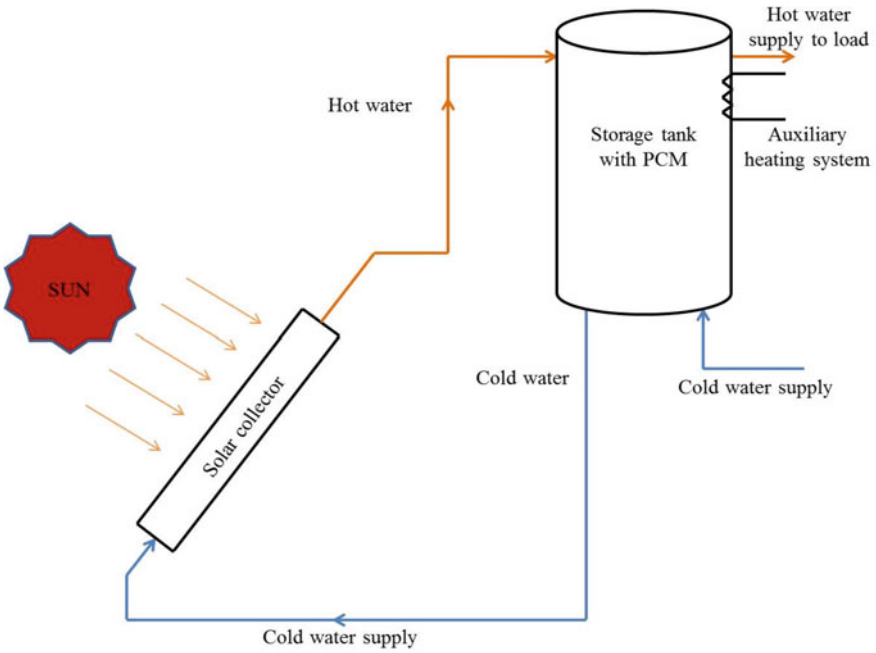

Fig. 1 SWH system with PCM

availability duration and intensity of solar radiation cannot be altered or modified, but the storage of heat can be performed through the application of suitable PCMs inside of storage tank of SWHs. The schematic arrangement of the solar collector, storage tank along with PCM, auxiliary heating system, and piping system is shown in Fig. 1.

The PCMs are capable to store heat energy during the daytime duration when these materials are incorporated inside of the storage tank. And when heat is required during off sunshine hours, these PCMs provide heating action of water. The PCMs absorb heat in form of latent heat, and these materials are capable of exchanging heat energy with water in several thermal cycles. These PCMs are generally kept inside metallic containers in the submerged condition of the water. When the temperature of the water around these containers rises from the melting temperature of PCM, then PCM becomes melted inside of these containers, and latent heat is stored in PCM. And when the temperature of the water goes down well below from solidification temperature of PCM, then heating of water by PCM takes place. The storing heat of PCMs along with the rise of temperature is shown in Fig. 2.

The amount of sensible heat collected in PCMs is described by the following equation as [1],

$$\mathrm{Q} = Q = \int_{\mathrm{Ti}}^{\mathrm{Tf}} \mathrm{mCpdT}$$

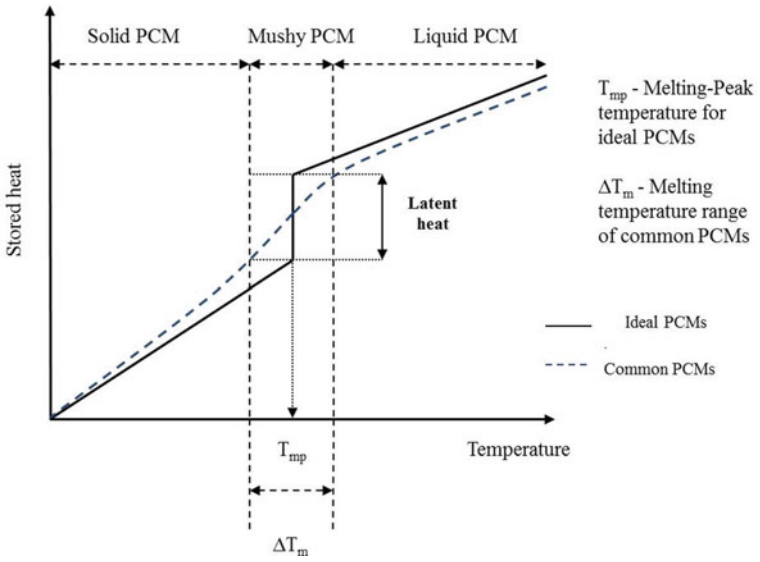

Fig. 2 Stored heat of PCMs

$$= m\, C_p(T_f - T_i)$$

where m is the mass of PCM, C_p is the specific heat of PCM, T_i is the initial temperature of PCM, and T_f is the final temperature of PCM.

In the same sequence, the total amount of heat stored in PCMs is described by the following equations as of [1],

$$Q = \int_{Ti}^{Tm} mCpdT + m\, a_m \Delta h_m + \int_{Tm}^{Tf} mCpdT$$

$$Q = m\left[C_{sp}(T_m - T_i) + a_m \Delta h_m + C_{lp}(T_f - T_i)\right]$$

where T_m is the melting temperature of PCM, subscript "s" denotes the specific heat of PCM in the solid phase, and subscript "l" denotes the specific heat in the liquid phase of PCM.

It is also observed that when PCMs are kept inside of container materials in an encapsulated condition, then the overall size requirement of the storage tank could be decreased up to an appreciable amount. So, by using PCMs inside of the storage tank, the existing design of the storage tank can be reduced compactly. Here, one thing should be noted the selection of PCMs should be also important for successfully improving the performance of the storage tank of the SWH system. The selected materials should be capable of storing an appreciable amount of heat energy within themselves.

2 Role of PCMs

2.1 Application of PCMs for Storage Tank of SWH System

Canbazoglu et al. [2] have examined the impact of PCM when it is incorporated inside of storage tank of the SWH system. They have compared the two situations of the storage tank in which one is filled with PCMs, and another is not filled as a conventional storage tank. They found that the storage tank filled with PCM is capable to give better thermal performance about 2 to 3 times more than a conventional storage tank. In their experimental study, they found that sodium thiosulfate pentahydrate is the most effective PCM for storing heat energy. Regin et al. [3] have calculated the effect of storage tanks filled with PCM in spherical balls in shape. They applied the enthalpy method for their study and found that to investigate the impact of PCM-filled storage tanks, the accurate phase transforming temperature of PCM should be known. While the study of a storage tank filled with spherical balls of PCM is also carried out by Reddy et al. [4]. They investigated two types of PCM balls, namely stearic acid PCM balls and paraffin wax PCM balls. They carried out their experiment with different values of flow rate and different values of the diameter of PCM balls. They found that the PCM balls of 38 mm diameter have a respectable impact in enhancing the enactment of the storage tank. Fazilati and Alemrajabi [5] have also examined the performance of spherical ball-shaped PCM encapsulated inside the storage tank. During their experiment, they apply three types of solar radiation intensities, namely weak, medium, and strong. They utilize paraffin wax as PCM balls and found that the energy storage capacity of the tank is improved by 39% along with a 16% increase in exergy efficiency. Huang et al. [6] have examined experimentally the thermal enactment of the storage tank by application of sodium acetate trihydrate PCM balls. They have identified the optimal situation of PCM balls for improved thermal stratification of the tank. They found that the lower position of PCM balls is preferred along with the 0.42 m^3/h inlet flow rate of water. Bazri et al. [7] have developed an evacuated tube type of storage tank in which they applied multiple layers of PCMs for enhancing the thermal performance. They carried out their experiment for different values of flow rate and various climatic conditions ultimately, they found that their PCM embodied evacuated tube SWH system has better thermal performance in comparison with conventional storage tanks. Dadollahi and Mehrpooya [8] have investigated the charging phenomenon of high-temperature PCMs for storage tanks. They identified that the ratio of surface area to volume of PCMs plays an imperative role in the charging of PCMs. If this ratio is high, then the charging time of PCMs in the tanks will be less. Bouhal et al. [9] have explored the new design model of the PCM embodied storage tank. They have applied specific heat capacity and enthalpy techniques for their study. They found complete melting time of PCMs inside of storage tank is 2.5 h. And if the amount of PCMs will be increase in quantity, then it will lead to a decrease in the melting quantity of PCMs and an increase in heat loss by the storage tank. Wang et al. [10] have studied the application of PCMs for SWH systems in the ways of structural analysis and

methodological point of view. They found that PCMs are suitable and recommended for applications. Sadhishkumar and Balusamy [11] have studied the SWH system with PCM and without PCM for domestic applications. They did their experiment by filling paraffin wax as PCM in aluminum containers. They found that by application of PCM, the efficiency of the SWH system is increased from 36 to 47%. Teamah et al. [12] have done a study of a storage tank containing PCMs in vertical bars. They analyzed the PCM melting in bars by enthalpy porosity method. They calculated the benefits of PCMs through the performance parameter of solar fraction.

2.2 Suitable Compounds Used as PCMs for Storage Tank of SWH System

Many substances proved themselves as suitable PCMs for storing heat energy. Among them few are listed here in Tables 1, 2, 3, 4 and 5, these substances are the most suitable materials for encapsulation purposes as PCM material in the storage tank of SWHs. These materials are recommended here due to their favorable properties of melting temperature and latent heat of fusion.

2.3 Governing Mathematical Equations of PCMs

In this section, the governing mathematical equations are described by considering the two cases of storage tanks of the SWHs as presented in Fig. 3. In one case, PCMs are not used, and in another case, the PCMs are used in encapsulated conditions.

The amount of heat collected per unit time without PCMs in the storage tank of the SWH system is described as

$$\dot{Q}_w = \dot{m}_w c_{p,w}(T_h - T_c) \tag{1}$$

where $\dot{m}_w$= mass flow rate of water, $c_{p,w}$= specific heat of water, T_h = hot water temperature, T_c = temperature of inlet cold water.

The complete heat collected in the form of the sensible heat of water mass in the heat storage tank without PCM is presented as

$$Q_w = m_w c_{p,w}(T_{max} - T_{mean}) \tag{2}$$

Here T_{max} and T_{mean} are maximum and mean temperature of water without PCM.

The time (t_w) for storage of hot water in the storage tank without PCM is intended by the Eqs. (1) and (2) as

Table 1 Inorganic compounds as PCMs

Compound	Melting temperature, T_m (°C)	Heat of fusion (KJ/Kg)	References
$LiNO_3 \cdot 3H_2O$	30.0	296.0	Zalba et al. [13]
$Na_2SO_4 \cdot 10H_2O$	31–32	–	Zalba et al. [13]
	32.0	251.1	Zalba et al. [13]
	32.4	254.0	Abhat [14] Naumann et al. [15] Hawes et al. [16]
$Na_2CO_3 \cdot 10H_2O$	33.0	247.0	Naumann et al. [15]
	32.0–36.0	246.5	Zalba et al. [13]
$CaBr_2 \cdot 6H_2O$	34.0	115.5	Dincer et al. [17] Naumann et al. [15] Lane [18]
$Na_2HPO_4 \cdot 12H_2O$	35.0	281.0	Hawes et al. [16]
	35.2	–	Naumann et al. [15]
	35.5	265.0	Zalba et al. [13]
	36.0	280.0	Zalba et al. [13]
$Zn(NO_3)_2 \cdot 6H_2O$	36.0	146.9	Dincer et al. [17] Naumann et al. [15] Lane [18]
	36.4	147.0	Abhat [14] Hawes et al. [16]
$KF \cdot 2H_2O$	41.4	–	Naumann et al. [15]
$K(CH_3COO)0.1\ \frac{1}{2}\ H_2O$	42.0	–	Zalba et al. [13]
$K_3PO_4 \cdot 7H_2O$	45.0	–	Zalba et al. [13]
$Zn(NO_3)_2 \cdot 4H_2O$	45.5	–	Zalba et al. [13]
$Ca(NO_3)_2 \cdot 4H_2O$	42.7	–	Naumann et al. [15]
	47.0	–	Zalba et al. [13]
$Na_2\ HPO_4 \cdot 7H_2O$	48.0	–	Naumann et al. [15]
$Na_2S_2O_3 \cdot 5H_2O$	48.0	201.0	Abhat [14] Naumann et al. [15]
	48.0–49.0	209.3	Zalba et al. [13]
$Zn(NO_3)_2 \cdot 2H_2O$	54.0	–	Zalba et al. [13]
$NaOH \cdot H_2O$	58.0	–	Naumann et al. [15]
$Na(CH_3COO)0.3H_2O$	58.0	264.0	Zalba et al. [13]
	58.4	226.0	Naumann et al. [15] Zalba et al. [13]
$Cd(NO_3)_2 \cdot 4H_2O$	59.5	–	Naumann et al. [15]
$Fe(NO_3)_2 \cdot 6H_2O$	60.0	–	Zalba et al. [13]

(continued)

Table 1 (continued)

Compound	Melting temperature, T_m (°C)	Heat of fusion (KJ/Kg)	References
NaOH	64.3	227.6	Zalba et al. [13]
$Na_2B_4O_7{\cdot}10H_2O$	68.1	–	Naumann et al. [15]
$Na_3PO_4{\cdot}12H_2O$	69.0	–	Naumann et al. [15]
$Na_2P_2O_7{\cdot}10H_2O$	70.0	184.0	Zalba et al. [13]
$Ba(OH)_2{\cdot}8H_2O$	78.0	265.7	Abhat [14] Dincer et al. [17] Naumann et al. [15] Lane [18] Zalba et al. [13]
	–	267.0	
	–	280.0	
$AlK(SO_4)_2{\cdot}12H_2O$	80.0	–	Zalba et al. [13]
$Kal(SO_4)_2{\cdot}12H_2O$	85.8	–	Naumann et al. [15]
$Al_2(SO_4)_3{\cdot}18H_2O$	88.0	–	Naumann et al. [15]
$Al(NO_3)_3{\cdot}8H_2O$	89.0	–	Zalba et al. [13]
$Mg(NO_3)_2{\cdot}6H_2O$	89.0	162.8	Dincer et al. [17] Lane [18]
	90.0	149.5	Naumann et al. [15] Zalba et al. [13]
$(NH_4)Al(SO_4)0.6H_2O$	95.0	269.0	Zalba et al. [13]
$Na_2S.5\ \frac{1}{2}\ H_2O$	97.5	–	Zalba et al. [13]
$CaBr_2{\cdot}4H_2O$	110	–	Zalba et al. [13]

$$t_w = \frac{Q_w}{\dot{Q}_w}$$

The mass of hot water prepared through the SWHs without PCM is calculated as

$$m = \dot{m}_w \times t_w$$

In the case of the PCM storage tank, the sensible heat (Q_S) is calculated by Eq. (3) as

$$Q_S = m_w c_{p,w} \Delta T + m_{PCM}\left(c_{P,PCM-L}\Delta T_1 + c_{P,PCM-S}\Delta T_2\right) \tag{3}$$

The latent heat (Q_L) is calculated by Eq. (4) as

$$Q_L = m_{PCM} h_{SL} \tag{4}$$

The total heat (Q_{PCM}) for the PCM storage tank is calculated by Eq. (5) as

$$Q_{PCM} = Q_S + Q_L \tag{5}$$

Table 2 Inorganic eutectics as PCMs

Compound	Melting temperature, T_m (°C)	Heat of fusion (KJ/Kg)	References
47% $Ca(NO_3)_2{\cdot}4H_2O$ + 33% $Mg(NO_3)_2{\cdot}6H_2O$	30	136	Abhat [14]
60% $Na(CH_3COO)0.3H_2O$ + 40% $CO(NH_2)_2$	30	200.5	Zalba et al. [13]
	31.5	226	
61.5% $Mg(NO_3)_2{\cdot}6H_2O$ + 38.5% NH_4NO_3	52.0	125.5	Lane [18]
	–	–	
	–	–	
58.7% $Mg(NO_3)0.6H_2O$ + 41.3% $MgCl_2{\cdot}6H_2O$	58.0	132.0	Zalba et al. [13]
	–	–	
	–	–	
	59.0	132.2	Lane [18]
53% $Mg(NO_3)_2{\cdot}6H_2O$ + 47% $Al(NO_3)_2{\cdot}9H_2O$	61.0	148.0	Abhat [14]
14% $LiNO_3$ + 86% $Mg(NO_3)_2{\cdot}6H_2O$	72	180.0	Zalba et al. [13]
66.6% urea + 33.4% NH_4Br	76	161.0	Lane [18]
	–	–	
	–	–	
	–	–	

2.4 Desired Properties of PCM for Encapsulation in the Storage Tank of the SWH System

In this section, some utmost important desired properties of PCMs for encapsulation purposes in the storage tank of SWHs are presented here,

- Thermal Properties

During encapsulation of PCMs, they should be in the desired temperature range of phase transition. It is also favorable that PCMs should have high-latent heat of transition along with high-thermal conductivity.

- Physical Properties

According to the need for physical properties, the PCMs should have high density, low-vapor pressure, negligible volume change, and desired phase equilibrium.

- Kinetic properties

According to the need for kinetic properties, PCMs should have an adequate rate of crystallization along with no supercooling.

Table 3 Organic compounds as PCMs

Compound	Melting temperature, T_m (°C)	Heat of fusion (KJ/Kg)	References
Paraffin C_{18}	27.5	243.5	Sasaguchi et al. [19]
	–	–	
	28.0	244.0	Abhat [14]
1-Tetradecanol	38.0	205.0	Hawes et al. [16]
Paraffin C_{16}–C_{28}	42.0–44.0	189.0	Abhat [14]
Paraffin C_{20}–C_{33}	48.0–50.0	189.0	Abhat [14]
Paraffin C_{22}–C_{45}	58.0–60.0	189.0	Abhat [14]
Paraffin wax	64.0	173.6	Dincer et al. [17]
	–	266	
	–	–	
Polyglycol E6000	66.0	190.0	Dincer et al. [17] Lane [18]
Paraffin C_{21}–C_{50}	66.0–68.0	189.0	Abhat [14]
Biphenyl	71.0	119.2	Dincer et al. [17] Lane [18]
Naphthalene	80.0	147.7	Dincer et al. [17] Lane [18]
	–	–	
Erythritol	118.0	339.8	Zalba et al. [13]

- Chemical properties

In case of desirable chemical properties, PCMs should not be decomposed, and they have to be in chemical stability for a long duration of time. It is also desirable that PCMs have good compatibility with encapsulated container materials along with non-toxic, non-explosive, and non-flammable in nature.

- Technical criteria

According to the requirement of technical criteria, it is desirable that the PCMs should be reliable, effective, compatible, and viable in nature for storage inside tanks of SWHs.

- Economics

According to the economic point of view of PCMs, they should be available at a cheaper cost for use in the storage tank of SWHs.

Table 4 Fatty acids as PCMs

Compound	Melting temperature, T_m (°C)	Heat of fusion (KJ/Kg)	References
Vinyl stearate	27.0–29.0	122.0	Feldman et al. [20]
Capric acid	31.5	153.0	Abhat [14]
	–	–	
	32	152.7	Dincer et al. [17] Lane [18]
Methyl-12 hydroxy-stearate	42.0–43.0	120.0–126.0	Feldman et al. [20]
Lauric acid	42.0–44.0	178.0	Abhat [14]
	44.0	177.4	Lane [18]
Myristic acid	49.0–51.0	204.5	Zalba et.al. [13]
	54.0	187.0	Abhat [14]
	58.0	186.6	Lane [18]
Palmitic acid	61.0	203.4	Sari et al. [21]
	63.0	187.0	Abhat [14]
	64.0	185.4	Dincer et al. [17] Lane [18]
Stearic acid	60.0–61.0	186.5	Sari et al. [22]
	69.0	202.5	IDincer et al. [17] Lane [18]
	70.0	203.0	Abhat [14]

2.5 Recommend Design Modules of PCMs for the SWH System

In this section, some favorable design modules for encapsulation purposes are described as shown in Fig. 4.

It is evident from several studies that PCM modules should be arranged in such a manner that they should be able to perform maximum thermal stratification for the storage tank. It is observed that the biggest challenge of encapsulation is that PCMs should be completely melted and solidified as per the design temperature range of the storage tank. In this regard, PCMs should be encapsulated in the shape of cylindrical cans, spherical balls, and inside hollow tubes as shown in Fig. 4. Even some other parameters also play an important role like mass flow rate of water, spacing among the PCM encapsulation, and container materials for encapsulation. It is recommended that the flow rate should not be very high in place it should be in a moderate range so that proper heat interaction between water and encapsulated PCMs can take place. Some experimental studies are suggested that random packaging of PCMs is more useful for enhancing the thermal stratification in place of a special packaging system. The material selection of containers for encapsulation of PCM is

Table 5 Commercial PCMs

Compound	Melting temperature, T_m (°C)	Heat of fusion (KJ/Kg)	Source
ClimSel C 32	32	212	Climator
RT40	43	181	Rubitherm GmbH
STL47	47	221	Mitsubishi chemical
ClimSel C 48	48	227	Climator
STL52	52	201	Mitsubishi chemical
RT50	54	195	Rubitherm GmbH
STL55	55	242	Mitsubishi chemical
TH58	58	226	TEAP
ClimSel C 58	58	259	Climator
RT65	64	207	Rubitherm GmbH
ClimSel C 70	70	194	Climator
PCM72	72	–	Zalba et al. [13]
RT80	79	209	Rubitherm GmbH
TH89	89	149	TEAP
RT90	90	197	Rubitherm GmbH
RT110	112	213	Rubitherm GmbH

an essential characteristic for heat interaction in the storage tank of the SWH system. These materials should be capable to allow the maximum amount of heat without any hindrance, and these should be non-corrosive. Some common container materials are listed in the Table 6.

3 Challenges of PCMs

It has been revealed by many studies that at some time, PCMs are not performing the desired tasks of charging and discharging latent heat during melting and solidification inside of container materials. Due to this reason, PCMs will not be thermally beneficial as much as should be. It is desirable that PCMs should be capable to store plenty

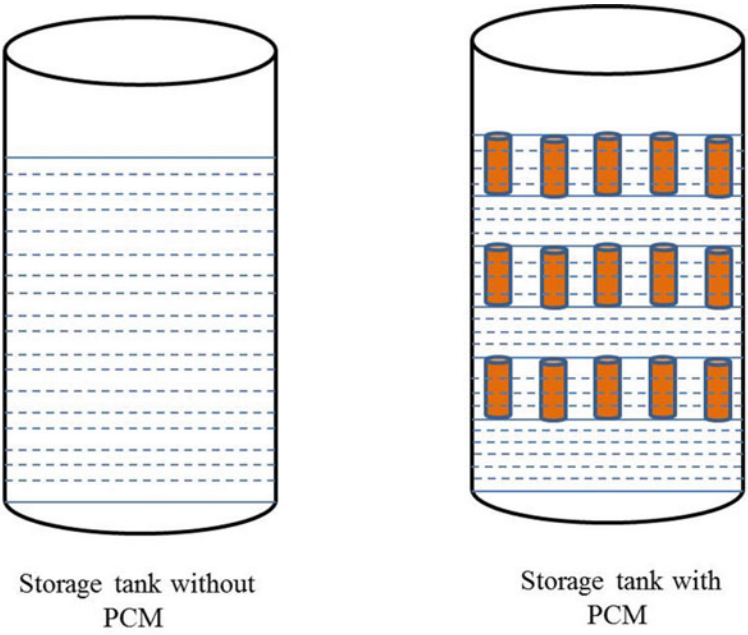

Fig. 3 Storage tanks with PCM and without PCM

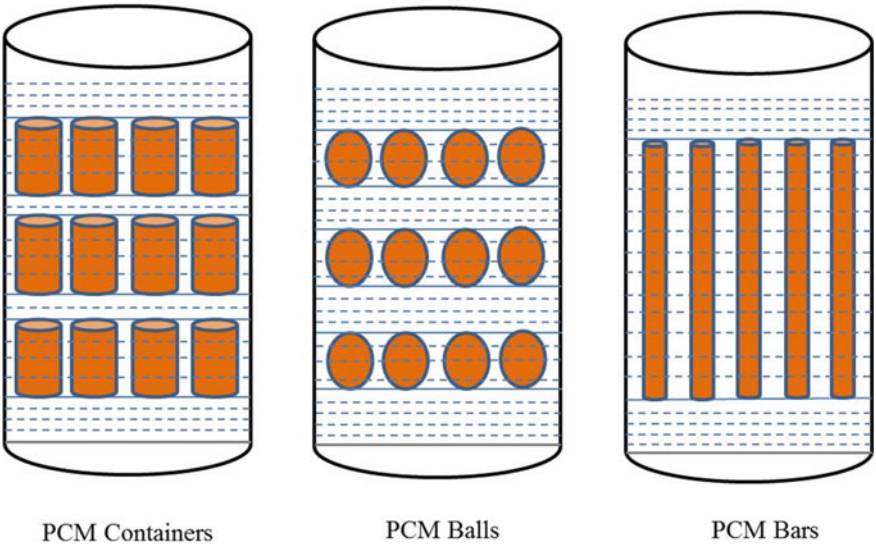

Fig. 4 Encapsulated PCM modules

Table 6 Common container materials [23]

Container materials	Density (kg/m^3)	Thermal conductivity (W/m °C)	Specific heat (kJ/kg °C)
Glass	2700	0.78	0.840
Stainless steel	8010	7.7	0.500
Tin	7304	64	0.226
Aluminum	2707	204	0.896
Aluminum mixed	2659	137	0.867
Copper	8954	386	0.383

amount of latent heat as per the design criteria of the thermal system. Otherwise, PCMs will enhance the rate of heat transfer from the storage tank to the surroundings due to the addition of extra weight and surface area of it. So that it becomes essential to know some microstructural confines of PCMs. So, in this section of the chapter, some most occurring obstacles to encapsulation of PCMs inside container materials in the storage tank of the SWH system are discussed here as [17, 24],

- Freezing or solidification

It is observed that some materials are not fit to consider as PCM due to their freezing or solidification performance. It is found that few materials show incongruent freezing behavior during solidification which is not desired at all for PCMs.

- Supercooling

Supercooling occurs when a material attempts to freeze well below the melting temperature, but it could not be frozen. Some research studies have concluded that it happens due to the viscosity of liquid at the melting point.

- Nucleation

The nucleation of PCMs can take place in homogeneous and heterogeneous ways. In the case of homogeneous nucleation, without adding any materials, the rate of nucleation from the melt is amplified. While in the case of homogeneous nucleation, the nucleation is formed due to the presence of some impurities within the melt.

- Thermal cycling

In actual practice, PCMs must go through no cycles of operations, so PCMs must retain their properties throughout their service time. Some inappropriate PCM materials lose their properties after some period of thermal cycles.

- Encapsulation

In encapsulation, viewpoint shows that PCMs must be incorporated in such type of material which should be a respectable conductor of heat so it makes effective heat transfer and must be tough to break.

It is recommended that the above-discussed limitations of PCMs should be paid attention to while designing the thermal storage tank of the SWH system for getting a more effective thermal performance.

4 Conclusion

It is evident from the above discussion and published literature that, the PCMs used in the storage tank of SWHs are greatly advantageous for enhancing the thermal performance of the solar system. The most recommended PCM materials for encapsulation purposes are sodium thiosulfate pentahydrate, paraffin wax, stearic acid, sodium acetate trihydrate, etc. The encapsulated arrangement of PCMs should be in such a way that the maximum thermal stratification should be performed so that the overall mean temperature of the tank should be increased. The shape of encapsulation of PCMs plays an important role in the complete melting and solidification process. In this viewpoint, spherical ball or capsule-shaped PCMs are recommended and found suitable in many experimental studies. While selecting the desired PCM, it should be given attention to the total quantity used in the storage tank if the total mass of PCM is in a very large quantity, then the heat transfer rate from the storage tank may be increased and extra insulation of the tank is required. The used PCMs should be capable to retain their thermal properties in many thermal cycles, so frequent replacement of PCMs should be avoidable. The type of PCM and its quantity should be chosen in such a way that the cost of the SWH system should not be very expensive.

Acknowledgements This research work is supported by the Indo-Australian joint project entitled "Thermal Energy Storage for Food/Grain Drying with CST/RE to Lower Pollution".

References

1. Sharma A, Tyagi VV, Chen CR, Buddhi D (2009) Review on thermal energy storage with phase change materials and applications. Renew Sustain Energy Rev 13(2):318–345. https://doi.org/10.1016/j.rser.2007.10.005
2. Canbazoğlu S, Şahinaslan A, Ekmekyapar A, Aksoy ÝG, Akarsu F (2005) Enhancement of solar thermal energy storage performance using sodium thiosulfate pentahydrate of a conventional solar water-heating system. Energy Build 37(3):235–242. https://doi.org/10.1016/j.enbuild.2004.06.016
3. Felix Regin A, Solanki SC, Saini JS (2009) An analysis of a packed bed latent heat thermal energy storage system using PCM capsules: numerical investigation. Renew Energy 34(7):1765–1773. https://doi.org/10.1016/j.renene.2008.12.012
4. Reddy RM, Nallusamy N, Reddy KH (2012) Experimental studies on phase change material-based thermal energy storage system for solar water heating applications. J Fundam Renew Energy Appl 2:1–6. https://doi.org/10.4303/jfrea/R120314

5. Fazilati MA, Alemrajabi AA (2013) Phase change material for enhancing solar water heater, an experimental approach. Energy Convers Manag 71:138–145. https://doi.org/10.1016/j.enconman.2013.03.034
6. Huang H et al (2019) An experimental investigation on thermal stratification characteristics with PCMs in solar water tank. Sol Energy 177:8–21. https://doi.org/10.1016/j.solener.2018.11.004
7. Bazri S, Badruddin IA, Naghavi MS, Seng OK, Wongwises S (2019) An analytical and comparative study of the charging and discharging processes in a latent heat thermal storage tank for solar water heater system. Sol Energy 185(April):424–438. https://doi.org/10.1016/j.solener.2019.04.046
8. Dadollahi M, Mehrpooya M (2017) Modeling and investigation of high temperature phase change materials (PCM) in different storage tank configurations. J Clean Prod 161:831–839. https://doi.org/10.1016/j.jclepro.2017.05.171
9. Bouhal T, El Rhafiki T, Kousksou T, Jamil A, Zeraouli Y (2018) PCM addition inside solar water heaters: numerical comparative approach. J Energy Storage 19(August):232–246. https://doi.org/10.1016/j.est.2018.08.005
10. Wang Z, Qiu F, Yang W, Zhao X (2015) Applications of solar water heating system with phase change material. Renew Sustain Energy Rev 52:645–652. https://doi.org/10.1016/j.rser.2015.07.184
11. Sadhishkumar S, Balusamy T (2017) Comparison of solar water heater with and without phase change material as latent heat storage. Adv Nat Appl Sci 11(4):605–611. http://www.aensiweb.com/http://creativecommons.org/licenses/by/4.0/
12. Teamah HM, Lightstone MF, Cotton JS (2017) An alternative approach for assessing the benefit of phase change materials in solar domestic hot water systems. Sol Energy 158(August):875–888. https://doi.org/10.1016/j.solener.2017.10.033
13. Cabeza LF, Mehling H (2003) Review on thermal energy storage with phase change: materials, heat transfer analysis and applications, vol 23
14. Abhat A (1983) Low temperature latent heat thermal energy storage: heat storage materials. Sol Energy 30(4):313–332. https://doi.org/10.1016/0038-092X(83)90186-X
15. Naumann R, Emons HH (1989) Results of thermal analysis for investigation of salt hydrates as latent heat-storage materials. J Therm Anal 35(3):1009–1031. https://doi.org/10.1007/BF02057256
16. Hawes DW, Feldman D, Banu D (1993) Latent heat storage in building materials. Energy Build 20(1):77–86. https://doi.org/10.1016/0378-7788(93)90040-2
17. Ibrahim D (2011) Thermal energy storage: systems and applications/Ibrahim Dinçer and Marc Rosen
18. Taylor P, Lane GA, Lane GA (2011) Low temperature heat storage with phase change materials low temperature heat storage with phase change materials, October 2013, pp 37–41. https://doi.org/10.1080/01430750.1980.9675731
19. Sasaguchi K, Viskanta R (2016) Phase change heat transfer during melting and resolidification of melt around cylindrical heat source(s)/sink(s), vol 111, March 1989
20. Feldman D, Shapiro MM, Banu D (1986) Organic phase change materials for thermal energy storage. Sol Energy Mater Sol Cells 13:1–10
21. Sari A, Kaygusuz K (2002) Thermal performance of palmitic acid as a phase change energy storage material, vol 43, pp 863–876
22. Sari A, Kaygusuz K (2001) Thermal energy storage system using stearic acid as a phase change material. Sol Energy 71(6):365–376. https://doi.org/10.1016/S0038-092X(01)00075-5
23. Anand A, Shukla A, Sharma A (2020) Numerical heat transfer study of energy storage materials used in the latent heat storage system. Mater Sci Energy Technol 3:633–639. https://doi.org/10.1016/j.mset.2020.06.007
24. Duffie JA, Beckman WA, McGowan J (1985) Solar engineering of thermal processes. Am J Phys 53(4):382–382. https://doi.org/10.1119/1.14178

Chapter 6
Different Degradation Modes of PV Modules: An Overview

Shubham Sharma, Gautam Raina, Prashant Malik, Vikrant Sharma, and Sunanda Sinha

Abstract The technological advancements and lower energy costs have provided a smooth pathway for solar photovoltaic (PV) technology to grow as one of the leading renewable energy resources in the twenty-first century. However, for long-term operations, the reliability of a PV module is compromised throughout its lifetime as a result of various degradation mechanisms. It is necessary to address the issue of degradation in order to accurately assess the power declination with time as well as to overcome the financial losses. This manuscript provides a detailed review of the major degradation processes acting on the PV cells or modules which gradually diminish their power generation capabilities and result in lower output. The main causes of these deteriorating effects and the extent to which these exploit various performance characteristics of PV modules have also been discussed. This paper also gives a short overview of detection techniques used for visualization of defects in PV modules. Discoloration, delamination and corrosion are the most dominating modes of PV module degradation, while light-induced degradation (LID) can affect the module in its early stages. High ambient temperature, moisture and UV radiations strongly enhance the possibility of this phenomenon to occur. Thus, in order to have long-term operations, time-to-time monitoring and maintenance of modules are recommended.

Keywords Degradation · Reliability · Monitoring · Solar PV

S. Sharma · G. Raina · S. Sinha (✉)
Centre for Energy and Environment, Malaviya National Institute of Technology, Jaipur 302017, Rajasthan, India
e-mail: sunandasinha123@gmail.com; sunanda.cee@mnit.ac.in

P. Malik
Centre of Excellence in Energy Science & Technology, Shoolini University, Solan 173212, Himachal Pradesh, India

V. Sharma
National Institute of Solar Energy, Gurugram 122003, Haryana, India

D. Tripathi et al. (eds.), *Advancements in Nanotechnology for Energy and Environment*,
Advances in Sustainability Science and Technology,
https://doi.org/10.1007/978-981-19-5201-2_6

Abbreviations

PV	Photovoltaic
EVA	Ethyl vinyl acetate
LID	Light-induced degradation
CZ	Czochralski process
LeTID	Light and elevated temperature-induced degradation
PERC	Passivated emitter rear cells
c-Si	Crystalline silicon
PID	Potential-induced degradation
IEC	International Electrotechnical Commission
UV	Ultraviolet
Na	Sodium
TCO	Transparent conductive oxide
NREL	National Renewable Energy Laboratory
TID	Temperature induced degradation
EL	Electroluminescence
IR	Infrared
NDT	Non-destructive testing
MOSFET	Metal oxide semiconductor field effector transistor
STC	Standard test conditions

1 Introduction

Solar photovoltaic technology has evolved as a leading renewable energy source in the past few decades with better energy conversion techniques and improved efficiencies. The popularity of solar power generation can be ascertained from the fact that solar PV installed capacity has grown to 760 GW worldwide [1]. Solar panels play a dominating role in determining the reliability of any PV power system. As the solar energy market is growing worldwide, researchers are more inclined towards investigating and determining the extent of degradation modes affecting the performance of PV modules. A degraded module may keep serving its key function of harnessing power from sunlight but at the same time, output of these systems might be comparatively low and there could be a variety of factors and degradation modes responsible for it, which, if not detected and eradicated, may cause failure of module. Degradation is any phenomenon which deteriorates the characteristics of any system and affects its ability to perform a desired task within the acceptable limits, mainly caused by the operating conditions. The degradation of any system over some time period is known as degradation rate which is generally expressed in the units of %/year. A solar module is considered as degraded if its power producing capabilities fall below 80% of its initial maximum power [2]. This definition of degradation has got manufacturers to provide a guarantee of 25 years on PV modules which includes

up to 10% decline in maximum power after initial 10–12 years and 20% decline after 25 years of operation [3]. This 20% decline in power cannot be regarded as failure because a more efficient module degraded by 50% can still perform with higher efficiency as compared to a non-degraded module with less efficient technology. The study of degradation is important because for long term, the power output of the module decreases with time and it affects the return on investment and thus the economy of the PV system. The inaccuracy in degradation prediction can cause irrelevant financial investments; thus, accurate lifetime degradation prediction studies must be carried out. There are various environmental and meteorological factors such as geographical location, relative humidity, wind speed, ambient temperature and solar radiation which affect the PV electricity generation [4]. Mechanical shocks which usually occur during the transportation and handling of modules may sometimes cause damage to the cells as well as the glass covering used to protect the module from external environment. There are various degradation modes which have been observed in a PV module [5–9]; these include corrosion, light-induced degradation (LID), soiling, temperature-induced degradation, encapsulant degradation (delamination and discoloration), solder fatigue, breakage and cracking of cells, potential-induced degradation (PID), hotspots and bubble formation. The lifetime of a PV module can be categorized under three phases: infant phase, midlife phase and wear-out phase, and it can be seen in Fig. 1 that a module is subjected to various degradation modes during its lifetime from the beginning period of its installation. Infant phase of PV module perceives a sudden decline in power mainly dominated by LID. EVA discolouring and delamination occur gradually and exist from midlife till the wear-out phase of the module. The literature and past observations suggest that delamination, discoloration and corrosion are the dominant modes of module degradation.

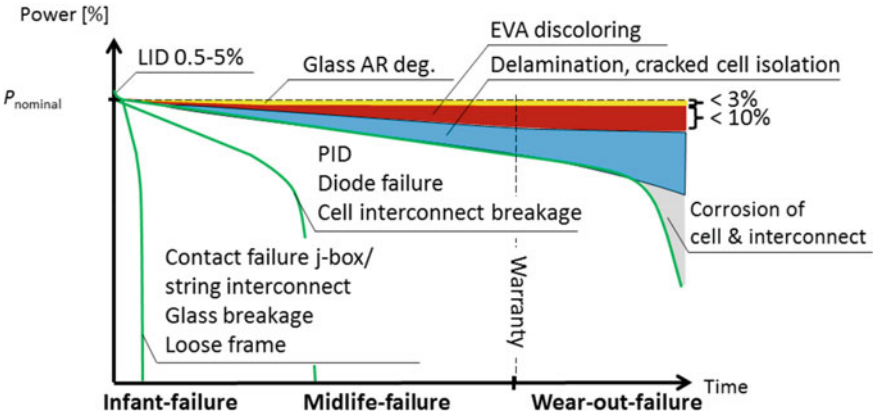

Fig. 1 Wafer-based crystalline module subjected to various degradation modes during its lifetime [10]

This chapter is organized in two parts, the first of which shows the major degradation modes for failure of PV modules and second part describes the extent of these modes on the performance of PV modules. Section 1 gives a brief introduction to the concept of degradation of PV modules, Sect. 2 provides a detailed elaboration of various degradation phenomenon ultimately causing power declination and even failure, Sect. 3 explains the cause of origination of each degradation phenomenon and its impact on the performance of PV modules, and Sect. 4 describes testing and detection techniques for visualizing defects in solar cells/modules followed by conclusive remarks in Sect. 5.

2 Degradation Modes in PV Modules

(a) **Corrosion**: Penetration of moisture and oxygen in the housing of PV module through laminated edges causes corrosion. Corrosion weakens the metallic interconnections within the cells of PV module and also attacks the adhesion between cells and metallic frames. Since the ageing of a module in outdoor field is quite long process, therefore, in Jet propulsion laboratory (JPL), researchers developed an accelerated test which consisted of 85% relative humidity and 85 °C temperature environment and a voltage as high as 500 V applied between the metallic frames and the module (in short circuit conditions with both polarities) in order to observe electrochemical corrosion [11]. Osterwald et al. [12] studied the electrochemical corrosion occurring in thin-film modules and reported that elevated temperature and presence of moisture greatly enhance the corrosion. Moisture which enters through laminate edges, being a good electrical conductor, also increases leakage current which ultimately causes the loss of power. Thin-film PV modules are generally fabricated by providing a coating of thin transparent conductive oxide (TCO) layer of tin oxide doped with fluorine (SnO_2:F) on a soda-lime glass substrate. The solar cell films are then deposited over tin oxide layer. A study conducted by [13] stated that combination of sodium accumulation between the tin oxide coating and glass interface with the moisture entering through the edges creates corrosion which in turn causes delamination of tin oxide coating from the glass substrate. In crystalline Si modules, metallic interconnections (fingers and busbars) are provided within the solar cells for collecting the generated current. For front and rear contact, Ag–Al paste is used and ethyl vinyl acetate (EVA) encapsulant is used as a protection layer against environment. EVA generates acetic acid by reacting with the moisture and corrodes the Ag–Al metallization [14, 15]. Corrosion not only affects the internal metallic connections but also weakens the junction box metal contacts (Fig. 2). According to [16], the moisture diffusion into the EVA is quite significant during the entire lifetime of a PV module. Thus, either a true hermetic seal or a low diffusivity seal containing enough amount of desiccant must be provided to the edges to avoid the moisture ingression into the module.

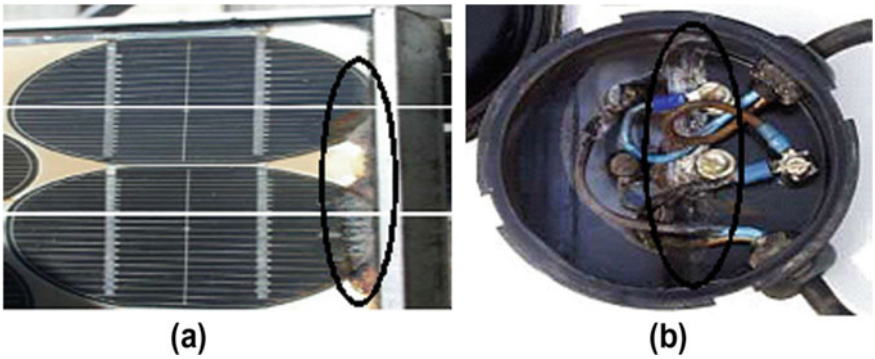

Fig. 2 Corrosion in the **a** edges of a module and **b** junction box [7]

(b) **Light-Induced Degradation (LID)**: LID is the loss of power incurred during the infant stage of a PV module due to the initial exposure to sunlight. LID occurs in amorphous as well as crystalline silicon solar cells. It is more severe in a-Si solar cells and degrades its efficiency by up to 30% [17] and better described as "Staebler-Wronski" effect. It enhances the recombination current in the base and affects the performance of c-Si modules by 0.5–3% [10], while some of the crystalline modules have also shown performance loss up to 5%. The a-Si has very large defects and weak electrical properties and thus cannot be used as solar cell. The a-Si in its hydrogenated (a-si:H) form has low defects, and it is used for solar cell manufacturing. In a-Si, there are about 10^{21} per cm^3 defects, while a-Si:H has 10^{15} to 10^{16} per cm^3 defects [18]. The efficiencies of these thin-film cells are quite low (5–7%) as compared to other solar cell technologies [19]. The initial illumination causes a great amount of performance/efficiency loss which is known as light-induced degradation. The physics behind this phenomenon was well studied by Staebler and Wronski in the year 1977 [20] and thus the name "Stabler-Wronski effect". In a-Si, the atoms are not arranged in order and atomic characteristics such as the bond length and bond angles have quite distinct values for each atom. It consists of missing bonds, popularly known as dangling bonds, which serve as defect centres and give rise to carrier recombination. Although these defects are low in a-Si:H cells, which are used in solar cell fabrication, but, due to variation in bond lengths and bond angles, the silicon-hydrogen bonds are also weak, less stable and strained in nature. In the presence of heat or radiation, the breakdown of these bonds creates additional defects and these defects act as the recombination centres of electron–hole pairs resulting in an initial drop in a-Si:H solar cell performance. This initial decrement in efficiency of a-Si:H solar cells due to exposure to sunlight is known as "Staebler-Wronski effect". The electrical and optical characteristics of the material are highly deteriorated by this phenomenon. The accelerated test for the LID involves radiation intensity of 1000 W/m^2 at a temperature of 50 °C for continuous 1000 h in open circuit conditions [19]. LID affects the crystalline

silicon solar cells which are developed on Czochralski (CZ) wafers. Almost 95% of the commercially available modules are developed using p-type (boron based) substrates. The two main reasons of LID in c-Si are ascribed to boron-oxygen (B-O) defects and iron-boron pair dissociation [21]. In CZ process, melting down hot silicon involves heating the quartz crucible to 1412 °C which provides oxygen for B-O complex formation. A carrier-driven recombination takes place due to light exposure as a result of the formation of boron-oxygen complex which acts as recombination centres in CZ wafers. Interstitial iron (Fe_i) present as an impurity in c-Si solar cells forms a pair with boron. When illuminated, these FeB pairs dissociate and create recombination defect centres in the form of interstitial iron. This dissociation under the light or irradiation is quite rapid and gives rise to LID. Ramspeck et al. [21] studied LID in rear passivated multi-crystalline Si solar cells and observed a strange dependence of degradation on module temperatures higher than 50 °C under initial illumination. The effect of LID with increasing temperature is shown in Fig. 3. This degradation is slow but stronger than those occurring in a-Si and c-Si modules. In passivated emitter rear cells (PERC), the impact of LID multiplies at elevated temperatures (50–80 °C) and is commonly termed as "light and elevated temperature-induced degradation (LeTID)" [22].

LeTID can degrade the performance of PERC solar cells by up to 10%. The exact reason behind this temperature-dependent LID in PERC solar cells is still unknown but it is believed that LeTID might occur due to the degradation of dielectric passivation layers. LeTID is also speculated to occur as a result of bulk recombination defect [23]. The negative impact of LID on a-Si and c-Si cells can be reversed by thermal recovery via annealing. Reverse electric field is applied to a-Si modules in order to recover from Staebler-Wronski effect. LID in CZ-based c-Si wafers can be avoided by using different materials to stop the formation of B-O complex. Modification in

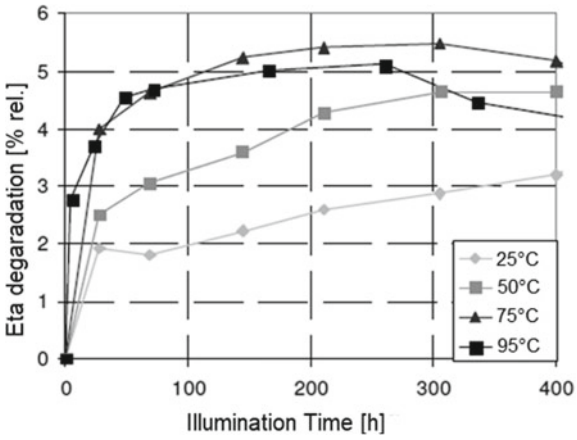

Fig. 3 Light-induced degradation in PERC multi-crystalline Si solar cells at different temperatures [21]

doping and "current-induced regeneration" are the other methods which can be used to recover from LID in c-Si cells fabricated on CZ wafers [24].

(c) **Soiling**: The accumulation of certain airborne contaminants on the glass surface of a PV module is called soiling. The examples of these deposited contaminants include mineral dirt/dust particles, salt particulates (near coastal areas), bird droppings, algae, fungi, bacterial films in wet climates, pollen, agricultural emission (rice husk, feed dust, etc.), vehicular emission and industrial emission (fly ash, cement, charcoal, etc.) [25–27]. Soiling obstructs the transmission of incident solar radiation and significantly reduces the PV power generation. Figure 4 shows the typical impact of soiling on the transmission and reflectance of incident solar radiation over a glass substrate. Soiling can cause cumulative power losses which may surpass a rate of 1%/day [28]. Densely deposited soiling particles partially cover the surface of PV modules which may result in high temperature zones [5, 29]. Accumulation of soiling on a PV panel's glass surface is mostly influenced by tilt angle, orientation of the module, wind speed, characteristics of glazing surface, particulate matter size, rain, atmosphere temperature and relative humidity [30]. Since the soiling issue has detrimental impact on performance of PV modules, cleaning of modules is quite mandatory in order to avoid power as well as associated financial losses.

(d) **Potential-Induced Degradation (PID)**: In solar power plants**,** modules are connected in series to form a string in order to enhance the voltage up to several hundreds of volts, while same amount of current is maintained through each module. The solar cells are laminated and provided with backsheet and then mounted on metallic frames, and these frames are then grounded or earthed for safety reasons. This earthing often develops a strong voltaic potential between solar cells and frame. When the insulation between metallic structure and active solar cell layers is weak, the leakage of current may take place from the cells to the frames (or vice versa, this leakage direction mainly depends on the positioning of module/cell in the string). This phenomenon causes a polarization effect which may deteriorate the health of solar cells and popularly known as "potential-induced degradation (PID)" [3]. Current that traverses from base to emitter without contributing to the connected load is called leakage current. The leakage currents are drastically enhanced due to PID, and there may be several pathways for these leakages to take place which include [17]:

- along front glass surface and moisture present on the surface
- through top surface of cells via electronic and ionic conduction
- through bulk of the EVA encapsulant layer
- through the back contact.

Different types of module technologies are affected in a unique manner by PID. In p-type c-Si modules, reduction in shunt resistance due to PID occurs and it is described by the term PID shunting (PID-s). Soda-lime glass is used in module fabrication and when p-type c-Si PV cells are subjected to negative biased conditions,

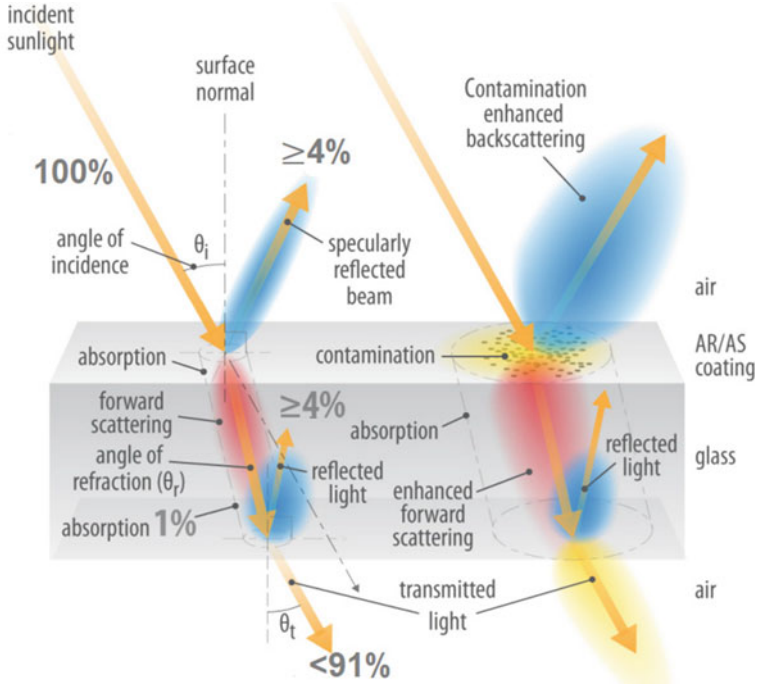

Fig. 4 Effect of soiling on light transmission over a transparent glass surface [Image courtesy—Al Hicks (NREL)] (*Source* Bessa et al. [31])

sodium (Na) ions diffuse through SiN_x-based anti-reflective coating (ARC) and pierce into crystal defects. This causes ohmic as well as nonlinear shunting and decreases the efficiency of the solar cells. Swanson et al. [32] found that surface polarization effect in n-type silicon modules which have oxide interface passivation and operate at very high voltage in positive polarity suffers extensive degradation. It was observed that surface recombination of electrons increases and the magnitude of generated current drops simultaneously due to PID, which was termed as "surface polarization effect" [32]. According to [33], thin-film solar cells are also affected by PID when subjected to negative biasing. Sodium ion migration is the most widely observed cause of PID in thin-film cells. The moisture plays a dominant role in PID mechanisms of thin-film modules, and the PID mechanisms differ depending on the presence and absence of moisture. The presence of moisture inside module packaging can cause electrochemical corrosion of tin oxide-based transparent conductive oxide (TCO) film. The degradation of electrical characteristics in the absence of moisture is another major PID issue in thin-film solar cells. PID can be tested at module as well as cell level [33]. The IEC 62804-1 describes a standard stress test for PID detection, in which module is kept in a chamber maintained at minimum 60 °C and 85% (relative humidity) with terminal voltage equal to the module's rated maximum voltage (or as a standard it is taken as −1000 V) for a duration of 96 h [34]. Sometimes, a conductive

layer of Al or Cu is placed atop the glass surface of module for carrying out chamber PID test. At cell levels, corona discharge technique is quite effective which involves generation of positive ions in an electric field and inducing PID. The mitigation and prevention of PID in PV modules can be achieved at cell, module and system level [35]. The refractive index of ARC can be increased by increasing the amount of Si in SiN_x layer which can minimize its susceptibility to PID. At module level, PID can be avoided by replacing soda-lime glass with borosilicate glass. At system level, to avoid PID, the supply terminal voltages can be biased with appropriate polarity (positive for p-type and negative for n-type c-Si). In bifacial PERC modules, the phenomenon of PID is quite a mystery as it involves current generation from front as well as rear sides.

(e) **Discoloration**: PV modules suffer optical degradation due to discoloration of EVA (ethyl vinyl acetate) or other encapsulation materials between glass and PV cells. Discoloration is a result of a photothermal degradation of polymeric encapsulant (EVA) under the direct exposure to UV rays and high temperature. This discoloration is visible in the form of yellow to dark-brown spots occurring on the affected portion of PV module. Figure 5 shows severe discoloration of EVA.

Discoloration may also take place due to penetration of moisture and soiling dirt from edges into the glass covering of modules [5]. Figure 6 shows the ways in which discoloration can affect the performance of PV module. Discoloration reduces the transmission of solar radiation and thus decreases short circuit current of the module and thus causes power losses. Peike et al. [37] investigated the root cause of EVA degradation due to discoloration. It was found that additives used with EVA deplete with time and not the EVA itself results in discoloration. UV stabilizers and antioxidants are used as additives with EVA to prevent it from UV degradation. Due to continuous UV exposure and high temperature, the concentration of stabilizers decreases with time and degrades the EVA causing yellowness of the material

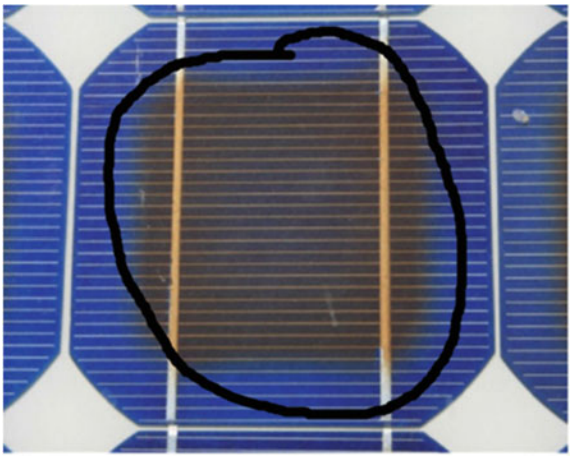

Fig. 5 EVA encapsulant browning of a PV module [36]

[38]. Due to this degradation, acetic acid is formed which can react with metallic connections and causes corrosion, which elevates the series resistance and degrades the power. Sometimes, chemical reaction of acetic acid with other substances may emit gases which remain trapped and may cause bubble formation or delamination. The physical visualization of discoloration can be divided into three colours: yellow, brown and dark brown. As the exposure time increases, the brown colour darkens simultaneously. Discoloration can be visualized with bare eyes easily. Electroluminescence images can be used to get a clear image of the extent of discoloration of EVA. Discoloration of EVA polymer is not uniform and thus may cause mismatch between cells due to partial shading. Effect of discoloration on electrical insulation of PV modules can be determined by DC dielectric insulation test of degraded modules by applying a voltage of 500 V keeping ambient temperature at 25 °C and maintaining relative humidity below 75% [39].

(f) **Delamination**: Delamination is one of the dominating early-stage field failure mode of PV modules. It is described as a phenomenon of adhesion loss and subsequent detachment of various adjoining layers of a PV module. It mostly occurs between polymeric encapsulation material layer and solar cells and between solar cells and glass cover interface layer. Delamination is responsible for moisture penetration into modules, and it also enhances the reflection losses on PV

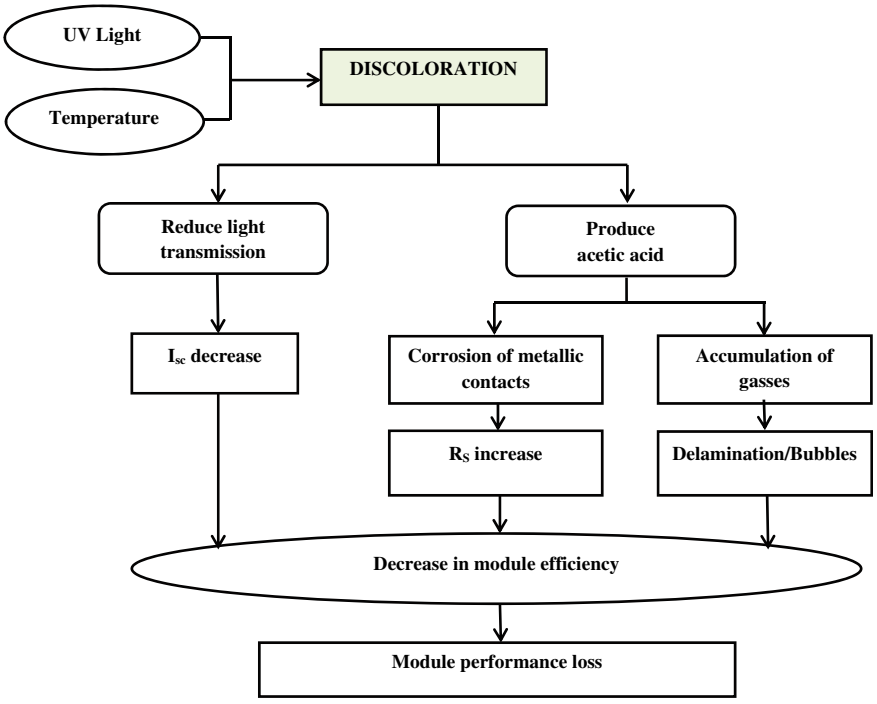

Fig. 6 Impact of EVA discoloration on PV performance [40]

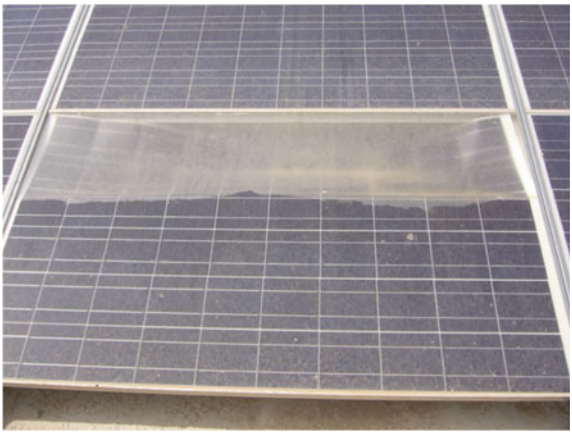

Fig. 7 PV module affected by delamination [6]

module surface [6]. The presence of moisture can cause severe reaction leading to corrosion of interparts. Figure 7 shows a module affected by delamination. Delamination is more problematic if it arises at the edges of module which can create electrical leakage. In hot and humid climatic zones, the chances of delamination are more as both moisture and elevated temperature loosen the adhesive bonding between active polymeric back layers of PV module. Optical degradation due to delamination occurs in the form of transmittance loss, as the detached material obstructs the path of incident light. Visual inspection of field aged PV modules at NREL identified various types of delaminations which include [41]:

- Encapsulant-glass delamination
- Encapsulant-cell delamination
- Encapsulant-backsheet delamination
- Delamination in conjunction with snail trails.

Encapsulant-glass delamination generally does not occur in EVA-based encapsulants. Modules with EVA suffer encapsulant-cell surface delamination more often, which exist selectively along the metallic ribbon interconnections. The possible causes of delamination along metallic ribbons could be attributed to: (a). residue from fluxing process, (b). EVA flow beneath the ribbons which leave null spaces where water remains trapped due to moisture infiltration and this water on heating up may evaporate and form bubbles (described later), (c). Na ions from other degradation processes can cause a chemical reaction and produce volatile gases, or (d). metal connections may act as catalyst with voltage and enhance chemical reactions. In a study done by [42], failure analysis of 25-year-old mono-Si modules revealed that delamination transpired across interface between EVA encapsulant and solar cells and the delaminated portion was also affected by corrosion.

Encapsulant-backsheet delamination mostly occurs due to the formation of blisters or bubbles due to the release of entrapped gases or vapours. This may lead to electrical risks as the backsheet provides necessary insulation to protect the panels

from external environment. Dark grey/black and irregular traces on the surface of PV cells causing discoloration defects are called snail trails. These trails mainly occur from corrosion of metallic fingers of screen-printed solar cells. These defects occur during infant stage of a PV module between 3 months to 1 year after its installation. It has been observed that these snail trails are associated with delamination in modules having EVA encapsulant and lack UV absorbers. This delamination could be a major challenge in the near future as the modules now being manufactured using EVA do not contain UV absorbers in order to take advantage of shortwave UV rays which can easily transmit through EVA into the solar cells [41]. Delamination in thin-film solar cell technologies is encountered in between TCO layers and soda-lime glass substrate. This happens because of an electrochemical reaction between TCO-glass interface due to moisture ingress through module edges [11]. IEC-61215 provides standard damp heat test (85 °C and 85% RH with 1000 h exposure) procedure for inspection of delamination [42, 43]. The bonding strength of encapsulant-glass and encapsulant-solar cell layers is tested using double cantilever beam (DCB) (ISO25217) methods [44] and compressive shear tests [45] or overlap shear tests [46].

(g) **Temperature-Induced Degradation (TID)**: The module temperature is generally influenced by solar radiation, ambient temperature and wind speed. When the ambient temperature is around 35 °C, the temperature of the module can reach up to 60 °C [18]. The rise in module temperature is because of the low-iron glass cover which does not allow long wavelength infrared (IR) waves to escape back into the atmosphere developing greenhouse effect and thus higher temperature. At such high temperature, the bandgap of the semiconductors usually decreases which implies that absorption of low energy IR radiations can also take place easily. Due to this, short circuit current (I_{sc}) increases and there is a simultaneous drop in open circuit voltage (V_{oc}). The increment in I_{sc} is quite small as compared to V_{oc} drop which ultimately leads to low power output and lower efficiency. The high value of I_{sc} at elevated module temperature is due to decrease in bandgap and more absorption of low energy photons while drop in V_{oc} occurs due to surge in carrier recombination.

Dyk et al. [47] investigated the effect of temperature rise on PV performance and noticed declination of power with rising temperatures. Figure 8 shows the typical I-V characteristics of a module at various temperature levels. The declination of power due to increasing temperature is not the only problem with PV modules, and the high ambient temperature along with moisture gives rise to various other degradation modes such as corrosion, discoloration and delamination. PV installations in hot and humid climatic conditions suffer from most severe degradations.

(h) **Hotspots**: Hotspot is a localized high temperature zone which could possibly harm the cell or other parts of a PV module. There are many reasons behind the development of hotspots in PV modules which include partial shading, defects in interconnected cells or possible mismatch among various solar cells connected in series and parallel [49]. A partially shaded or defected solar cell functioning

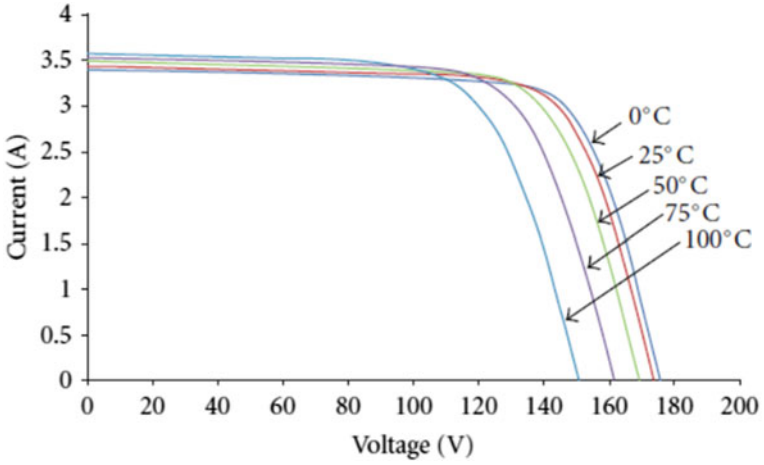

Fig. 8 Effect of temperature on current and voltage of a PV module [48]

in a module produces less current and thus allows only limited amount of current to pass through it, and the surplus power gets dissipated in the form of heat, developing a hotspot. The voltage of a shaded PV cell is reversed in short circuit conditions, and thus, it acts in opposite sense with respect to other connected cells making the shaded cell a consumer rather than a generator of energy. Depending on the duration of cell being shaded, the hotspots can be recognized as being temporary or permanent [50]. Temporary hotspots pose less of a risk to modules while the permanent ones may damage PV module entirely. Hotspots diminish the power producing capabilities of a PV module and enhance ageing failure. Studies by Wu et al. [51] and Tang et al. [52] have shown that severe hotspots could be responsible for burn marks and may also initiate hazardous fire (Fig. 9). Mismatching of cells or modules is generally caused by deploying modules manufactured by different manufacturers in series-parallel connection, using different rating modules which generate distinct current/power or using modules having same power rating but differ in properties or technologies. The I-V and power curves can help in detecting power drop but to confirm that the loss of power occurred due to overheating/hotspot, lock-in thermography [53] and infrared images are used. A passive method to prevent overheating of modules from hotspot generation is usually achieved by using a bypass diode which is connected in parallel with the solar panel and placed inside the junction box. The diode bypasses all the current through it without the participation of affected module and hence prevents overheating and power losses. Active method for mitigation of hotspot uses a power MOSFET device with the PV module, connected in series, which also minimizes the reverse voltage as well as reduces the losses due to hotspot. The hotspot formation can also be prevented by optimizing the topology of PV array [52].

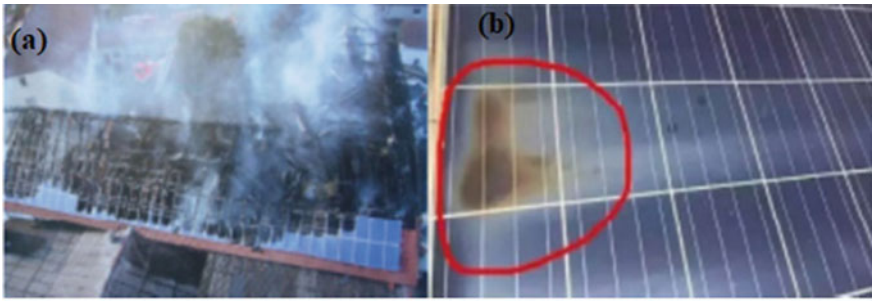

Fig. 9 PV panels affected from hotspots by **a** catching fire and **b** burn marks [51]

(i) **Solder bond fatigue**: In a PV module, solder joints are used to interconnect metallic ribbons of solar cells. Generally, flattened copper (Cu) wires are used to manufacture ribbons which are soldered using tin/lead paste. When modules are exposed to outdoor/field for operation, these joints are subjected to thermomechanical stresses and give rise to power losses which usually occur as a consequence of increment in series resistance. The rate of this degradation mainly depends upon factors like module design, outdoor conditions, types of material used for soldering and the geometry of joint [54]. Jiang et al. [55] used finite element modelling to investigate solder joint fatigue failure in hot climatic conditions under the influence of thermal cycling. The results from their work showed that with a 50 °C rise in temperature, the fatigue life of bonding joint reduces by 34%. Thermal cycling in conjunction with mechanical stresses may lead to solder bond fatigue. Figure 10 shows various parametric characteristics of a 22-year-old field aged PV string, in which hotspot formation due to solder bond failure occurred. It was observed from the parametric analysis of the I-V curves that power losses due to these hotspots were correlated with fill factor losses [56]. Accelerated thermal cycle (ATC) testing is used to enhance thermal stresses on solder joints that can impact the PV module's degradation and failure mechanisms.

(j) **Bubbles**: The loss of EVA adhesion not only causes delamination but also sometimes may cause bubble formation. Chemical reaction occurring within the lamination films of PV module often originates from thermal decomposition [57]. These reactions in turn give rise to gaseous emissions which lead to swelling of the delaminated small portions of PV modules, and bubbles are created. This swelling can occur at the front as well as back surface of a module (as shown in Fig. 11). The air is trapped inside the bubbles forming an air chamber in having lower temperature than the surrounding cells. Bubbles affect the natural cooling of PV modules, and thermal dissipation from heated cells becomes hard. This overheating of the cells due to lack of heat dissipation may cause damage to the module [6]. Sometimes, a bubble could be so tiny to be observed with bare eyes but can cause a temperature change. Such tiny bubbles can be observed

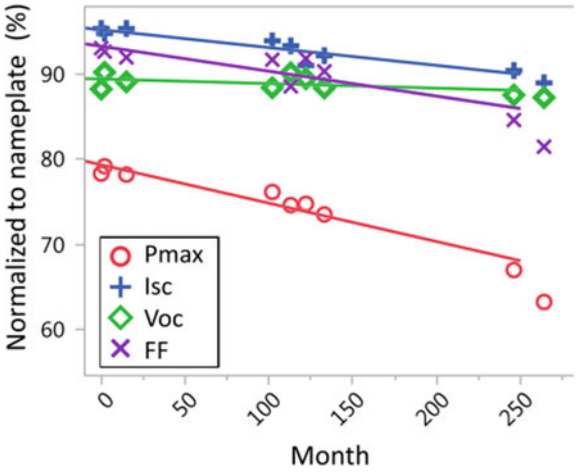

Fig. 10 Time series effect of hotspot induced from solder bond failure on various electric characteristics of a PV module [56]

with the help of infrared (IR) images. Bubbles at front side of module occur between top glass cover and cells. Similar to backside, bubbles at front side also form air chambers and cause overheating of nearby solar cells in addition to that reflection of solar irradiation and decoupling of incident light also occurs which negatively impact the PV performance.

(k) **Cracking of cells**: Very thin films of silicon wafers are used in manufacturing solar cells in order to cut production costs. These thin cells are quite fragile and brittle in nature. Cracks in solar cells occur either during the manufacturing processes or due to mechanical stresses imposed by handling and transportation, high wind speeds, snowfall, etc. [17]. Different layers of PV modules are bonded using adhesives, and the bonding strength of adhesives between various laminations of PV module should be good enough to avoid moisture penetration and corrosion. If this adhesion is stronger than what is necessary, then it can impose mechanical stresses on solar cells. During solar cell manufacturing, various processes like wafer slicing, cell wafer manufacturing, stringing and

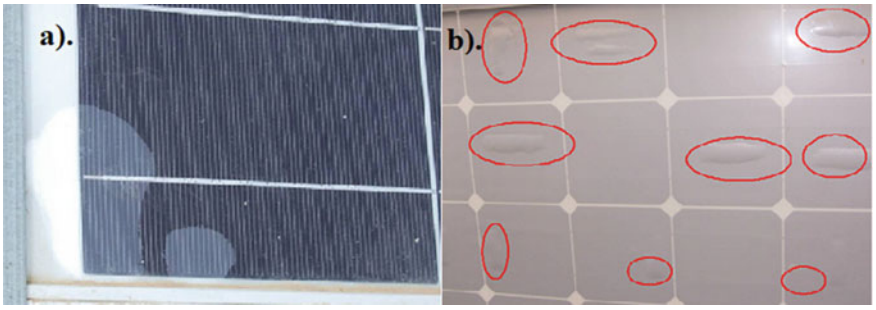

Fig. 11 Bubbles at **a** front side and **b** back side of PV modules [6]

embedding may create cracks in PV cells. Stringing process has the highest potential to cause cracks in the solar cell [58, 59]. During fabrication of solar cells, cracks mostly originate from three different sources [58]:

1. Cracks originating within the ribbon interconnection as a result of residual stress.
2. Cross cracks occurring as a consequence of needle pressing action on wafer during solar cell manufacturing.
3. Cracks at the edges of cell because of the impact of cells against hard object.

Thermomechanical stresses as a result of seasonal and regular climatic variations of temperatures can cause the enhancement in sizes of already existing small cracks [59]. These cracks are classified as micro-cracks when they have width less than 30 μm and as macro-cracks when critical length is 1 cm [60]. Micro-cracks are quite small and sometimes not visible from bare eyes. The cell crack with sufficient sizes can limit the current producing capabilities of PV cell depending upon the direction and location of crack propagation. Once the crack is developed in a cell, it may not be harmful for the cell if the direction of crack is perpendicular to busbars or if it is parallel to the busbars and lies in between those busbars. But when a crack occurs in edges of a PV module, it divides the cell into two regions (as shown in Fig. 12b). Such cracks can disintegrate or isolate a part of cell from the string of other power generating cells, and thus, there could be overall power losses due to less current generation by cracked cell. Depending upon the direction of the propagation of cracks, busbars help in preventing a cell from comparatively lower current generation as shown in Fig. 12a. Both destructive and non-destructive testing (NDT) techniques are used for detecting micro- and macro-cracks in PV solar cells. Electroluminescence (EL) and ultraviolet fluorescence (UVF) [61] are the two visual techniques which are also used to detect these cracks.

3 Causes and Effects of Various Degradation Mechanisms

Photovoltaic modules are exposed to different environmental stresses which either individually or in conjunction with each other affect the health and performance of solar photovoltaic panels (Fig. 13). Due to the complexity of environmental stresses on PV modules, accurate measurement and prediction of degradation mechanisms are quite rigorous task. Ambient temperature, solar irradiation and humidity are the major environmental factors which not only influence the performance of modules but are also responsible for various degradation mechanisms. High voltage, chemical reactions and thermal cycling are few other factors which cause degradation of PV modules. The main sources of origination of various degradation mechanisms and the effect of these degradation mechanism on electrical performance of PV module are shown in Table 1.

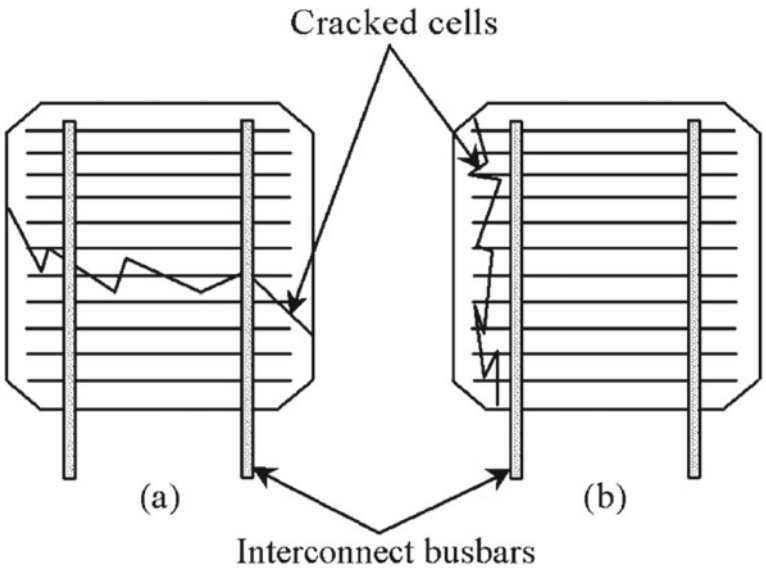

Fig. 12 Propagation of crack in a cell **a** perpendicular to the busbars and **b** parallel to the busbars along the edge of the cell [5]

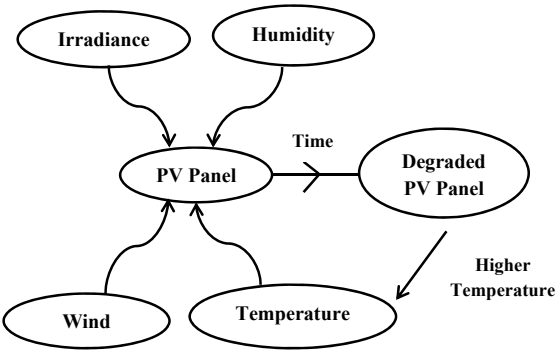

Fig. 13 Various environmental factors responsible for PV panel degradation [62]

4 Accelerated Testing and Degradation Inspection Techniques

Accelerated tests are carried out on PV modules before their on-field deployment to ensure long-term reliability and durability in extreme weather conditions. Accelerated testing procedures involve subjecting the PV module to severe stress conditions generally higher than actual field-stress levels. International Electrotechnical Commission (IEC) has proposed a standard methodology for module qualification under IEC-61215. Test sequences involved under IEC-61215 are shown in Fig. 14, in which the modules go through electrical, thermal and mechanical stresses.

Table 1 Main causes of origination of various degradation modes and their effect on the performance characteristics of PV modules

S. No	Degradation mode	Cause of origination	Effect on performance of PV modules
(1)	Corrosion	Moisture + oxygen ingress	The author in [15] exposed c-Si module to accelerated test conditions comprising of high temperature (95 °C) and relative humidity (95%); the losses due to front metallization corrosion showed a drop in fill factor by 26.4%, reduced maximum power by 30.4% and short circuit current by 3.6% while series resistance increased by 60%
(2)	LID	(1) Due to "Staebler-Wronski" effect in a-Si modules (2) Due to boron-oxygen defects + initial solar exposure in CZ-based c-Si modules	(1) Three different a-Si technologies were field exposed for more than a year by Radue et al. [63] to investigate the degradation encountered by the modules. It was observed that almost 30% loss in maximum power occurred in single junction a-Si solar cell (2) Sopori et al. [64] performed light soaking experiments under 1-sun and 25 °C conditions on monocrystalline Si solar cell after 72 h of exposure and observed minor reduction in open circuit voltage, current density and fill factor. The efficiency of solar cell was reduced from 17.45 to 16.96%, series resistance increased from 1.45 to 1.65 mΩ, and shunt resistance reduced drastically from 135 to 32 kΩ
(3)	Soiling	Accumulation of unwanted dust/dirt	As per experimental study conducted by [65], year-long dust accumulation on mono c-Si PV module can decrease the power output by 77.75% and short circuit current by 75.32%. However, the output voltage remained unaffected

(continued)

Table 1 (continued)

S. No	Degradation mode	Cause of origination	Effect on performance of PV modules
(4)	PID	High voltage stress + temperature + humidity	Accelerated PID test (1000 V and 100 h) was used in [65] to quantify the effect of PID on electrical parameters of p-type silicon solar cell. The power was degraded by 52% because the leakage current was enhanced due to nearly 100% reduction in shunt resistance after 100th hour of testing. Short circuit current and open circuit voltage were also reduced by 7% and 4%, respectively
(5)	Discoloration	UV radiation + high temperature	Sinha et al. [40] studied the effect of discoloration on c-Si PV modules using non-destructive characterization techniques. The effect of discoloration on 20-year-old brown and non-brown module pair was examined, and it was seen that short circuit current of module with severe browning was 4% lower than non-brown module, while output power was decreased by up to 14% and fill factor was lowered by almost 12%
(6)	Delamination	Moisture + high temperature	Delamination is generally followed by discoloration and corrosion of modules. Park et al. [42] investigated delamination and discoloration effect on 25-year-old module, and it was discovered that reflection and transmission losses drop the short circuit current of modules and it can cause power losses up to 17.9%

(continued)

To prevent complete failure of modules, the detection of the degradation modes at an early stage can be quite beneficial. Thus, it becomes necessary to keep a regular check on the modules after they are field exposed and following measurement techniques are used for detecting different types of degradations occurring in PV modules [9, 58, 72]:

Table 1 (continued)

S. No	Degradation mode	Cause of origination	Effect on performance of PV modules
(7)	TID	High temperature	Piliougine et al. [66] quantified the degradation of 21-year-old field aged monocrystalline Si modules in terms of temperature coefficients, and it was observed that temperature coefficients of field aged modules decrease as a result of thermal degradation with time. Bensalem et al. [67] experimentally investigated the impact of increasing temperature on the electrical performance of polycrystalline solar cell (12.5 × 12.5) cm^2 under 1-sun constant illumination and for a temperature rise of 15–50 °C, the short circuit current rise from 5.1261 to 5.1997 A, while open circuit voltage reduced from 0.6380 to 0.5645 V and efficiency changed from 16.25 to 14.04%
(8)	Hotspots	Partial shading/cell defects/mismatch losses	Ahsan et al. [68] evaluated the performance of c-Si and thin-film solar modules under hotspot conditions arising due to partial shading of cells. The temperature at hotspots was as high as 86 °C, while the unaffected module temperature was 49 °C. Hotspots not only reduce the short circuit current but also affect the open circuit voltage. The power reduction in case of partial shading depends mainly on the shaded area
(9)	Solder bond fatigue	Thermochemical stresses	Increment in series resistance is the major reason of power degradation in PV modules subjected to thermal cycle stressing and developing solder bond failures [69]

(continued)

Table 1 (continued)

S. No	Degradation mode	Cause of origination	Effect on performance of PV modules
(10)	Bubbles	Adhesion loss + gas entrapment	Kouadri-Boudjelthia et al. [70] carried out visual inspection of 30 years module and detected the bubble formation on front side metallization of modules. The bubble causes spectral losses and thus ultimately degrades the power of PV cells
(11)	Cracking of cells	Mechanical stresses	The authors of [58] developed micro-cracks in a cell using mechanical load test instrument, and it was found that the cracks of different modes classified on the basis of electroluminescence images obtained can cause power losses from 1 to 10%

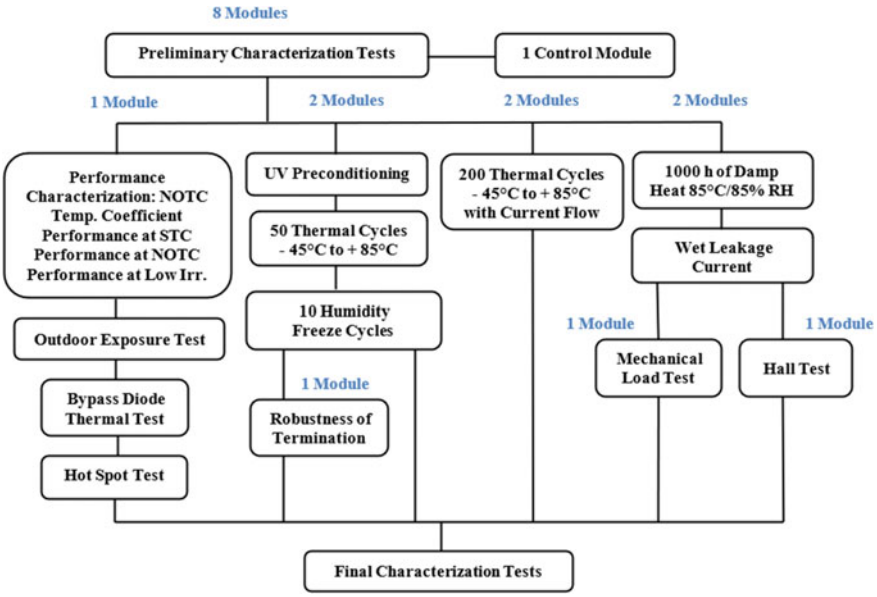

Fig. 14 IEC-61215 PV module testing procedure [71]

i. **Visual inspection**: Visual inspection is one of the easiest and frequent ways to recognize and locate visual defects. The simplicity of visual inspection allows the possibility of collecting data very widely. Visual inspection techniques assist in identifying defects such as delamination, corrosion, discoloration, snail tracks, burn marks/hotspots, cracks in glass and cells, bubbles and junction box or module frame failure [9]. The defects in frames or junction boxes can cause field failures, while cracked cells and delamination defects have huge possibility of causing power losses as well as safety failures.

ii. **I-V characterization**: The I-V measurements of PV modules can be taken under natural or artificial illumination source. By analysing the I-V curve, information about short circuit current, open circuit voltage, maximum power and fill factor can easily be obtained. Sun simulators are used for indoor testing of PV modules under controlled standard test conditions (STC) of AM1.5 spectrum, 1000 W/m^2 radiation and 25 °C temperature. The reference values of I-V characteristics at STC are obtained for modules before their deployment to the field, and the measured values of electrical characteristics serve as reference for measurement of any further power declination due to field exposure. The I-V curves of field aged module at STC are compared with those reference values, and any observed deterioration in current, power or voltage of module is a sign of degradation. The slope of I-V curve is a measure of series and shunt resistance (as shown in Fig. 15). The lumped resistance in the path of current through emitter and base of cell, cell material (silicon) and metal contacts and top and real metal contacts is called series resistance, while shunt resistance illustrates a shunt path for the current flow bypassing the active solar cell. Losses in short circuit current (I_{sc}) could arise due to delamination, discoloration or glass corrosion, while slope in I_{sc} denotes increasing shunt resistance arising as a consequence of shunt paths developed in cells or interconnections. The possible causes of drop in open circuit voltage (V_{oc}) could be TID, LID, PID or broken cell interconnections. The lower slope of I-V curve around V_{oc} is a measure of increased series resistance due to increased resistance in cell interconnections or corrosion in junction box. Shading and mismatch losses can also be visualized as steps or inflexion points in the I-V curve.

iii. **Infrared imaging**: Thermal or infrared (IR) imaging is a most widely used technique to inspect possible thermal and electrical failures in PV modules. It is a contactless non-destructive technique with real-time and fast diagnosis of faults in PV modules. This method can be used for individual PV module as well as large-scale PV arrays. Thermal camera recognizes and captures different wavelengths of infrared light. Hotter bodies emit high intensity IR radiations which are detected by thermal cameras, and the images produced on the screen of the device show the variation in temperature of an object due to different levels of IR emission. Hot to cool temperatures are indicated on the display using red to blue colours (as shown in Fig. 16). The wavelength of cameras used in thermography or thermal imaging ranges between 3 and 15 μm. In PV modules, lose or broken contacts, leakage currents and possible shading or

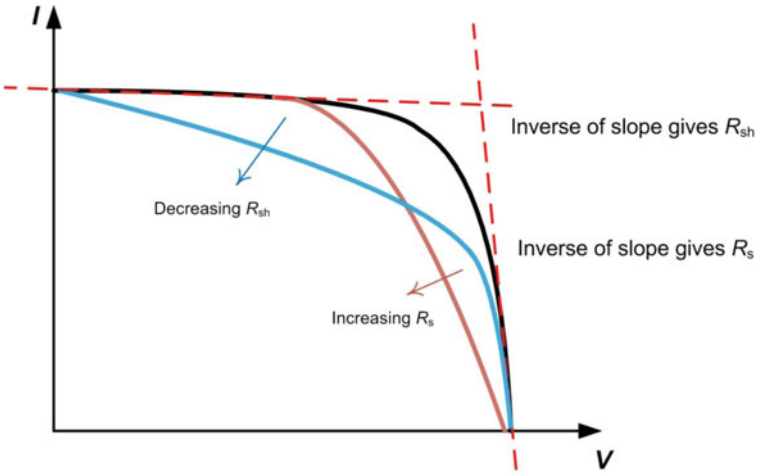

Fig. 15 Effect of variation in series and shunt resistance on slopes of I-V curve [9]

mismatch losses cause heating effect. The localized heating around the affected solar cell gives bright spot on the display screen of thermal cameras which represents high temperature. IR imaging of both front and rear side of module is captured in order to discover hotspots on PV modules.

iv. **Electroluminescence (EL) imaging**: EL imaging uses the principle of photocurrent generation of PV modules through an externally applied bias. EL image of a PV module is shown in Fig. 16. EL imaging is generally carried out in dark environment because of the difference between intensities of IR radiation (near 1150 nm) emitted by PV module and background light source. High-resolution camera is required to precisely capture the metal fingers of the solar cells. EL imaging assists in detecting cell cracks in PV modules. Not only the cell cracks but also the crystallographic defects in poly/multi-crystalline solar cells in the form of dark lines can be diagnosed using EL images. EL imaging is also helpful in assessing the discrepancies between increased series resistance and reduced shunt resistance which is hard to differentiate using IR images [58].

v. **UV Fluorescence (UVF)**: This technique is used to detect the defects in wafer-based crystalline Si solar cells. Figure 16 shows UVF image of a crystalline Si modules. Pern et al. [74] used UVF for analysing the discoloration of EVA encapsulants in solar cells. The UVF technique utilizes the principle of fluorescence effect of polymeric layer comprising of EVA along with oxidation stabilizers, UV absorbers and other additives in PV module. The phenomenon in which a substance absorbs light or electromagnetic radiation and emits the same (but different wavelength) is termed as fluorescence. UV radiations, coming from the sun that have high energy and lower wavelength, are generally absorbed, and the re-emitted light has low energy and higher wavelength belonging to visible region of solar spectrum. A fluorophore is a microscopic compound which can

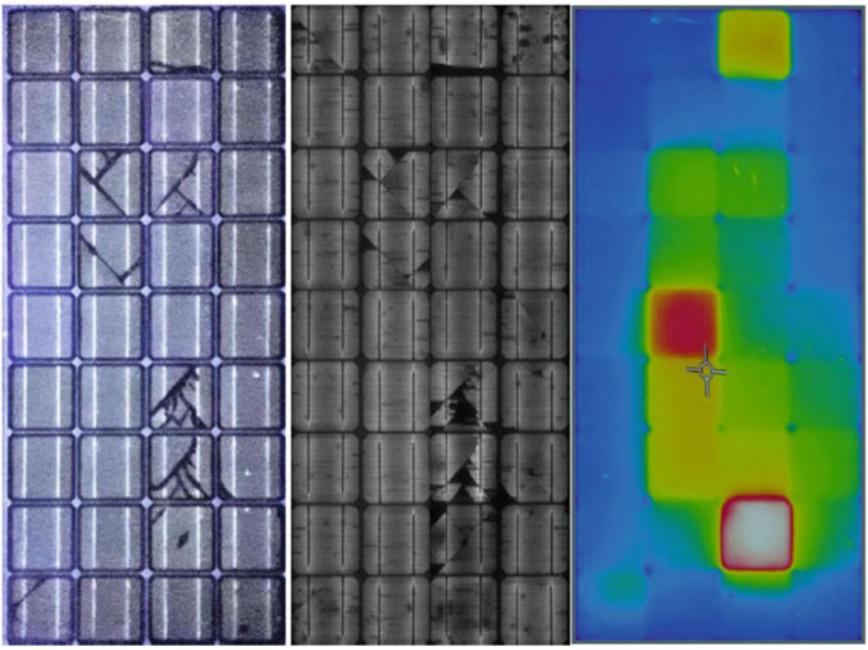

Fig. 16 UVF (left), EL (middle) and IR (right) images of a PV module [73]

re-emit light at higher wavelengths on being excited by UV light, and it is a typical source of degradation products in PV modules. The "photobleaching" effects occurring in various substances due to chemical reactions of fluorophore materials with oxygen or other elements are used to extinguish fluorescence of materials. UVF can be performed spatially resolved using a spectrometer and a UV irradiation source [74]. UVF can be used for the detection of defects like cell cracks, hotspots and EVA degradation.

vi. **X-ray scanning and ultrasonic inspection**: These are non-destructive inspection methods used in the detection of possible misalignment and delamination in PV modules. The two-dimensional (2-D) X-ray images are used to analyse the locations in backsheet lamination to check the possibility of copper etching and to inspect alignment between the backsheet foil, the electrically conductive adhesive and the back contact cells [75]. The ultrasonic inspection typically comprises two different 2-D scanning methods: transmission methods and echo pulse methods (as shown in Fig. 17). Both the methods utilize a moving ultrasonic transducer having an X–Y indicator to scan the PV modules [74]. The ultrasonic pulses reflecting back after striking the defects are identified by echo pulse method, whereas in transmission method, an ultrasonic energy scan is performed and the attenuation in the path of ultrasonic signals due to possible

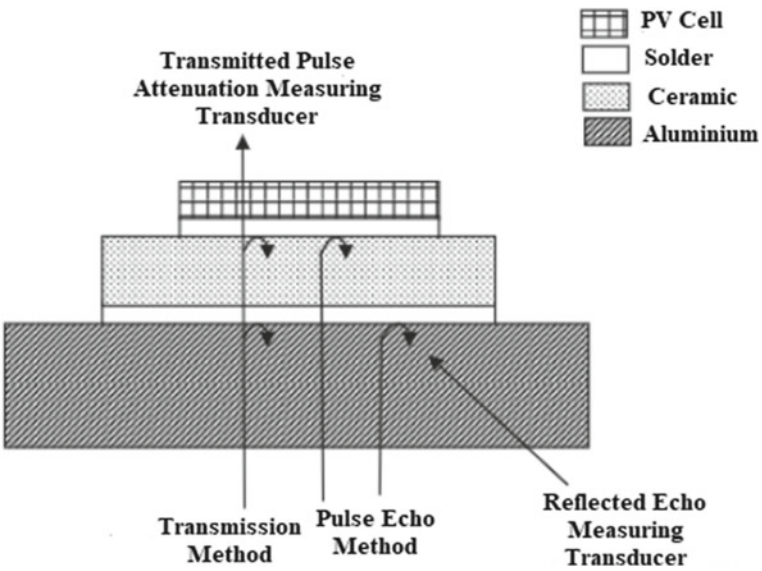

Fig. 17 Ultrasonic inspection methodology [72]

interference with the defects is recorded. This determines the exact location and size of the defects.

5 Conclusion

The modules go through several accelerated testing procedures (as described in Sect. 4) for various degradation modes before being exposed to the field. It is hard to test each module because this will increase the cost of testing; thus, only few samples are tested from a lot of modules. After field installation, sometimes, the harsh climatic conditions induce degradation phenomena in PV modules even after the modules are tested for their reliability. Throughout its operation, a PV module is affected by various degradation modes. Out of these modes, delamination, discoloration and corrosion are the major candidates which not only affect the performance of PV modules but also deteriorate their physical form. Discoloration can affect the performance of PV panels by 10–14%, delamination can reduce the maximum power by more than 15%, and corrosion can reduce the performance of PV modules by up to 30%. LID has significant effect on a-Si modules and can decrease the efficiency of a-Si modules by up to 30%, while the new technology crystalline silicon modules such as PERC are being affected by the modern version of the same phenomenon acting in conjunction with elevated temperatures known as light and elevated temperature-induced degradation (LeTID) which can potentially reduce the performance of PERC solar cells by 10%. Soiling is the natural phenomenon which

needs major attention, and cleaning of modules is the only solution to get rid of the negative impacts of soiling. PID can be minimized by safe installations of PV modules so that leakage currents can be avoided. In extreme conditions, PID can cause more than 50% losses in power due to leakage currents. Hotspots are quite hazardous and can cause fire accidents; thus, module installation in sites that cast unwanted shadows over the modules causing shading should be avoided. Thermochemical and mechanical stresses arising due to human activities also affect the module reliability. Hot and humid climatic conditions with high UV radiation availability can impact the module health severely. For long run of modules, health monitoring and inspections on a regular basis should be adopted by the plant owners. New technologies such as drone and IOT (Internet of Things) should be implemented for field inspection, and advanced cleaning techniques such as robotic arms should be commercialized for large-scale plants.

References

1. Global Status Report, REN21 (2021). https://www.ren21.net/wp-content/uploads/2019/05/GSR2021_Full_Report.pdf
2. Jordan DC, Kurtz SR (2013) Photovoltaic degradation rates—an analytical review. Prog Photovoltaics Res Appl 21(1):12–29
3. Satpathy RK, Pamuru V (2020) Solar PV power: design, manufacturing and applications from sand to systems. Academic Press
4. Rao RR, Mani M, Ramamurthy PC (2018) An updated review on factors and their inter-linked influences on photovoltaic system performance. Heliyon 4(9):e00815
5. Meyer EL, Van Dyk EE (2004) Assessing the reliability and degradation of photovoltaic module performance parameters. IEEE Trans Reliab 53(1):83–92
6. Munoz MA, Alonso-García MC, Vela N, Chenlo F (2011) Early degradation of silicon PV modules and guaranty conditions. Sol Energy 85(9):2264–2274
7. Ndiaye A, Charki A, Kobi A, Kébé CM, Ndiaye PA, Sambou V (2013) Degradations of silicon photovoltaic modules: a literature review. Sol Energy 96:140–151
8. Jordan DC, Silverman TJ, Wohlgemuth JH, Kurtz SR, VanSant KT (2017) Photovoltaic failure and degradation modes. Prog Photovoltaics Res Appl 25(4):318–326
9. Kumar M, Kumar A (2017) Performance assessment and degradation analysis of solar photovoltaic technologies: a review. Renew Sustain Energy Rev 78:554–587
10. Băjenescu TMI (2020) Some reliability aspects of photovoltaic modules. Reliability and ecological aspects of photovoltaic modules. IntechOpen
11. Jansen KW, Delahoy AE (2003) A laboratory technique for the evaluation of electrochemical transparent conductive oxide delamination from glass substrates. Thin Solid Films 423(2):153–160
12. Osterwald CR, McMahon TJ, Del Cueto JA (2003) Electrochemical corrosion of SnO_2: F transparent conducting layers in thin-film photovoltaic modules. Sol Energy Mater Sol Cells 79(1):21–33
13. Carlson DE, Romero R, Willing F, Meakin D, Gonzalez L, Murphy R, Moutinho HR, Al-Jassim M (2003) Corrosion effects in thin-film photovoltaic modules. Prog Photovoltaics Res Appl 11(6):377–386
14. Jorgensen GJ, Terwilliger KM, DelCueto JA, Glick SH, Kempe MD, Pankow JW, Pern FJ, McMahon TJ (2006) Moisture transport, adhesion, and corrosion protection of PV module packaging materials. Sol Energy Mater Sol Cells 90(16):2739–2775

15. Semba T (2020) Corrosion mechanism analysis of the front-side metallization of a crystalline silicon PV module by a high-temperature and high-humidity test. Jpn J Appl Phys 59(5):054001
16. Kempe MD (2005) Control of moisture ingress into photovoltaic modules. In: Conference record of the thirty-first IEEE photovoltaic specialists conference. IEEE, pp 503–506
17. Nehme B, M'Sirdi NK, Akiki T, Naamane A (2014) Contribution to the modeling of ageing effects in PV cells and modules. Energy Procedia 62:565–575
18. Solanki CS (2015) Solar photovoltaics: fundamentals, technologies and applications. Phi learning Pvt. Ltd.
19. Hamelmann FU, Weicht JA, Behrens G (2016) Light-induced degradation of thin film silicon solar cells. J Phys Conf Ser 682(1):012002. IOP Publishing
20. Wronski CR (1984) The staebler-wronski effect. Semicond Semimetals 21:347–374
21. Ramspeck K, Zimmermann S, Nagel H, Metz A, Gassenbauer Y, Birkmann B, Seidl A (2012) Light induced degradation of rear passivated mc-Si solar cells
22. Fertig F, Kersten F, Petter K, Bartzsch M, Stenzel F, Mette A, Klöter B, Müller JW (2016) Light and elevated temperature induced degradation of multicrystalline silicon solar cells and modules. Hanwha Q CELLS GmbH, Bitterfeld-Wolfen, Germany
23. Niewelt T, Schindler F, Kwapil W, Eberle R, Schön J, Schubert MC (2018) Understanding the light-induced degradation at elevated temperatures: similarities between multicrystalline and floatzone p-type silicon. Prog Photovoltaics Res Appl 26(8):533–542
24. Hallam B, Herguth A, Hamer P, Nampalli N, Wilking S, Abbott M, Wenham S, Hahn G (2017) Eliminating light-induced degradation in commercial p-type Czochralski silicon solar cells. Appl Sci 8(1):10
25. Ghosh A (2020) Soiling losses: a barrier for India's energy security dependency from photovoltaic power. Challenges 11(1):9
26. Chanchangi YN, Ghosh A, Sundaram S, Mallick TK (2020) An analytical indoor experimental study on the effect of soiling on PV, focusing on dust properties and PV surface material. Sol Energy 203:46–68
27. Ilse K, Micheli L, Figgis BW, Lange K, Daßler D, Hanifi H, Wolfertstetter F, Naumann V, Hagendorf C, Gottschalg R, Bagdahn J (2019) Techno-economic assessment of soiling losses and mitigation strategies for solar power generation. Joule 3(10):2303–2321
28. Ilse KK, Figgis BW, Werner M, Naumann V, Hagendorf C, Pöllmann H, Bagdahn J (2018) Comprehensive analysis of soiling and cementation processes on PV modules in Qatar. Sol Energy Mater Sol Cells 186:309–323
29. Schill C, Brachmann S, Koehl M (2015) Impact of soiling on IV-curves and efficiency of PV-modules. Sol Energy 112:259–262
30. Mani M, Pillai R (2010) Impact of dust on solar photovoltaic (PV) performance: research status, challenges and recommendations. Renew Sustain Energy Rev 14(9):3124–3131
31. Bessa JG, Micheli L, Almonacid F, Fernández EF (2021) Monitoring photovoltaic soiling: assessment, challenges, and perspectives of current and potential strategies. Iscience 24(3):102165
32. Swanson R, Cudzinovic M, DeCeuster D, Desai V, Jürgens J, Kaminar N, Mulligan W, Rodrigues-Barbarosa L, Rose D, Smith D, Terao A (2005) The surface polarization effect in high-efficiency silicon solar cells. In: 15th PVSEC. Shanghai, China
33. Luo W, Khoo YS, Hacke P, Naumann V, Lausch D, Harvey SP, Singh JP, Chai J, Wang Y, Aberle AG, Ramakrishna S (2017) Potential-induced degradation in photovoltaic modules: a critical review. Energy Environ Sci 10(1):43–68
34. Gou X, Li X, Zhou S, Wang S, Fan W, Huang Q (2015) PID testing method suitable for process control of solar cells mass production. Int J Photoenergy 2015
35. Carolus J, Tsanakas JA, van der Heide A, Voroshazi E, De Ceuninck W, Daenen M (2019) Physics of potential-induced degradation in bifacial p-PERC solar cells. Sol Energy Mater Sol Cells 200:109950
36. Wohlgemuth JH, Kempe MD, Miller DC (2013) Discoloration of PV encapsulants. In: 2013 IEEE 39th photovoltaic specialists conference (PVSC). IEEE, pp 3260–3265

37. Peike C, Purschke L, Weiss KA, Köhl M, Kempe M (2013) Towards the origin of photochemical EVA discoloration. In: 2013 IEEE 39th photovoltaic specialists conference (PVSC). IEEE, pp 1579–1584
38. Pern FJ, Czanderna AW (1992) EVA degradation mechanisms simulating those in PV modules. AIP Conf Proc 268(1):445–452. American Institute of Physics
39. Dechthummarong C, Wiengmoon B, Chenvidhya D, Jivacate C, Kirtikara K (2010) Physical deterioration of encapsulation and electrical insulation properties of PV modules after long-term operation in Thailand. Sol Energy Mater Sol Cells 94(9):1437–1440
40. Sinha A, Sastry OS, Gupta R (2016) Nondestructive characterization of encapsulant discoloration effects in crystalline-silicon PV modules. Sol Energy Mater Sol Cells 155:234–242
41. Wohlgemuth JH, Hacke P, Bosco N, Miller DC, Kempe MD, Kurtz SR (2016) Assessing the causes of encapsulant delamination in PV modules. In: 2016 IEEE 43rd photovoltaic specialists conference (PVSC). IEEE, pp 0248–0254
42. Park NC, Jeong JS, Kang BJ, Kim DH (2013) The effect of encapsulant discoloration and delamination on the electrical characteristics of photovoltaic module. Microelectron Reliab 53(9–11):1818–1822
43. Jones CB, Hamzavy B, Hobbs WB, Libby C, Lavrova O (2018) IEC 61215 qualification tests vs outdoor performance using module level in situ IV curve tracing devices. In: 2018 IEEE 7th world conference on photovoltaic energy conversion (WCPEC) (A joint conference of 45th IEEE PVSC, 28th PVSEC & 34th EU PVSEC). IEEE, pp 1286–1291
44. ISO (2014) Adhesives determination of the mode 1 adhesive fracture energy of structural adhesive joints using double cantilever beam and tapered double cantilever beam specimens. ISO 25217:2009. International Organization for Standardization, Geneva, Switzerland
45. Chapuis V, Pélisset S, Raeis-Barnéoud M, Li HY, Ballif C, Perret-Aebi LE (2014) Compressive-shear adhesion characterization of polyvinyl-butyral and ethylene-vinyl acetate at different curing times before and after exposure to damp-heat conditions. Prog Photovoltaics Res Appl 22(4):405–414
46. Kempe MD, Kilkenny M, Moricone TJ, Zhang JZ (2009) Accelerated stress testing of hydrocarbon-based encapsulants for medium-concentration CPV applications. In: 2009 34th IEEE photovoltaic specialists conference (PVSC). IEEE, pp 001826–001831
47. Van Dyk EE, Scott BJ, Meyer EL, Leitch AWR (2000) Temperature dependence of performance of crystalline silicon photovoltaic modules. S Afr J Sci 96(4):198–200
48. Wang MH, Chen MJ (2012) Two-stage fault diagnosis method based on the extension theory for PV power systems. Int J Photoenergy 2012
49. Bharadwaj P, Karnataki K, John V (2018) Formation of hotspots on healthy PV modules and their effect on output performance. In: 2018 IEEE 7th world conference on photovoltaic energy conversion (WCPEC) (A joint conference of 45th IEEE PVSC, 28th PVSEC & 34th EU PVSEC). IEEE, pp 0676–0680
50. Niazi KAK, Yang Y, Sera D (2019) Review of mismatch mitigation techniques for PV modules. IET Renew Power Gener 13(12):2035–2050
51. Wu Z, Hu Y, Wen JX, Zhou F, Ye X (2020) A review for solar panel fire accident prevention in large-scale PV applications. IEEE Access 8:132466–132480
52. Tang S, Xing Y, Chen L, Song X, Yao F (2021) Review and a novel strategy for mitigating hot spot of PV panels. Sol Energy 214:51–61
53. Gallon J, Horner GS, Hudson JE, Vasilyev LA, Lu K (2015) PV module hotspot detection. Tau Science Corporation
54. Bosco N, Silverman TJ, Kurtz S (2016) The influence of PV module materials and design on solder joint thermal fatigue durability. IEEE J Photovoltaics 6(6):1407–1412
55. Jiang N, Ebadi AG, Kishore KH, Yousif QA, Salmani M (2019) Thermomechanical reliability assessment of solder joints in a photovoltaic module operated in a hot climate. IEEE Trans Compon Packag Manuf Technol 10(1):160–167
56. Manganiello P, Balato M, Vitelli M (2015) A survey on mismatching and aging of PV modules: the closed loop. IEEE Trans Industr Electron 62(11):7276–7286

57. Köntges M, Kurtz S, Packard CE, Jahn U, Berger K, Kato K, Friesen T, Liu H, Van Iseghem M (2014) Review of failures of photovoltaic modules. IEA PVPS
58. Sander M, Dietrich S, Pander M, Schweizer S, Ebert M, Bagdahn J (2011) Investigations on crack development and crack growth in embedded solar cells. Reliab Photovolt Cells Modul Compon Syst IV 8112:811209. International Society for Optics and Photonics
59. Kajari-Schröder S, Kunze I, Eitner U, Köntges M (2011) Spatial and orientational distribution of cracks in crystalline photovoltaic modules generated by mechanical load tests. Sol Energy Mater Sol Cells 95(11):3054–3059
60. Köntges M, Kunze I, Kajari-Schröder S, Breitenmoser X, Bjørneklett B (2011) The risk of power loss in crystalline silicon based photovoltaic modules due to micro-cracks. Sol Energy Mater Sol Cells 95(4):1131–1137
61. Nehme BF, Akiki TK, Naamane A, M'Sirdi NK (2017) Real-time thermoelectrical model of PV panels for degradation assessment. IEEE J Photovoltaics 7(5):1362–1375
62. Radue C, Van Dyk EE (2010) A comparison of degradation in three amorphous silicon PV module technologies. Sol Energy Mater Sol Cells 94(3):617–622
63. Sopori B, Basnyat P, Devayajanam S, Shet S, Mehta V, Binns J, Appel J (2012) Understanding light-induced degradation of c-Si solar cells. In: 2012 38th IEEE photovoltaic specialists conference. IEEE, pp 001115–001120
64. Ndiaye A, Kébé CM, Ndiaye PA, Charki A, Kobi A, Sambou V (2013) Impact of dust on the photovoltaic (PV) modules characteristics after an exposition year in Sahelian environment: the case of Senegal. Int J Phys Sci 8(21):1166–1173
65. Pingel S, Frank O, Winkler M, Daryan S, Geipel T, Hoehne H, Berghold J (2010) Potential induced degradation of solar cells and panels. In: 2010 35th IEEE photovoltaic specialists conference. IEEE, pp 002817–002822
66. Bensalem S, Chegaar M, Aillerie M (2013) Solar cells electrical behavior under thermal gradient. Energy Procedia 36:1249–1254
67. Ahsan S, Niazi KAK, Khan HA, Yang Y (2018) Hotspots and performance evaluation of crystalline-silicon and thin-film photovoltaic modules. Microelectron Reliab 88:1014–1018
68. Kumar S, Gupta R (2018) Investigation and analysis of thermo-mechanical degradation of fingers in a photovoltaic module under thermal cyclic stress conditions. Sol Energy 174:1044–1052
69. Belhaouas N, Mehareb F, Assem H, Kouadri-Boudjelthia E, Bensalem S, Hadjrioua F, Aissaoui A, Bakria K (2021) A new approach of PV system structure to enhance performance of PV generator under partial shading effect. J Clean Prod 317:128349
70. Kim J, Rabelo M, Padi SP, Yousuf H, Cho EC, Yi J (2021) A review of the degradation of photovoltaic modules for life expectancy. Energies 14(14):4278
71. Vorster F, Van Dyk E (2019) UV fluorescence imaging of photovoltaic modules. In: 6th Southern African solar energy conference, pp 1–5
72. Pern FJ (1996) Factors that affect the EVA encapsulant discoloration rate upon accelerated exposure. Sol Energy Mater Sol Cells 41:587–615
73. Sharma V, Chandel SS (2013) Performance and degradation analysis for long term reliability of solar photovoltaic systems: a review. Renew Sustain Energy Rev 27:753–767
74. Köntges M, Morlier A, Eder G, Fleiß E, Kubicek B, Lin J (2020) Ultraviolet fluorescence as assessment tool for photovoltaic modules. IEEE J Photovolt 10(2):616–633
75. Jordan DC, Silverman TJ, Sekulic B, Kurtz SR (2017) PV degradation curves: non-linearities and failure modes. Progr Photovoltaics Res Appl 25(7):583–591
76. Ennemri A, Logerais PO, Balistrou M, Durastanti JF, Belaidi I (2019) Cracks in silicon photovoltaic modules: a review. J Optoelectron Adv Mater 21(1–2):74–92
77. Piliougine M, Oukaja A, Sidrach-de-Cardona M, Spagnuolo G (2021) Temperature coefficients of degraded crystalline silicon photovoltaic modules at outdoor conditions. Prog Photovoltaics Res Appl 29(5):558–570
78. Veldman D, Bennett IJ, Brockholz B, de Jong PC (2011) Non-destructive testing of crystalline silicon photovoltaic back-contact modules. In: 2011 37th IEEE photovoltaic specialists conference. IEEE, pp 003237–003240

Chapter 7
Thermal Performance Assessment Review of the Solar Concentrator System's Receiver Utilized for High-Temperature Applications

Hemant Raj Singh and Dilip Sharma

Abstract The present unprecedented lockdown scenario due to COVID-19 and the ever-concerning energy crisis impels researchers to find more self-sustainable energy solutions for all anthropogenic basic needs. Solar systems seem to be a good option for future energy use. Solar thermal energy plays a vital role in achieving Sustainable Development Goals (SDG). The receiver is one of the important components in any solar concentrating thermal system as it contains the highest temperature of the system, and inherently, maximum heat losses are also associated with it. In this study, energy and exergy analyses have been done on all available receivers of solar concentrators hitherto. The solar concentrators are categorized according to their prime mover, i.e. the artificial and actual solar heat-driven (solarized) systems. Receivers are also categorized according to their shape, with special attention to cavity receivers. The thermal performance parameter assessment study also helps researchers and policymakers in the selection and decision-making process.

Keywords Receiver · Focus · Solar concentrator · Energy · Exergy · Cavity receiver

1 Introduction

The living standard of any country is always relying on energy security. Researchers and policymakers are always working for energy fulfilment. The energy crisis is always being a challenge for society. The demand for energy is increasing daily. The world's marketed energy consumption is expected to increase from 549 quadrillion Btu in 2012 to 815 quadrillion Btu in 2040 [1].

H. R. Singh (✉)
Manipal University Jaipur, Jaipur, Rajasthan 303007, India
e-mail: hemant.singh@jaipur.manipal.edu

D. Sharma
Malaviya National Institute of Technology Jaipur, Jaipur, Rajasthan 302017, India

D. Tripathi et al. (eds.), *Advancements in Nanotechnology for Energy and Environment*,
Advances in Sustainability Science and Technology,
https://doi.org/10.1007/978-981-19-5201-2_7

The achievement of Sustainable Development Goal (SDG7) and all other Sustainable Development Goals, especially those dealing with equality, health, poverty reduction, and combating global warming, is dependent on the 2030 target for affordable, reliable, sustainable, and modern energy for all people [2].

Apart from that, the world is also suffering from the novel "Corona" VIRUS "COVID-19" (WHO 2020). Globally, it creates an unprecedented lockdown. It reinforces the researcher to find more sustainable solutions for the society to cope up/survive with this type of situations and which would also decrease the dependency on ever depleting fossil fuels. A record amount of additional power capacity was added to the grid by renewable energy sources in 2020, notwithstanding the COVID-19 pandemic's negative effects [3].

1.1 Renewable Energy

United Nations officials consider fossil fuel depletion and its associated environmental harm to be among the most important global concerns confronting the globe today. Coal and oil are the most used energy sources, hence, the amount of each is directly proportional to how much people need. It becomes increasingly harder to maintain and sustain life support systems as energy consumption grows. These days, there are several reasons to be concerned about the environment, including dwindling fossil fuel supplies, oil shortages, scarcity, rising temperatures, and a rise in pollution. There is a growing need to address climate justice in the age of global warming. In addition to the academic community, the public is becoming more interested in alternative sources, which has led to an increase in their utilization. Scientists are investigating the possibility of harnessing solar energy for space heating and cooling, both individually and together [4–7, 10–13]

1.1.1 Solar Thermal Energy

Solar energy is generally divided into two parts, i.e. solar thermal energy and solar photovoltaic. Solar thermal energy is a low-grade energy and does not degrade energy quality in further process. As per Fig. 1, implication of renewable energy in total final energy consumption by Final Energy Use could be seen.

Solar Radiation

Solar radiation strikes the earth's surface at a rate of 8×10^6 W, which is more than 10,000 times the current global energy consumption. There is no question that the resource basis exists to support a society powered by solar energy. The cost of the equipment required to capture solar energy will determine whether solar energy will be accepted. Even though sunshine is free, one must pay a capital charge to cover

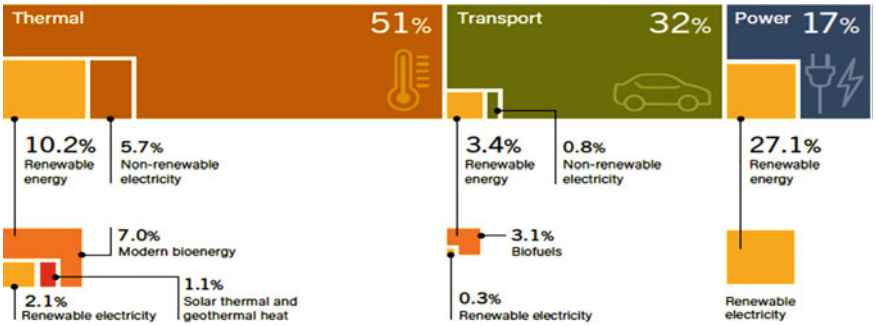

Fig. 1 Renewable energy in total final energy consumption, by Final Energy Use, 2018 [11]

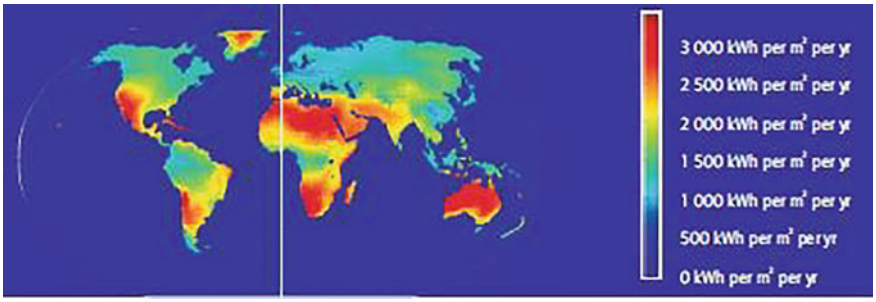

Fig. 2 Solar resource for concentrated solar power technologies (DNI in kWh/m^2/y) [9]

the cost of amortizing the collecting apparatus. Solar energy is a high-capital-input technology. For solar-powered equipment, a lifespan of 20–25 years is commonly assumed to be reasonable [8] (Fig. 2).

Solar Angles

Solar geometry is very vital to understand if researcher wanted to harness actual solar energy for efficient functionality of solar thermal devices/prototypes.

- Elevation Angle (α): It shows how high the Sun's beams are. It is a measure of distance from the Sun's geometric centre.
- Zenith Angle (Θ_z): The angle of incidence of beam radiation on a horizontal surface.
- Declination Angle (δ) = When the Sun is at solar noon, its angular position with regard to the plane of the equator. The value of declination angle of Sun varies between $+23.45°$ and $-23.45°$. The declination can be found from the approximate $\delta = 23.45 \sin\left(360\frac{284+n}{365}\right)$ equation of Cooper (1969) [8]

- Azimuth Angle (z) = It is the angle formed by the perpendicular projection of the Sundown onto the horizon line.
- Hour Angle (ω) = The angular distance between the observer's meridian and the meridian containing the Sun.

2 Literature Review

2.1 Solar Concentrators

Prime energy sources/prime movers are the cornerstones of any thermal systems, since they are responsible for the generation of electricity or mechanical power/energy conversion. Given the critical nature of prime energy sources and prime movers, the decision of prime energy sources and prime movers is vital.

Depending on the type of concentrator, concentration ratios might range from less than one to as high as 10^5 (Figs. 3, 4, 5 and 6).

3 Methodology

The receiver is a critical component of any solar thermal concentrator system since it serves as the central energy house for all solar thermal devices. There are a lot of things to think about when researchers build a solar concentrating thermal system. The receiver is one of them because it has the highest temperature and the most heat losses. In this study, the energy and entropy of all the receivers of solar concentrators that have been available so far have been looked at in this way. The solar concentrators

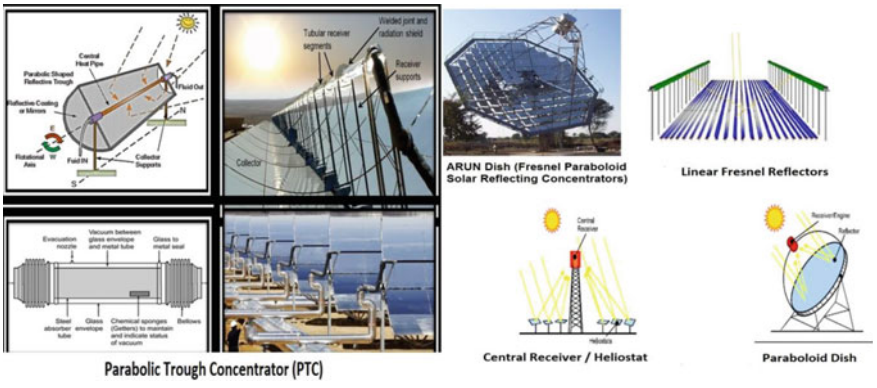

Fig. 3 Concentrated solar thermal technologies

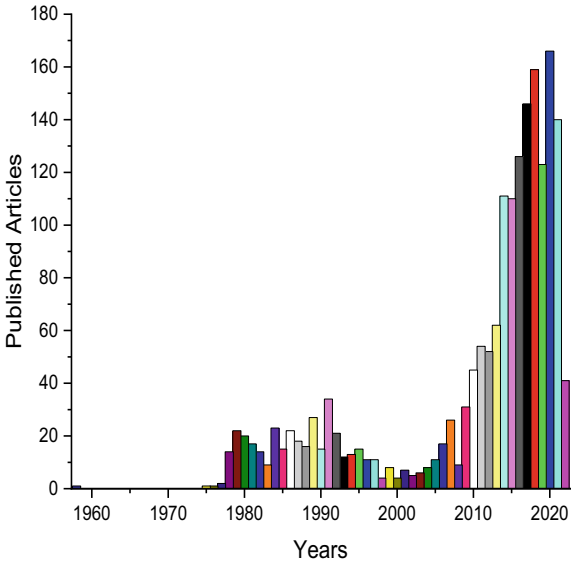

Fig. 4 Year-wise published literatures related with receiver of solar concentrator

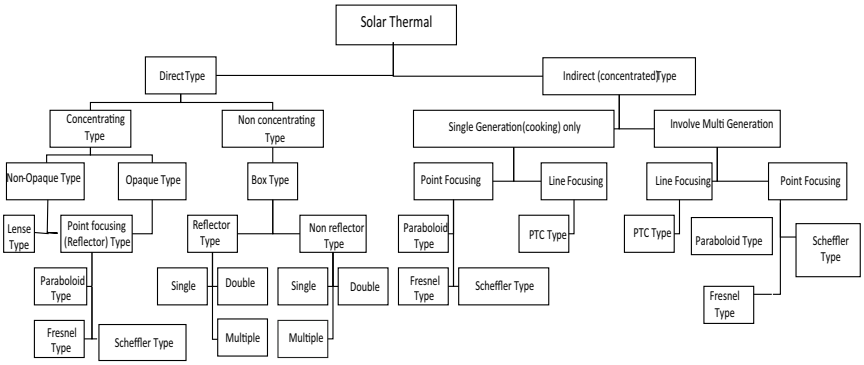

Fig. 5 Solar thermal devices-categorization [8]

are broken down into two groups based on how they get their power, which is either from an artificial or real source of heat. Another way to group receivers is by how they look, with special attention paid to the type of receivers that fit inside a space. It helps researchers and policymakers choose and decide on what to buy and how it should be made. Above stated, major findings from the latest literature are given in Table 1 (Fig. 7).

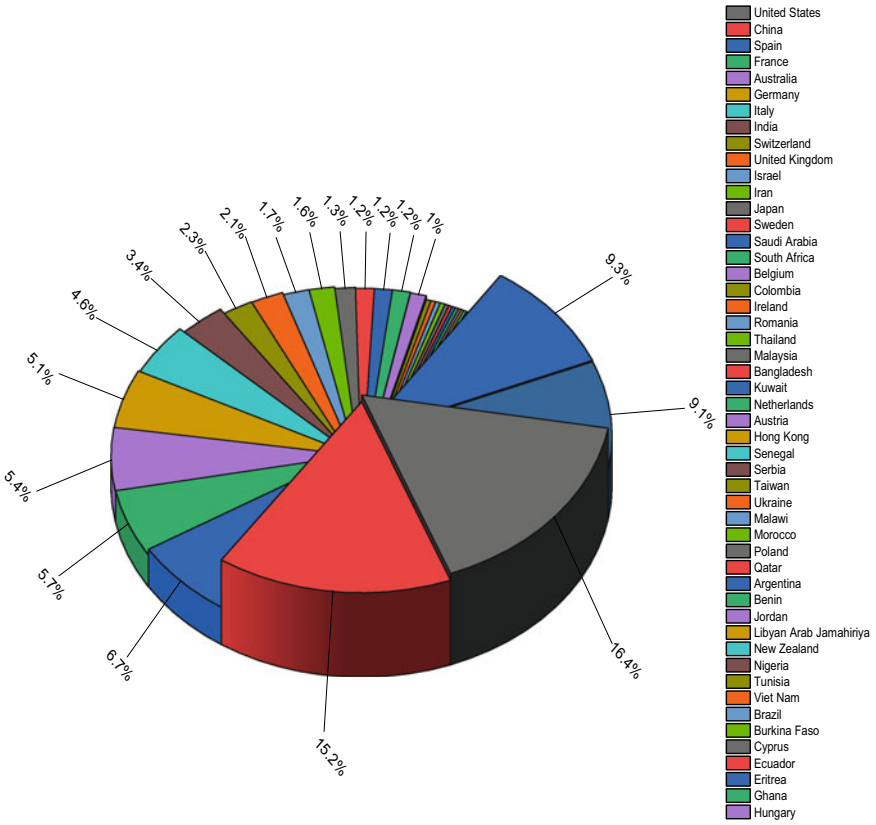

Fig. 6 Country-wise published literatures related with receiver of solar concentrator

4 Conclusion

The review includes a historical overview, classification, operation, and thermodynamic analysis of several solar receivers, as well as the rationale for their use now, lacking technology to gain any real extent of popularity.

The study showed that the thermal performance of any solar thermal system depends mainly on its receiver's characteristics, e.g. type of receiver, exact location (perfect focus), coating on the receiving surface, etc.

A blocked mouth makes it a little easier to lose heat in windy weather. Receiver facing a head-on wind will lose more heat through convection in all shapes of cavities. Conical cavities have the lowest number of convective losses for both types of cavities (with and without mouth blockage). A blocked mouth makes it a little easier to lose heat in windy weather. The blockage of the mouth is found to be more effective for cavities that are conical. Not every increase in the area of your mouth that is blocked

Table 1 Major findings of RHX literatures

S. No	Author	Year	Major findings
1	Dashora and Gupta [14]	1996	With this work, not only does it explain why linear amorphous polymers' thermal conductivities fluctuate, but it also helps us comprehend how their structure and bulk physical characteristics are connected. There is no certainty that the measured values can be extrapolated with confidence since polymers have a wide variety of temperature ranges. Polymers' thermal conductivity varies with temperature, which explains this
2	Ramji et al. [15]	2012	Indian families' usage of energy and the factors that impact their access to and use of energy in rural regions is examined in new research. Cooking and lighting in rural houses in India are becoming more dependent on sources of energy
3	Buck and Friedmann [16]	2007	The entrance aperture of the receiver has been placed It was tested for its thermal and financial efficiency. According to the findings, such a strategy can be beneficial in some situations. Power and heat were believed to be available. The double-effect absorption chiller outperforms both thermally and economically
4	Reddy and Sendhil Kumar [17]	2008	Using a two-dimensional model, researchers can figure out how much heat is lost through natural convection from redesigned cavity receivers with and without insulation on the bottom of the aperture plane
5	Sendhil Kumar and Reddy [18]	2008	Cavity, semi-cavity, and modified cavity receivers are all computed numerically for a fuzzy focused solar dish concentrator. The angle of 0° to 90° is used to measure natural convection heat loss from receivers. (Aperture downward) The receiver's position and shape influence natural convection heat loss

(continued)

does not mean you will lose more heat. The convective loss may actually get worse in some places. Because of this, its selection should be done in this way, as well.

The study concluded direct and indirect solar thermal device's performance based on their thermal performance, which inherently depends on their receivers, which primarily absorb, transfer, and utilize the precious solar energy.

Table 1 (continued)

S. No	Author	Year	Major findings
6	Prakash et al. [19]	2009	This study investigated the steady-state convective losses from a cylindrical cavity receiver with a 0.25 m length, width, and wind skirt width Heat and optical losses can degrade a solar parabolic dish-cavity receiver's performance. Convective and radiative heat losses account for most thermal loss
7	Reddy and Sendhil Kumar [20]	2009	A fuzzy focused solar dish concentrator's modified cavity receiver (WOI) is tested to evaluate how effectively a three-dimensional computer model can forecast how much heat is lost by natural convection. Comparing 2D and 3D heat loss from the new receiver is the goal
8	NREL [21]	2009	CSP system components are examined for their durability, performance, and heat loss, as well as potential enhancements. 5 competencies are highlighted in this project. Optical efficiency and heat loss are taken into consideration while designing and testing concentrators
9	Wu et al. [22]	2010	In a parabolic dish concentrator, a lot of heat passes through the cavity receiver. As a result, its efficiency and cost-effectiveness can be greatly reduced by this method. Determine how much heat is being wasted, and then increase the receiver's thermal performance
10	Al-Sulaiman et al. [23]	2011	Trigeneration systems combining parabolic trough solar collectors (PTSC) and organic Rankine cycles (ORCs) are studied in this study using exergy modelling to determine how well the new systems perform (ORC)
11	Platzer and Hildebrandt [24]	2012	For receivers in parabolic trough and Fresnel collectors, absorber coatings are examined in this investigation. Solar energy conversion and heat loss optical efficiency measurements rely heavily on the receiver. Low thermal emittance and high solar absorptance are critical considerations. These critical defining characteristics are discussed in detail. Receivers that are expected to last for a long time must have good degradation processes and long service lives

(continued)

Table 1 (continued)

S. No	Author	Year	Major findings
12	Blackmon [25]	2012	Heliostat receivers get more expensive as the area of a solar power plant grows. This is a good example of what the study is all about. Cost data from the US Department of Energy shows that the cost per square foot for small heliostats ranges from about 25 to 40 square feet. A 148-square foot heliostat is too expensive for the DOE to use as its standard heliostat because it costs so much
13	Barigozzi et al. [26]	2012	To assess the performance of solar receiver, advanced thermal simulation software's, i.e. TRNSYS and Thermoflex were used. This work is about how to model a solar hybrid gas turbine so that you can see how it works. The method is used to make electricity with a heliostat field, a receiver, and a 36 MW commercial gas turbine. Concentrated solar power and fossil fuel are used to make the heat. To figure out how well commercial gas turbines will work, a detailed model of the machine is suggested
14	Sardeshpande and Pillai [27]	2012	Along the focal line of the parabolic reflector is a metal black tube with a glass tube covering it to limit heat transfer. Parallel rays incident on the reflector are reflected onto the receiving tube when the parabola is directed towards the Sun
15	Jamel et al. [28]	2013	Advanced thermal simulation software, like TRNSYS and Thermoflex, were used by many people to figure out how well a solar receiver worked. Some people used more traditional methods, like the first and second laws of thermodynamics, to figure out how well a solar receiver worked. A method based on exergy principles is the most useful one used by the authors to look at their work. Also, the authors used a lot of different ways to make these hybrid systems more efficient when they made them, ran them, and designed them

(continued)

Table 1 (continued)

S. No	Author	Year	Major findings
16	Franchini [29]	2013	This research focuses on CSP systems using a steam Rankine cycle and two types of solar fields. The two types of solar fields are PTC and heliostats with a central receiver (HCR). For both places, PTC technology needs a bigger aperture area than HCR to get the heat into the Rankine cycle, so it needs more space than HCR. In Sevilla, HCR appears to outperform PTCs. A solar tower is the greatest choice for a CSP plant since it can meet demand in both Upington and Sevilla
17	Ho and Iverson [30]	2014	This paper looks at three different types of receivers: gas receivers, liquid receivers, and solid particle receivers. Gas receivers are the most common, but liquid and solid particle receivers are also important. In this paper, we look at different designs for central receivers for concentrated solar power applications, where the power cycles are very hot. Materials that are cheap and long-lasting are what people want. They can handle high concentration ratios There are several high-temperature receiver designs and technologies that work well with central receiver power tower systems that have been looked at in the study. Most people have worked on receiver concepts so far, but only a few have been used to show how they work in a real plant. Tubular receivers with either liquid or gas/liquid working fluids are the most common type of receiver. Improve receiver efficiency and change working fluids in many cases to get better turbine efficiency and higher temperatures
18	Jilte et al. [31]	2014	The numerical three-dimensional analyses of forced convective heat loss from cavity receivers of various shapes under wind circumstances. In addition to cylindrical and conical cavities, dome-cylindrical (combination of hemispherical and cylindrical cavities) and hetero-conical cavities are also utilized

(continued)

Table 1 (continued)

S. No	Author	Year	Major findings
19	Ruelas et al. [32]	2014	For predicting solar receiver performance of Scheffler dish operated Stirling engine, a ray tracing software was used and its result was validated through thermographic image
20	Sedighi and Zakariapour [33]	2014	The authors reviewed direct and indirect solar cookers' performance on the basis of their thermal performance, which inherently depends on their receivers, which primarily absorb, transfer, and utilize the precious solar energy
21	Samanes et al. [34]	2015	As the main problem with modelling cavity receivers is figuring out how much heat is lost through natural convection, this paper looks at the different natural convection correlations that have been used by different authors to figure out how much heat is lost through natural convection through cavity receivers. On a real cavity receiver, simulations are done to examine the different correlations utilized to estimate convective heat losses
22	Abbasi-Shavazi et al. [35]	2015	This study looks at how much heat is lost from a model solar cavity receiver. This was done to see how these models would work. Each cavity had a constant amount of heat coming from the outside through heating cables, and it was run at different angles. Pyromark-2500, a heat-resistant paint, was carefully applied to the surface of the cavities Convective heat loss from a cylindrical cavity receiver has been looked at in this work. It looked at how much heat was lost through convection in a range of boundary conditions. Because of local radiation and convection heat transfer, the temperature distribution on the cavity walls changes naturally. This is because the inclination of the cavity changes the amount of heat that moves through it. It has been used to get upper and lower limits on the total amount of heat lost through convection and radiation
23	Franchini et al. [36]	2015	To assess the thermal performance of solar receiver, TRNSYS® and in-house developed computer codes are used Power blocks were made by Thermoflex®, which was used to model how the solar field worked all year long

(continued)

Table 1 (continued)

S. No	Author	Year	Major findings
24	Nakakura et al. [37]	2015	The point concentration receiver evaluation system was made with the help of an artificial heat source. The system has a receiver unit, heat exchanger, blower, chiller, and light source, as well as all the other parts. It was very easy to figure out how much heat air took in because the enthalpy rise of the coolant water and the air that came out were both very high
25	Borunda et al. [38]	2016	There are more storage technologies that could be looked into to improve the system and increase the amount of solar power. Molten salts could be a great way to increase the amount of sunlight that gets into your home, but they are a lot more expensive. On the other hand, concrete storage is much cheaper, but it does not hold as much heat. There are other options, such as phase change materials, that could be good and interesting. They could be a good balance between heat capacity and cost, though
26	Pavlovic et al. [39]	2016	It describes the process of developing a low-cost solar concentrator for medium temperature applications, from design to fabrication and analysis. An offset parabolic antenna is utilized to produce the reflector instead of a specific shaped surface. A novel mathematical methodology for determining the intercept factor of a new solar concentrator is developed and applied here. An inexpensive instrument for laboratory study on medium temperature thermal processes, hot water systems, heating, cooling, and poly generation systems is presented in this work. An offset parabolic dish reflector with three offset parabolic dish reflectors is also studied in the research
27	Mokheimer et al. [40]	2017	On three different gas turbine sizes, THERMOFLEX with PEACE simulation software was utilized to assess solar receiver performance. The gas turbine cogeneration plant will use parabolic trough collectors, linear Fresnel reflectors, and solar towers as solar concentrator technology

(continued)

Table 1 (continued)

S. No	Author	Year	Major findings
28	Wang et al. [41]	2019	As a fixed receiver, the cavity receiver with bottom reflecting cone was utilized. To improve the optical performance of the system and receiver, the impacts of receiver parameters were explored. A significance test of relevant variables was run to assess the impact. A comparison of the Scheffler dish type food cooking method was made. The analysis reveals average optical efficiency utilizing a cavity receiver with a spherical, cylindrical, or conical bottom
29	Thappa et al. [42]	2020	To increase the solar parabolic trough collector's thermal performance, two distinct receiver tubes were proposed and compared The results reported here describe the effects of varying the diameter of the receiver tube on the loss coefficient, energy gain, and overall system performance
30	Singh et al. [43]	2021	A low-cost indigenously designed modified dome-shaped cavity receiver was developed using locally available material as an outcome of experimental studies using Scheffler-type solar concentrator as prime mover

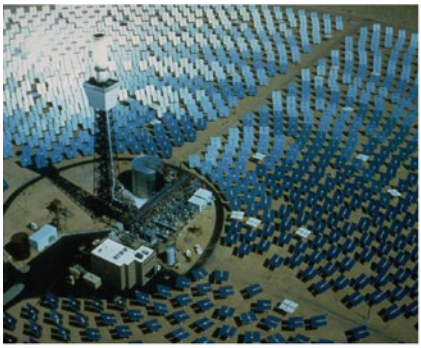

a [45]

b [45]

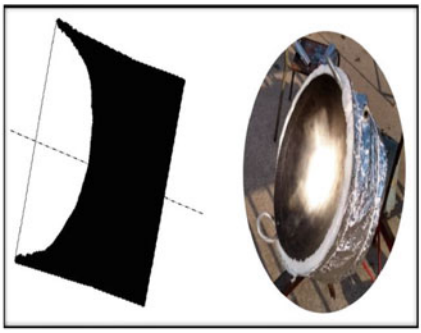

c [44]

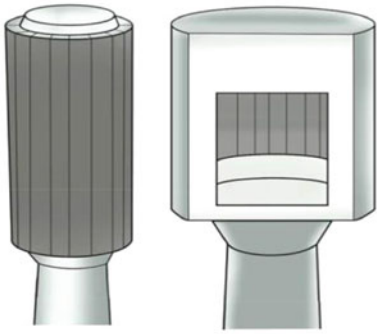

d [31]

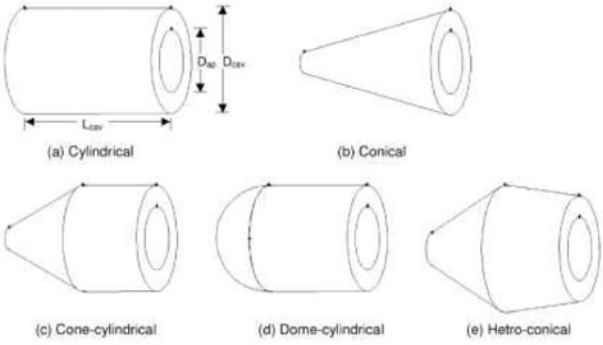

e [32]

Fig. 7 Receiver of solar concentrator. **a** Solar One [45]. **b** SAIC SolMaT heliostat design [45]. **c** Modified dome-shape shallow cavity receiver [44]. **d**. Tubular (left) external and (right) cavity receivers [31]. **e** Cavity shapes [32]

References

1. U.S. Energy Information Administration (EIA) International energy outlook 2016. https://www.eia.gov/outlooks/ieo/. Accessed 12 Mar 2017
2. Powering Equality Women's entrepreneurship transforming Asia's energy sector (n.d.)
3. I. E. A. India Energy Outlook. World Energy Outlook Spec. Rep. 1–191 (2015). https://www.iea.org/publications/freepublications/publication/africa-energy-outlook. Accessed 13 Mar 2017
4. Duffie JA, Beckman WA (2000) Solar engineering of thermal process, 3rd edn. Wliey, New York
5. Shekhawat et al (2019) Development and operationalization of solar-assisted rapid bulk milk cooler. ASME J Sol Energy Eng 141(4). https://doi.org/10.1115/1.4042524
6. Singh et al (2021) Dissemination of sustainable cooking: a detailed review on solar cooking system. IOP Conf Ser Mater Sci Eng 1127(1):012011. https://doi.org/10.1088/1757-899X/1127/1/012011
7. Moonka et al (2022) Study on some aspects of Stirling engine: a path to solar Stirling engines. Mater Today: Proc 63:737–744. ISSN 2214-7853. https://doi.org/10.1016/j.matpr.2022.05.107
8. Rabl A (1985) Active solar collectors and their applications. Oxford University Press, New York. http://public.eblib.com/choice/publicfullrecord.aspx?p=270919
9. Lohmann S et al (2006) Validation of DLR-ISIS data. German Aerospace Center, Oberpfaffenhofen. www.pa.op.dlr.de/ISIS
10. Singh et al (2021) Study on some aspects of adoption of solar cooking system: a review. Mater Today Proc. https://doi.org/10.1016/j.matpr.2021.05.323
11. REN21 Renewable 2021 Global status Report. REN21 Secretariat, UN Environment Programme, France. ISBN 978-3-948393-03-8. http://ren21.net
12. Sayigh AAM, McVeigh JC (1992) Solar air conditioning and refrigeration. Pergamon Press
13. Nahar, N. M., Gupta, J. P., & Sharma, P. (1996). PERFORMANCE AND TESTING OF TWO MODELS OF SOLAR COOKER FOR ANIMAL FEED. In Renewable Energy (Vol. 7, Issue 95).
14. Dashora P, Gupta G (1996) On the temperature dependence of the thermal conductivity of linear amorphous polymers. 37(2)
15. Ramji A, Soni A, Sehjpal R, Das S, Singh R (1999) The Energy and Resources Institute
16. Buck R, Friedmann S (2007) Solar-assisted small solar tower trigeneration systems. J Sol Energy Eng Trans ASME 129(4):349–354. https://doi.org/10.1115/1.2769688
17. Reddy KS, Sendhil Kumar N (2008) Combined laminar natural convection and surface radiation heat transfer in a modified cavity receiver of solar parabolic dish. Int J Therm Sci 47(12):1647–1657. https://doi.org/10.1016/j.ijthermalsci.2007.12.001
18. Sendhil Kumar N, Reddy KS (2008) Comparison of receivers for solar dish collector system. Energy Convers Manag 49(4):812–819. https://doi.org/10.1016/j.enconman.2007.07.026
19. Prakash M, Kedare SB, Nayak JK (2009) Investigations on heat losses from a solar cavity receiver. Sol Energy 83(2):157–170. https://doi.org/10.1016/j.solener.2008.07.011
20. Reddy KS, Sendhil Kumar N (2009) An improved model for natural convection heat loss from modified cavity receiver of solar dish concentrator. Sol Energy 83(10):1884–1892. https://doi.org/10.1016/j.solener.2009.07.001
21. NREL (2009) Collector/receiver characterization. Thermal Systems Group. CSP Capabilities. www.nrel.gov
22. Wu SY, Xiao L, Cao Y, Li YR (2010) Convection heat loss from cavity receiver in parabolic dish solar thermal power system: a review. Sol Energy 84(8):1342–1355. https://doi.org/10.1016/j.solener.2010.04.008
23. Al-Sulaiman FA, Dincer I, Hamdullahpur F (2011) Exergy modeling of a new solar driven trigeneration system. Sol Energy 85(9):2228–2243. https://doi.org/10.1016/j.solener.2011.06.009

24. Platzer W, Hildebrandt C (2012) Absorber materials for solar thermal receivers in concentrating solar power (CSP) systems. Concentrating solar power technology. Elsevier, pp 469–494. https://doi.org/10.1533/9780857096173.3.469
25. Blackmon JB (2012) Heliostat size optimization for central receiver solar power plants. Concentrating solar power technology. Elsevier, pp 536–576. https://doi.org/10.1533/9780857096173.3.536
26. Barigozzi G, Bonetti G, Franchini G, Perdichizzi A, Ravelli S (2012) Thermal performance prediction of a solar hybrid gas turbine. Sol Energy 86(7):2116–2127. https://doi.org/10.1016/j.solener.2012.04.014
27. Sardeshpande V, Pillai IR (2012) Effect of micro-level and macro-level factors on adoption potential of solar concentrators for medium temperature thermal applications. Energy Sustain Dev 16(2):216–223. https://doi.org/10.1016/j.esd.2012.01.001
28. Jamel MS, Abd Rahman A, Shamsuddin AH (2013) Advances in the integration of solar thermal energy with conventional and non-conventional power plants. Renew Sustain Energy Rev 20:71–81. https://doi.org/10.1016/j.rser.2012.10.027
29. Franchini G (2013) Hybrid CSP plants modeling: comparison between steam plants and solar combined cycles
30. Ho CK, Iverson BD (2014) Review of high-temperature central receiver designs for concentrating solar power. Renew Sustain Energy Rev 29:835–846. https://doi.org/10.1016/j.rser.2013.08.099
31. Jilte RD, Kedare SB, Nayak JK (2014) Investigation on convective heat losses from solar cavities under wind conditions. Energy Procedia 57:437–446. https://doi.org/10.1016/j.egypro.2014.10.197
32. Ruelas J, Pando G, Lucero B, Tzab J (2014) Ray tracing study to determine the characteristics of the solar image in the receiver for a scheffler-type solar concentrator coupled with a stirling engine. Energy Procedia 57:2858–2866. https://doi.org/10.1016/j.egypro.2014.10.319
33. Sedighi M, Zakariapour M (2014) A review of direct and indirect solar cookers. Sustain Energy 2(2):44–51. https://doi.org/10.12691/rse-2-2-2
34. Samanes J, García-Barberena J, Zaversky F (2015) Modeling solar cavity receivers: a review and comparison of natural convection heat loss correlations. Energy Procedia 69:543–552. https://doi.org/10.1016/j.egypro.2015.03.063
35. Abbasi-Shavazi E, Hughes GO, Pye JD (2015) Investigation of heat loss from a solar cavity receiver. Energy Procedia 69:269–278. https://doi.org/10.1016/j.egypro.2015.03.031
36. Franchini G, Barigozzi G, Perdichizzi A, Ravelli S (2015) Simulation and performance assessment of load-following CSP plants. Kruger
37. Nakakura M, Ohtake M, Matsubara K, Yoshida K, Cho HS, Kodama T, Gokon N (2015) Development of a receiver evaluation system using 30 kWth point concentration solar simulator. Energy Procedia 69:497–505. https://doi.org/10.1016/j.egypro.2015.03.058
38. Borunda M, Jaramillo OA, Dorantes R, Reyes A (2016) Organic Rankine cycle coupling with a parabolic trough solar power plant for cogeneration and industrial processes. Renew Energy 86:651–663. https://doi.org/10.1016/j.renene.2015.08.041
39. Pavlovic S, Stefanovic V, Mancic M, Spasic Z (2016) Development of mathematical model of offset type solar parabolic concentrating collector. Fascicule 1. Ann Fac Eng Hunedoara-Int J Eng Tome XIV 1
40. Mokheimer EMA, Dabwan YN, Habib MA (2017) Optimal integration of solar energy with fossil fuel gas turbine cogeneration plants using three different CSP technologies in Saudi Arabia. Appl Energy 185:1268–1280. https://doi.org/10.1016/j.apenergy.2015.12.029
41. Wang H, Huang J, Song M, Yan J (2019) Effects of receiver parameters on the optical performance of a fixed-focus Fresnel lens solar concentrator/cavity receiver system in solar cooker. Appl Energy 237:70–82. https://doi.org/10.1016/j.apenergy.2018.12.092
42. Thappa S, Chauhan A, Anand Y, Anand S (2020) Analytical comparison of two distinct receiver tubes of a parabolic trough solar collector system for thermal application. Mater Today Proc 28:2212–2217. https://doi.org/10.1016/j.matpr.2020.04.257

43. Singh HR, Sharma D, Sharma DK, Chadha S (2021) Low-cost novel designed receiver heat exchanger for household solarized cooking system: development and operationalization. Mater Today Proc 47:3018–3023. https://doi.org/10.1016/j.matpr.2021.05.494
44. Kolb G, Jones S, Donnelly M, Gorman D, Lumia R, Davenport R, Thomas R (2007) Heliostat cost reduction study. https://doi.org/10.2172/912923

Chapter 8
Performance of Solar Adsorption Refrigeration System: A case Study of a Two-Stage Freezing System with Varying Thermal Conductivity, Permeability of Adsorbents

Nidal H. Abu-Hamdeh and Hakan F. Öztop

Abstract This research presents an improved design of a solar adsorption refrigeration system with certain specifications and requirements. In the traditional simulation of the performance of the solar adsorption refrigeration, the constant permeability and thermal conductivity were always selected for the establishment for the mathematic model. Latest research revealed that the permeability and thermal conductivity vary appreciably in the processes of adsorption and desorption, which indicates the consequential adsorption refrigeration performance will likewise be affected. The varying permeability and thermal conductivity in the $CaCl_2$ and $BaCl_2$ adsorption processes were tested, and the two-stage adsorption refrigeration system using $CaCl_2$–$BaCl_2$–NH_3 as working pair was simulated to evaluate the effect of varying adsorbents' permeability and thermal conductivity on the refrigeration system adsorption performance. The variable thermal conductivity and permeability simulation findings are compared to the constant thermal conductivity and permeability simulation results, as well as the experimental data. According to the results obtained, the greatest relative error between the simulation result with variable characteristics and the actual result is 8.3% for cooling capacity, 9.1% for SCP and 12% for COP, while the maximum relative error between the simulation result with constant properties and the experimental result is as high as 41.4% for cooling capacity, 42.8% for SCP and 36% for

N. H. Abu-Hamdeh (✉)
Department of Mechanical Engineering, Faculty of Engineering, King Abdulaziz University, Jeddah, Saudi Arabia
e-mail: nabuhamdeh@kau.edu.sa

K. A. CARE Energy Research and Innovation Center, King Abdulaziz University, Jeddah 21589, Saudi Arabia

Energy Efficiency Group/Center of Research Excellence in Renewable Energy and Power Systems, King Abdulaziz University, Jeddah, Saudi Arabia

H. F. Öztop
Department of Mechanical Engineering, Technology Faculty, Fırat University, Elazığ, Turkey

D. Tripathi et al. (eds.), *Advancements in Nanotechnology for Energy and Environment*,
Advances in Sustainability Science and Technology,
https://doi.org/10.1007/978-981-19-5201-2_8

COP. This finding shows that variable characteristics have a major impact on simulation results and should be explored first before developing mathematical models for chemical and solar adsorption refrigeration systems.

Keywords Two-stage adsorption refrigeration · Simulation · Thermal conductivity · Permeability · Calcium chloride · Barium chloride

Nomenclature

c	specific heat (kJ/(kg K))
COP	coefficient of performance
D	finned tube diameter (mm)
d	finned tube base tube diameter (mm)
F	heat transfer area (mm^2)
h	heat transfer coefficient ($W/(m^2\ K)$)
K	heat transfer coefficient ($W/(m^2\ K)$)
L	adsorbent bed axial Length (m)
M_{MTS}	mass of middle temperature salt
m	mass (kg)
n	numbers of tube
P	pressure (Pa)
Q	power (W)
q	water mass flow (kg/s)
R	gas constant (J/kg K)
r	radius (m)
SCP	specific cooling power
s	fin thickness (mm)
t	time (s)
T	temperature (K)
x	adsorption rate (kg/kg)

Greek letters

δ	variable parameter
Δx	cycle adsorption quantity (kg/kg)
ε	the mass ratio of salts
ε_t	porosity
λ	thermal conductivity (W/mK)
ν	fin spacing (mm)
ρ	density (kg/m^3)

Subscripts

ad	adsorbent
al	aluminum
am	ammonia
c	cycle
co	cooling
cond	condenser
de	desorption
e	evaporation
eq	equilibrium state
eff	effective
f	working fluid
g	expand natural graphite
LTS	middle temperature salt
lq	liquid ammonia
h	heating
in	inlet
MTS	middle temperature salt
l	low temperature reactor
m	middle temperature reactor
out	outlet
P	permeability
ref	refrigeration
s	steel
ref	refrigeration
w	water
y	reaction process

1 Introduction

Because it is driven by low-grade heat and employs a green refrigerant with 0% ODP and GWP [1–3], solar adsorption refrigeration technology is gaining traction as an energy-saving and environmentally friendly technology. Because the efficiency of mass and heat transfer in a fixed bed reactor substantially influences the performance of a solar adsorption system, research on thermal conductivity and permeability of adsorbent has recently received a lot of attention. Expanded natural graphite (ENG) is used as a matrix for the adsorbent to increase heat and mass transfer performance [4–6] looked at using ENG as a matrix for adsorption heat pumps in silica gel compound blocks. The permeability and thermal conductivity ratings of the blocks were excellent. Furthermore, Shanghai Jiao Tong University created a novel form of compound

adsorbent based on $CaCl_2$ and ENG that increased $CaCl_2$'s thermal conductivity by 36 times [7].

One feature of chemical adsorbents for adsorption refrigeration is that they expand throughout the adsorption process, causing the density to change. Consequently, the thermal conductivity and permeability of the material will vary. Freni et al. [8] examined the thermal conductivity of compound sorbents under various temperature, pressure, and water uptake circumstances, and discovered that the value increases considerably as adsorbate uptake increases but is dependent on pressure and temperature within the studied range. Research work above showed that the improvement of thermal conductivity and permeability as well as notable variable value in the adsorption and desorption process will have an impact on adsorption refrigeration performance. As an important type of chemical adsorbents for the refrigeration, chlorides always utilized for the air conditioner as well as freezing systems. When the evaporation temperature and cooling temperature are −25 °C and 30 °C, respectively, [9] investigated $MnCl_2$–NH_3, and the findings indicated that the driving temperature may reach 180 °C. The equilibrium concentration characteristics of ammonia using $BaCl_2$ composite adsorbent material were examined by Zhong et al. [10], and the COP of a basic adsorption cycle for typical air-conditioning and ice-making applications was 0.6 under typical circumstances. But for the simulation process of the chemical adsorption refrigeration systems, the study mostly concentrates on the simulation with the constant properties of the thermal conductivity and permeability. Maggio et al. [11], for example, developed a two-dimensional mathematical model of an adsorption cooling machine to investigate the effect of constant heat and mass transfer parameters on the machine's performance. The findings were used to determine the best adsorbent bed design for heat and mass transport, as well as the most lucrative heat recovery circumstances. Recently, Shanghai Jiao Tong University had investigated the thermal conductivities for both physical and chemical adsorbents in the adsorption and desorption processes, and results showed that the thermal conductivity and permeability of activated carbon does not change very much in the adsorption process, while the thermal conductivity of $CaCl_2$ increased by 1.52 times, while the permeability decreases by as high as 121 times in the adsorption process. A two-stage test unit in the laboratory, which has low refrigeration temperature under the condition of low heat source temperature [15], is chosen as a study object in this work to assess the variable characteristics of thermal conductivity and permeability on the simulation process. The thermal conductivity and permeability of the adsorbents in the two-stage system, namely the composite adsorbents of $CaCl_2$ and $BaCl_2$ with densities of 400 kg/m^3 and a mass ratio of 80%, were investigated, and the system's performance was simulated and assessed using the experimental results. The simulation findings are compared to experimental data and results with constant thermal conductivity and permeability.

2 Experimental

2.1 Consolidated Composite Adsorbents Preparation

Natural graphite is produced in China by Shanghai YiFan Graphite Company, with specifications of 50–80 mesh and a purity of more than 99%. ENG is made by heating untreated natural graphite in an oven for 10 min at 600 °C. The compact $CaCl_2$-ENG and compact $BaCl_2$-ENG samples were created because they provide an equal dispersion of salts within the ENG. When it comes to heat transfer, mass transfer, and refrigeration, adsorbent density cannot be too low because volume cooling power and thermal conductivity will be affected; density also cannot be too high because permeability will be poor and mass transfer performance will be crucial [12]. The density of samples is 400 kg/m^3, and the mass ratio of the salt in the composite adsorbent is 80%, which is in accord with the adsorbent in the two-stage adsorption experiment.

2.2 Test Unit for Permeability and Thermal Conductivity

Figure 1 shows the test system of the thermal conductivity and permeability. The steady-state heat source technique, which is based on British Standard GB-T 10,294–1988, is used to examine the thermal conductivity of adsorbents in adsorption and desorption processes [13]. Value of thermal conductivity λ is determined by Fourier heat conduction equation. Because the compound adsorbents to be evaluated are porous media with very low gas velocity, the Ergun model may be used to calculate permeability K [14].

2.3 Thermal Conductivity and Permeability of Adsorbents

The findings of the thermal conductivity and permeability in the adsorption and desorption processes are given in Table 1. The experimental data of samples rises fast with increasing adsorbent concentration in the region of 0–4 mol/mol, before slowing down at adsorption concentrations of 5–8 mol/mol. When compared to the results before adsorption, the maximum thermal conductivity of compound ammoniated $CaCl_2$ and $BaCl_2$ is 1.75 and 1.78 W/(mK), respectively, which rose by 52 and 98% at most. Permeability for two adsorbents in adsorption and desorption process decreases from 10^{-11} to 10^{-13}m^2.

Figures 2 and 3 show the trend of thermal conductivity changing with the rising adsorption quantity for $CaCl_2$ and $BaCl_2$, respectively. The relationship between thermal conductivity and adsorption quantity is fitted with the curves as follows:

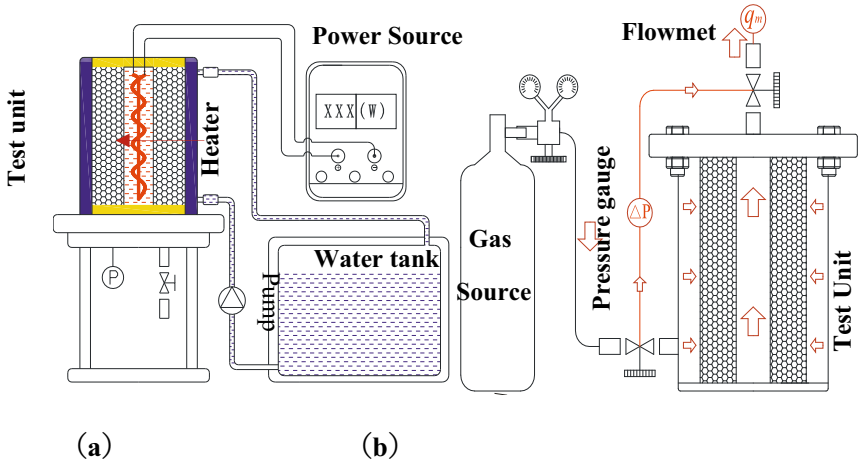

Fig. 1 Test system for thermal conductivity and permeability of adsorbents to be used in the solar adsorption refrigeration system **a** Thermal conductivity test unit, **b** Permeability test unit

Table 1 Thermal conductivity and permeability of adsorbents

Adsorption quantity (kg/kg)	Conductivity W/(mK) $CaCl_2$	Permeability (m^2)	Adsorption quantity (kg/kg)	Conductivity W/(mK) $BaCl_2$	Permeability (m^2)
0	1.15	6.38×10^{-11}	0	0.9	4.44×10^{-12}
0.15	1.35	1.43×10^{-11}	0.08	1.06	4.01×10^{-12}
0.31	1.62	1.24×10^{-11}	0.16	1.19	3.61×10^{-12}
0.46	1.68	8.33×10^{-12}	0.25	1.4	2.91×10^{-12}
0.61	1.62	5.33×10^{-12}	0.33	1.5	2.85×10^{-12}
0.77	1.65	2.16×10^{-12}	0.41	1.54	2.08×10^{-12}
0.91	1.69	1.26×10^{-12}	0.49	1.66	1.45×10^{-12}
1.07	1.67	2.05×10^{-12}	0.57	1.73	9.96×10^{-13}
1.23	1.75	5.25×10^{-13}	0.65	1.78	9.72×10^{-13}

$$\text{Cacl}_2: \quad \lambda = -3.825x^5 + 11.65x^4 - 11.07x^3 + 2.316x^2 + 1.455x + 1.1421.142 \tag{1}$$

$$\text{Bacl}_2: \quad \lambda = -1.331x^2 + 2.218x + 0.8940.894 \tag{2}$$

where λ is thermal conductivity and x is adsorption quantity (kg/kg).

Figures 4 and 5 show the trend of permeability changing with the rising adsorption quantity for $CaCl_2$ and $BaCl_2$, respectively. The relationship between permeability and adsorption quantity by fitting the curves is as follows:

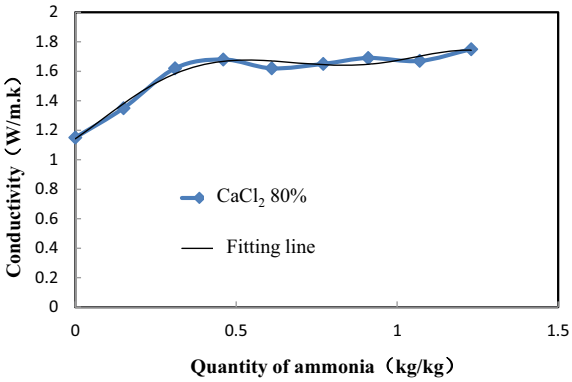

Fig. 2 Thermal conductivity of $CaCl_2$ change with rising adsorption quantity

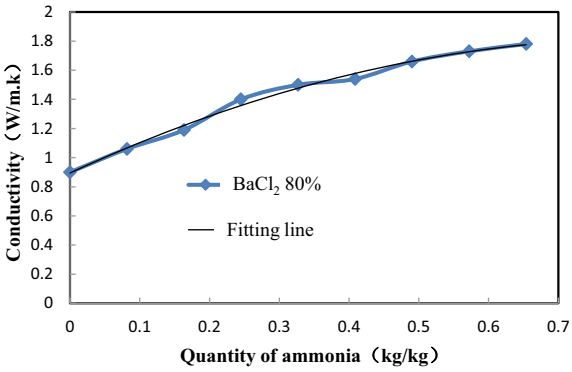

Fig. 3 Thermal conductivity of $BaCl_2$ change with rising adsorption quantity

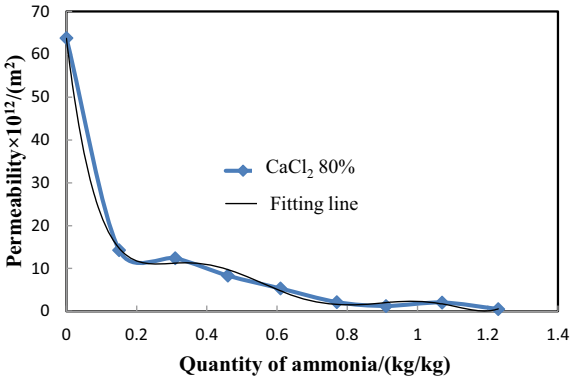

Fig. 4 Permeability of $CaCl_2$ change with rising adsorption quantity

$$\text{Cacl}_2: \quad P = \left(1381.x^6 - 5925.x^5 + 9909.x^4 - 8130x^3 + 3385.x^2 - 681.9x + 63.72\right) \times 10^{-12} \tag{3}$$

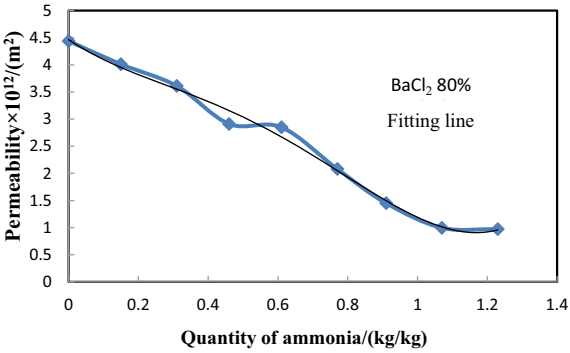

Fig. 5 Permeability of $BaCl_2$ change with rising adsorption quantity

$$\text{Bacl}_2: \quad P = \left(6.142x^4 - 13.08x^3 + 8.040x^2 - 4.373x + 4.467\right) \times 10^{-12} \quad (4)$$

where P is permeability and x is adsorption quantity

3 Mathematical Model

Figure 6 depicts a two-stage adsorption freezing machine for simulation. A medium temperature salt (MTS) reactor, a low temperature salt (LTS) reaction, a condenser, and an evaporator are the components of a two-stage cycle. For one cycle, there are two functioning processes:

(1) The resorption process. The MTS is heated by an external heat source in this process, and the refrigerant is desorbed from the MTS and pumped into the LTS reactor. LTS adsorbs the refrigerant and transfers the heat generated by the process to a heat sink.
(2) Desorption/adsorption process. The LTS is heated by the heat source and desorbs refrigerant to the condenser, where the refrigerant rejects heat to the condenser's surroundings before entering the evaporator. Meanwhile, the heat sink cools MTS and adsorbs the refrigerant from the evaporator; the refrigerant's evaporation provides the refrigeration output.

The main assumptions for the simulation process of the system are as follows:

(1) The pressure and temperature in the adsorber remain consistent throughout, and the refrigerant is adsorbed evenly.
(2) There are no heat losses to the environment as a result of the system.
(3) The evaporator and condenser are perfectly built to meet the evaporation and condensation needs of the system.

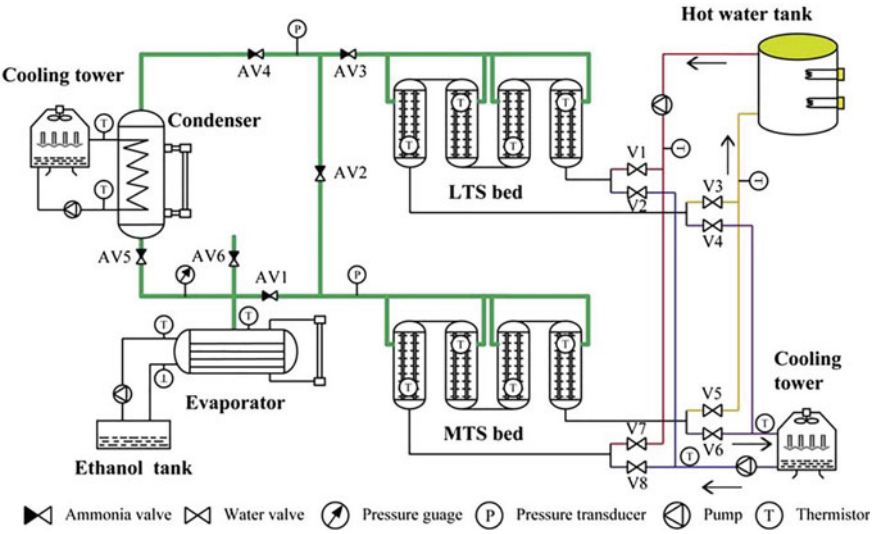

Fig. 6 Schematic of the design of a two-stage adsorption refrigeration cycle in the solar adsorption system

(4) The flowing resistance of the refrigerant is neglected, i.e., the pressure difference between the condenser and the adsorber, and between the adsorber and the evaporator, is ignored.

3.1 Heat transfer equations

The temperature of water flow through middle temperature and low temperature reactor:

$$Tmw, out = Tm + (Tmw, in - Tm)\exp(-\frac{K_{adm}A_m}{q_{mw}c_{mw}}) \tag{5}$$

$$Tlw, out = Tl + (Tlw, in - Tl)\exp(-\frac{K_{adl}A_l}{q_{hw}c_{hw}}) \tag{6}$$

where $T_{mw,out}$ is the temperature of the middle temperature reactor's output water (K), $T_{mw,in}$ is the temperature of the middle temperature reactor's input water (K), T_{m} is temperature of middle temperature reactor (K), K_{adm} is heat transfer coefficient of middle temperature reactor, A_m is heat transfer area of middle temperature reactor (W/(m^{2}K)), q_{mw} is water mass flow of middle temperature reactor (kg/s), and c_{mw} is the water specific heat capacity at the middle temperature reactor (kJ/kg K). Likewise, subscript l represents the parameter of low temperature.

The following equation can be used to compute the overall heat transfer coefficient for an adsorption bed:

$$\frac{1}{K_{ad}F_f} = \frac{1}{K_f F_f} + R_f + \frac{1}{K_{me}F_{me}} + R_c + \frac{1}{K_{a,eff}F_a} \tag{7}$$

where F_f is the working fluid heat transfer area of (mm^2), K_{ad} is the overall heat transfer coefficient (kJ/kg K), R_f is the fouling resistance in between the heating wall and the fluid (m K/W), K_f is the coefficient of heat transfer of the working fluid side (kJ/kg K), F_m is the area of the heat transfer of the metal of the adsorption bed side (mm^2), h_m is the coefficient of the effective heat transfer of the metal of the adsorption bed side (kJ/kg K), $K_{a,eff}$ is effective heat transfer coefficient inside the adsorbent (kJ/kg K), R_c is the metal-to-adsorbent contact resistance (m K/W), and F_a is the effective area of heat transfer inside adsorbent (mm^2).

The desorption or adsorption energy equation of middle temperature and low temperature reactor:

$$\begin{aligned}&(m_{al}c_{al} + m_s c_s + m_{MTS}c_{MTS} + m_g c_g + m_{MTS}c_{am,lq}x)\frac{dT_{m,y}}{dt} = m_{MTS}\Delta H_y \frac{dx}{dt}\\ &+q_{mw}c_{mw}(T_{mw,in} - T_{mw,out}) - \delta m_{MTS}c_{am,y}\frac{dx}{dt}(T_{m,y} - T_e)\end{aligned} \tag{8}$$

$$\begin{aligned}&(m_{al}c_{al} + m_s c_s + m_{LTS}c_{LTS} + m_g c_g + m_{LTS}c_{am,lq}x)\frac{dT_{h,y}}{dt} = m_{LTS}\Delta H_y \frac{dx}{dt}\\ &+q_{lw}c_{lw}(T_{lw,in} - T_{lw,out}) - \delta m_{LTS}c_{am,y}\frac{dx}{dt}(T_{l,y} - T_e)\end{aligned} \tag{9}$$

where $m_{\mathrm{g,}}$ m_{al}, $m_{\mathrm{MTS,\,and}}$ m_{s} are the mass of ENG, aluminum, MTS, steel, respectively (kg). The specific heat capacities of ENG, aluminum, MTS, steel, and liquid ammonia, respectively, are c_{g}, c_{al}, c_{MTS}, c_{s}, $c_{\mathrm{am,lq}}$ (J/kg K). c_{lw} is the low temperature reactor's water specific heat capacity (J/kg K). The specific heat capacity of ammonia throughout the reaction process is $c_{\mathrm{am,y}}$ (J/kg K). The adsorption quantity is denoted by x (kg/kg), $T_{\mathrm{m,y}}$ is temperature of middle temperature reactor during the reaction process (K), T_{e} is evaporating temperature (K), and q_{lw} is water mass flow of secondary reactor (kg/s). $\triangle H_{\mathrm{y}}$ is the reaction enthalpy (J/kg) during the reaction process, t is the duration time, δ is equal to 0 if the adsorbent bed is in the desorption state and 1 if the adsorbent bed is in the adsorption state.

Mass balance equation for the adsorption reactor is:

$$\varepsilon_t \frac{\partial \rho_g}{\partial t} + \frac{1}{r}\frac{\partial}{\partial r}\left(r\rho_g v_0\right) + (1 - \varepsilon_t)\rho_{ad}\frac{\partial x}{\partial t} = 0 \tag{10}$$

Table 2 Data that was utilized to run the simulation

Parameter	Symbol	Value
Outer diameter of a finned tube	D_o	48 mm
Root diameter of a finned tube	D_i	26 mm
Outer diameter of a finned tube's base	d_o	25 mm
Base tube inlet diameter of a finned tube	d_i	20 mm
Fin thickness	s	0.4 mm
Fin spacing	v	2.5 mm
The number of finned tubes	n	37
The length of the finned tube	L	500 mm
Mass of MTS	m_{MTS}	8.2 kg
Mass of LTS	m_{LTS}	8.2 kg
The mass ratio of salts/ENG		4:1
Flow of bulk water	q	1 kg/s
Density of adsorbent	ρ	400 kg/m^3
Heat transfer coefficient	h	300 W/(m^2·K)
Maximum cycle temperature	$T_{b,max}$	85 °C
Minimum cycle temperature	$T_{b,min}$	35 °C
Evaporating temperature	T_e	−15 °C
Condensing temperature	T_c	30 °C
Inlet heat source temperature	$T_{hw,in}$	85 °C
Inlet cooling temperature	$T_{lw,in}$	25 °C

where ε_t is total porosity of the solid adsorbent, ρ_g is the density of gas, and x is adsorption quantity.

Table 2 lists all of the parameters utilized in the mathematical model, which accords with the experimental rig of two-stage system.

3.2 Experimental Equations

The relationship between the adsorption quantity and temperature was tested by Wang [15], which is shown as follows (the range for the evaporation temperature is from 248 to 278 K):

$$\text{Cacl}_2: \quad x = 1718/T - 5.233 \qquad 308 \le T \le 328328 \tag{11}$$

$$\text{Bacl}_2: \quad x = 1997/T - 5.589 \qquad 338 \le T \le 358358 \tag{12}$$

3.3 Calculating Performance

The refrigeration power is determined as follows:

$$Q_{ref} = (M_{MTS}\Delta x L(T_e) - M_{MTS}\Delta x C_p(T_{co} - T_e))/t_c \tag{13}$$

where Q_{ref} denotes refrigerating power (kW), $\triangle x$ is the cycle adsorption quantity of adsorbent (kg/kg), M_{MTS} is the mass of the MTS (kg), the latent heat of vaporization of liquid ammonia (kJ/kg) is denoted by $L\,(T_{\text{e}})$, C_{p} stands for saturated liquid ammonia's specific heat capacity (4.7218 kJ/K kg), T_{e} and T_{c} are the evaporation temperature and cooling temperature, respectively ($^{\text{o}}$C), t_{c} is the cycle time of refrigerator (s).

The heating power is:

$$Q_{heat} = (M_{MTS}\Delta x \Delta H_{MTS} + M_{MTS}\Delta x \Delta H_{LTS})/t_c \tag{14}$$

where Q_{heat} is the heating power (kW),ΔH_{MTS} is the enthalpy difference of MTS reaction (kJ/kg), and ΔH_{LTS} is the enthalpy difference of LTS reaction (kJ/kg).

If refrigerant desorbs completely from the MTS reactor to the LTS reactor, refrigeration coefficient of performance (COP) is:

$$COP = Q_{ref}/Q_{heat} \tag{15}$$

Specific cooling power (SCP, W/kg) is:

$$SCP = Q_{ref}/M_{MTS}/(1+\varepsilon) \tag{16}$$

where ε is the mass ratio of MTS and LTS (kg/kg)

4 Results and Discussion

Figures 7, 8 and 9 show the simulation results of cooling capacity, SCP and COP. Among them, three situations are discussed as follows:Simulation 1 by using constant thermal conductivity and permeability, simulation 2 by using variable thermal conductivity and permeability in desorption and adsorption process and the experimental results.

For simulation 1, adsorption proceeds with the adsorption time and cooling capacity, and SCP first increases sharply then declines gradually. Correspondingly, the maximum cooling capacity and SCP for $CaCl_2$–$BaCl_2$–NH_3 is 2.56 kW and 156 W/kg, respectively, when desorption time is 15 min. Furthermore, time for the maximum values of SCP and cooling capacity happens between 1340 and 1360s as well as the highest value of COP is 0.17 at 1600s. Comparatively, maximum of

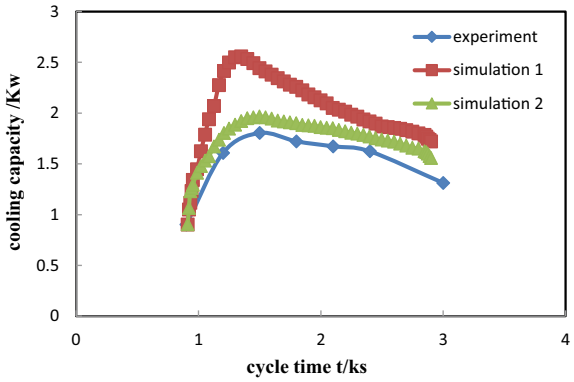

Fig. 7 Cooling capacity vs. cycle time for the desorption time of 15 min

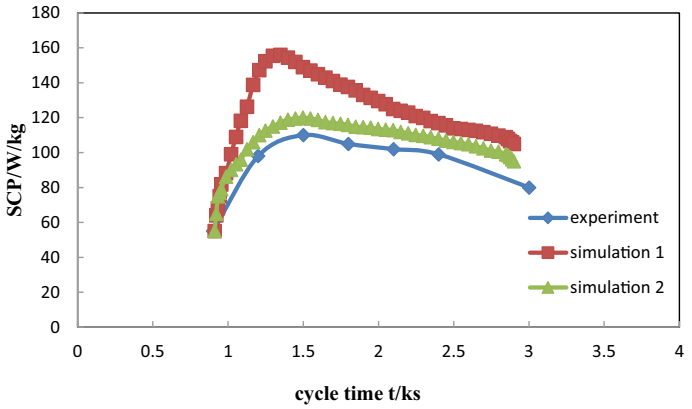

Fig. 8 SCP vs. cycle time for the desorption time of 15 min

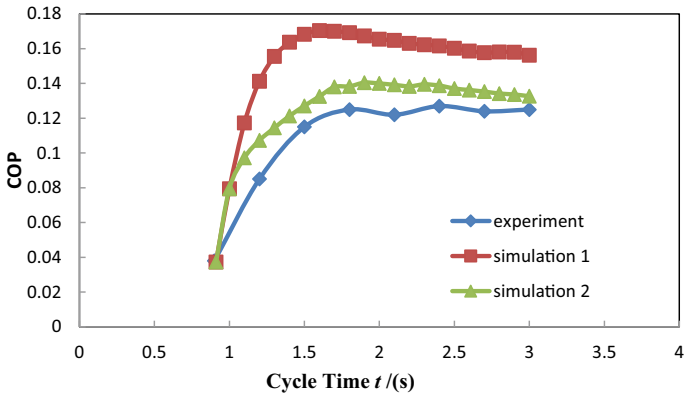

Fig. 9 COP versus cycle time for the desorption time of 15 min

cooling capacity and SCP for simulation 2 is 1.96 kW and 120 W/kg at 1497s as well as the highest value of COP is 0.14 at 1900s. Compared with the experimental results of maximum SCP, cooling capacity and COP, the SCP, cooling capacity and COP for simulation 2 increased by 9.1, 8.3 and 12%, while the results for simulation 1 increased by 42.8, 41.4 and 36%, separately. When considering the variable values of heat conductivity and permeability in the adsorption and desorption processes, adsorption refrigeration performance was considerably impacted. Constant thermal permeability and conductivity will cause the trend of excessive increment and less time for cooling capacity and SCP. Comparably, variable thermal conductivity and permeability will coordinate the refrigeration performance.

For simulation 2, the thermal conductivity takes the leading role that the SCP as well cooling capacity varies fast at the early period of time. Later, thermal conductivity varies slightly, meanwhile the permeability becomes lowering, which causes SCP and cooling capacity declines slowly. The time of the maximum values lags behind of the simulation 1, which will be closer to the real situation. Since the coordination for the variable thermal conductivity and permeability, COP is similar to that of SCP and cooling capacity.

5 Conclusions

This paper selected a two-stage refrigeration system as a case study to demonstrate the different impact under the conditions of using the constant and variable thermal conductivity and permeability for simulation, and the findings of the simulation are compared to the outcomes of the experiments. Conclusions are as follows:

(1) In the adsorption and desorption processes, thermal conductivity and permeability fluctuate dramatically, and this fluctuation has a major impact on the performance of an adsorption refrigeration system.
(2) Compared with the experimental results of two-stage refrigeration system, simulation 2 is more applicable and close to the real situation. The maximum of cooling capacity and SCP of $CaCl_2$–$BaCl_2$–NH_3 is 1.96 kW and 120 W/kg for the time of 1497 s. Besides, the highest value of COP is 0.32 at the time of 1900s. Constant thermal conductivity and permeability will cause the trend of excessive increment and less time for cooling capacity and SCP. Comparably, variable thermal conductivity and permeability will coordinate the refrigeration performance. For simulation 1, all the heat and mass transfer parameters are ensured that leads to faster trend of adsorption and desorption. For simulation 2, the thermal conductivity takes leading role that the SCP as well cooling capacity changes fast at the early period of time. Later, the thermal conductivity changes slightly, while the permeability becomes lower, causing SCP and cooling capacity decline slowly. The time of the maximum values lags behind of the simulation 1, which is in accord with the experimental variation better.

References

1. Meunier F, Poyelle F, LeVan MD (1997) Second-law analysis of adsorptive refrigeration cycles: the role of thermal coupling entropy production. Appl Thermal Eng 1743–55
2. Yumrutas R, Kunduz M, Kanoglu M (2002) Exergy analysis of vapor compression refrigeration systems. Exergy 2:266–272
3. Cortez LAB, Larson DL, Silva AD (1997) Energy and exergy evaluation of ice production by absorption refrigeration. Trans ASAE 40:395–403
4. Mauran S, Prades P, L'haridon F (1993) Heat and mass transfer in consolidated reacting beds for thermochemical systems. Heat Recov Syst CHP 4:315–319
5. Eun TH, Song HK, Han JH (2000) Enhancement of heat and mass transfer in silica-expanded graphite composite blocks for adsorption heat pumps: Part I. Characterization of the composite blocks. Int J Refrig 23:64–73
6. Wang LW, Tamainot-Telto Z, Metcalf SJ, Critoph RE, Wang RZ (2010) Anisotropic thermal conductivity and permeability of compact expanded natural graphite. Appl Therm Eng 30:1805–1811
7. Wang K, Wu JY, Wang RZ, Wang LW (2006) Effective thermal conductivity of expanded graphite-$CaCl_2$ composite adsorbent for chemical adsorption chillers. Energy Convers Manage 47:1902–1912
8. Freni A, Tokarev MM, Restuccia G, Okunev AG, Aristov Y (2002) Thermal conductivity of selective water sorbents under the working conditions of a sorption chiller. Appl Therm Eng 22:1631–1642
9. Li TX, Wang RZ, Kiplagat JK (2009) Performance study of a consolidated manganese chloride—expnaded graphite compound for sorption deep-freezing processes. Appl Energy 86:1201–1209
10. Zhong Y, Critoph RE, Thorpe RN, Tamainot-telto Z, Aristov Y (2007) Isothermal sorption characteristics of the $BaCl_2$–NH_3 pair in a vermiculite host matrix. Appl Therm Eng 27:2455–2462
11. Maggio G, Freni A, Restuccia G (2006) A dynamic model of heat and mass transfer in a double-bed adsorption machine with internal heat recovery. Int J Refrig 29:589–600
12. Tian B (2011) Experimental study on the permeability and thermal conductivity of compound adsorbent. Shanghai Jiao Tong University, Shanghai
13. SAC Standardization Administration of China, Thermal insulation—determination of steady-state thermal resistance and related properties—guarded hot plate apparatus (In Chinese). National Standard of China, GB-T, pp 10294–1988
14. Jiang L, Wang LW, Jin ZQ, Tian B, Wang RZ (2012) Permeability and thermal conductivity of compact adsorbent of salts for sorption refrigeration. ASME J Heat Trans 134:104503–104505
15. Wang J (2012) Experiments on adsorption performance and simulation on freezing system for $CaCl_2$-$BaCl_2$-NH_3 two-stage adsorption. Shanghai Jiao Tong University, Shanghai

Chapter 9
Combined Utilization of Inclined Fins and CNT Nanofluid on Thermoelectric Energy Conversion Performance in Channel Flow

Fatih Selimefendigil, Damla Okulu, and Hakan F. Öztop

Abstract In this study, the performance of the thermoelectric generator (TEG) module placed between two channels was analyzed by integrating fins inner the channels. The effects of parameters such as fin length and height and fin inclination angle on TEG output power were investigated. In the designed TEG system, water-based CNT nanofluid with a volume fraction of 0.02 nanoparticles was used as hot and cold fluid in the channels. Finite element method was used to investigate the effect of fin usage on the TEG output power features. In the results obtained, when the fins were used, enhancement of TEG output power was obtained. At Reynolds number of 1500, the TEG output power increased by about 10% when comparisons were made between the fin geometry and the model without fins. When CNT nanofluid under the same conditions was used, an increase of 7.23% was achieved as compared to pure water. Fin inclination angle did not show any significant enhancement on TEG output. By using combined utilization of fins and CNT-nanofluid, an increase of approximately 12% power generation was obtained at Re = 1500 Reynolds as compared to the case without the fin.

Keywords Thermoelectric conversion · Nanofluids · Fins · Finite element method · Computational fluid dynamics

1 Introduction

Researchers seeking solutions for the energy crisis that may cause major problems for the coming years, are working to expand the applications of clean energy resources and to use energy resources in the most effective way, taking into account caused to the environment damage by existing fossil resources. Renewable energy

F. Selimefendigil · D. Okulu
Department of Mechanical Engineering, Manisa Celal Bayar University, Manisa, Turkey

H. F. Öztop (✉)
Department of Mechanical Engineering, Technology Faculty, Fırat University, Elazığ, Turkey
e-mail: hakanfoztop@firat.edu.tr

D. Tripathi et al. (eds.), *Advancements in Nanotechnology for Energy and Environment*,
Advances in Sustainability Science and Technology,
https://doi.org/10.1007/978-981-19-5201-2_9

technologies have created solutions to problems in many aspects in the applications of clean resources, and their unlimited use has intensified research on these technologies. Renewable energy technologies, which generally benefit from natural resources such as wind and sun, offer us different designs. These technologies, which have many advantages such as being unlimited and clean, have disadvantages such as being costly and difficulties in installation which increase the importance of alternative applications.

Systems where thermoelectric energy conversions take place in the searches for alternative sources appear as promising applications. Thermoelectric devices, which can be designed as coolers and generators by applying the principles of thermoelectric effects, tend to solve some problems that exist in other clean energy technologies. They directly convert electrical energy into heat energy with the dominance of the Peltier effect or directly into electrical energy with the dominance of the Seebeck effect [1–4]. Thermoelectric devices attract attention with their features such as being able to be designed in desired dimensions and not requiring much maintenance and repair as steady-state devices [5, 6]. Among these devices, which are used in many fields, especially thermoelectric generators have taken their place in a wide range. The biggest drawback of these systems is that generally their efficiency values are around 5–8%. Although there are various approaches to overcome this negative situation, their low efficiency still poses a major problem for these devices. The geometries and materials of the designed thermoelectric devices allow us to determine their performance, and studies are being made to obtain they that work with optimum efficiency with the changes in these parameters. It is essential to establish the temperature difference in both Peltier (cooler) and Seebeck (generator) devices and possible to design various systems as heat source and heat sink to create this temperature difference. Improvements in heat transfer properties of heat sinks and heat sources should be considered due to the temperature difference included in the performance evaluation of thermoelectric devices. Gases for the recovery of waste heat, natural heat provided by solar energy, chemical reactions or systems that occur through fluids can be used to occur the temperature difference. Thermoelectric systems, which are designed by means of hot and cold fluids, which function as heat exchangers, are among the systems mentioned, and they inspire researchers by taking place in the literature with different combinations. Studies in which nanofluids are integrated into thermoelectric systems have resulted in a significant increase in performance when compared to the results obtained with conventional fluids.

Nanofluid, another clean technology, can be briefly defined as the suspension of nano sized solid particles in base fluid [7, 8]. It is known that solid materials such as metal and metal oxide generally have superior thermal properties compared to conventional working fluids [9, 10]. The idea of nanofluid that emerged in line with this approach is an innovative fluid type obtained with conventional fluid and solid particle with higher thermophysical properties. With the development of their thermophysical properties, the increase in heat transfer performance has enabled the use of nanofluids in thermoelectric generators (TEG). There are various studies on TEG-nanofluid systems in the literature. For example, Selimefendigil et al. [11] designed the TEG-corrugation system, which included Ag/MgO nanofluid, and examined the

improvement in TEG performance. They considered the hybrid nanofluid in different parameters such as volume fraction (0–0.02) and Reynolds number (250–1000). They observed an increase in the output power of the TEG module with increasing Reynolds number and volume fraction. While the solid particle volume fraction was 0.02, they found the TEG output power of 250 and 1000 Reynolds numbers to be 7.50 and 10.95%, respectively. Kolahan et al. [12] conducted a study in which they compared the water-based Al_2O_3 nanofluid TEG-PVT system with the conventional PVT system. 0.2 wt% water-based Al_2O_3 nanofluid was used as the cooling fluid. The TEG-PVT system produced almost the same amount of electrical power as the conventional PVT system. On the other hand, the electrical energy efficiency ratio resulted in an improvement in the range of 2.5–4% in the TEG-PVT system compared to the conventional PVT. In another study, Selimefendigil et al. [13] included the water-based CNT nanofluid in the TEG system and examined the effects of the pulsating flow form on this system. They investigated the TEG output power in the volume fraction (0–0.04) and Reynolds number (250–1000) parameters for the water-based CNT nanofluid and also observed the effect of pulsating flow amplitude (0.25–0.95) and frequency (Strouhal number: 0.01–0.1) on the output power. In the pulsating flow form, TEG output power resulted in an increase of 28.5% when they compared at the highest and lowest Reynolds numbers. In their comparison of the highest and lowest pulsation amplitudes, they observed an increase of 7.4 and 24.4% in TEG output power for water and 0.04 volume fraction nanofluid, respectively. Karana et al. [14] designed a TEG system for waste heat recovery and using SiO_2, ZnO nanofluid and EG-W as coolant, performance of the system was comparatively examined. SiO_2 nanofluid provided an increase in conversion efficiency and electrical power by 11.39 and 11.80% compared to EG-W when the exhaust inlet temperature was at 500 K. The ZnO nanofluid increased the TEG output power by 9.86% compared to the EG-W fluid. They calculated the conversion efficiency for SiO_2 and ZnO nanofluids as 5.864 and 5.442%, respectively, at the optimum volume concentration (7%) for nanofluids. Selimefendigil et al. [15] integrated TEG into branching channels and used Fe_3O_4/nanodiamond hybrid nanofluid (volume fractions of particles 0–0.2%) as heat transfer fluid. Considering the analysis results ($Re_1 = 1000$, $Re_2 = 200$) in different branching channel configurations, the TEG output power showed a 15.5% increase in the case of only the upper branching channel and 33% in the case of both branching channels.

The use of fins can be suggested as a different approach to increase the heat transfer performance of the heat source and heat sinks in the TEG system. In previous studies, fins of different designs caused enhancements in heat transfer performance and accordingly allowed increases in TEG performance. Kim et al. [16] investigated the effect of using fins on heat transfer in a TEG system. When they evaluated the simulation results for the optimum fin design, they observed that the fin thickness of 2.5 mm provides the maximum heat transfer rate for the system they designed for the maximum temperature allowed for TEMs at 473 K. However, when they consider not only the heat transfer performance but also the parameters such as the material used and the pressure drop, they saw the suitability of the 2 mm fin design. When they examined the maximum temperature values on the profiles, they found 425, 447,

462, and 470 K for 1, 1.5, 2, and 2.5 mm fin thickness, respectively. Cao et al. [17] designed a TEG system with 36 TEMs for exhaust gas recovery. They also added a heat pipe (HP) to this system for the improvement of heat transfer. They observed that the optimum values for the TEG-HP system were reached with an angle of 15° at a depth of 60 mm. In this system, in which they also included the fin, they reached an open circuit voltage of 5.21 V with the use of fins at a depth of 60 mm. This value showed an increase of 43% compared to the without fin system. Using the fin, they have reached an output power of about 0.38 W with an increase of 105% for each TEM. Seo et al. [18] integrated an inclined finned hot heat exchanger into the TEG system and analyzed the electrical and thermal performance of this system they designed using the Taguchi method. In determining the system performance, parameters such as design (D), gap between fins (G), flow rate (M), and hot gas inlet temperature (T) are taken into account. In the results of the analysis, they observed that the combined effect of the pressure drop and temperature difference of the fin gaps in the TEG system corresponds to 11.03% of the total effect. They calculated that the fin gap parameter has a ratio of 11.93% of the total effect in the combined effect of maximum power and conversion efficiency of the system. Liu et al. [19] used fins to improve the heat exchanger performance in the TEG system. In the system they designed, the fins were evaluated in five different parameters (fin angle, internal distance, height, length, and fin thickness). They observed that among the fin parameters, the fin height, which provided a 34% increase, had the most significant effect on the average temperature rise. They determined that the fin spacing distance was the best parameter on the pressure drop decrease. It was with the fin angle that the longitudinal temperature difference was significant, resulting in a reduction. As a result of the optimization of these parameters, the longitudinal temperature difference was reduced from 29.36 to 28.9 °C, and the average temperature difference was increased from 222.46 to 226.4 °C. He et al. [20] investigated the effect of flat fin heat exchanger on TEG performance. They considered the effects of fin height, spacing, and thickness. TEG output power was calculated at 40% (A), 60% (B), and 80% (C) engine loads. By increasing the fin thickness from 0.3 to 1 mm, TEG output power increased by 10.4, 14.1, and 20.3 W at A, B, and C engine loads, respectively. When they increased the fin spacing from 0.5 to 3.1 mm, Q_h decreased by 3358, 5132, and 6753 kW and output power of 103.9, 130.3 and 179.0 W, respectively, at engine loads A, B, and C, respectively.

The aim is to use nanofluids with TEG mounted in channel. In order to enhance the heat transfer and thermal transport properties, which depends on the thermophysical properties of the solid particles that will form the nanofluid, nanomaterial selection will be important. We consider the thermal performance of nanofluids in parallel with the thermal conductivity value of the materials used, which leads us to carbon-based nanofluids with high thermal conductivity. In this study, water-based carbon nanotube (CNT) nanofluid, which is known to have higher thermophysical properties, was used. In addition, fins were placed in the channel where the fluid streams take place for better thermal transport and their effects on the TEG output power were examined.

2 Numerical Model

The thermoelectric (TE) phenomenon, which entered our lives with Seebeck's discovery, was developed with the work of Peltier and Thomson, and paved the way for the design of devices that can directly transform energy with the working approach of these three main TE effects. TEGs, one of these devices, enable the generation of electrical energy from heat energy with the help of TE effects, especially the Seebeck effect [21]. Seebeck effect is basically a TE phenomenon, which states that we can generate electric potential called Seebeck electromotive force (Seebeck voltage) in the presence of temperature difference [22, 23]. Seebeck coefficient (α) and temperature (T) are used to calculate the produced Seebeck electromotive force (e_{emf}) [24]:

$$e_{emf} = -\alpha \nabla T \tag{1}$$

The ratio of the electric potential difference to the temperature difference allows us to obtain the Seebeck coefficient [25]:

$$\alpha = -\frac{\Delta V}{\Delta T} \tag{2}$$

Thermoelectric modules (TEMs) are used in the design of thermoelectric generators (TEG), which enables the electric potential to be produced by the Seebeck effect. TE legs (p and n type), electrodes, and ceramic plates (cold and hot side) are used to build the TEG module [26, 27]. The TE legs, where energy conversion takes place, are electrically connected in series and thermally in parallel. Although different material classes are used for TE legs, semiconductor materials are the most preferred materials in the design of these legs. The most important reason for this situation is that the figure of merit (Z) value of the material forming the TE legs is an important criterion. Z should have a high value, allowing us to determine the energy conversion efficiency of both thermoelectric coolers (TECs) and TEGs [28, 29]. The thermophysical properties of the material are used to determine the temperature-dependent figure of merit (ZT) value [30]:

$$ZT = \frac{\alpha^2 \sigma}{k} T \tag{3}$$

where σ is electrical conductivity and k is thermal conductivity of the material. In the equation, $\alpha^2\sigma$ represents the power factor [31]. For the TE material to be defined as high quality, the power factor must be at a high value. It is desirable that the thermal conductivity value, which is another parameter, is low. Considering these factors, semiconductor materials perform thermoelectric energy conversion with higher efficiency than other materials. The point that draws attention here is the difference in

the temperature ranges in which semiconductor materials exhibit maximum performance. In the design of TE devices, SiGe (silicon germanium), Bi_2Te_3 (bismuth telluride), and PbTe (lead telluride) are the material group that we can call the conventional TE materials that are often preferred [32–34]. SiGe generally achieves high performance values at high temperatures, PbTe at medium temperature ranges and Bi_2Te_3 at room temperatures. Conductive materials are included in TEM since the electrodes that provide the electrical connection of the TE legs must have high electrical conductivity. Finally, the TE leg-electrode component is clamped between two ceramic plates and the necessary insulation is provided. In the TEG module designed in this way, in temperature difference created by the heat source and the heat sink, Seebeck open circuit (V_{oc}) voltage is produced when other thermoelectric effects and thermodynamic processes accompanied the Seebeck effect [35]. Equation 4 is obtained by adapting the Seebeck electromotive force to the open circuit voltage [36].

$$V_{oc} = \alpha \cdot \Delta T = \left(\alpha_p - \alpha_n\right)\Delta T \tag{4}$$

TE legs have different Seebeck coefficients, and α_p represents Seebeck coefficient of the p-type semiconductor leg, while α_n is Seebeck coefficient of the n-type semiconductor legs. The temperature applied to the system by the heat source and the heat sink is expressed by T_h and T_c, respectively. In TEG, if the TEMs in contact with the heat source (T_h) and the heat sink (T_c) are connected to an external load resistance [37], we can observe that load current flow occurs in the closed circuit (Fig. 1). With the existence of current flow, electric potential and accordingly TE power generation are realized. The load resistance R_l, internal resistance and open circuit voltage (V_{oc}) are used to calculate the electrical potential (V) produced by TEG [38]:

$$V = \frac{V_{OC} R_l}{R_l + R_i} \tag{5}$$

Electrical resistances and geometries of the TE legs and electrodes designed in the internal resistance calculation of the TEG module are important parameters. In addition to the material selection, attention should be paid to the TEM geometry. If the height of the TE legs and electrodes is expressed as h, their cross-sectional area A, and their electrical resistance γ, the internal resistance of the TEG module is [39]:

$$R_i = \frac{h_p \gamma_p}{A_p} + \frac{h_n \gamma_n}{A_n} + 2\frac{h_c \gamma_C}{A_C} \tag{6}$$

Very small amounts of voltage are produced with a single module, so multiple TEMs are used to increase the voltage value produced by the TEG [40]. The determined internal resistance calculation is valid for a single TEG module, and this value is calculated for multiple modules by multiplying the number of modules with Eq. 6. By defining the voltage value produced by the TEG with Ohm's law (Eq. 7), we can

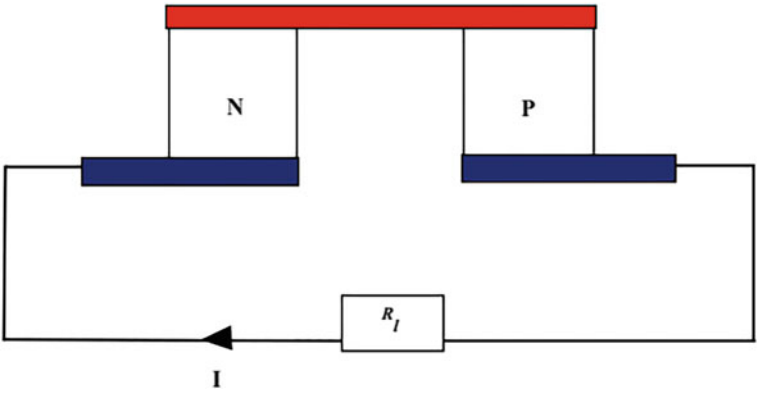

Fig. 1 TEG module connected to an external load

also determine the current value produced [41]. Likewise, the TEG output power (Eq. 8) can be calculated by Joule heating law [42].

$$I \cdot R_l = \frac{V_{OC} R_l}{R_l + R_i} \tag{7}$$

$$P_{\text{out}} = I^2 \cdot R_l \tag{8}$$

To calculate the TEG output power, the amount of heat obtained by the heat transfer mechanisms on the hot and cold side can also be used. Earlier, we stated that although we basically base TEG on the Seebeck effect, we also consider other TE effects and thermodynamic processes. In particular, the Peltier effect, Joule effect and Kelvin relations are taken into account in calculating the amount of heat absorbed and released from the system [43]. Q_h is the amount of heat entering the system from the external source and Q_c is the amount of heat released from the cold side, and they are obtained by the following equations [44, 45]:

$$Q_h = k_{tot} \Delta T + \alpha_{tot} T_h I - \frac{1}{2} I^2 R_i \tag{9}$$

$$Q_c = k_{tot} \Delta T + \alpha_{tot} T_c I + \frac{1}{2} I^2 R_i \tag{10}$$

k_{tot} and α_{tot} represent the total thermal conductivity and Seebecek coefficient values, respectively. Using the Eqs. 9 and 10, the TEG output power is obtained by Eq. 11.

$$P = Q_h - Q_c = \alpha_{tot} I (T_h - T_c) - I^2 R_i \tag{11}$$

In the designed model, TEG consists of a total of 80 TEMs, TE legs have a cross-sectional area of 4 mm^2 and height of 2.5 mm. Figure 2 presents the heights of the materials that make up the TEM and the designed TEG. Bismuth telluride leg, copper electrode, and alumina ceramic plate are used. Thermophysical properties of these materials are given in Table 1. TEG with the mentioned features is placed between two channels where hot and cold fluid stream takes place. Nanofluid was used to compose the temperature difference of the system, at different Reynolds numbers. The fins used to enhance the heat transfer of the system are mounted on the inner channel walls at different angles (Fig. 3).

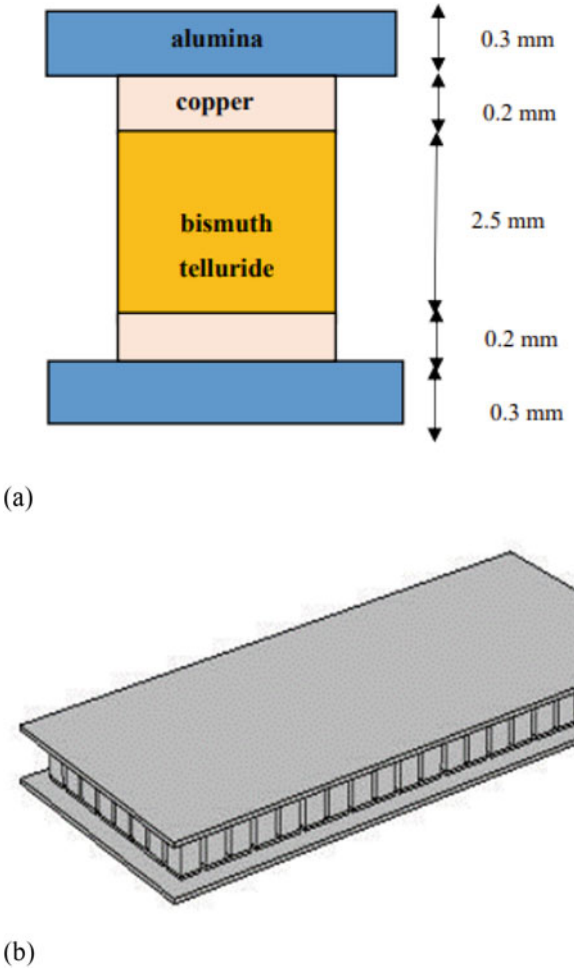

Fig. 2 TE dimensions (**a**) and TEG module (**b**)

Table 1 Properties of the materials that build TEG [46]

Material properties	p type (Bi_2Te_3)	n type (Bi_2Te_3)	Cu (electrode)	Al_2O_3(alumina)
k (W/K m)	1.6	1.6	400	27
α (V/K)	2.1×10^{-4}	-2.1×10^{-4}	6.5×10^{-6}	–
σ (S/m)	0.8×10^{5}	0.8×10^{5}	5.9×10^{8}	–
ρ (kg/m^3)	7700	7700	8960	3900
C_p(J/kg K)	154	154	385	900

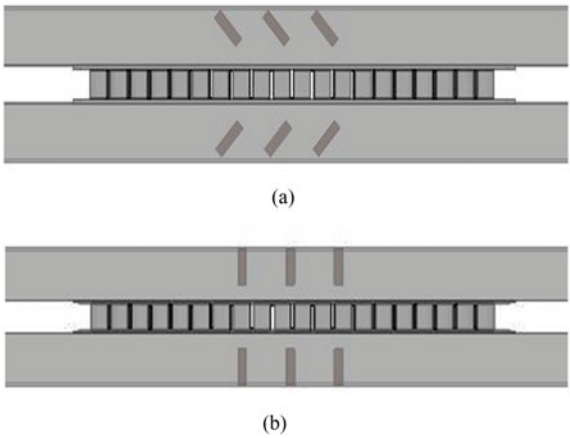

Fig. 3 Installation of fins designed in the same dimensions **a** at 45° angle, **b** in upright position

2.1 Nanofluid Property Equation

The thermal performances of the working fluids in engineering systems also affect the system performances. The search for alternative fluids with higher performance to the conventional fluids that have served as the working fluid for these systems for a very long time has become stronger. The nanofluid idea, which came to the fore in this search, has been applied to engineering systems, allowing favorable developments on performance. The nanofluid, which is basically a combination of the base fluid and nano-sized solid particles, contributes to the enhancement of heat transfer with its high thermal performance properties. The differences in the thermophysical properties of both fluids and solid particles will lead to different properties of the designed nanofluids. Since the aim is to provide high thermal properties, the select of material to form the nanofluid is important. At this point, carbon-based nanofluids, which have been the subject of many research in recent years, have made a difference in energy systems. In particular, both the advantage of carbon's high thermal conductivity and their special geometric designs have made carbon nanotube (CNT)-based nanofluids a rising trend by separating them from most nanofluids. The water-based CNT nanofluid, which was also used in the TEG system before, allowed the performance of the system to improve. In the system we designed, water-based CNT

Table 2 Water and SWCNT particle properties [47]

Material properties	Water	SWCNT (single-walled CNT)
k (W/K m)	0.61	2600
C_p(J/kg K)	4179	425
ρ (kg/m^3)	997.1	6600
μ (kg/m s)	8.55×10^{-4}	–

nanofluid contributed to the formation of temperature difference, and the material properties of water and CNT are given in the Table 2 in the calculation of their thermophysical properties. Using the material properties in Table 2, where ∅ is the particle volume fraction, the thermophysical properties of the water-based CNT nanofluid are obtained with the following equations [48–50].

Thermal conductivity:

$$\frac{k_{nf}}{k_f} = \frac{(1-\emptyset) + 2\emptyset \frac{k_p}{k_p - k_f} \ln \frac{k_p + k_f}{2k_f}}{(1-\emptyset) + 2\emptyset \frac{k_f}{k_p - k_f} \ln \frac{k_p + k_p}{2k_f}} \tag{12}$$

Density:

$$\rho_{nf} = (1-\emptyset)\rho_f + \emptyset\rho_p \tag{13}$$

Specific heat capacity:

$$\left(\rho C_p\right)_{nf} = (1-\emptyset)\left(\rho C_p\right)_f + \emptyset\left(\rho C_p\right)_p \tag{14}$$

Dynamic viscosity:

$$\mu_{nf} = \frac{\mu_f}{(1-\emptyset)^{2.5}} \tag{15}$$

2.2 *Governing Equation*

Equations regulating multidimensional temperature and electric potential profiles are developed by taking into account the coupling mechanisms of TE effects (Seebeck, Peltier, and Thomson) in TE materials under steady-state conditions and in the absence of an applied magnetic field [51]. The energy conservation equation for solid domain can be expressed by the Joule heating effect, which includes Fourier's law. The developing equations for TEG analysis are expressed as follows [43, 52, 53]:

$$\nabla\left(k_i \nabla T\right) + \frac{J^2}{\sigma} - TJ \cdot \nabla\alpha = 0 \tag{16}$$

The thermoelectric effect application of electric charge and heat flow is expressed by the continuity equations:

$$\nabla \cdot J = 0 \tag{17}$$

$$E = \sigma \cdot J + \alpha \nabla T \tag{18}$$

$$q = \Pi J - k \nabla T \tag{19}$$

where defines J current density, E electric field, Π Peltier coefficient and q heat flux vector. Current density, and Peltier coefficient relations are:

$$J = \sigma(E - \alpha \nabla T) \tag{20}$$

$$\Pi = \alpha T \tag{21}$$

E obtained in relation to V:

$$E = -\nabla V \tag{22}$$

Continuity, momentum and energy equations for fluids in channels:
Continuity:

$$\nabla \cdot (u) = 0 \tag{23}$$

Momentum:

$$\rho(u \cdot \nabla)u = \nabla\left[-p + \mu\left(\nabla u + (\nabla u)^T\right) - \frac{2}{3}\mu(\nabla \cdot u)l\right] + F \tag{24}$$

Energy:

$$\rho_\mu C_p u \cdot \nabla T + \nabla \cdot (-k \cdot \nabla T) = Q \tag{25}$$

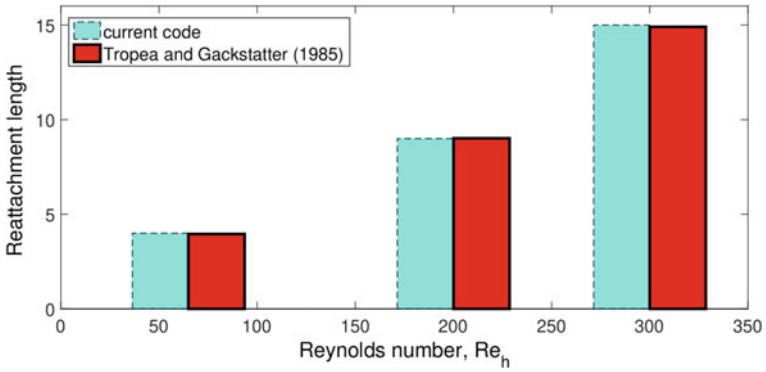

Fig. 4 Code validation: Reattachment length comparisons behind a block in channel with the available values in Ref. [54] (l = 2H, h = 0.25H, l = 20 mm)

2.3 Solver

Galerkin weighted residual finite element is used as the solution technique. Field variables of interest in the channel and TEG domain are approximated by using Lagrange FEs of different orders. When they are used in the governing equations, residual will be obtained. A weighted average of the residual is set to be zero by using weight function (W) as:

$$\int WRdV = 0 \tag{26}$$

Artificial diffusion with the streamline upwind Petrov–Galerkin method (SUPG) is considered for handling the local numerical instabilities, while biconjugate gradient stabilized iterative method (BICGStab) is used. A convergence criterion of 10^{-8} is utilized while for time-dependent part, a variable-order backward differentiation formula (BDF) is considered. Grid independence of the solution is assured by using different number of elements. A grid size with 1,516,714 number of elements is used with refinements in the vicinity of the wall regions and interfaces to resolve higher gradients in those zones. The numerical code is validated by using the results of Ref. [54], where flow separation behind a block mounted in a channel was analyzed experimentally. Figure 4 shows the comparisons of reattachment length for different Reynolds numbers. Highest deviation below 1% is obtained between the results.

3 Results and Discussion

In this study, the temperature difference required for TEG electric potential generation is created by the flow of hot and cold fluids in the channel. The heat transfer

performance of fluids acting as heat exchangers is one of the effective parameters for TEG electric potential generation. Water-based CNT nanofluid (volume fraction of nanoparticle 0.02), which has been used in TEG systems before and achieved successful results, was chosen as the fluid. The CNT nanofluid and water entered the channels at a cold temperature of 293.15 K and a hot temperature of 323.15 K. Fluids evaluated at various Reynolds numbers (100–1500) enter the channel while both water and nanofluid are considered. To enhance the thermal transport of this TEG system, fins were placed in the channels. Parameters such as fin length, height, and fin angle are considered and its effect on TEG output power is investigated. Copper is used as the material in the fin design. The fins with the size of $1 \times 1 \times 1$ mm were mounted on the walls inside the channel at 45° angles. The fins were used three pieces each in the upper and lower channels, and the distance between the fins was determined as 6 mm. In this model, where $\mathrm{Re} = 1000$ water-based CNT nanofluid flow is realized through channels, TEG electric potential generation is approximately 0.843 V and TEG output power is 0.591 W. When the fin height was evaluated in the range of 1–3.5 mm in the model, it had a positive effect on the TEG output power. But at 3.5 mm fin height, TEG output power increased by 2% and reached 0.602 W with CNT nanofluid. Figure 5 shows the effect of fin height on TEG output power with a Reynolds number of 1000 for water-based CNT nanofluid and water. Considering the case where the fin is not applied, electric potential produced by the water-based CNT nanofluid with a volume fraction of 0.02 is found to be 0.828 V and the TEG output power was 0.571 W. When the fins with $1 \times 1 \times 3.75$ mm geometry are mounted on the walls inside the channel with the same inclination angle and fin spacing, 0.869 V electrical potential and 0.63 W TEG output power are obtained at Reynolds number of 1500 for water-based CNT nanofluid. The increase in the TEG power results from the higher local velocity due to the presence of the fins near the TE interface while further performance increment is obtained by adding CNT nanoparticles in water.

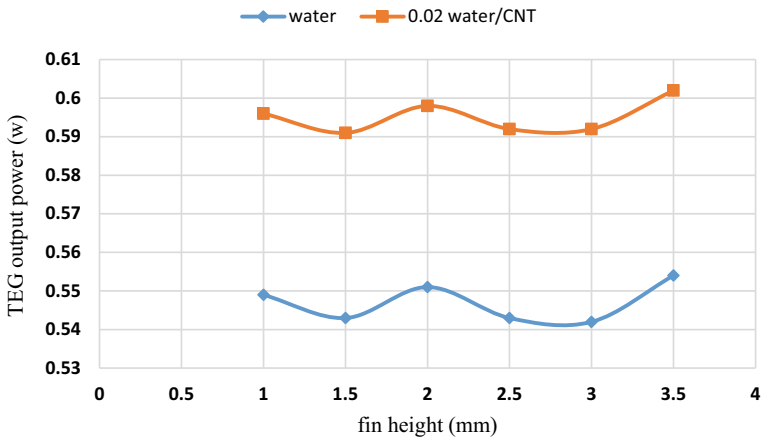

Fig. 5 TEG output power dependent on fin height

Figure 6 shows the voltage values obtained with CNT nanofluid at Re = 1500 in case of channel with fin and without fin. In the 1 × 1 × 3.75 mm geometry model, the electric potential produced at Re = 750 for water and water-based CNT nanofluid was calculated as 0.802 and 0.823 V, respectively, while the TEG output power was calculated as 0.516 and 0.564 W, respectively. Figure 7 presents the electrical potential and output power generated at varying Reynolds numbers in the TEG system using water and water-based CNT nanofluid.

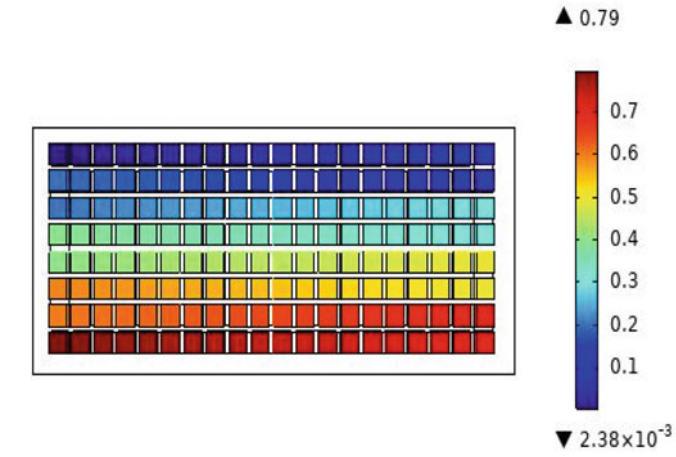

(a) water

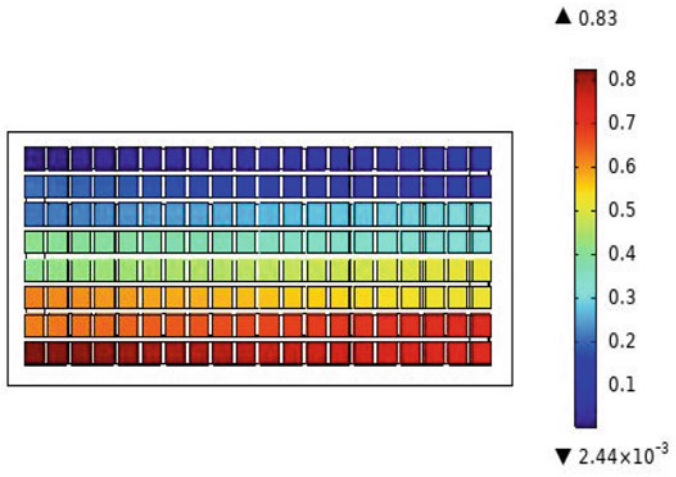

(b) water-based CNT nanofluid

Fig. 6 TEG voltage values obtained with non-fin (**a**, **b**) and fin-used (**c**, **d**) channels

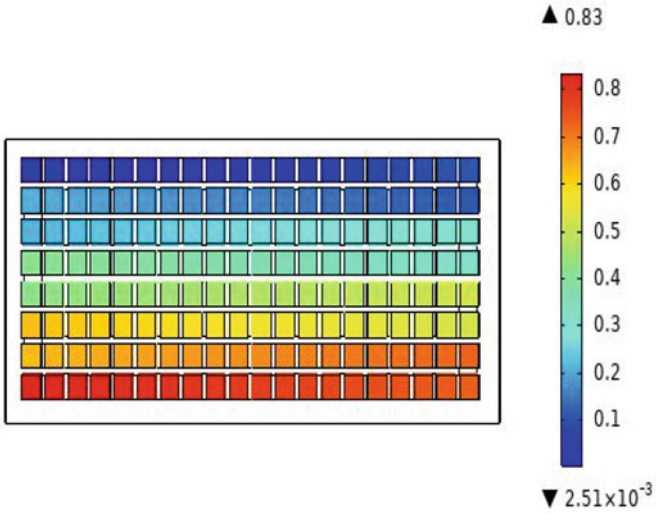

(c) water

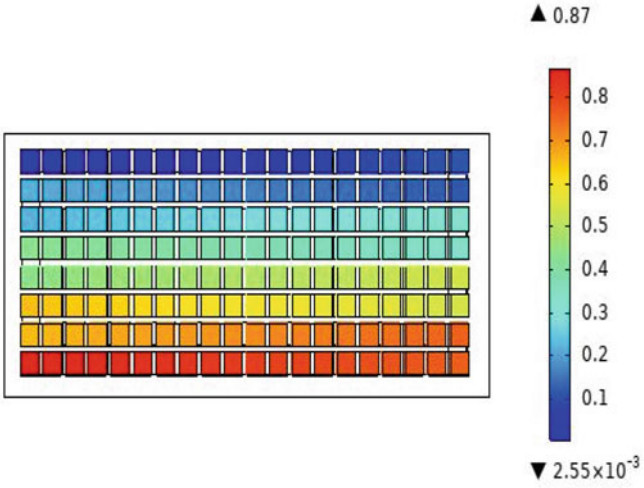

(d) water-based CNT nanofluid

Fig. 6 (continued)

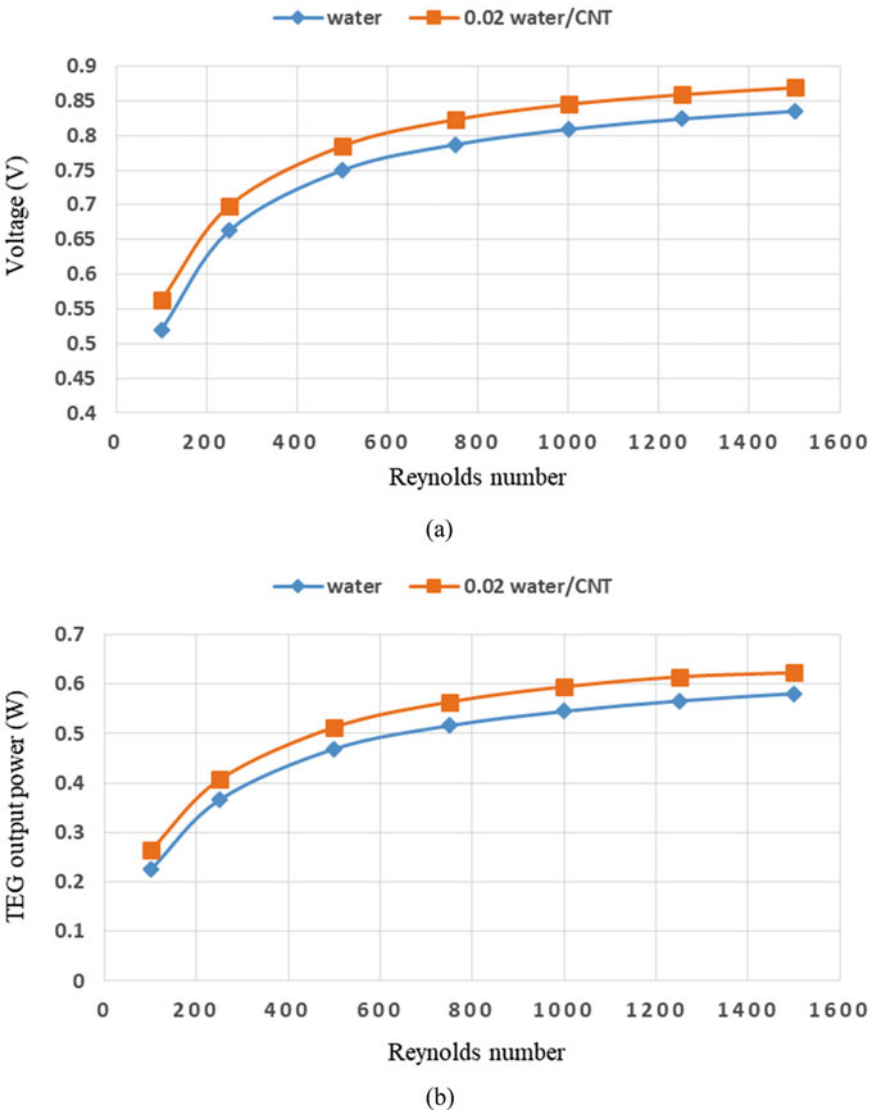

Fig. 7 Voltage (**a**) and TEG output power (**b**) obtained with water and water-based CNT nanofluid dependent on Reynolds number in 1 × 1 × 3.75 mm fin model

A slight increase in TEG electric potential occurs when the length of the fins is increased from 1 to 4 mm. When fins with 1 × 4 × 3.75 mm geometry are placed at an angle of 45°, TEG electric potential of 0.872 V was calculated with CNT nanofluid at Re = 1500 When the fins with the same geometry are given an angle of 30° and 60°, the electric potential values of 0.87 and 0.873 V, respectively, are reached. On the other hand, the highest electric potential value of 0.875 V was calculated by placing

the fins perpendicular to the inner channel walls. Higher TEG output power values were achieved with the fins placed in the vertical position, and the output power was calculated as 0.638 W at Re = 1500. When the fins are placed along the depth in the channel under the same conditions with the water-based CNT nanofluid, the TEG electrical potential and output power were 0.88 V and 0.6453 W, respectively, and the placement positions of the fins influences the TEG output power. Figure 8 shows the electrical potential and temperature distribution obtained with CNT nanofluid in models with fins placed along the length and depth in the channel. When water was used instead of nanofluid, 0.841 V electric potential and 0.589 W output power were obtained. With the CNT nanofluid, an increase of 4.6 and 8%, respectively, is achieved in electric potential and output power compared to water. Figure 9 presents the TEG output power obtained at various Reynolds numbers with water and nanofluid in the 1 × 4 × 3.75 mm design fin model placed along the channel depth. In the presence of fins, using CNT-nanofluid brings performance enhancement for TEG system for all Reynolds numbers. At Re = 100, the increment amount is 9.4%, while at Re = 1500, it is obtained as 8.3%.

4 Conclusions

The performance of TEG, which is mounted on the walls of two channels where hot and cold fluid streams were applied, was evaluated with the fins included in the system. The effect of the fins placed on the inner walls of the channels on the system was explored. The fin used system was analyzed with water-based CNT nanofluid. An increase in TEG output power was observed with the increase in fin height. Fin thickness and length of 1 mm, considering the fin heights in the range of 1–3.5 mm, an increase of 2% on the TEG output power was achieved in case of going from the lowest height to the highest height with CNT nanofluid (Reynolds number is 1000 and the nanoparticle volume fraction is 0.02). When 1 × 1 × 3.75 mm three fins were placed on the inner channel wall at 45° angles and upright position, the TEG electrical potential increased by 5 and 5.3%, respectively, with water-based CNT nanofluid (with Re = 1500) compared to the case where without fin. At Reynolds number of 750, 1 × 1 × 3.75 mm three fins model, TEG output power increased by about 9% with water-based nanofluid compared to pure water. With the optimization of the fin length and height, an increase of approximately 12% was obtained with the CNT nanofluid at Re = 1500 by using the 1 × 4 × 3.75 mm fin design, compared to the case without fin. In this case, when water is used instead of CNT nanofluid, an increase of 10% was obtained compared to the model without fin. The use of fins influenced the TEG output power. By using appropriate fin geometry optimization and material, further enhancement of TEG output power may be possible.

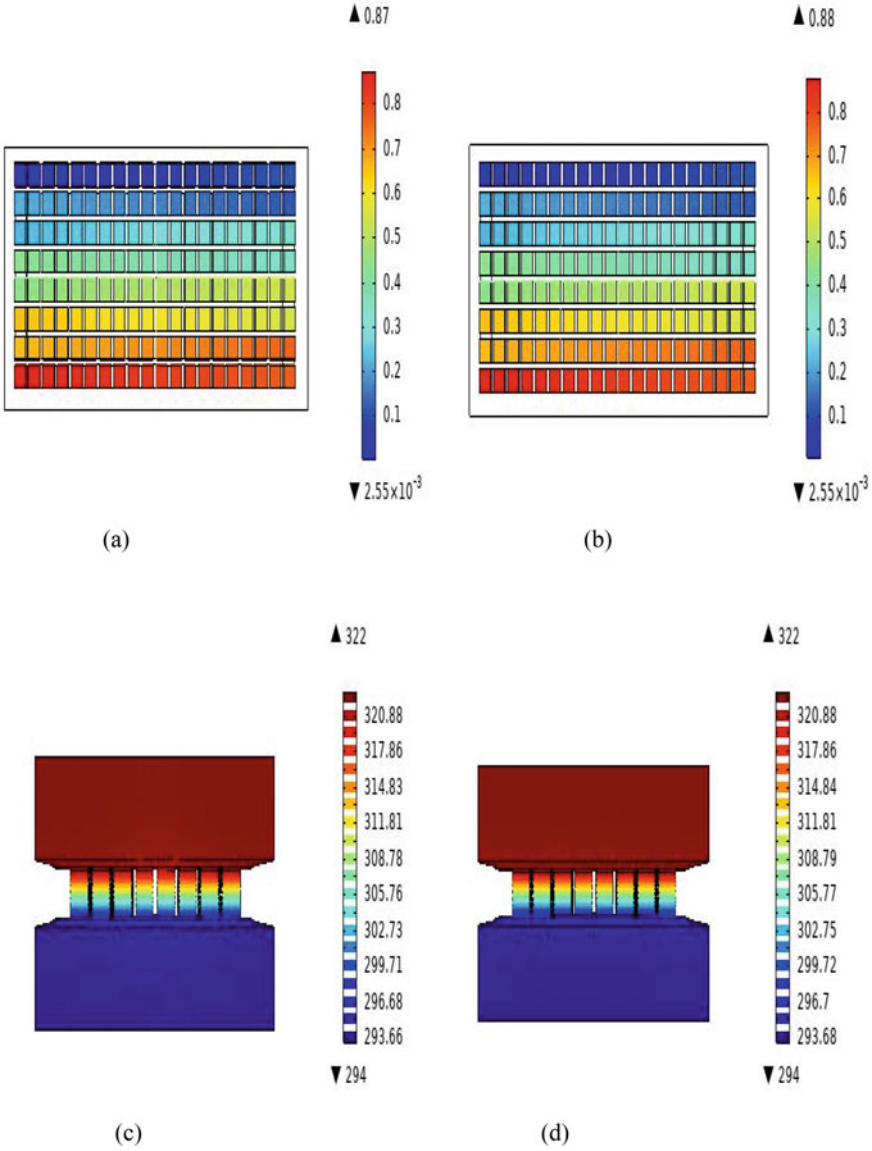

Fig. 8 The electric potential (**a**) and temperature distribution (**b**) obtained by placing the fins along the length of channel, electric potential (**c**) and temperature distribution (**d**) by placing the fins along the depth of channel

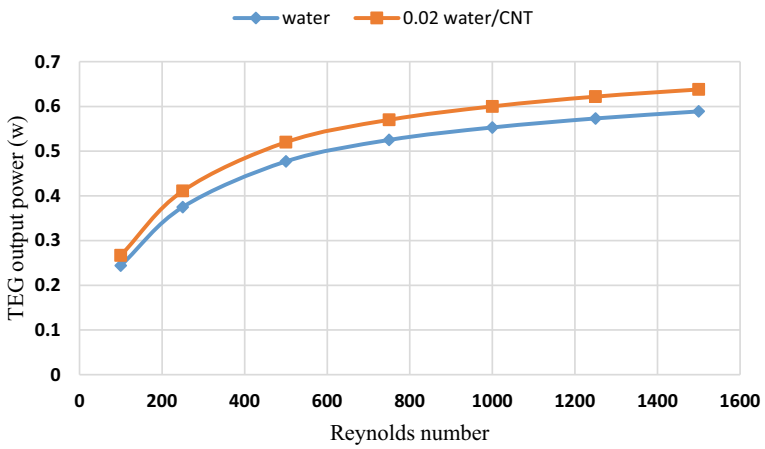

Fig. 9 TEG output powers obtained at various Reynolds numbers with the 1 × 4 × 3.75 mm finned model placed along the channel depth

References

1. Hewawasam LS, Jayasena AS, Afnan MMM, Ranasinghe RACP, Wijewardane MA (2020) Waste heat recovery from thermo-electric generators (TEGs). Energy Rep 6:474–479
2. Liu J, Zhang Y, Zhang D, Jiao S, Zhang Z, Zhou Z (2020) Model development and performance evaluation of thermoelectric generator with radiative cooling heat sink. Energy Convers Manag 216:112923
3. Qiu C, Shi W (2020) Comprehensive modeling for optimized design of a thermoelectric cooler with non-constant cross-section: theoretical considerations. Appl Therm Eng 176:115384
4. Gong T, Gao L, Wu Y, Tan H, Qin F, Ming T, Li J (2019) Transient thermal stress analysis of a thermoelectric cooler under pulsed thermal loading. Appl Therm Eng 114240
5. Lyu Y, Siddique ARM, Majid SH, Biglarbegian M, Gadsden SA, Mahmud S (2019) Electric vehicle battery thermal management system with thermoelectric cooling. Energy Rep 5:822–827
6. Jimenez Aispuro JE, Bédécarrats J-P, Gibout S, Champier D (2019) Description of a 3D transient model to predict the performance of an experimental thermoelectric generator under varying inlet gas conditions. Mater Today Proc 8:632–641
7. Behi M, Shakoorian M, Mirmohammadi SA, Behi H, Rubio JI, Nikkam N et al (2019) Experimental and numerical investigation on hydrothermal performance of nanofluids in micro-tubes. Energy 116658
8. Tassaddiq A, Khan I, Nisar KS (2020) Heat transfer analysis in sodium alginate based nanofluid using MoS2 nanoparticles: Atangana-Baleanu fractional model. Chaos Solitons Fractals 130:109445
9. Ahmed W, Kazi SN, Chowdhury ZZ, Johan MRB, Mehmood S, Soudagar MEM et al (2021) Heat transfer growth of sonochemically synthesized novel mixed metal oxide ZnO+Al2O3+TiO2/DW based ternary hybrid nanofluids in a square flow conduit. Renew Sustain Energy Rev 145:111025
10. Geng Y, Khodadadi H, Karimipour A, Reza Safaei M, Nguyen TK (2019) A comprehensive presentation on nanoparticles electrical conductivity of nanofluids: statistical study concerned effects of temperature, nanoparticles type and solid volume concentration. Phys A Stat Mech Appl

11. Selimefendigil F, Öztop HF (2020) The potential benefits of surface corrugation and hybrid nanofluids in channel flow on the performance enhancement of a thermo-electric module in energy systems. Energy 118520
12. Kolahan A, Maadi SR, Kazemian A, Schenone C, Ma T (2020) Semi-3D transient simulation of a nanofluid-base photovoltaic thermal system integrated with a thermoelectric generator. Energy Convers Manag 220:113073
13. Selimefendigil F, Öztop HF (2020) Identification of pulsating flow effects with CNT nanoparticles on the performance enhancements of thermoelectric generator (TEG) module in renewable energy applications. Renew Energy
14. Karana DR, Sahoo RR (2018) Performance effect on the TEG system for waste heat recovery in automobiles using ZnO and SiO2 nanofluid coolants. Heat Transf Asian Res
15. Selimefendigil F, Öztop HF (2021) Thermoelectric generation in bifurcating channels and efficient modeling by using hybrid CFD and artificial neural networks. Renew Energy 172:582–598
16. Kim TY, Lee S, Lee J (2016) Fabrication of thermoelectric modules and heat transfer analysis on internal plate fin structures of a thermoelectric generator. Energy Convers Manag 124:470–479
17. Cao Q, Luan W, Wang T (2018) Performance enhancement of heat pipes assisted thermoelectric generator for automobile exhaust heat recovery. Appl Therm Eng 130:1472–1479
18. Seo J-H, Sandip Garud K, Lee M-Y (2020) Grey relational based Taguchi analysis on thermal and electrical performances of thermoelectric generator system with inclined fins hot heat exchanger. Appl Therm Eng 116279
19. Liu C, Deng YD, Wang XY, Liu X, Wang YP, Su CQ (2016) Multi-objective optimization of heat exchanger in an automotive exhaust thermoelectric generator. Appl Therm Eng 108:916–926
20. He M, Wang E, Zhang Y, Zhang W, Zhang F, Zhao C (2020) Performance analysis of a multilayer thermoelectric generator for exhaust heat recovery of a heavy-duty diesel engine. Appl Energy 274:115298
21. Kwan TH, Wu X, Yao Q (2018) Bidirectional operation of the thermoelectric device for active temperature control of fuel cells. Appl Energy 222:410–422
22. Buchalik R, Nowak G, Nowak I (2021) Mathematical model of a thermoelectric system based on steady- and rapid-state measurements. Appl Energy 293:116943
23. Nour Eddine A, Chalet D, Faure X, Aixala L, Chessé P (2018) Optimization and characterization of a thermoelectric generator prototype for marine engine application. Energy 143:682–695
24. Kim T, Ko Y, Lee Y, Cha C, Kim N (2020) Experimental analysis of flexible thermoelectric generators used for self-powered devices. Energy 117544
25. Van Toan N, Tuoi TTK, Ono T (2020) Thermoelectric generators for heat harvesting: from material synthesis to device fabrication. Energy Convers Manag 225:113442
26. Luo D, Wang R, Yu W, Zhou W (2020) Performance optimization of a converging thermoelectric generator system via multiphysics simulations. Energy 117974
27. Zaher MH, Abdelsalam MY, Cotton JS (2020) Study of the effects of axial conduction on the performance of thermoelectric generators integrated in a heat exchanger for waste heat recovery applications. Appl Energy 261:114434
28. Nozariasbmarz A, Saparamadu U, Li W, Kang HB, Dettor C, Zhu H et al (2021) High-performance half-Heusler thermoelectric devices through direct bonding technique. J Power Sources 493:229695
29. Acharya M, Jana SS, Ranjan M, Maiti T (2021) High performance (ZT > 1) n-type oxide thermoelectric composites from earth abundant materials. Nano Energy 84:105905
30. Zhu L, Li H, Chen S, Tian X, Kang X, Jiang X, Qiu S (2020) Optimization analysis of a segmented thermoelectric generator based on genetic algorithm. Renew Energy
31. Karami Rad M, Rezania A, Omid M, Rajabipour A, Rosendahl L (2019) Study on material properties effect for maximization of thermoelectric power generation. Renew Energy
32. Zhu Y-K, Wu P, Guo J, Zhou Y, Chong X, Ge Z-H, Feng J (2020) Achieving a fine balance in mechanical properties and thermoelectric performance in commercial Bi2Te3 materials. Ceram Int

33. Usenko A, Moskovskikh D, Gorshenkov M, Voronin A, Stepashkin A, Kaloshkin S et al (2017) Enhanced thermoelectric figure of merit of p-type Si 0.8 Ge 0.2 nanostructured spark plasma sintered alloys with embedded SiO2 nanoinclusions. Scr Mater 127:63–67
34. Luo D, Wang R, Yu W, Zhou W (2020) Parametric study of a thermoelectric module used for both power generation and cooling. Renew Energy
35. Gomaa MR, Rezk H (2020) Passive cooling system for enhancement the energy conversion efficiency of thermo-electric generator. Energy Rep 6:687–692
36. Merienne R, Lynn J, McSweeney E, O'Shaughnessy SM (2019) Thermal cycling of thermoelectric generators: the effect of heating rate. Appl Energy 237:671–681
37. Wen ZF, Sun Y, Zhang AB, Wang BL, Wang J, Du JK (2020) Performance analysis of a segmented annular thermoelectric generator. J Electron Mater
38. Yuan J, Zhu R (2020) A fully self-powered wearable monitoring system with systematically optimized flexible thermoelectric generator. Appl Energy 271:115250
39. Weera S, Lee H, Attar A (2020) Utilizing effective material properties to validate the performance of thermoelectric cooler and generator modules. Energy Convers Manag 205:112427
40. Yang H, Shu G, Tian H, Ma X, Chen T, Liu P (2018) Optimization of thermoelectric generator (TEG) integrated with three-way catalytic converter (TWC) for harvesting engine's exhaust waste heat. Appl Therm Eng
41. Kumar Bhukesh S, Kumar A, Kumar Gaware S (2020) Bismuth telluride (Bi2Te3) thermoelectric material as a transducer for solar energy application. Mater Today Proc
42. Abderezzak B, Randi S (2020) Experimental investigation of waste heat recovery potential from car radiator with thermoelectric generator. Therm Sci Eng Prog 100686
43. Dunham MT, Hendricks TJ, Goodson KE (2019) Thermoelectric generators: a case study in multi-scale thermal engineering design. Adv Heat Transf 299–350
44. Barma MC, Riaz M, Saidur R, Long BD (2015) Estimation of thermoelectric power generation by recovering waste heat from biomass fired thermal oil heater. Energy Convers Manag 98:303–313
45. He H, Wu Y, Liu W, Rong M, Fang Z, Tang X (2019) Comprehensive modeling for geometric optimization of a thermoelectric generator module. Energy Convers Manag 183:645–659
46. COMSOL (2005) FEMLAB 3.2 user's guide. Comsol AB
47. Kolsi L, Alrashed AA, Al-Salem K, Oztop HF, Borjini MN (2017) Control of natural convection via inclined plate of CNT-water nanofluid in an open sided cubical enclosure under magnetic field. Int J Heat Mass Transf 111:1007–1018
48. Khan MR, Pan K, Khan AU, Ullah N (2020) Comparative study on heat transfer in CNTs-water nanofluid over a curved surface. Int Commun Heat Mass Transf 116:104707
49. Zaim A, Aissa A, Mebarek-Oudina F, Mahanthesh B, Lorenzini G, Sahnoun M, El Ganoui M (2020) Galerkin finite element analysis of magneto-hydrodynamic natural convection of Cu-water nanoliquid in a baffled U-shaped enclosure. Propuls Power Res
50. Fares M, AL-Mayyahi M, AL-Saad M (2020) Heat transfer analysis of a shell and tube heat exchanger operated with graphene nanofluids. Case Stud Therm Eng 18:100584
51. Kim CN (2018) Development of a numerical method for the performance analysis of thermoelectric generators with thermal and electric contact resistance. Appl Therm Eng 130:408–417
52. Jia X, Guo Q (2019) Design study of Bismuth-Telluride-based thermoelectric generators based on thermoelectric and mechanical performance. Energy 116226
53. Luo D, Yan Y, Wang R, Zhou W (2021) Numerical investigation on the dynamic response characteristics of a thermoelectric generator module under transient temperature excitations. Renew Energy 170:811–823
54. Tropea C, Gackstatter R (1985) The flow over two-dimensional surface-mounted obstacles at low Reynolds numbers. J Fluids Eng 107:489–494

Chapter 10
Analogy Between Darcy-Bénard Convection Problems Involving a Clear Fluid and a Nanofluid: An Illustration

Davita Devi Soibam and P. G. Siddheshwar

Abstract We extend the work reported by Barletta et al. (Int J Heat Mass Transf 89:75–89, 2015) on the onset of Darcy-Bénard convection to steady finite-amplitude convection, considering both clear fluids and nanofluids that are Newtonian in character. The minimal Fourier-Galerkin expansion is used for the case of a free surface along with the convective thermal boundary condition. The heat transport is represented in terms of the Nusselt number, Nu. On comparing the Nusselt number of the present problem with that of the classical Darcy-Bénard problem, it is found that the former is much smaller or larger than the latter depending on the Biot number. An analogy between the problems of a clear fluid and a nanofluid is shown indicating that the results of a nanofluid can be obtained from that of a clear fluid.

Nomenclature

Bi	Is the Biot number
$(C_p)_f$	Is the specific heat at constant pressure, [J kg^{-1} k^{-1}]
$(C_p)_l$	Is the heat capacity of the carrier liquid, [J kg^{-1} k^{-1}]
$(C_p)_{np}$	Is the heat capacity of the nanoparticle, [J kg^{-1} k^{-1}]
$(C_p)_{nl}$	Is the heat capacity of the nanoliquid, [J kg^{-1} k^{-1}]
$Da = \frac{K}{L^2}$	Is the Darcy number
e_z	Is the unit vector along the z-axis
g	Is the acceleration due to gravity, [m/s^2]
h_{ef}	Is the heat transfer coefficient, [W/(m^{2}K)]
k_{eff}	Is the effective thermal conductivity, [W/(mK)]
k_l	Is the thermal conductivity of the carrier liquid, [W/(mK)]
k_{np}	Is the thermal conductivity of the nanoparticle, [W/(mK)]

D. D. Soibam (✉) · P. G. Siddheshwar
Centre for Mathematical Needs, Mathematics Department, CHRIST (Deemed to be University), Bengaluru 560029, India
e-mail: davitadevi.soibam@res.christuniversity.in

D. Tripathi et al. (eds.), *Advancements in Nanotechnology for Energy and Environment*, Advances in Sustainability Science and Technology,
https://doi.org/10.1007/978-981-19-5201-2_10

$Pr = \frac{\mu}{\rho_0 \alpha_{eff}}$	Is the Prandtl number
$Pr_D = \frac{Pr}{Da}$	Is the Darcy-Prandtl number
$Pr_{nl} = \frac{\mu_{nl}}{\rho_{nl}\alpha_{nl}}$	Is the nanoliquid Prandtl number
$\vec{q}$	Is the velocity, [m/s]
$R = \frac{\rho_0 g \beta \Delta T K L}{\mu \alpha_{eff}}$	Is the Darcy-Rayleigh number
$R_{nl} = \frac{(\rho\beta)_{nl} g \Delta T L^3}{\alpha_{nl}\mu_{nl}}$	Is the nanoliquid Rayleigh number
$\alpha_{eff} = \frac{k_{eff}}{(\rho_0 C_p)_f}$	Is the effective thermal diffusivity, [m^2/s]
α_{nl}	Is the thermal diffusivity of the nanoliquid, [m^2/s]
β	Is the thermal expansion coefficient, $\left[K^{-1}\right]$
β_{nl}	Is the thermal expansion coefficient of the nanoliquid, $\left[K^{-1}\right]$
μ	Is the dynamic viscosity, [PaS]
μ_{nl}	Is the dynamic coefficient of viscosity of the nanoliquid, [PaS]
ρ_0	Is the density at the reference temperature T_0, [kg/m^3]
ρ_l	Is the density of the carrier liquid, [kg/m^3]
ρ_{np}	Is the density of the nanoparticle, [kg/m^3]
ρ_{nl}	Is the density of the nanoliquid at $T = T_0$, [kg/m^3]
χ	Is the nanoparticle volume fraction
L	Is the layer thickness, $[m]$
K	Is the permeability, $\left[m^2\right]$
T	Is the temperature, $[K]$

1 Introduction

The porous medium analog of the classical Rayleigh-B*é*nard convection problem (RBC) is known as Darcy-B*é*nard convection (DBC) when the medium is of low porosity. This problem has been addressed by many authors (Horton and Rogers [1], Lapwood [2], Rees [3], Suthar et al. [4], Siddheshwar and Lakshmi [5] and references therein). This problem has also found mention in books (Vafai [6], Nield and Bejan [7], Rees and Pop [8], Straughan [9]). The works reported in the above papers and books refer to an isothermal boundary with Dirichlet boundary condition on the stream function. Such a DBC problem is called as the classical DBC. The present problem involves a free upper surface (Neumann boundary condition on the stream function) with third type boundary condition on temperature, and isothermal boundaries on the lower surface with Dirichlet boundary condition. Such a DBC problem is a non-classical problem and the same was initiated by Barletta et al. [10]. There is no reported work on the analog of the Barletta-Darcy-B*é*nard convection (BDBC) problem in a nanofluid using the single-phase description (Khanafer-Vafai-Lightstone model [6]). Generally, in all problems that investigate classical Darcy-B*é*nard convection (CDBC) problem, it is simply assumed that the two problems are different and are thereby reported as separate problems. In the present problem, we

show that the results of the nanofluid problem can be obtained from those of the clear fluid problem. Such a result applies to other types of Bénard problems as well.

2 Mathematical Formulation

We consider a plane porous layer with uniform thickness L in which a uniform temperature, T_w, is maintained at the lower impermeable wall, $z = 0$, while the upper boundary is a free surface, with uniform pressure, that exchanges heat with an external fluid environment having a reference temperature, T_0, such that $T_0 < T_w$. The physical configuration of the Darcy-Bénard setup that is considered in the study is shown in Fig. 1.

The equation of continuity, pressure-eliminated unsteady Darcy equation with buoyancy term, and energy equation are given by:

$$\nabla \cdot \vec{q} = 0, \tag{1}$$

$$\rho_0 \frac{\partial}{\partial t}(\nabla \times \vec{q}) + \frac{\mu}{K}\nabla \times \vec{q} = \rho_0 g \beta \nabla \times \left[(T - T_0)e_z\right], \tag{2}$$

$$\frac{\partial T}{\partial t} + (\vec{q}.\nabla)T = \alpha_{\text{eff}}\nabla^2 T. \tag{3}$$

Equations (1)–(3) are subject to the boundary condition given by:

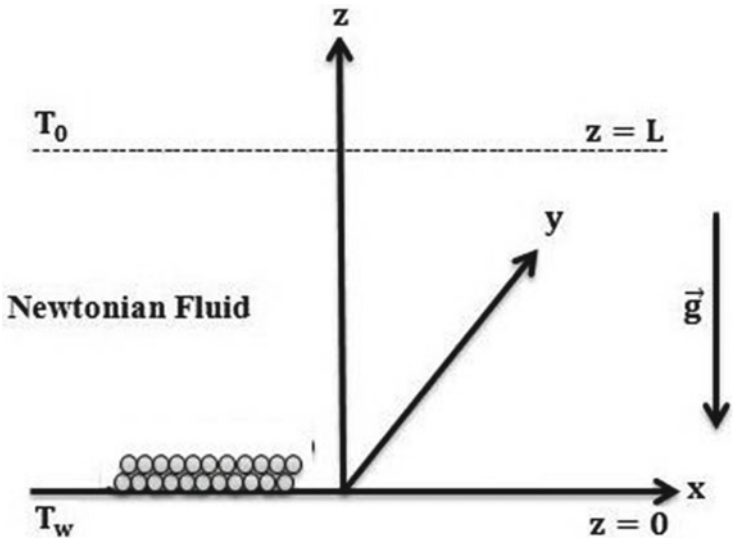

Fig. 1 Physical configuration of the Darcy-Bénard setup

$$\vec{q} \cdot \widehat{e_z} = 0, T = T_w at z = 0, \tag{4}$$

$$\frac{\partial w}{\partial z} = 0, -k_{\text{eff}} \frac{\partial T}{\partial z} = h_{ef}(T - T_0) \text{at } z = L. \tag{5}$$

We rewrite the governing Eqs. (1)–(3) and the boundary condition (4) and (5) in dimensionless form by defining

$$\left.\begin{array}{c} t = \frac{\tau L^2}{\alpha_{\text{eff}}}, \\ (x, y, z) = (X, Y, Z)L, \\ \vec{q} = (u, v, w)\frac{\alpha_{\text{eff}}}{L}, \\ T = T_0 + \theta \Delta T \end{array}\right\}, \tag{6}$$

where $\Delta T = T_w - T_0$ is the temperature difference between the two horizontal boundaries. The dimensionless set of governing equations obtained on using Eq. (6) in Eqs. (1)–(3) now reads as

$$\nabla \cdot \vec{q} = 0, \tag{7}$$

$$\frac{1}{Pr_D} \frac{\partial}{\partial \tau}(\nabla \times \vec{q}) = -\nabla \times \vec{q} + R \nabla \times (\theta e_z), \tag{8}$$

$$\frac{\partial \theta}{\partial \tau} = \nabla^2 \theta - (\vec{q} \cdot \nabla)\theta. \tag{9}$$

The dimensionless version of the boundary condition in Eqs. (4) and (5) is given by:

$$w = 0, \theta = 1 \text{ at } Z = 0, \tag{10}$$

$$\frac{\partial w}{\partial Z} = 0, \frac{\partial \theta}{\partial Z} + Bi\theta = 0 \text{ at } Z = 1. \tag{11}$$

The field variables $\vec{q}$ and θ can be written as a superposition of quantities of the quiescent basic state and the dynamic perturbation state as follows:

$$\left.\begin{array}{l} \vec{q} = \overrightarrow{q_b} + \overrightarrow{\hat{q}}(X, Z, \tau), \\ \theta = \theta_b(Z) + \hat{\theta}(X, Z, \tau) \end{array}\right\}, \tag{12}$$

where

$$\overrightarrow{q_b} = 0, \overrightarrow{\hat{q}} = \big(\hat{u}(X, Z, \tau), 0, \hat{w}(X, Z, \tau)\big). \tag{13}$$

The quiescent basic state quantity, $\theta_b(Z)$, assumes the following expression:

$$\theta_b(Z) = \frac{-Bi}{1+Bi}Z + 1. \tag{14}$$

Clearly $\theta_b(Z)$ satisfies the boundary condition on θ given in Eqs. (10) and (11) imposed at the boundaries $Z = 0$ and $Z = 1$.

By substituting Eq. (12) into Eqs. (7)–(11), we get

$$\nabla . \vec{\hat{q}} = 0, \tag{15}$$

$$\frac{1}{Pr_D}\frac{\partial}{\partial \tau}\left(\nabla \times \vec{\hat{q}}\right) = -\nabla \times \vec{\hat{q}} + R\nabla \times \left(\hat{\theta} e_z\right), \tag{16}$$

$$\frac{\partial \hat{\theta}}{\partial \tau} + \left(\vec{\hat{q}} . \nabla\right)\hat{\theta} + \frac{d\theta_b}{dZ}\hat{w} = \nabla^2 \hat{\theta}, \tag{17}$$

with boundary condition

$$\hat{w} = 0, \hat{\theta} = 0 at Z = 0, \tag{18}$$

$$\frac{\partial \hat{w}}{\partial Z} = 0, \frac{\partial \hat{\theta}}{\partial Z} + Bi\hat{\theta} = 0 \text{ at } Z = 1. \tag{19}$$

Now, we consider only two-dimensional disturbances, and hence, we introduce the stream function as follows:

$$\hat{u} = \frac{\partial \hat{\psi}}{\partial Z}, \hat{w} = -\frac{\partial \hat{\psi}}{\partial X}. \tag{20}$$

Equation (20) satisfies Eq. (15). Using Eq. (20) in Eq. (16) and (17), we get

$$\frac{1}{Pr_D}\frac{\partial}{\partial \tau}\left(\nabla^2 \hat{\psi}\right) + \nabla^2 \hat{\psi} + R\frac{\partial \hat{\theta}}{\partial X} = 0, \tag{21}$$

$$\frac{\partial \hat{\theta}}{\partial \tau} + \left(\frac{\partial \hat{\psi}}{\partial Z}\frac{\partial \hat{\theta}}{\partial X} - \frac{\partial \hat{\psi}}{\partial X}\frac{\partial \hat{\theta}}{\partial Z}\right) - \frac{d\theta_b}{dZ}\frac{\partial \hat{\psi}}{\partial X} - \nabla^2 \hat{\theta} = 0, \tag{22}$$

with the boundary condition

$$\hat{\psi} = 0, \hat{\theta} = 0 \text{ at } Z = 0, \tag{23}$$

$$\frac{\partial \hat{\psi}}{\partial Z} = 0, \frac{\partial \hat{\theta}}{\partial Z} + Bi\hat{\theta} = 0 \text{ at } Z = 1. \tag{24}$$

3 Linear Stability Analysis

Solution of the boundary eigenvalue problem of Eqs. (21)–(24) can be expressed as normal modes given by

$$\left.\begin{aligned}\hat{\psi}(X, Z) &= \sin(aX)\psi(Z),\\ \hat{\theta}(X, Z) &= \cos(aX)\theta(Z)\end{aligned}\right\}, \tag{25}$$

where $\psi(Z)$ and $\theta(Z)$ are the amplitude functions of the normal modes, and a is the horizontal wave number for a longitudinal roll. Assuming the principle of exchange of stabilities and substituting Eq. (25) in Eqs. (21) and (22), we get

$$\left(\frac{d^2}{dZ^2} - a^2\right)\psi(Z) + aR\theta(Z) = 0, \tag{26}$$

$$\left(\frac{d^2}{dZ^2} - a^2\right)\theta(Z) + a\left(\frac{Bi}{1 + Bi}\right)\psi(Z) = 0. \tag{27}$$

The boundary condition to solve Eqs. (26) and (27) is:

$$\left.\begin{aligned}\hat{\psi} = 0, \hat{\theta} = 0 \text{ at } Z = 0,\\ \tfrac{\partial\hat{\psi}}{\partial Z} = 0, \tfrac{\partial\hat{\theta}}{\partial Z} + Bi\hat{\theta} = 0 \text{ at } Z = 1\end{aligned}\right\}. \tag{28}$$

We solve Eqs. (26) and (27), subject to Eq. (28), by the Galerkin method.

In order to apply the Galerkin method to obtain the eigenvalue, R, for stationary convection, we consider

$$\left.\begin{aligned}\psi(Z) &= A_1\psi_1(Z),\\ \theta(Z) &= A_2\theta_1(Z)\end{aligned}\right\}, \tag{29}$$

where the trial functions $\psi_1(Z)$ and $\theta_1(Z)$ satisfy Eq. (28) and are given by:

$$\left.\begin{aligned}\psi_1(Z) &= Z^2 - 2Z,\\ \theta_1(Z) &= Z^2 - \tfrac{2+Bi}{1+Bi}Z\end{aligned}\right\}. \tag{30}$$

Substituting Eq. (29) in Eq. (26), multiplying the resulting equation by $\psi_1(Z)$ and integrating with respect to Z in [0, 1], we get

$$a_{11}A_1 + a_{12}RA_2 = 0, \tag{31}$$

where

$$a_{11} = -\left[\frac{4}{3} + \frac{8a^2}{15}\right], a_{12} = a\left[\left(\frac{2+Bi}{1+Bi}\right)\frac{5}{12} - \frac{3}{10}\right]. \tag{32}$$

Now, substituting Eq. (29) in Eq. (27), multiplying the resulting equation by $\theta_1(Z)$, and integrating with respect to Z in [0, 1], we get

$$a_{21}A_1 + a_{22}A_2 = 0, \tag{33}$$

where

$$\left.\begin{aligned} a_{21} &= a\left(\tfrac{Bi}{1+Bi}\right)\left[\tfrac{1}{5} - \tfrac{1}{4}\left(2 + \tfrac{2+Bi}{1+Bi}\right) + \tfrac{2}{3}\left(\tfrac{2+Bi}{1+Bi}\right)\right], \\ a_{22} &= \tfrac{2}{3} - \left(\tfrac{2+Bi}{1+Bi}\right) - a^2\left[\tfrac{1}{5} - \tfrac{1}{2}\left(\tfrac{2+Bi}{1+Bi}\right) + \tfrac{1}{3}\left(\tfrac{2+Bi}{1+Bi}\right)^2\right] \end{aligned}\right\}. \tag{34}$$

Equations (31) and (33) are two homogeneous equations in A_1 and A_2.
For a non-trivial solution to A_1 and A_2, we require

$$\begin{vmatrix} a_{11} & a_{12}R \\ a_{21} & a_{22} \end{vmatrix} = 0. \tag{35}$$

Expanding the determinant (35) and rearranging the resulting equation for R, we get

$$R = \frac{a_{11}a_{22}}{a_{12}a_{21}}. \tag{36}$$

Then, $\frac{dR}{da^2} = 0$ implies that

$$a^4 = -\frac{5}{2}\left(\frac{2}{3} - \frac{2+Bi}{1+Bi}\right)\left[\frac{1}{\frac{1}{5} - \frac{1}{2}\left(\frac{2+Bi}{1+Bi}\right) + \frac{1}{3}\left(\frac{2+Bi}{1+Bi}\right)^2}\right].$$

In the next section, we present a weakly nonlinear stability analysis.

4 Weakly Nonlinear Stability Analysis for Steady Convection

The Fourier-Galerkin minimal representation for the stream function and temperature is considered in the form:

$$\left.\begin{aligned} \hat{\psi}(X, Z, \tau) &= A\sin(a_c X)\psi_1(Z), \\ \hat{\theta}(X, Z, \tau) &= B\cos(a_c X)\theta_1(Z) + \mathrm{CH}(Z) \end{aligned}\right\}, \tag{37}$$

where

$$H(Z) = -\left(\frac{Bi}{1+Bi}\right)\frac{1}{2}\left[Z^2 - \frac{2+Bi}{1+Bi}Z\right], \tag{38}$$

and $\psi_1(Z)$ and $\theta_1(Z)$ are given by Eq. (30). The minimal system (37) obviously satisfies the boundary condition in (28). Substituting Eq. (37) in Eqs. (21) and (22), making use of Eq. (14) for $\theta_b(Z)$ in the resulting equation and projecting them on the individual eigenfunctions, we obtain the system of nonlinear algebraic equations in A, B, and C in the form:

$$\tilde{k}RB - A = 0, \tag{39}$$

$$a_c\left(\frac{Bi}{1+Bi}\right)\frac{k_9}{k_3}A - \frac{k_5}{k_3}B - a_c\frac{k_4}{k_3}AC = 0, \tag{40}$$

$$\pi\frac{(k_7+k_8)}{k_6}AB - \frac{k_{10}}{k_6}C = 0, \tag{41}$$

where

$$k_1 = \frac{4}{5}a_c^2 + \frac{2}{3}(1-2a_c^2) - 2,$$

$$k_2 = a_c\left[\frac{1}{5} - \left(2+\frac{2+Bi}{1+Bi}\right)\frac{1}{4} + \frac{2}{3}\left(\frac{2+Bi}{1+Bi}\right)\right],$$

$$k_3 = \frac{1}{5} - \frac{1}{2}\left(\frac{2+Bi}{1+Bi}\right) + \frac{1}{3}\left(\frac{2+Bi}{1+Bi}\right)^2,$$

$$k_4 = -\left[\frac{7}{30}\left(\frac{Bi}{1+Bi}\right) + \frac{Bi(2+Bi)}{(1+Bi)^2}\left\{\frac{3}{10} + \frac{5}{24}\left(\frac{2+Bi}{1+Bi}\right) - \frac{3}{4}\right\}\right],$$

$$k_5 = -\left(\frac{2}{3} - \frac{a_c^2}{5}\right) - \frac{1}{2}\left(\frac{2+Bi}{1+Bi}\right)(a_c^2-2) + \frac{a_c^2}{3}\left(\frac{2+Bi}{1+Bi}\right)^2,$$

$$k_6 = -\left(\frac{Bi}{1+Bi}\right)\left[\frac{1}{20} - \frac{1}{8}\left(\frac{2+Bi}{1+Bi}\right) + \frac{1}{12}\left(\frac{2+Bi}{1+Bi}\right)^2\right],$$

$$k_7 = 2\left[-\frac{1}{60} + \frac{1}{20}\left(\frac{2+Bi}{1+Bi}\right) - \frac{1}{24}\left(\frac{2+Bi}{1+Bi}\right)^2\right],$$

$$k_8 = -\frac{7}{30} + \frac{7}{20}\left(\frac{2+Bi}{1+Bi}\right) - \frac{5}{24}\left(\frac{2+Bi}{1+Bi}\right)^2,$$

$$k_9 = -\frac{5}{12}\left(\frac{2+Bi}{1+Bi}\right) + \frac{3}{10},$$

$$k_{10} = \left(\frac{Bi}{1+Bi}\right)\left[\frac{1}{6} - \frac{1}{4}\left(\frac{2+Bi}{1+Bi}\right)\right],$$

$$\tilde{k} = \frac{k_2}{k_1}.$$

The Eqs. (39)–(41) have the following solution for the convective state:

$$A = \pm\sqrt{\frac{\tilde{k}Rk_{10}k_3}{a_c\pi\,(k_7+k_8)k_4}\left[a_c\left(\frac{Bi}{1+Bi}\right)\frac{k_9}{k_3} - \frac{1}{\tilde{k}R}\left(\frac{k_5}{k_3}\right)\right]}, \tag{42}$$

$$B = \frac{A}{\tilde{k}R}, \tag{43}$$

$$C = \frac{k_3}{a_c k_4}\left[a_c\left(\frac{Bi}{1+Bi}\right)\frac{k_9}{k_3} - \frac{1}{\tilde{k}R}\left(\frac{k_5}{k_3}\right)\right]. \tag{44}$$

From the above proceeding, it is clear that subcritical motion cannot exist in this system.

5 Derivation of the Nusselt Number

The Nusselt number is given by

$$Nu = 1 + \frac{\left[\int_0^{\frac{2\pi}{a_c}} \frac{\partial\hat{\theta}}{\partial Z}dX\right]_{Z=0}}{\left[\int_0^{\frac{2\pi}{a_c}} \frac{d\theta_b}{dZ}dX\right]_{Z=0}}, \tag{45}$$

where

$$\hat{\theta} = B\cos(a_c X)\theta_1(Z) + \mathrm{CH}(Z). \tag{46}$$

Substituting Eq. (46) and Eq. (14) in Eq. (45) and completing the integration, we get

$$Nu = 1 - \frac{2+Bi}{2(1+Bi)}C. \tag{47}$$

Substituting Eq. (44) in Eq. (47), we get

$$Nu = 1 + 2F_1(Bi)\left[1 - \frac{1}{r}\right], \tag{48}$$

where

$$F_1(Bi) = \frac{2 + Bi}{4(1 + Bi)^2}\left(\frac{k_9 Bi}{k_4}\right).$$

6 Analogous Problem in Water-Copper Nanofluid

If we consider a Newtonian nanofluid in place of the Newtonian clear fluid (water without copper nanoparticles, say), then in the governing Eqs. (21) and (22), we would replace R by R_{nl} and Pr_D by Pr_{nl}. A quantity a_1 also appears (see Siddheshwar and Meenakshi [11]). The parameters R_{nl} and Pr_{nl} are, respectively, the nanofluid Darcy-Rayleigh number and nanofluid Darcy-Prandtl number. The boundary condition in (23) and (24) shall not, however, get altered. Thus, the governing equations for the analogous problem are:

$$\left(\frac{1}{Pr_{nl}}\frac{\partial}{\partial \tau} + a_1\right)\nabla^2\hat{\psi} + a_1^2 R_{nl}\frac{\partial \hat{\theta}}{\partial X} = 0, \tag{49}$$

$$\left(\frac{\partial}{\partial \tau} - a_1\nabla^2\right)\hat{\theta} - \frac{d\theta_b}{dZ}\frac{\partial \hat{\psi}}{\partial X} = \frac{\partial \hat{\psi}}{\partial X}\frac{\partial \hat{\theta}}{\partial Z} - \frac{\partial \hat{\psi}}{\partial Z}\frac{\partial \hat{\theta}}{\partial X}, \tag{50}$$

where

$$a_1 = \frac{\left[1 - \frac{3\chi\left(1-\frac{k_{np}}{k_l}\right)}{\left(\frac{k_{np}}{k_l}+2\right)+\chi\left(1-\frac{k_{np}}{k_l}\right)}\right]}{(1-\chi) + \chi\frac{(\rho C_p)_{np}}{(\rho C_p)_l}}, \text{ (see[11])} \tag{51}$$

Equations (49) and (50) are to be solved subject to the boundary condition in Eqs. (23) and (24). We now transform Eqs. (49) and (50) to Eqs. (21) and (22) and thereby prove that the results of the nanofluid using a single-phase description can be obtained from those of Newtonian clear fluids.

Dividing Eq. (49) by a_1^2 and Eq. (50) by a_1, and using the scaling

$$a_1\tau = \tilde{\tau}, \frac{\hat{\psi}}{a_1} = \tilde{\psi}, \hat{\theta} = \tilde{\theta}, \tag{52}$$

we get the following equations:

$$\left(\frac{1}{Pr_{nl}}\frac{\partial}{\partial\tilde{\tau}}+1\right)\nabla^2\tilde{\psi}+R_{nl}\frac{\partial\tilde{\theta}}{\partial X}=0, \tag{53}$$

$$\left(\frac{\partial}{\partial\tilde{\tau}}-\nabla^2\right)\tilde{\theta}-\frac{d\theta_b}{dZ}\frac{\partial\tilde{\psi}}{\partial X}=\frac{\partial\tilde{\psi}}{\partial X}\frac{\partial\tilde{\theta}}{\partial Z}-\frac{\partial\tilde{\psi}}{\partial Z}\frac{\partial\tilde{\theta}}{\partial X}, \tag{54}$$

which are same as Eqs. (21) and (22), except for different symbols.

Now, on using the scaling (52) in the Eqs. (23) and (24), we get

$$\tilde{\psi}=0,\tilde{\theta}=0 \text{ at } Z=0, \tag{55}$$

$$\frac{\partial\tilde{\psi}}{\partial Z}=0,\frac{\partial\tilde{\theta}}{\partial Z}+Bi\tilde{\theta}=0 \text{ at } Z=1. \tag{56}$$

Equations (55)–(56) and Eqs. (23)–(24) are identical except for different symbols. We have thus proved that there is no need to pursue the nanofluid problem with a single-phase description as its results can be obtained from that of the clear fluid. This result is true of any nanofluid. Here, water-copper has been considered as a representative nanofluid. Further, this analogy in respect of Darcy-Bénard convection is in conformity with the requirement of the Buckingham π theorem.

7 Results and Discussion

In the paper, we consider Darcy-Bénard convection under the effects of a free surface and convective thermal boundary condition. Using this as an illustrative example, we show the analogy between two Darcy-Bénard problems involving a clear fluid and a nanofluid. We first consider the clear fluid problem. The results of the linear theory are essentially reiterations of the reported results by Barletta et al. [10]. We found that the critical Rayleigh number decreases with increase in the values of Bi for small values, and increases for large values of Bi (see Fig. 2). The critical wave number increases with increase in the value of Bi (see Fig. 3). As Bi increases, one gets the result of isothermal boundaries, whereas at very small values of Bi, we get the results of the adiabatic boundary. The results of the present paper in the extreme cases of Bi do not coincide with the results of the classical Darcy-Bénard convection problem due to the velocity boundary condition being different in the two cases. On comparing the results of the two Darcy-Bénard problems, we can infer that

$$R_c^{CDBC}<R_c^{BDBC},$$

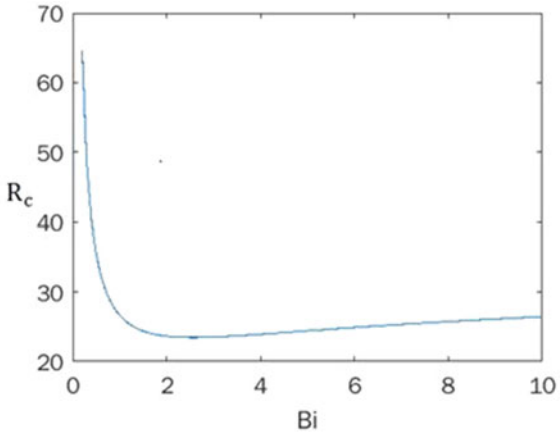

Fig. 2 Plot of R_c versus Bi.

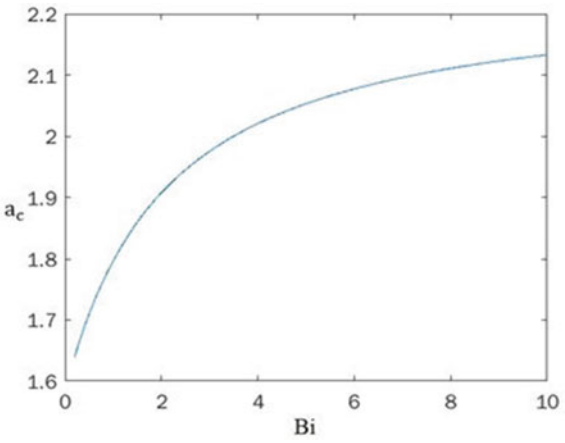

Fig. 3 Plot of a_c versus Bi.

where superscripts $CDBC$ and $BDBC$ refer to classical Darcy-Bénard convection and Barletta-Darcy-Bénard convection. The above result is true for clear fluids as well as nanofluids.

Steady finite-amplitude convection reveals that subcritical motion is impossible in the system. The heat transport is represented in terms of the Nusselt number, Nu, and the same is obtained in terms of Bi, a_c, and r. To understand the effect of Bi on Nu, we have plotted the factor $F_1(Bi)$ in Eq. (48) versus Bi (see in Fig. 4). Clearly this is a decreasing function of Bi, i.e., $\frac{dF_1}{dBi} < 0$. In the case of the isothermal boundaries, one can easily show that $F_1(Bi) = 1$. In the $BDBC$, $F_1(Bi)$ takes a value less than 1 and hence

$$Nu^{CDBC} > Nu^{BDBC},$$

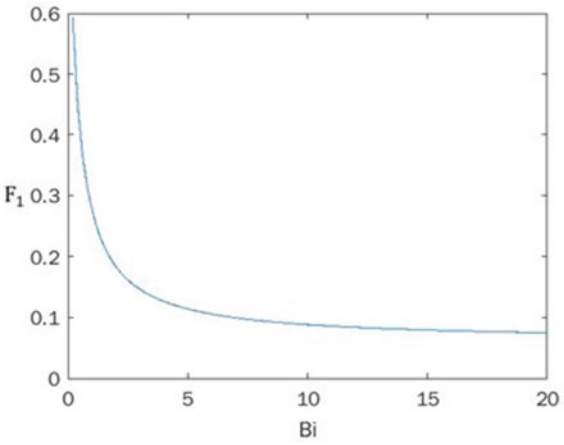

Fig. 4 Plot of F_1 versus Bi.

and this result is in conformity with the corresponding result of the critical Rayleigh number mentioned earlier.

We have proved the analogy between the two $BDBCs$ in a clear fluid and a nanofluid. This clearly points out to the fact that the results of the nanofluid can be obtained from those of the clear fluid. This result is true when we consider the single-phase description for the nanofluid. The proving of the analogy between the two problems is in conformity with the requirements of the Buckingham π theorem which is a consequence of the fundamental theorem of linear algebra. Two conclusions that we can make as a consequence of this analogy are:

1. Critical Rayleigh number of a nanofluid is less than that of a clear fluid.
2. Critical Rayleigh number of a nanofluid decreases with an increase in the value of volume friction of nanoparticles.

References

1. Horton CW, Rogers FT Jr (1945) Convection currents in a porous medium. J Appl Phys 16(6):367–370
2. Lapwood ER (1948) Convection of a fluid in a porous medium. Math Proc Cambridge Philos Soc 44(4):508–521
3. Rees DAS, Bassom AP (2000) The onset of Darcy-Bénard convection in an inclined layer heated from below. Acta Mech 144(1):103–118
4. Suthar OP, Siddheshwar PG, Bhadauria BS (2016) A study on the onset of thermally modulated Darcy-Bénard convection. J Eng Math 101(1):175–188
5. Siddheshwar PG, Lakshmi KM (2019) Darcy-Bénard convection of Newtonian liquids and Newtonian nanoliquids in cylindrical enclosures and cylindrical annuli. Phys Fluids 31(8):084102
6. Khanafer K, Vafai K, Lightstone M (2003) Buoyancy-driven heat transfer enhancement in a two-dimensional enclosure utilizing nanofluids. Int J Heat Mass Transf 46(19):3639–3653

7. Nield DA, Bejan A et al (2006) Convection in porous media, vol 3. Springer, New York
8. Rees DAS, Pop I (2005) Local thermal non-equilibrium in porous medium convection. In: Transport phenomena in porous media III. Elsevier, pp 147–173
9. Straughan B (2008) Stability and wave motion in porous media, vol 165. Springer Science & Business Media, New York
10. Barletta A, Celli M, Lagziri H (2015) Instability of a horizontal porous layer with local thermal non-equilibrium: effects of free surface and convective boundary conditions. Int J Heat Mass Transf 89:75–89
11. Siddheshwar PG, Meenakshi N (2017) Amplitude equation and heat transport for Rayleigh-Bénard convection in Newtonian liquids with nanoparticles. Int J Appl Comput Math 3(1):271–292

Chapter 11
Thermal Radiation and Natural Convection in the Flow of Hybrid Nanofluid Across a Permeable Longitudinal Moving Fin Using TOPSIS

Jawad Raza and Khalid Saleem

Abstract This chapter deals with the hybrid nanofluid (H-NF) over a moving porous fin under the influence of thermal radiation effect. The main objective of the present study is to increase the heat transfer (HT) rate by H-NF of the porous fin and select the appropriate values of the parameters where HT rate is maximum. This can help in the manufacturing process like glass fiber drawing, casting, etc. To accomplish this objective, we employed TOPSIS method which leads us to take the certain values of the parameters to enhance the HT. This will be very helpful for the engineers to investigate the results experimentally. For this, dimensionless differential equations are solved with the help of midpoint method, and then we employed TOPSIS method. The study revealed that the radiative and convective parameters increase heat transfer rate from the fin face surrounded by water-based H-NF. For that reason, status of radiation and convection parameters are important for transfer of heat from the fin area. Moreover, alternative A12, with value of operating parameters as Nc = 0.000688, Nr = 0.006586, m_2 = 0.000299, ϴa = 0.006173, n = 0, and Pe = 0.003574 have maximum value 0.952634 of performance score (Pi) so ranked as 1.

Keywords Nanofluid · Hybrid nanofluid · Heat transfer · Natural convection · TOPSIS

Nomenclature

Bi	Biot number
n	power index of temperature dependent h
C_p	Specific heat at constant pressure (J/kgK)

J. Raza (✉)
Department of Mathematics, The COMSATS University Islamabad, Vehari Campus, Pakistan
e-mail: jawad_6890@yahoo.com

K. Saleem
Department of Mathematics, National College of Business Administration & Economics Multan, Campus 66000, Multan, Pakistan

D. Tripathi et al. (eds.), *Advancements in Nanotechnology for Energy and Environment*, Advances in Sustainability Science and Technology,
https://doi.org/10.1007/978-981-19-5201-2_11

t	fin thickness m
F_{f-a}	shape factor for radiation heat transfer
x	axial coordinate (m)
K	Permeability$/A^2$
w	width (m)
sL	Length of the fin (m)

Greek Symbols

Nc	Convective parameter
ρ	density $\left(kg/m^3\right)$
Nr	Radiative parameter
θ_a	dimensionless ambient temperature
Pe	Peclet number
μ	dynamic viscosity (kg/ms)
T	Local fin temperature (K)
ω	humidity ratio of the saturated air
T_a	Ambient temperature (K)
ω_a	humidity ratio of the surrounding air
T_b	Base temperature (K)
v	kinematic viscosity $\left(m^2/s\right)$
U	Constant velocity of the fin (m/s)
i_{fg}	latent heat of water evaporation (J/kg)
X	Dimensionless axial coordinate
θ	non-dimensional temperature
b_2	Variable parameter $(1/K)$
ϕ^-	porosity
g	Acceleration due to gravity $\left(m/s^2\right)$
ϕ	solid volume fraction of nanoparticles
h	Heat transfer coefficient $\left(W/m^2K\right)$
σ	Stefan–Boltzmann constant $\left(W/m^2K^4\right)$
h_a	Heat transfer coefficient at temperature $T_a\left(W/m^2K\right)$
ε	surface emissivity of fin
h_D	Uniform mass transfer coefficient
β	volumetric thermal expansion coefficient $(1/K)$
k	Thermal conductivity (W/mK)
m_0, m_1	Constants and $m_2 = m_0 + m_1$
m_2	wet porous parameter

Subscripts

a	ambient
b	base of fin
bf	base fluid
f	fluid
hnf	hybrid nanofluid
p_1, p_2	nanoparticles

1 Background of the Study

In the area of modern sciences, some sectors like automobile, electronics, power generation, etc., progressed very fastly in the some past years. Heat transport is essential for all these fields. Due to matchless progress in these sectors, the devices with enhanced storage capacity and efficient HT efficiency have been invented. Maxwell [20] improved system thermal performance by including a high thermal conductivity solid into the base fluid. Afterward, quantity of researches has made on the nanometer-sized particles. Then, [4] created the term "nanofluid" by combining nanometer-sized particles with a normal base fluid. This approach answered several previously unresolved issues with agglomeration, settlement, and sedimentation. However, latest study on nanofluids (NFs) has revealed that combining two distinct types of Np in a water (base fluid) improves heat transmission and thermophysical characteristics of the fluid, which is referred to as "hybrid nanofluid." Different Np should be selected for hybrid nanofluids (HyNFs) in such a manner that they cover the negative aspects of each on one of them. Certain important investigations done by [7] on the uses of HyNFs [12, 21, 27, 16, 13].

Previously, it was believed that NFs improved HT performance and system efficiency discussed by [24]. Recently, a quantity of theoretical and investigational studies has made by Fernández et al. [8] to know the consequence of Np on thermal qualities and heat transport performance. Due to scientific improvements, very small size electronic devices (silicon chip) have been invented. These improvements have increased the requirement of extra compact thermal managing system for these devices. Bumataria et al. [3] analyzed that heat pipes (made of mono and HyNFs) are the newest trends in meeting the requirement for a better HT system. Kaggwa and Carson [17] addressed in their current literature, mixing of solid Np in conventional base fluids increased HT rates and thermal conductivity. The objectives of the study work of [2] were to discover the convective HT rate of propanol-based NFs for cooling uses. Coccia et al. [5] studied that energy needs in the world are constantly increasing, and fossil fuel resources must be changed by renewable means, and solar collectors seem to be very favorable for that purpose. Baskar et al. [2] researched the theoretical learning of carbon nanotube (CNT) and thermophysical characteristics.

The analysis done by [22] showed the effects of NFs in solar evacuated tubes and solar collectors (ETSCs).

2 Literature Review

Solar energy has been employed for household heating, industrial heating, electrical energy production, and thermochemical processes during the previous century and a half. Goel et al. [11] discussed that several techniques have been used to increase the performance of converting incoming solar energy into useful heat due to the huge number of uses. Sui et al. [26] investigated that NFs are fluid mixtures in which Np are dispersed throughout a base fluid. The thermophysical properties of NFs were enhanced by nano-scale additions. Fossil fuels have determined pollution impacts on the atmosphere. However, clean and reusable energy resources must be used. There are numerous forms of renewable energy, but solar energy is the most advantageous and cost-effective source, which has focused emphasis on efficient and low-cost solar energy collection for public use discussed by Eltaweel and Abdel-Rehim [6]. The increasing thermophysical characteristics of mono NFs show enormous potential in a wide range of HT applications. The characteristics of mono NFs may be customized by varying the quantities of Np in the NFs. Furthermore, the mono NFs show the uniform thermophysical features in the limited range. HyNFs have been developed in recent years to increase the thermophysical and HT characteristics of the base fluid. The key benefit of utilizing HyNF is that it can be modified by incorporating two or more Np into the basic fluids. Because Np are entirely dissolved in the base fluids, HyNFs can offer significant paybacks. Xue [30] investigated the flow of HyNF with various types of Np using a generalized HyNF model. Fallah et al. [9] also investigated the flow of HyNF caused by a rotating disk.

Maisuria et al. [19] attempted to use TOPSIS methodology for nanoparticle selection in a HT applications. Copper oxide (CuO) was discovered to be the best among the other nanoparticles, those they analyzed. The HT parameters of the falling film horizontal heated tube were investigated by Kaushal and Kumar [18]. They discovered that the spiral tube had a higher HT rate than the other investigated tubes. Raj and Prabhu [23] employed the abrasive water jet machining (AWJM) technique to investigate the slicing properties of silicon by adjusting operating parameters such as abrasive flow rate (QA), traverse rate (TR), water pressure (P), and stand-off distance (SOD). The experiments were conducted using a Taguchi L9 orthogonal array with TOPSIS. Amani et al. [1] studied the prediction ability of using a correlation and an artificial neural network to determine the thermal conductivity and dynamic viscosity of clove-treated nanofluid. Gupta et al. [15] found that using NFMQL in titanium alloy processing effectively decreases cutting forces, tool wear, and surface roughness, all of which are essential from both an industrial and academic perspective. Tassaddiq et al. [28] compared NF and HyNF, as well as heat and mass transport studies. Farooq et al. [10] considered the irreversibility investigation of HyNF flow. Usman et al. [29] determined the nonlinear thermal radiation for HyNF flow. Gireesha

et al. [14] used the Runge Kutta Fehlberg (RKF) method to solved governing equations mathematically with two boundary conditions. For the flow behavior, they used the DM model. They investigated the parametric effect on HT rate of fin. They also find that, the fin with known convective tip dominates the insulated fin.

2.1 Topsis Method

Technique for order preference by similarity to ideal solution (TOPSIS) is a numerical decision-making approach with several criteria. This is a method with a broad range of applications and a simple mathematical steps. We study m alternatives $(A_1, \ldots\ldots A_m)$, every alternative A_i has n criteria $(x_1, \ldots\ldots x_n)$, expressed by positive numbers (x_{ij}). The criteria $(x_1, \ldots\ldots x_k)$ are benefitial (monotonically increasing preference), and criteria $(x_{(k+1)}, \ldots\ldots x_n)$ are non-benefitial (monotonically decreasing preference).

Initial Matrix

Criteria	Crt. 1 x_1	Crt. 2 x_2	....	Crt. N x_n
Alt. 1 $A_{1.}$	x_{11}	x_{12}	....	x_{1n}
Alt. 2 $A_{2.}$	x_{21}	x_{22}	....	x_{2n}
⋮	⋮	⋮	⋮	⋮
Alt.m A_m	x_{m1}	x_{m2}	...	x_{mn}

The steps of TOPSIS method are given as:

Step 1

First of all we take a decision matrix,

$$\mathrm{X} = \begin{bmatrix} x_{11} & \cdots & x_{1n} \\ \vdots & \ddots & \vdots \\ x_{m1} & \cdots & x_{mn} \end{bmatrix}$$

Step 2

In 2nd step, the numbers X_{ij} of criteria X_j is replaced with the normalized numbers $\boldsymbol{r_{ij}}$, which calculated by using formula,

$$r_{ij} = \frac{X_{ij}}{\sqrt{\sum_{ij}^{m} X_{ij}^2}} r_{ij} \in (0, 1)$$

Thus a normalized decision matrix R is obtained as,

$$R = \begin{bmatrix} r_{11} & \cdots & r_{1n} \\ \vdots & \ddots & \vdots \\ r_{m1} & \cdots & r_{mn} \end{bmatrix}$$

Step 3

In this step, normalized decision matrix R is multiplied with the weight $w_j = (w_1, w_2, w_3, \ldots\ldots\ldots\ldots\ldots w_n)$, which are given or calculated by using different techniques such as analytic hierarchy process (AHP). $\therefore (\sum w_j = 1)$.

Then we get a normalized weighted matrix $\boldsymbol{A}$ is $a_{ij} = W_j * r_{ij}$,

$$\mathrm{A} = \begin{bmatrix} a_{11} & \cdots & a_{1n} \\ \vdots & \ddots & \vdots \\ a_{m1} & \cdots & a_{mn} \end{bmatrix}$$

Step 4

Next, we determine the matrix of ideal solutions, i.e., ideal best or positive and ideal worst or negative solution with the help of formula $V^+ = \{(\max.V_{ij} \text{where} j \in \mathrm{J}), (\min.V_{ij} \text{where} j \in \mathrm{J}'), (i = 1, 2, 3, \ldots, m)$, where j is the column of beneficial criteria and $\boldsymbol{j}'$ is the column of non-beneficial criteria.

$$V^+ = \left\{V_1^+, V_2^+, \ldots\ldots\ldots V_n^+\right\}$$

$$V^- = \left\{(\min . V_{ij}\ where\ j \in J),\ (\max\ V_{ij}\ where\ j \in J'),\ (i = 1, 2, 3, \ldots, m)\right\}$$
$$= \left\{V_1^-,\ V_2^-,\ V_3^-,\ \ldots,\ V_n^-\right\}$$

Step 5

$S+$ is a Euclidian distance from the ideal best (positive ideal) solution, calculated by the formula,

$$S_i^+ = \sqrt{\sum_{j=1}^{n} \left(V_{ij} - V_j^+\right)^2}$$

$(I = 1, 2, 3, , , m)$.

$S-$ is a Euclidian distance from the ideal worst (negative ideal) solution, is given as,

$$S_i^- = \sqrt{\sum_{j=1}^{n} \left(V_{ij} - V_j^-\right)^2}$$

where $I = 1, 2, 3, , , m$

Step 6

In this step, we calculate the performance score or closeness index,

$$\boldsymbol{P_i} = \frac{\boldsymbol{S_i^-}}{\boldsymbol{S_i^- + S_i^+}}$$

Step 7

In the last step, the set of alternatives (P_i) ranked in descending order. The alternative of highest value consider the best solution (Fig. 1) [25].

The problem for HyNF over a wet porous fin has many physical implications in the field of engineering. So, it is hard to gain the certain parameters accurately. In order to define the exact or appropriate values of the parameters and their rank according to the optimized value of HT rate, researcher may take MCDM process called TOPSIS. With the aid of above mentioned results, in this research, we shall examine the rate of thermal conductivity of permeable longitudinal moving fin. Here we shall use Midpoint method to solve leading equations. In our investigations, we shall use nanoparticles of copper–aluminum oxide with base fluid (water). We shall also describe the effect of different parameters on main equations numerically. We shall use the TOPSIS method, which is a new technique. By using this method, we shall get optimal set of operating parameters. To understand the problem physically, different graphs and tables will be drawn.

2.2 Objectives of the Study

OS 1: In this study, we will find the numerical solution of the HyNF across permeable longitudinal moving fin by midrich method under the influence of thermal radiation and natural convection.

OS 2: Moreover, we will apply TOPSIS method in order to select the optimum values of the various parameters involved in the study.

OS 3: Additionally, we will investigate the thermal conductivity of proposed system with $Cu - Al_2O_3 - H_2O$-based HyNF.

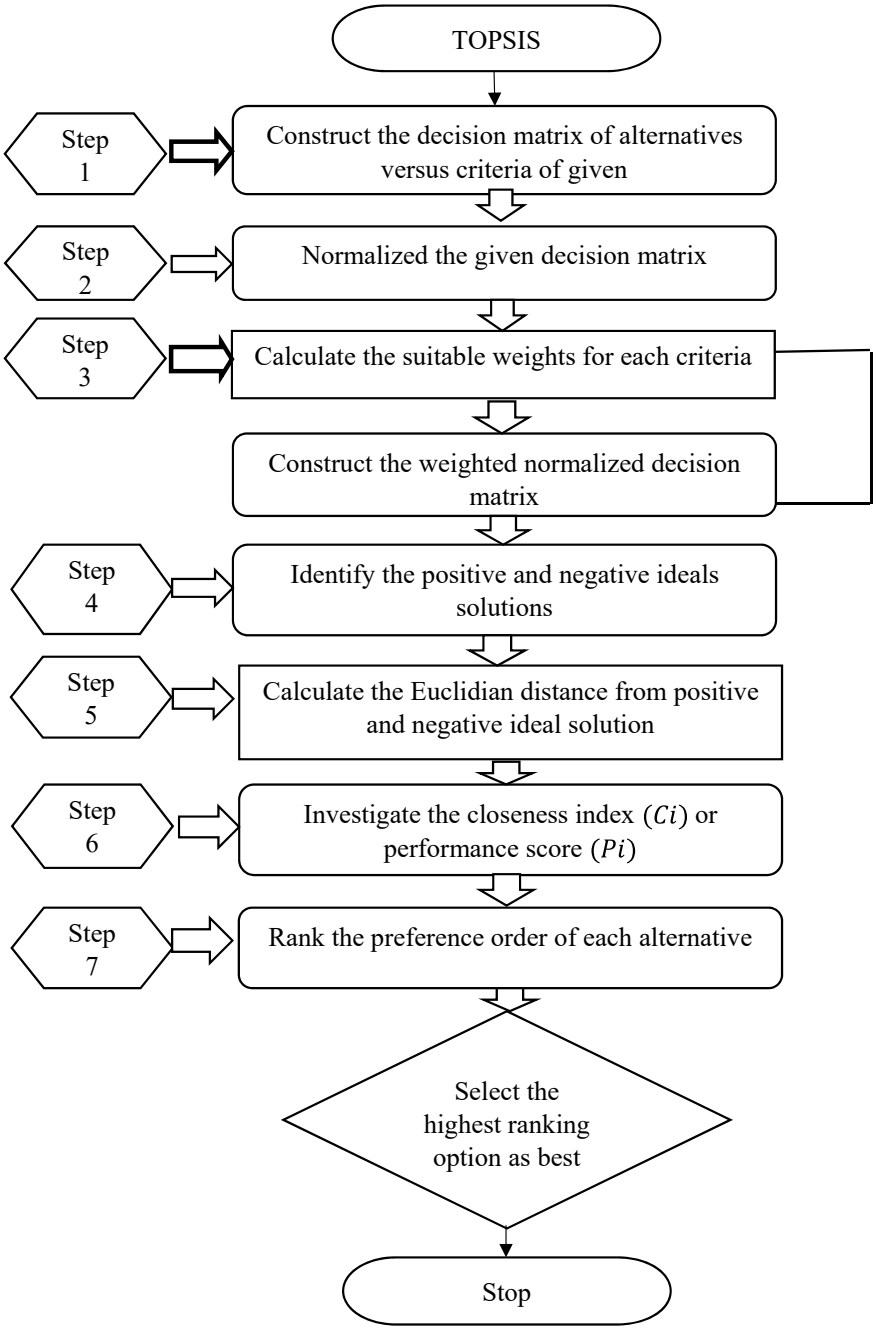

Fig. 1 Flow diagram of TOPSIS algorithm

OS 4: Furthermore, we will find HT rate of proposed system with convective tip conditions.

2.3 Research Questions

Moreover, current work provides the solutions of following research queries:

- What are the impacts of Nc (convective parameter) and Nr (radiative parameter) on $\theta(X)$?
- How does the effect of Peclet number, dimensionless ambient temperature, Biot number, radiative parameter, convective parameter, wet porous parameter, dimensionless axial distance, and power index on thermal profile?
- Can we carry out parametric investigations by TOPSIS?
- Does the thermal gradient of fin with convective tip condition dominates than insulated tip fin?
- What are the results of Cu and Al_2O_3 on the thermal conductivity of hybrid nanofluid?

3 Mathematical Formulation

The flow of HyNF along the moving fin is seen in Fig. 2. The cross-sectional area of the fin is considered to remain constant. The fin has longitudinal profile and porous nature. In this case, Darcy's model (DM) is applied. T_b is the base temperature and and T_a is the ambient temperature when the fin is first at rest. The fin moves horizontally at a constant velocity U, losing heat by radiation and natural convection. The assumptions listed below are used to explain the situation:

- Time has no effect on flow behavior and temperatures.
- The surrounding temperature of fin is consistent.
- The main surface and the fin base have no contact resistance.
- The temperature of fin base is uniform.
- The continuous phase fluid and HyNFs are in state of thermal equilibrium.

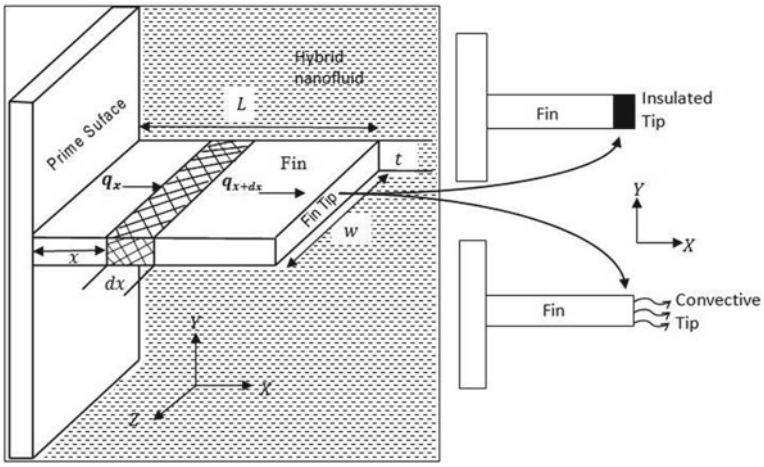

Fig. 2 Schematic plot of proposed model

$$\frac{d^2T}{dx^2} - \frac{\left(\rho c_p\right)_{hnf} U}{k_{hnf}} \frac{dT}{dx} - \frac{2h_D i_{fg}\left(1-\overline{\emptyset}\right)(\omega-\omega_a)}{k_{hnf} t} - \frac{2h\left(1-\overline{\emptyset}\right)(T-T_a)}{k_{hnf} t} - \frac{2gK\left(\rho c_p\right)_{hnf}(\rho\beta)_{hnf}}{\mu_{hnf} k_{hnf} t}(T-T_a)^2 - \frac{2\varepsilon\sigma F_{f-a}}{k_{hnf} t}\left(T^4 - T_a^4\right) = 0 \tag{1}$$

Here, k_{hnf}, $\mu_{hnf,}\rho_{hnf}$, $\left(C_p\right)_{hnf}$, and β_{hnf} correspondingly represent the thermal conductivity of HyNFs, effective dynamic viscosity of HyNFs, effective density of HyNFs, specific heat of HyNFs, where hnf means HyNFs. Mathematically, it is written as;

$$\frac{k_{hnf}}{k_{bf}} = \frac{\left(k_{p^2} + 2k_{bf}\right) - 2\emptyset_2\left(k_{bf} - k_{p^2}\right)}{\left(k_{p^2} + 2k_{bf}\right) + \emptyset_2\left(k_{bf} - k_{p^2}\right)} \tag{2}$$

$$\frac{k_{bf}}{k_f} = \frac{\left(k_{p^1} + 2k_f\right) - 2\emptyset_1\left(k_f - k_{p^1}\right)}{\left(k_{p^1} + 2k_f\right) + \emptyset_1\left(k_f - k_{p^1}\right)}, \tag{3}$$

$$\mu_{hnf} = \frac{\mu_f}{(1-\emptyset_1)^{2.5}(1-\emptyset_2)^{2.5}}, \tag{4}$$

$$\rho_{hnf} = \left\{(1-\emptyset_2)\left[(1-\emptyset_1)\rho_f + \emptyset_1\rho_{p1}\right]\right\} + \emptyset_2\rho_{p^2.} \tag{5}$$

Table 1 Nanomaterials and base liquid numeric values

Physical properties		$k(W/mK)$		$C_p(J/kgK)$		$\beta * 10^{-5}(1K^{-1})$		$\rho(kgm^{-3})$	
H_2O	f	k_f	0.613	C_{p_f}	4179	β_f	21	ρ_f	997.1
Cu	p_1	k_{p_1}	400	C_{p_1}	385	β_{p_1}	7.6	ρ_{p_1}	8933
Al_2O_3	p_2	k_{p_2}	40	C_{p_2}	765	β_{p_2}	5.1	ρ_{p_2}	3970

$$\left(\rho C_p\right)_{hnf} = \left\{(1-\emptyset_2)\left[(1-\emptyset_1)\left(\rho C_p\right)_f + \emptyset_1\left(\rho C_p\right)_{p^1}\right]\right\} + \emptyset_2\left(\rho C_p\right)_{p^2} \tag{6}$$

$$(\rho\beta)_{hnf} = \left\{(1-\emptyset_2)\left[(1-\emptyset_1)(\rho\beta)_f + \emptyset_1(\rho\beta)_{p^1}\right]\right\} + \emptyset_2(\rho\beta)_{p^2} \tag{7}$$

We examined Cu and Al_2O_3 as Nps and water as the base fluid in this case. Table 1 gives their thermophysical properties. The values ϕ_1 and ϕ_2 indicate the Np volume fractions of Cu and Al_2O_3, respectively. ($\phi_1 = 0, \phi_2 = 0$ Indicates base fluid water and $\phi_1 = 1, \phi_2 = 1$ denotes HyNF).

The HT coefficient (h) is known as a function of temperature and given as;

$$h = h_a\left[\frac{T - T_a}{\mathrm{T_b} - T_a}\right]^n = h_D c_p L e^{\frac{2}{3}} \tag{8}$$

h_a means coefficient of HT at temperature T_a.

There are two types of boundary conditions.

Case 1: Finite fin with insulated tip condition.

There is no HT from the tip in this case. Therefore, the temperature at the tip stays constant. The condition is given as;

$$\begin{aligned} &at\ x = 0, T(0) = T\_b: \\ &at\ x = L, (dT(L))/dx = 0. \end{aligned} \tag{9}$$

Case 2: Finite fin tip with convective coefficient condition.

$$\begin{aligned} &at\ x = 0, T(0) = T_b \\ &at\ x = L, k_{hnf}\frac{dT(L)}{dx} + h_a T(L) = 0 \end{aligned} \tag{10}$$

For non-dimensionalize the differential equation, consider,

$$\theta = \frac{T}{T_b}, \theta_a = \frac{T_a}{T_b}, X = \frac{x}{L}, Pe = \frac{\left(\rho c_p\right)_f U L}{k_f},$$
$$Nc = \frac{2(\rho\beta)_f g K \left(\rho c_p\right)_f T_b L^2}{\mu_f k_f t}, Nr = \frac{2\varepsilon\sigma T_b^3 L^2 F_{f-a}}{k_f t},$$
$$(\omega - \omega_a) = b_2(T - T_a), m_0 = \frac{2h_a L^2\left(1 - \overline{\emptyset}\right)}{k_f t}, \tag{11}$$
$$m_1 = \frac{2h_a i_{fg}\left(1 - \overline{\emptyset}\right) b_2 L^2}{k_f t c_{pf} L e^{\frac{2}{3}}}, m_2 = m_0 + m_1, Bi = \frac{L h_a}{k_f}$$

By using these equations in Eq. (1), we get.

$$\frac{T_b}{L^2}\frac{d}{dX}\frac{d\theta}{dX} - \frac{\left(\rho c_p\right)_{hnf} U}{k_{hnf}}\frac{T_b}{L}\frac{d\theta}{dX} - \frac{2h_D i_{fg}\left(1 - \overline{\emptyset}\right)}{k_{hnf} t} b_2 T_b(\theta - \theta_a)$$
$$- \frac{2h_a(\theta - \theta_a)^{n+1}}{(1 - \theta_a)^n}\frac{\left(1 - \overline{\emptyset}\right)}{k_{hnf} t} T_b - \frac{2gK\left(\rho c_p\right)_{hnf}(\rho\beta)_{hnf}}{\mu_{hnf} k_{hnf} t} T_b^2(\theta - \theta_a)^2 \tag{12}$$
$$- \frac{2\varepsilon\sigma F_{f-a}}{k_{hnf} t} T_b^4\left(\theta^4 - \theta_a^4\right) = 0$$

It can be written as;

$$\frac{d}{dX}\frac{d\theta}{dX} - \frac{\left(\rho c_p\right)_{hnf} U L}{k_{hnf}}\frac{d\theta}{dX} - \frac{2h_D i_{fg}\left(1 - \overline{\emptyset}\right)}{k_{hnf} t} b_2 L^2(\theta - \theta_a)$$
$$- \frac{2h_a(\theta - \theta_a)^{n+1}}{(1 - \theta_a)^n}\frac{\left(1 - \overline{\emptyset}\right)}{k_{hnf} t} L^2 - \frac{2gK\left(\rho c_p\right)_{hnf}(\rho\beta)_{hnf}}{\mu_{hnf} k_{hnf} t} T_b L^2(\theta - \theta_a)^2 \tag{13}$$
$$- \frac{2\varepsilon\sigma F_{f-a}}{k_{hnf} t} T_b^3 L^2\left(\theta^4 - \theta_a^4\right) = 0$$

Now for solving, we make substitutions,

$$\begin{aligned}
&\frac{d}{dX}\frac{d\theta}{dX} - \frac{\left(\rho c_p\right)_{hnf} UL}{k_{hnf}}\frac{d\theta}{dX}\frac{\left(\rho c_p\right)_f}{\left(\rho c_p\right)_f}\frac{k_f}{k_f} \\
&-\frac{2h_D i_{fg}\left(1-\overline{\emptyset}\right)}{k_{hnf}t} b_2 L^2(\theta-\theta_a)\frac{(k)_f}{(k)_f} - \frac{2h_a(\theta-\theta_a)^{n+1}}{(1-\theta_a)^n}\frac{\left(1-\overline{\emptyset}\right)}{k_{hnf}t} L^2\frac{(k)_f}{(k)_f} \\
&-\frac{2gK\left(\rho c_p\right)_{hnf}(\rho\beta)_{hnf}}{\mu_{hnf}k_{hnf}t} T_b L^2(\theta-\theta_a)^2\frac{\left(\rho c_p\right)_f}{\left(\rho c_p\right)_f}\frac{(\rho\beta)_f}{(\rho\beta)_f}\frac{\left(\mu_f\right)}{\left(\mu_f\right)}\frac{k_f}{k_f} \\
&-\frac{2\varepsilon\sigma F_{f-a}}{k_{hnf}t} T_b^3 L^2\left(\theta^4-\theta_a^4\right)\left(\frac{k_f}{k_f}\right) = 0
\end{aligned} \tag{14}$$

Re arranging the above equation,

$$\begin{aligned}
&\frac{d}{dX}\frac{d\theta}{dX} - \left(\frac{\left(\rho c_p\right)_f UL}{k_f}\right)\left(\frac{\left(\rho c_p\right)_{hnf}}{\left(\rho c_p\right)_f}\right)\left(\frac{k_f}{k_{hnf}}\right)\frac{d\theta}{dX} \\
&-\left(\frac{2(\rho\beta)_f gK\left(\rho c_p\right)_f T_b L^2}{\mu_f k_f t}\right)(\theta-\theta_a)^2\left(\frac{\left(\rho c_p\right)_{hnf}}{\left(\rho c_p\right)_f}\right)\left(\frac{(\rho\beta)_{hnf}}{(\rho\beta)_f}\right)\left(\frac{k_f}{k_{hnf}}\right)\left(\frac{\mu_f}{\mu_{hnf}}\right) \\
&+\left[-\frac{2h_D i_{fg}\left(1-\overline{\emptyset}\right)}{k_{hnf}t} b_2 L^2(\theta-\theta_a)\frac{(k)_f}{(k)_f} - \frac{2h_a(\theta-\theta_a)^{n+1}}{(1-\theta_a)^n}\frac{\left(1-\overline{\emptyset}\right)}{k_{hnf}t} L^2\frac{(k)_f}{(k)_f}\right] \\
&-\left(\frac{2\varepsilon\sigma T_b^3 L^2}{k_f t}\right) F_{f-a}\left(\theta^4-\theta_a^4\right)\left(\frac{k_f}{k_{hnf}}\right) = 0
\end{aligned} \tag{15}$$

Now we make,

$$\begin{aligned}
&h = h_a\left[\frac{T-T_a}{\mathrm{T_b}-T_a}\right]^n = h_a\left[\frac{T_b\theta-\theta_a T_b}{T_b-\theta_a T_b}\right]^n \\
&= h_a\frac{T_b^n}{T_b^n}\left[\frac{\theta-\theta_a}{1-\theta_a}\right]^n = h_a\left[\frac{\theta-\theta_a}{1-\theta_a}\right]^n \\
&\text{here } \mathrm{T_b} = \mathrm{T_b} \text{ and } T = T_b\theta, T_a = \theta_a T_b \\
&also\, h = h_D c_p Le^{\frac{2}{3}} \\
&then\, h_D c_p Le^{\frac{2}{3}} = h_a\left[\frac{\theta-\theta_a}{1-\theta_a}\right]^n then\, h_D \\
&= \frac{1}{c_{pf} Le^{\frac{2}{3}}} h_a\frac{(\theta-\theta_a)^n}{(1-\theta_a)^n}
\end{aligned} \tag{16}$$

Also,

$$\begin{aligned}
&\frac{2h_a(\theta-\theta_a)^{n+1}}{(1-\theta_a)^n}\frac{\left(1-\overline{\emptyset}\right)}{k_{hnf}t}L^2\frac{k_f}{k_f}-\frac{2h_D i_{fg}\left(1-\overline{\emptyset}\right)}{k_{hnf}t}b_2L^2(\theta-\theta_a)\frac{(k)_f}{(k)_f}\\
&=-\frac{2h_a(\theta-\theta_a)^{n+1}}{(1-\theta_a)^n}\frac{\left(1-\overline{\emptyset}\right)}{k_{hnf}t}L^2\frac{k_f}{k_f}\\
&-\frac{2i_{fg}\left(1-\overline{\emptyset}\right)}{k_{hnf}t}b_2L^2(\theta-\theta_a)\frac{k_f}{k_f}\frac{1}{c_{pf}Le^{\frac{2}{3}}}h_a\frac{(\theta-\theta_a)^n}{(1-\theta_a)^n}\\
&=-\left(\frac{2h_aL^2\left(1-\overline{\emptyset}\right)}{k_ft}\right)\frac{(\theta-\theta_a)^{n+1}}{(1-\theta_a)^n}\left(\frac{k_f}{k_{hnf}}\right)\\
&-\left(\frac{2h_ai_{fg}\left(1-\overline{\emptyset}\right)b_2L^2}{k_ftc_{pf}Le^{\frac{2}{3}}}\right)\frac{(\theta-\theta_a)^{n+1}}{(1-\theta_a)^n}\left(\frac{k_f}{k_{hnf}}\right)\\
&=-m_0\frac{(\theta-\theta_a)^{n+1}}{(1-\theta_a)^n}\left(\frac{k_f}{k_{hnf}}\right)-m_1\frac{(\theta-\theta_a)^{n+1}}{(1-\theta_a)^n}\left(\frac{k_f}{k_{hnf}}\right)\\
&=-(m_0+m_1)\frac{(\theta-\theta_a)^{n+1}}{(1-\theta_a)^n}\left(\frac{k_f}{k_{hnf}}\right)=-m_2\frac{(\theta-\theta_a)^{n+1}}{(1-\theta_a)^n}\left(\frac{k_f}{k_{hnf}}\right)
\end{aligned}\tag{17}$$

Using values from Eqs. (16) and (17) into Eq. (15), we get.

$$\begin{aligned}
&\frac{d}{dX}\frac{d\theta}{dX}-Pe\left[\frac{\left(\rho c_p\right)_{hnf}}{\left(\rho c_p\right)_f}\right]\left(\frac{(k)_f}{k_{hnf}}\right)\frac{d\theta}{dX}-Nc(\theta-\theta_a)^2\\
&\left(\frac{\left(\rho c_p\right)_{hnf}}{\left(\rho c_p\right)_f}\right)\left(\frac{(\rho\beta)_{hnf}}{(\rho\beta)_f}\right)\left(\frac{k_f}{k_{hnf}}\right)\left(\frac{\mu_f}{\mu_{hnf}}\right)\\
&-m_2\frac{(\theta-\theta_a)^{n+1}}{(1-\theta_a)^n}\left(\frac{k_f}{k_{hnf}}\right)-Nr\left(\theta^4-\theta_a^4\right)\left(\frac{k_f}{k_{hnf}}\right)=0
\end{aligned}\tag{18}$$

Here the dimensionless boundary conditions are given as;
Case 1: For insulated tip condition:

$$\begin{aligned}
&at\ X=0,\theta(0)=1;\\
&at\ X=1,\theta'(1)=0.
\end{aligned}\tag{19}$$

Case 2: For convective coefficient at the tip:

$$\begin{aligned}
&at\ X=0,\theta(0)=1;\\
&at\ X=1,\theta'(1)=-\frac{k_f}{k_{nf}}Bi.\theta(1).
\end{aligned}\tag{20}$$

Here, Pe is known as Peclet number, Nr represents the radiative parameter, m_2 is wet porous parameter, Bi is Biot number, n represents power index, X is known for dimentionless axial length, Nc is convective parameter, θ_a a is dimensionless ambient temperature, and θ is dimensionless temperature.

3.1 Results and Discussions

The parametric research conducted to investigate effect of the parameters on the thermal profile ($\theta(X)$) of a moving longitudinal permeable fin wetted with $Cu - Al_2O_3/H_2O$ HyNF under both known convective and insulated tip conditions.

For known convective and insulated tip circumstances, the effect of Peclet number (Pe) on $\theta(X)$ shown in Fig. 3a, b, respectively. Pe is the relation of advective heat to diffusive heat, and it represents the non-dimensional speed. When the value of Pe arises, the non-dimensional speed increases which minimize the contact between fin and the surrounding. Hence, the increment in Pe maximize $\theta(X)$ of the fin. Thus, the HT rate reduces with increase in Pe. Figure 4a, b represents the impact of convective parameter (Nc) on $\theta(X)$ for convective and insulated tip fin. It noticed that, when Nc increases then $\theta(X)$ will decrease. Nc is the product of Ra (Rayleigh number) and Da (Darcy number). The increment in Nc will enhance the Ra or Da. In other words, permeability or buoyancy impact increases. Hence, HT rate from fin to neighboring rises. Figure 5a, b shows the influence of radiative parameter (Nr) on $\theta(X)$ for both convective and insulated tip fin. Nr based on the radiation impact. The radiation effect rises with the increase of Nr, which magnifies HT from fin to surrounding area. For that reason, fin temperature goes down across the axial length. Figure 6a, b discloses the impact of power index (n) of convective HT on $\theta(X)$. The numerous calculations of n indicate different flow mechanism. The $n = 0$ shows the linear case, while $n > 0$ indicates the nonlinear case. Graph shows that, for linear case, $\theta(X)$ is less and its value increases with rise in n. This indicates that, HT rate decreases with the increase in n. Figure 7a, b displays the effect of wet porous parameter (m_2) on $\theta(X)$ of fin. The moist nature of fin surface removes more heat from the surface of fin, and the porous structure of the fin allows fluid to flow through it. As a result, m_2 aids in HT from the fin surface. As m_2 increases, the temperature of the fin diminishes. This improves the cooling effect of the fin. Figure 8a, b describes the impact of changes in dimensionless ambient temperature (θ_a) on $\theta(X)$ of fin with convective and insulated tip, respectively.θ_a is a ratio of neighboring temperature to base temperature. Graph shows that, rise in θ_a raises the temperature of the surrounding liquid, which reduces HT from the fin surface. Hence, $\theta(X)$ rises with increase in θ_a.

The overall observations from Figs. 3a, 4, 5, 6, 7, 8b shows that fin of convective tip emits more heat. This means that at this region (convective tip) temperature of fin decreases, but for insulated tip condition temperature remains constant. Thus, HT rate for convective tip condition is more than the insulated tip condition. Figure 9 displays the influence of Biot number (Bi) on $\theta(X)$ of fin. It is noticed that, increase of Bi minimize the $\theta(X)$. The condition $Bi > 0.1$ shows that heat convection release

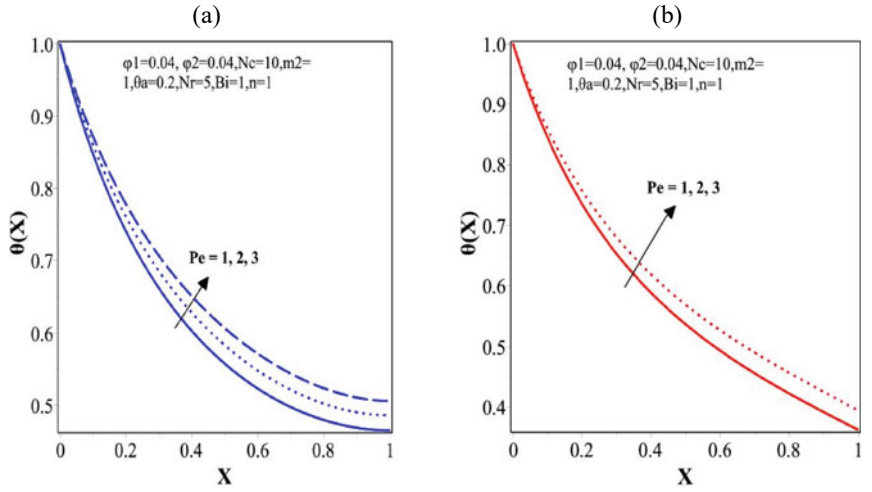

Fig. 3 **a** & **b**: Effect of Peclet Number (Pe) on thermal profile for convective and insulated tip condition, respectively

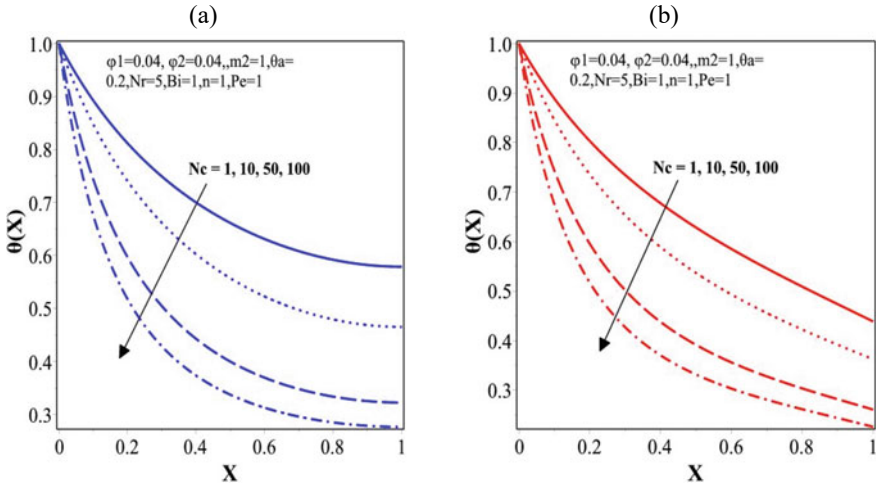

Fig. 4 **a** & **b**: Effect of convective parameter (Nc) on thermal profile for convective and insulated tip condition, respectively

through the fin surface is quicker than the heat conduction within the fin surface. Hence, rise in Bi increases the HT rate from fin surface, which means that Bi has positive effect on HT rate of fin.

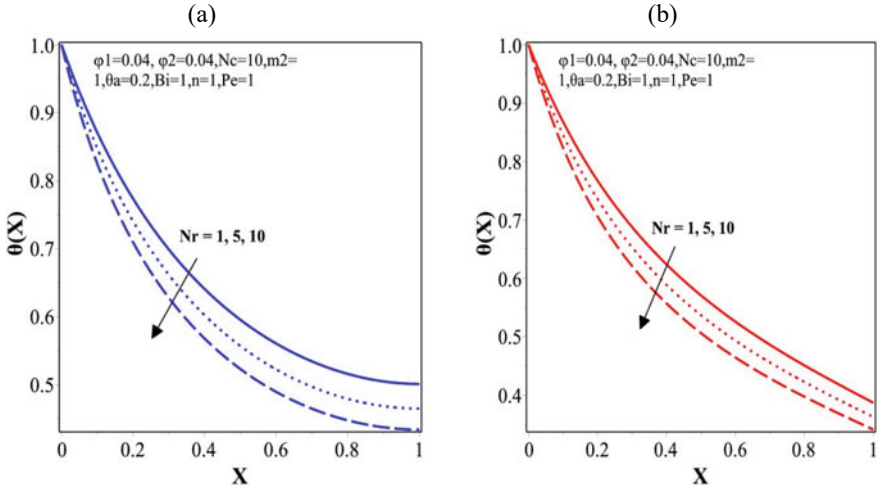

Fig. 5 **a** & **b**: Effect of radiative parameter (Nr) on thermal profile for convective and insulated tip condition, respectively

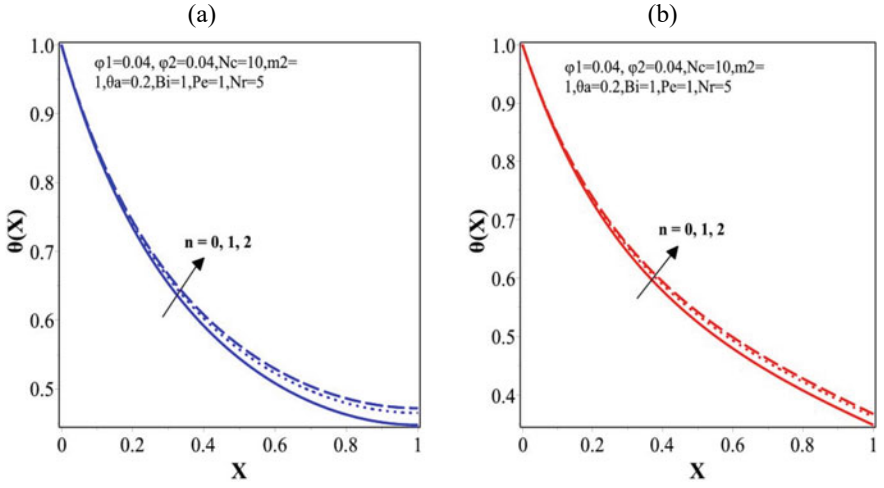

Fig. 6 **a** & **b**: Effect of Power index (n) on thermal profile for convective and insulated tip condition, respectively

3.2 The Results of Topsis

In first step, the decision matrix formed, given in Table 2. After this, we find normal values with the help of formula, seen in Table 3 and then decision matrix normalized by dividing the each entries of every column with its corresponding normal value given in Table 4. After this, weights were calculated with the help of AHP Technique,

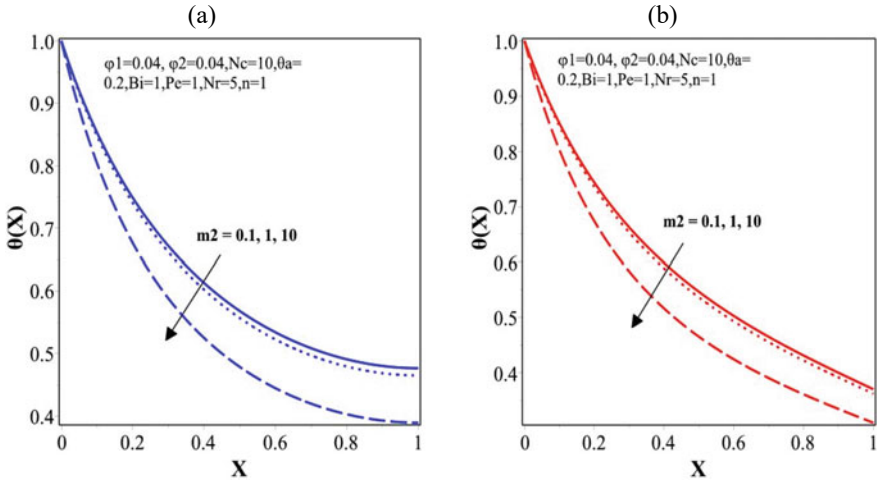

Fig. 7 **a** & **b**: Effect of wet porous variable (m_2) on thermal profile for convective and insulated tip condition, respectively

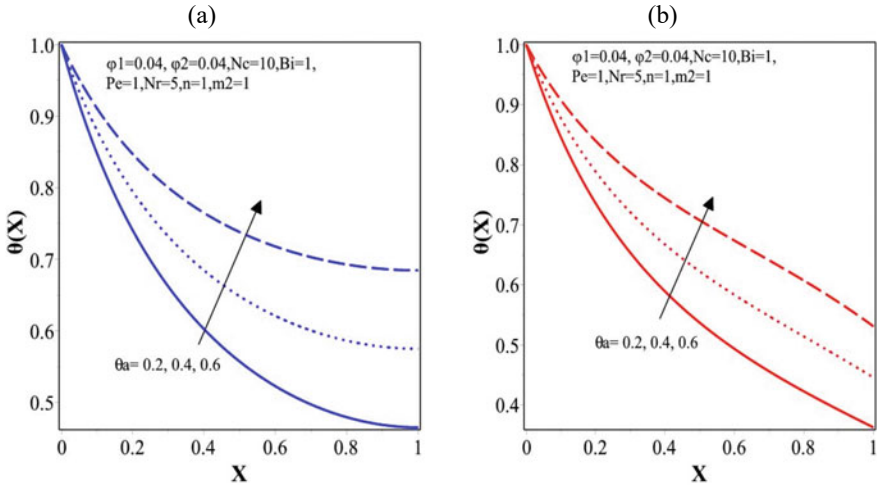

Fig. 8 **a** & **b**: Effect of ambient temperature (θ_a) on thermal profile for convective and insulated tip condition, respectively

which is given in Table 5. Then using these weights, weighted normalized matrix formed, which seen in Table 6. The value of $V+$ (positive ideal solutions) and $V-$ (negative ideal solutions) of every attributes were calculated in next step, given in Table 7. Next the Euclidean distances $(S+)$ and $(S-)$ were determined, presented in Table 8. After this, performance score (Pi) were determined, seen in Table 8. Finally, when all of the findings have been obtained, the ranking of alternatives were

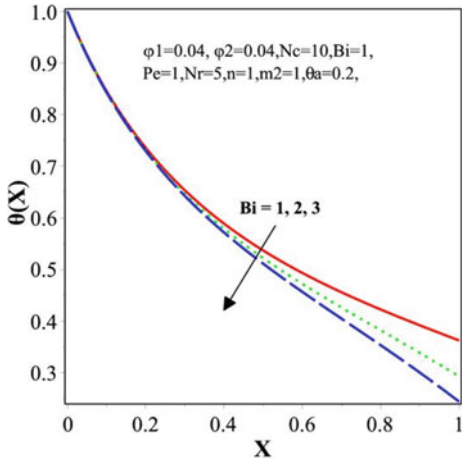

Fig. 9 Effect of Biot number (Bi) on thermal profile for convective condition

completed in order to obtain the best possible collection of choices, given in Table 8. The alternative with the highest Pi value chosen as the best option. The A12 with $Nc = 0.000688$, $Nr = 0.006586$, $m_2 = 0.000299$, $\theta_a = 0.006173$, $n = 0$, and $Pe = 0.003574$ has highest value 0.952634, so evaluated as 1. A29 has minimum value 0.018997 of Pi and ranked at position 53. The ranking of alternatives in descending order were based on the value of Pi given as A12 > A31 > A45 > A24 > A48 > A1 > A22 > A42 > A21 > A34 > A4 > A39 > A49 > A47 > A30 > A6 > A8 > A9 > A16 > A17 > A19 > A35 > A38 > A40 > A53 > A5 > A46 > A28 > A36 > A41 > A44 > A25 > A20 > A32 > A27 > A51 > A15 > A10 > A3 > A14 > A18 > A52 > A26 > A2 > A50 > A11 > A37 > A33 > A23 > A7 > A43 > A13 > A29.

3.3 Conclusion

The thermal properties of a HyNF were examined for a moving fin with two different boundary conditions. With the help of graphs, the results of the different variables were displayed. The features of heat transportation explained as:

- The effect of natural convection and thermal radiation is very important for cooling of fin.
- The bigger values of moist porous parameter upgrade HT rate.
- Lower value of Peclet number results greater HT rate.
- The power value and dimensionless surroundings temperature have negative effect on HT of fin.
- The Nc and Nr increases HT rate from the fin surface. For that reason, convection and radiation import heat from the fin.
- HyNF is supportive for the better HT aspect.

Table 2 Decision matrix

Hybrid nanofluid (Cu-Al_2O_3 water based)							
Sr. No	Nc	Nr	m_2	ϴa	n	Pe	con(−Θ(0))
1	1	1	10	0.6	0	1	1.105639
2	50	10	1	0.4	1	2	2.501558
3	50	5	10	0.4	1	2	2.547982
4	50	5	1	0.4	0	2	2.237797
5	50	5	1	0.4	1	3	2.092063
6	50	5	1	0.4	1	2	2.237797
7	100	10	10	0.2	0	3	4.937714
8	50	5	1	0.4	1	2	2.237797
9	50	5	1	0.4	1	2	2.237797
10	100	1	0.1	0.6	2	3	1.456658
11	100	10	0.1	0.2	0	1	4.939762
12	1	1	0.1	0.2	0	1	0.639338
13	100	10	10	0.2	2	1	5.177862
14	100	1	10	0.2	0	1	5.131094
15	100	1	0.1	0.2	2	1	4.65253
16	50	5	1	0.4	1	2	2.237797
17	50	5	1	0.4	1	2	2.237797
18	100	1	10	0.6	0	3	1.748274
19	50	5	1	0.4	1	2	2.237797
20	100	1	0.1	0.2	0	3	4.223508
21	1	1	10	0.6	2	3	0.685074
22	1	5	1	0.4	1	2	1.024565
23	100	10	0.1	0.6	2	1	2.133481
24	1	1	0.1	0.6	2	1	0.465723
25	1	10	10	0.6	0	3	1.467637
26	100	1	10	0.6	2	1	1.82979
27	1	10	10	0.6	2	1	1.552536
28	50	5	1	0.6	1	2	1.388754
29	100	10	10	0.6	2	3	2.042455
30	50	5	1	0.4	1	1	2.401603
31	1	1	0.1	0.6	0	3	0.273793
32	1	10	10	0.2	2	3	1.922524
33	100	10	0.1	0.2	2	3	4.509393
34	50	1	1	0.4	1	2	2.00585
35	50	5	1	0.4	1	2	2.237797

(continued)

Table 2 (continued)

Hybrid nanofluid (Cu-Al_2O_3 water based)							
Sr. No	Nc	Nr	m_2	ɵa	n	Pe	con(−Θ(0))
36	50	5	1	0.4	2	2	2.229811
37	100	10	0.1	0.6	0	3	1.902752
38	50	5	1	0.4	1	2	2.237797
39	50	5	1	0.2	1	2	3.257493
40	50	5	1	0.4	1	2	2.237797
41	1	10	0.1	0.6	2	3	1.119156
42	1	1	10	0.2	2	1	1.581234
43	100	10	10	0.6	0	1	2.387477
44	1	10	10	0.2	0	1	2.651105
45	1	1	0.1	0.2	2	3	0.395394
46	1	10	0.1	0.2	2	1	1.663055
47	1	10	0.1	0.2	0	3	1.362625
48	1	1	10	0.2	0	3	1.636133
49	50	5	0.1	0.4	1	2	2.204732
50	100	5	1	0.4	1	2	3.060252
51	100	1	0.1	0.6	0	1	1.659535
52	100	1	10	0.2	2	3	4.479007
53	1	10	0.1	0.6	0	1	1.350318

Table 3 Normal values

Nc	Nr	m_2	ɵa	n	Pe	con(−Θ(0))
466.3872	46.8188	41.46287	3.136877	9.327379	15.68439	18.75157

- The Biot number (Bi) has direct relation with the HT rate of fin surface. Bigger Bi enhances the rate of HT from the fin area.
- The fin which has insulated tip express constant temperature at the tip region. On the other hand, the fin of known convective tip efficiently transport the heat to the neighboring region. That's why for convective boundary condition the HT rate is more as compared to insulated tip condition.

Table 4 Normalized decision matrix

Sr. No	Nc	Nr	m_2	ɵa	N	Pe	con(−Θ(0))
1	0.002144	0.021359	0.24118	0.191273	0	0.063758	0.058963
2	0.107207	0.213589	0.024118	0.127515	0.107211	0.127515	0.133405
3	0.107207	0.106795	0.24118	0.127515	0.107211	0.127515	0.135881
4	0.107207	0.106795	0.024118	0.127515	0	0.127515	0.119339
5	0.107207	0.106795	0.024118	0.127515	0.107211	0.191273	0.111567
6	0.107207	0.106795	0.024118	0.127515	0.107211	0.127515	0.119339
7	0.214414	0.213589	0.24118	0.063758	0	0.191273	0.263323
8	0.107207	0.106795	0.024118	0.127515	0.107211	0.127515	0.119339
9	0.107207	0.106795	0.024118	0.127515	0.107211	0.127515	0.119339
10	0.214414	0.021359	0.002412	0.191273	0.214423	0.191273	0.077682
11	0.214414	0.213589	0.002412	0.063758	0	0.063758	0.263432
12	0.002144	0.021359	0.002412	0.063758	0	0.063758	0.034095
13	0.214414	0.213589	0.24118	0.063758	0.214423	0.063758	0.27613
14	0.214414	0.021359	0.24118	0.063758	0	0.063758	0.273636
15	0.214414	0.021359	0.002412	0.063758	0.214423	0.063758	0.248114
16	0.107207	0.106795	0.024118	0.127515	0.107211	0.127515	0.119339
17	0.107207	0.106795	0.024118	0.127515	0.107211	0.127515	0.119339
18	0.214414	0.021359	0.24118	0.191273	0	0.191273	0.093234
19	0.107207	0.106795	0.024118	0.127515	0.107211	0.127515	0.119339
20	0.214414	0.021359	0.002412	0.063758	0	0.191273	0.225235
21	0.002144	0.021359	0.24118	0.191273	0.214423	0.191273	0.036534
22	0.002144	0.106795	0.024118	0.127515	0.107211	0.127515	0.054639
23	0.214414	0.213589	0.002412	0.191273	0.214423	0.063758	0.113776
24	0.002144	0.021359	0.002412	0.191273	0.214423	0.063758	0.024837
25	0.002144	0.213589	0.24118	0.191273	0	0.191273	0.078267
26	0.214414	0.021359	0.24118	0.191273	0.214423	0.063758	0.097581
27	0.002144	0.213589	0.24118	0.191273	0.214423	0.063758	0.082795
28	0.107207	0.106795	0.024118	0.191273	0.107211	0.127515	0.074061
29	0.214414	0.213589	0.24118	0.191273	0.214423	0.191273	0.108922
30	0.107207	0.106795	0.024118	0.127515	0.107211	0.063758	0.128075
31	0.002144	0.021359	0.002412	0.191273	0	0.191273	0.014601
32	0.002144	0.213589	0.24118	0.063758	0.214423	0.191273	0.102526
33	0.214414	0.213589	0.002412	0.063758	0.214423	0.191273	0.240481
34	0.107207	0.021359	0.024118	0.127515	0.107211	0.127515	0.10697
35	0.107207	0.106795	0.024118	0.127515	0.107211	0.127515	0.119339
36	0.107207	0.106795	0.024118	0.127515	0.214423	0.127515	0.118913

(continued)

Table 4 (continued)

Sr. No	Nc	Nr	m_2	ɵa	N	Pe	con(−Θ(0))
37	0.214414	0.213589	0.002412	0.191273	0	0.191273	0.101472
38	0.107207	0.106795	0.024118	0.127515	0.107211	0.127515	0.119339
39	0.107207	0.106795	0.024118	0.063758	0.107211	0.127515	0.173718
40	0.107207	0.106795	0.024118	0.127515	0.107211	0.127515	0.119339
41	0.002144	0.213589	0.002412	0.191273	0.214423	0.191273	0.059683
42	0.002144	0.021359	0.24118	0.063758	0.214423	0.063758	0.084325
43	0.214414	0.213589	0.24118	0.191273	0	0.063758	0.127321
44	0.002144	0.213589	0.24118	0.063758	0	0.063758	0.14138
45	0.002144	0.021359	0.002412	0.063758	0.214423	0.191273	0.021086
46	0.002144	0.213589	0.002412	0.063758	0.214423	0.063758	0.088689
47	0.002144	0.213589	0.002412	0.063758	0	0.191273	0.072667
48	0.002144	0.021359	0.24118	0.063758	0	0.191273	0.087253
49	0.107207	0.106795	0.002412	0.127515	0.107211	0.127515	0.117576
50	0.214414	0.106795	0.024118	0.127515	0.107211	0.127515	0.1632
51	0.214414	0.021359	0.002412	0.191273	0	0.063758	0.088501
52	0.214414	0.021359	0.24118	0.063758	0.214423	0.191273	0.23886
53	0.002144	0.213589	0.002412	0.191273	0	0.063758	0.072011

Table 5 Weight matrix genenrated with the use of ahp (see Appendix 1)

	nc	nr	m_2	ɵa	n	pe	con(−Θ(0))	Weights
Nc	0.390456	0.515601	0.488941	0.214925	0.214925	0.238938	0.183673	0.321066
Nr	0.195228	0.257801	0.293364	0.501493	0.429851	0.358407	0.122449	0.30837
m_2	0.078091	0.085934	0.097788	0.143284	0.161194	0.159292	0.142857	0.124063
ɵa	0.130152	0.036829	0.048894	0.071642	0.107463	0.119469	0.163265	0.096816
N	0.097614	0.032225	0.032596	0.035821	0.053731	0.079646	0.183673	0.073615
Pe	0.065076	0.028645	0.024447	0.023881	0.026866	0.039823	0.183673	0.056059
con(−Θ(0))	0.043384	0.042967	0.01397	0.008955	0.00597	0.004425	0.020408	0.020011

Table 6 Weighted normalized decision matrix

Sr. No	Nc	Nr	m_2	ɵa	N	Pe	con(−Θ(0))
1	0.000688	0.006586	0.029921	0.018518	0	0.003574	0.00118
2	0.034421	0.065865	0.002992	0.012346	0.007892	0.007148	0.00267
3	0.034421	0.032932	0.029921	0.012346	0.007892	0.007148	0.002719
4	0.034421	0.032932	0.002992	0.012346	0	0.007148	0.002388
5	0.034421	0.032932	0.002992	0.012346	0.007892	0.010722	0.002233
6	0.034421	0.032932	0.002992	0.012346	0.007892	0.007148	0.002388
7	0.068841	0.065865	0.029921	0.006173	0	0.010722	0.005269
8	0.034421	0.032932	0.002992	0.012346	0.007892	0.007148	0.002388
9	0.034421	0.032932	0.002992	0.012346	0.007892	0.007148	0.002388
10	0.068841	0.006586	0.000299	0.018518	0.015785	0.010722	0.001555
11	0.068841	0.065865	0.000299	0.006173	0	0.003574	0.005272
12	0.000688	0.006586	0.000299	0.006173	0	0.003574	0.000682
13	0.068841	0.065865	0.029921	0.006173	0.015785	0.003574	0.005526
14	0.068841	0.006586	0.029921	0.006173	0	0.003574	0.005476
15	0.068841	0.006586	0.000299	0.006173	0.015785	0.003574	0.004965
16	0.034421	0.032932	0.002992	0.012346	0.007892	0.007148	0.002388
17	0.034421	0.032932	0.002992	0.012346	0.007892	0.007148	0.002388
18	0.068841	0.006586	0.029921	0.018518	0	0.010722	0.001866
19	0.034421	0.032932	0.002992	0.012346	0.007892	0.007148	0.002388
20	0.068841	0.006586	0.000299	0.006173	0	0.010722	0.004507
21	0.000688	0.006586	0.029921	0.018518	0.015785	0.010722	0.000731
22	0.000688	0.032932	0.002992	0.012346	0.007892	0.007148	0.001093
23	0.068841	0.065865	0.000299	0.018518	0.015785	0.003574	0.002277
24	0.000688	0.006586	0.000299	0.018518	0.015785	0.003574	0.000497
25	0.000688	0.065865	0.029921	0.018518	0	0.010722	0.001566
26	0.068841	0.006586	0.029921	0.018518	0.015785	0.003574	0.001953
27	0.000688	0.065865	0.029921	0.018518	0.015785	0.003574	0.001657
28	0.034421	0.032932	0.002992	0.018518	0.007892	0.007148	0.001482
29	0.068841	0.065865	0.029921	0.018518	0.015785	0.010722	0.00218
30	0.034421	0.032932	0.002992	0.012346	0.007892	0.003574	0.002563
31	0.000688	0.006586	0.000299	0.018518	0	0.010722	0.000292
32	0.000688	0.065865	0.029921	0.006173	0.015785	0.010722	0.002052
33	0.068841	0.065865	0.000299	0.006173	0.015785	0.010722	0.004812
34	0.034421	0.006586	0.002992	0.012346	0.007892	0.007148	0.002141
35	0.034421	0.032932	0.002992	0.012346	0.007892	0.007148	0.002388
36	0.034421	0.032932	0.002992	0.012346	0.015785	0.007148	0.00238

(continued)

Table 6 (continued)

Sr. No	Nc	Nr	m_2	ɵa	N	Pe	con(−Θ(0))
37	0.068841	0.065865	0.000299	0.018518	0	0.010722	0.002031
38	0.034421	0.032932	0.002992	0.012346	0.007892	0.007148	0.002388
39	0.034421	0.032932	0.002992	0.006173	0.007892	0.007148	0.003476
40	0.034421	0.032932	0.002992	0.012346	0.007892	0.007148	0.002388
41	0.000688	0.065865	0.000299	0.018518	0.015785	0.010722	0.001194
42	0.000688	0.006586	0.029921	0.006173	0.015785	0.003574	0.001687
43	0.068841	0.065865	0.029921	0.018518	0	0.003574	0.002548
44	0.000688	0.065865	0.029921	0.006173	0	0.003574	0.002829
45	0.000688	0.006586	0.000299	0.006173	0.015785	0.010722	0.000422
46	0.000688	0.065865	0.000299	0.006173	0.015785	0.003574	0.001775
47	0.000688	0.065865	0.000299	0.006173	0	0.010722	0.001454
48	0.000688	0.006586	0.029921	0.006173	0	0.010722	0.001746
49	0.034421	0.032932	0.000299	0.012346	0.007892	0.007148	0.002353
50	0.068841	0.032932	0.002992	0.012346	0.007892	0.007148	0.003266
51	0.068841	0.006586	0.000299	0.018518	0	0.003574	0.001771
52	0.068841	0.006586	0.029921	0.006173	0.015785	0.010722	0.00478
53	0.000688	0.065865	0.000299	0.018518	0	0.003574	0.001441

Table 7 Ideals best and ideals worst

V+	0.000688	0.006586	0.000299	0.006173	0	0.003574	0.005526
V−	0.068841	0.065865	0.029921	0.018518	0.015785	0.010722	0.000292

Table 8 Euclidean distance, performance score, or closeness index and ranking

Sr. No	S+	S−	p = s−/(s+) + (s−)	Rank
1	0.032385	0.091977	0.739592	6
2	0.06914	0.045042	0.394475	44
3	0.053202	0.048871	0.478783	39
4	0.043588	0.057436	0.568538	11
5	0.044739	0.055666	0.554415	26
6	0.044297	0.055786	0.557397	16
7	0.095327	0.020648	0.178038	50
8	0.044297	0.055786	0.557397	17
9	0.044297	0.055786	0.557397	18
10	0.071507	0.066279	0.481031	38
11	0.090326	0.03681	0.28953	46
12	0.004843	0.097411	0.952634	1
13	0.09636	0.015195	0.136214	52
14	0.074312	0.063194	0.459572	40
15	0.069959	0.067946	0.492704	37
16	0.044297	0.055786	0.557397	19
17	0.044297	0.055786	0.557397	20
18	0.075757	0.061364	0.447516	41
19	0.044297	0.055786	0.557397	21
20	0.068534	0.069359	0.502992	33
21	0.036785	0.090326	0.710609	9
22	0.028882	0.081045	0.737262	7
23	0.092579	0.030537	0.248035	49
24	0.020661	0.095327	0.821873	4
25	0.067901	0.069968	0.507497	32
26	0.077049	0.059731	0.436692	43
27	0.069339	0.06854	0.497102	35
28	0.04564	0.055416	0.548369	28
29	0.097468	0.001887	0.018997	53
30	0.04414	0.056135	0.559808	15
31	0.015195	0.09636	0.863786	2
32	0.068584	0.069284	0.502541	34
33	0.091975	0.032409	0.260553	48
34	0.035633	0.074434	0.676259	10
35	0.044297	0.055786	0.557397	22
36	0.046359	0.055224	0.543637	29

(continued)

Table 8 (continued)

Sr. No	S+	S−	p = s−/(s+) + (s−)	Rank
37	0.091512	0.03361	0.26862	47
38	0.044297	0.055786	0.557397	23
39	0.0438	0.056852	0.564834	12
40	0.044297	0.055786	0.557397	24
41	0.063129	0.074317	0.540699	30
42	0.033784	0.091456	0.730245	8
43	0.095903	0.017474	0.154124	51
44	0.066322	0.071441	0.51858	31
45	0.018064	0.095857	0.841435	3
46	0.061458	0.075683	0.551862	27
47	0.059846	0.076975	0.562596	14
48	0.030706	0.092533	0.750842	5
49	0.044218	0.057133	0.563717	13
50	0.073922	0.043951	0.372871	45
51	0.069363	0.068511	0.49691	36
52	0.076309	0.060716	0.443102	42
53	0.060688	0.076314	0.55703	25

Appendix 1 (Calculating weight function with the help of AHP)

Step 1

We make initial pairwise comparison matrix and developed entries according to preference scale.

	Nc	Nr	m_2	ɵa	n	Pe	con(−Θ(0))
Nc	1	2	5	3	4	6	9
Nr	0.5	1	3	7	8	9	6
m_2	0.2	0.333333	1	2	3	4	7
ɵa	0.333333	0.142857	0.5	1	2	3	8
N	0.25	0.125	0.333333	0.5	1	2	9
Pe	0.166667	0.111111	0.25	0.333333	0.5	1	9
con(−Θ(0))	0.111111	0.166667	0.142857	0.125	0.111111	0.111111	1

Step 2

In this step, we will calculate normalize value for each column by taking sum of all the entries of each column, then we will obtain the normalized matrix by dividing the each entry of a column with its corresponding normalized value.

	Nc	Nr	m_2	ɵa	n	Pe	con(−Θ(0))
Nc	1	2	5	3	4	6	9
Nr	0.5	1	3	7	8	9	6
m_2	0.2	0.333333	1	2	3	4	7
ɵa	0.333333	0.142857	0.5	1	2	3	8
N	0.25	0.125	0.333333	0.5	1	2	9
Pe	0.166667	0.111111	0.25	0.333333	0.5	1	9
con(−Θ(0))	0.111111	0.166667	0.142857	0.125	0.111111	0.111111	1
Average	2.561111	3.878968	10.22619	13.95833	18.61111	25.11111	49

	Nc	Nr	m_2	ɵa	n	Pe	con(−Θ(0))
Nc	0.390456	0.515601	0.488941	0.214925	0.214925	0.238938	0.183673
Nr	0.195228	0.257801	0.293364	0.501493	0.429851	0.358407	0.122449
m_2	0.078091	0.085934	0.097788	0.143284	0.161194	0.159292	0.142857
ɵa	0.130152	0.036829	0.048894	0.071642	0.107463	0.119469	0.163265
N	0.097614	0.032225	0.032596	0.035821	0.053731	0.079646	0.183673
Pe	0.065076	0.028645	0.024447	0.023881	0.026866	0.039823	0.183673
con(−Θ(0))	0.043384	0.042967	0.01397	0.008955	0.00597	0.004425	0.020408

Step 3

In last step we will take average value of each row, which is called assigned weight for each alternative.

	Nc	Nr	m_2	ɵa	n	Pe	con(−Θ(0))
Nc	0.390456	0.515601	0.488941	0.214925	0.214925	0.238938	0.183673
Nr	0.195228	0.257801	0.293364	0.501493	0.429851	0.358407	0.122449
m_2	0.078091	0.085934	0.097788	0.143284	0.161194	0.159292	0.142857
ɵa	0.130152	0.036829	0.048894	0.071642	0.107463	0.119469	0.163265
N	0.097614	0.032225	0.032596	0.035821	0.053731	0.079646	0.183673
Pe	0.065076	0.028645	0.024447	0.023881	0.026866	0.039823	0.183673
con(−Θ(0))	0.043384	0.042967	0.01397	0.008955	0.00597	0.004425	0.020408

Scale for relative importance

1	Equal importance
3	Moderate importance
5	Strong importance
7	Very strong importamce
9	Extreme importance
2, 4, 6, 8	Intermediate importance

References

1. Amani M, Amani P, Mahian O, Estellé P (2017) Multi-objective optimization of thermophysical properties of eco-friendly organic nanofluids. J Clean Prod 166:350–359
2. Baskar S, Chandrasekaran M, Vinod Kumar T, Vivek P, Karikalan L (2020) Experimental studies on convective heat transfer coefficient of water/ethylene glycol-carbon nanotube nanofluids. Int J Ambient Energy 41(3):296–299
3. Bumataria RK, Chavda NK, Panchal H (2019) Current research aspects in mono and hybrid nanofluid based heat pipe technologies. Heliyon 5(5):e01627
4. Choi SU, Eastman JA (1995) Enhancing thermal conductivity of fluids with nanoparticles (No. ANL/MSD/CP-84938; CONF-951135–29). Argonne National Lab, IL United States
5. Coccia G, Di Nicola G, Colla L, Fedele L, Scattolini M (2016) Adoption of nanofluids in low-enthalpy parabolic trough solar collectors: numerical simulation of the yearly yield. Energy Convers Manage 118:306–319
6. Eltaweel M, Abdel-Rehim AA (2021) Energy and exergy analysis for stationary solar collectors using nanofluids: a review. Int J Energy Res 45(3):3643–3670
7. Esfe MH, Behbahani PM, Arani AAA, Sarlak MR (2017) Thermal conductivity enhancement of SiO 2–MWCNT (85: 15%)–EG hybrid nanofluids. J Therm Anal Calorim 128(1):249–258
8. Fernández AG, Muñoz-Sánchez B, Nieto-Maestre J, García-Romero A (2019) High temperature corrosion behavior on molten nitrate salt-based nanofluids for CSP plants. Renew Energy 130:902–909
9. Fallah B, Dinarvand S, Eftekhari Yazdi M, Rostami MN, Pop I (2019) MHD flow and heat transfer of SiC-TiO2/DO hybrid nanofluid due to a permeable spinning disk by a novel algorithm. J Appl Comput Mech 5(5):976–988
10. Farooq U, Afridi MI, Qasim M, Lu DC (2018) Transpiration and viscous dissipation effects on entropy generation in hybrid nanofluid flow over a nonlinear radially stretching disk. Entropy 20(9):668
11. Goel N, Taylor RA, Otanicar T (2020) A review of nanofluid-based direct absorption solar collectors: design considerations and experiments with hybrid PV/Thermal and direct steam generation collectors. Renewable Energy 145:903–913
12. Ghalambaz M, Doostani A, Izadpanahi E, Chamkha AJ (2020) Conjugate natural convection flow of Ag–MgO/water hybrid nanofluid in a square cavity. J Therm Anal Calorim 139(3):2321–2336
13. Gholinia M, Hosseinzadeh K, Ganji DD (2020) Investigation of different base fluids suspend by CNTs hybrid nanoparticle over a vertical circular cylinder with sinusoidal radius. Case Stud Therm Eng 21:100666

14. Gireesha BJ, Sowmya G, Khan MI, Öztop HF (2020) Flow of hybrid nanofluid across a permeable longitudinal moving fin along with thermal radiation and natural convection. Comput Methods Program Biomed 185:105166
15. Gupta MK, Sood PK, Singh G, Sharma VS (2018) Investigations of performance parameters in NFMQL assisted turning of titanium alloy using TOPSIS and particle swarm optimisation method. Int J Mater Prod Technol 57(4):299–321
16. Hosseinzadeh K, Roghani S, Asadi A, Mogharrebi A, Ganji DD (2020) Investigation of micropolar hybrid ferrofluid flow over a vertical plate by considering various base fluid and nanoparticle shape factor. Int J Numer Method Heat Fluid Flow
17. Kaggwa A, Carson JK (2019) Developments and future insights of using nanofluids for heat transfer enhancements in thermal systems: a review of recent literature. Int Nano Lett 9(4):277–288
18. Kaushal R, Kumar R (2020) Heat transfer enhancement using augmented tubes for desalination using fuzzy-TOPSIS approach. Renew Energy Res Appl 1(1):19–26
19. Maisuria MB, Sonar DM, Rathod MK (2021) Nanofluid selection used for coolant in heat exchanger by multiple attribute decision-making method. J Mech Sci Technol 35(2):689–695
20. Maxwell JC (1873) A treatise on electricity and magnetism, vol 1. Clarendon Press
21. Mehryan SAM, Sheremet MA, Soltani M, Izadi M (2019) Natural convection of magnetic hybrid nanofluid inside a double-porous medium using two-equation energy model. J Mol Liq 277:959–970
22. Olfian H, Ajarostaghi SSM, Ebrahimnataj M (2020) Development on evacuated tube solar collectors: a review of the last decade results of using nanofluids. Sol Energy 211:265–282
23. Raj SON, Prabhu S (2020) Investigation on slicing behavior of single crystal silicon wafer in AWJM and influence of micro dimple textured surface for solar applications. Silicon, 1–19
24. Rashmi W, Ismail AF, Khalid M, Anuar A, Yusaf T (2014) Investigating corrosion effects and heat transfer enhancement in smaller size radiators using CNT-nanofluids. J Mater Sci 49(13):4544–4551
25. Saaty T (1980) The analytic hierarchy process (AHP) for decision making. In: Kobe, Japan, pp 1–69
26. Sui D, Langåker VH, Yu Z (2017) Investigation of thermophysical properties of Nanofluids for application in geothermal energy. Energy Procedia 105:5055–5060
27. Sheikholeslami M, Mehryan SAM, Shafee A, Sheremet MA (2019) Variable magnetic forces impact on magnetizablehybrid nanofluid heat transfer through a circular cavity. J Mol Liq 277:388–396
28. Tassaddiq A, Khan S, Bilal M, Gul T, Mukhtar S, Shah Z, Bonyah E (2020) Heat and mass transfer together with hybrid nanofluid flow over a rotating disk. AIP Adv 10(5):055317
29. Usman M, Hamid M, Zubair T, Haq RU, Wang W (2018) Cu-Al2O3/Water hybrid nanofluid through a permeable surface in the presence of nonlinear radiation and variable thermal conductivity via LSM. Int J Heat Mass Transf 126:1347–1356
30. Xue H (2019) Modelling unsteady mixed convection of a nanofluid suspended with multiple kinds of nanoparticles between two rotating disks by generalized hybrid model. Int Commun Heat Mass Transfer 108:104275

Chapter 12
Radiation Effect on Rayleigh-Bénard Convection in Nanofluids: General Boundary Condition

Heena Firdose, P. G. Siddheshwar, Reena Nandal, and Ruwaidiah Idris

Abstract The thermal radiation effects on the Rayleigh-Bénard convection in an absorbing and emitting Newtonian nanofluid, subjected to general boundary conditions, are studied analytically. Single-phase description is used for water-copper and water-alumina nanofluids considered for investigation. Transparent and opaque media are considered under the assumption of wave length being independent of the optical properties of the nanofluid. The opaque medium holds heat longer than that held by the transparent medium and hence onset of convection is much delayed in the first medium. Significant effects on cell size at the onset of convection due to radiation were observed in the case of transparent medium. In the presence of radiation, water-copper and water-alumina nanofluid continue to behave much the same way as in its absence. The general boundary condition bridges the gap between the results of free-free isothermal to rigid-rigid isothermal boundaries, and similarly for adiabatic boundaries.

Nomenclature

(x, y)	is the dimensional coordinate system [m],
$\vec{v}$	is the velocity vector [m/s],
$\vec{g}$	is the acceleration due to gravity [m/s^3],
p	is the hydrostatic pressure [Pa],
t	is the dimensional time [s],
T	is the dimensional temperature [K],
T_0	is the reference temperature [K],

H. Firdose (✉) · P. G. Siddheshwar · R. Nandal
Department of Mathematics, Centre for Mathematical Needs, CHRIST (Deemed to be University), Bengaluru 560029, India
e-mail: heena.firdose@res.christuniversity.in

R. Idris
Special Interest Group Modelling and Data Analytics, Faculty of Ocean Engineering Technology and Informatics, Universiti Malaysia Terengganu, 21030 Kuala Nerus, Terengganu, Malaysia

D. Tripathi et al. (eds.), *Advancements in Nanotechnology for Energy and Environment*, Advances in Sustainability Science and Technology,
https://doi.org/10.1007/978-981-19-5201-2_12

ΔT	is the temperature difference between the horizontal plates [K],
k_f	is the thermal conductivity [W/(mK)],
k_{np}	is the thermal conductivity of the nanoparticle [W/(mK)],
k_{nf}	is the thermal conductivity of the nanofluid [W/(mK)],
k_s	is the thermal conductivity of the tightly-packed porous medium [W/(mK)],
$(k_{nf})_m = \Phi k_{nf} + (1 - \Phi)k_s$	is the thermal conductivity of the nanofluid-saturated tightly-packed porous medium [W/(mK)],
h_l, h_u	are heat transfer coefficients of lower and upper horizontal walls [$W/(m^3K)$],
K_l, K_u	are permeabilities of underlying and overlying porous environments [m^2],
μ_f	is the dynamic coefficient of viscosity of the carrier fluid [kg/(ms)],
μ_{np}	is the dynamic coefficient of viscosity of the nanoparticle [kg/(ms)],
μ_{nf}	is the dynamic coefficient of viscosity of the nanofluid [kg/(ms)],
$(C_p)_f$	is the heat capacity at constant pressure of the carrier fluid [J/(KgK),
$(C_p)_{np}$	is the heat capacity at constant pressure of the nanoparticle [J/(KgK)],
$(C_p)_{nf}$	is the heat capacity at constant pressure of the nanofluid [J/(KgK)],
ρ_f	is the density of the carrier fluid [kg/m^3],
ρ_{np}	is the density of the nanoparticle [kg/m^3],
ρ_{nf}	is the density of the nanofluid [kg/m^3],
ρ_0	is the reference density [kg/m^3],
α_f	is the thermal diffusivity of the carrier fluid [m^2/s],
α_{nf}	is the thermal diffusivity of the nanofluid [m^2/s],
G	is the rate of radiative heating per unit volume [J/s],
s_r	is the heat content per unit volume [J/s],
ϕ_{np}	is the volume fraction of nanoparticles,
Φ	is the porosity of the tightly-packed porous medium,
Θ	is the non-dimensional temperature,
Ψ	is the non-dimensional stream function,
τ	is the absorptivity parameter,
χ	is the conduction-radiative parameter,
Pr_{nf}	is the nanofluid Prandtl number,
Ra_{nf}	is the nanofluid Rayleigh number,
Ds_l	is the slip-Darcy number at the lower boundary,
Ds_u	is the slip-Darcy number at the upper boundary,

Bi_l	is the Biot number at the lower boundary,
Bi_u	is the Biot number at the upper boundary,
a_1	is the thermal diffusivity ratio,
b_1	is the thermal conductivity ratio,
$\nabla^2 = \frac{\partial^2}{\partial x^2} + \frac{\partial^2}{\partial y^2}$	is the Laplacian operator.

1 Introduction

Rayleigh-Bénard convection (RBC) occurs in a plane horizontal layer of a fluid heated from below and cooled from above. It has been a topic of interest among the researchers for many years. Some of the earliest works on RBC problems were [1–5]. RBC in a Newtonian-Boussinesq fluid has intrigued many authors in the past decade and is now a part of standard content in books as well [6–11]. Compared to the study on RBC, the number of works available on studying the effect of radiation on RBC is quite sparse.

The convective instability problem with radiating fluids has a wide range of applications in astrophysics, geophysics, solar industries, smart materials, etc. Heat transfer in a Rayleigh-Bénard configuration is usually due to conduction and convection. But many a time in physical applications, radiative heat transfer also has a prominent role to play. Goody [12] studied the radiative heat transfer in transparent and opaque media, in the case of free isothermal boundaries. Spiegel [13] studied the thermal stability of a gray, radiating fluid layer with an adverse temperature gradient. It was shown that if the difference between the temperature gradient and the adiabatic gradient is constant, overstability cannot occur. The critical value of the Rayleigh number was computed for rigid bounding surfaces. Murugai and Khosla [14, 15] carried out a study to analyze the combined effect of thermal radiative transfer, magnetic field, and rotation on RBC. Gille and Goody [16] carried out a theoretical and experimental study of the effect of radiative transfer on the onset of convection through comparative experiments in dry air and ammonia contained between horizontal aluminum plates that were maintained at different temperatures. Christophorides and Davis [17] performed a linear stability analysis of RBC in a thin fluid layer bounded between rigid horizontal planes heated from below with radiation effects. The critical value of the Rayleigh number and the wavenumber were computed for a gray, transparent medium. The results were limited for the range of optical thickness, which shows molecular heat conduction is negligible in the whole range except when the optical thickness (opacity) approaches zero. Arpaci and Gozum [18] studied the RBC problem in a radiating non-gray fluid considering the Eddington approximation. The optical thickness, Planck number, non-grayness of the fluid, and emissivity of boundaries were the parameters that characterized effects of radiation in the problem. The results reported were for black-black, mirror-mirror, and black-mirror boundaries. Lienhard [19] studied the role of thermal radiation in plane layer instabilities under the assumption that the fluid medium is transparent.

Siegel and Howell [20] presented an analytical study which focused on radiation from opaque surfaces, radiation interchange between various types of surfaces enclosing a transparent medium, and radiation including the effects of partially transmitting media. Bdeoui and Soufiani [21] conducted a theoretical study on the onset of RBC considering the case of real molecular emitting and absorbing gases. Devi et al. [22] studied the effect of radiative transfer on Rayleigh-Bénard convection in a fluid-saturated porous layer. The approach of Goody [12] was adopted, and the critical Rayleigh number was obtained using the Galerkin method.

Lan et al. [23] conducted a study of RBC in the presence of radiation. The linear stability analysis was carried out for three-dimensional RBC using the spectral method, for black as well as gray boundaries. Ridouane et al. [24] investigated on the effect of surface radiation on RBC in a square enclosure. The influence of emissivities and Rayleigh number on the flow, temperature patterns and heat transfer rates were analyzed. Gad et al. [25] conducted a numerical study in an enclosure on RBC in the presence of surface radiation. The study was carried out with a view to determine the onset of convection and to arrive at a correlation between convection and radiation. A delayed onset of convection with an increase in the emissivity of side walls was observed and the effect of radiation was observed to diminish with an increase in the value of the aspect ratio. Mishra et al. [26] reported a numerical study of RBC in the presence of volumetric radiation. Using the Lattice-Boltzmann method, the momentum and energy equations were solved. The study reported that radiation significantly altered velocity and temperature fields in the medium. Chaabane et al. [27] also conducted a study on the interaction between transient Rayleigh-Bénard convection and volumetric radiation using the Lattice-Boltzmann method. The results obtained were quite accurate in estimating the critical Rayleigh number. In addition to the works surveyed so far on RBC in the presence of radiation, there are few books [28, 29] that elaborate on the theoretical basis of radiation.

The available work on the study on the influence of radiation on RBC mainly considers either free-free or rigid-free or rigid-rigid isothermal boundary combination. Further, these investigations adopted the simple model proposed by Goody [12] in considering the radiating media to be a gray body. Two types of such radiation-emitting and absorbing bodies are considered: Transparent (optically thin) and opaque (optically thick). In both the studies, the concerned quantities are wavelength independent. To make things simpler, Goody also considered the bounding surfaces to be of the black body type. The Goody [12] model facilitates an easy understanding of the effect of radiation on the onset of convection, and this is what was precisely investigated by a number of authors.

With the literature survey conducted, it was observed that single boundary conditions have been made use of in the reported works. The following aspects of the linear stability of the RBC problem in the presence of radiation have been unaddressed so far:

1. Permeable boundary conditions which are much different from free or rigid boundaries have not been considered.

2. Radiation type (third type) of boundary condition or Robin boundary condition has not been considered so far.
3. Transparent and opaque media do not seem to be investigated in an integrated way.
4. Accurate results for boundary conditions other than the classical ones are unavailable.

The aim of this paper is to consider all the above unaddressed features and present the results in a comprehensive way. The present work compiles and analyzes the effect of radiation on RBC subjected to general boundary combinations with respect to velocity and temperature. The general boundary condition with respect to velocity has been derived from Beavers and Joseph slip condition [30]. Siddheshwar [31] was the first to study RBC in a ferromagnetic fluid using general boundary condition on velocity. Also, studies using general boundary condition on temperature, or otherwise called as third-kind temperature condition or Robin boundary condition, were initiated by Weidmann and Kassoy [32]. Barletta and Storesletten [33–36] also carried out quite a few studies in various scenarios using general boundary condition on temperature. We now proceed to make the mathematical formulation of the problem.

2 Mathematical Formulation

Rayleigh-Bénard convection with a Newtonian radiating nanofluid between two infinitely extending horizontal plates is considered. The lower and upper horizontal walls are separated by a distance H. These walls also sandwich a nanofluid-saturated tightly-packed porous medium which enables exchange of heat and fluid with the horizontal walls. Owing to the fact that horizontal walls are permeable in nature, we consider general boundary condition in the present study. Our focus here is on two-dimensional rolls, and hence all physical quantities are assumed to be independent of z. We make the following assumptions in the present problem (Fig. 1):

1. The Oberbeck–Boussinesq approximation is valid.
2. There is thermal equilibrium between the Newtonian carrier fluid and nanoparticles.
3. There is thermal equilibrium between solid and fluid phases of nanofluid-saturated tightly-packed porous medium.

With the aforementioned facts, we now model the governing equations for the problem as follows:

$$\nabla . \overrightarrow{v} = 0, \tag{1}$$

$$\rho_{nf}\left[\frac{\partial \overrightarrow{v}}{\partial t} + \left(\overrightarrow{v}.\nabla\right)\overrightarrow{v}\right] = -\nabla \mathrm{p} + \mu_{nf}\nabla^2\overrightarrow{v} + \rho_{nf}\overrightarrow{g}, \tag{2}$$

$$\frac{\partial T}{\partial t} + \left(\overrightarrow{v}.\nabla\right)T = \alpha_{nf}\nabla^2 T + \frac{G}{s_r}, \tag{3}$$

$$\rho = \rho_0 - (\rho\beta)_{nf0}(T - T_0). \tag{4}$$

The thermophysical properties of nanofluids appearing in Eqs. (1)–(4) are obtained using phenomenological laws and mixture theory documented below:

Phenomenological laws

$$\frac{\mu_{nf}}{\mu_f} = \frac{1}{\left(1-\varphi_{np}\right)^{2.5}}[38], \tag{5}$$

$$\frac{\mathrm{k}_{nf}}{k_f} = \frac{\left(\frac{\mathrm{k}_{np}}{k_f}+2\right) - 2\varphi_{np}\left(1-\frac{\mathrm{k}_{np}}{k_f}\right)}{\left(\frac{\mathrm{k}_{np}}{k_f}+2\right) + \varphi_{np}\left(1-\frac{\mathrm{k}_{np}}{k_f}\right)}[39]. \tag{6}$$

Mixture theory

$$\left.\begin{array}{l} \alpha_{nf} = \frac{k_{nf}}{(\rho C_p)_{nf}}, \\ \frac{\rho_{nf}}{\rho_f} = \left(1-\varphi_{np}\right) + \varphi_{np}\frac{\rho_{np}}{\rho_f}, \\ \frac{(\rho C_p)_{nf}}{(\rho C_p)_f} = \left(1-\varphi_{np}\right) + \varphi_{np}\frac{(\rho C_p)_{np}}{(\rho C_p)_f}, \\ \frac{(\rho\beta)_{nf}}{(\rho\beta)_f} = \left(1-\varphi_{np}\right) + \varphi_{np}\frac{(\rho\beta)_{np}}{(\rho\beta)_f} \end{array}\right\}. \tag{7}$$

The horizontal walls at $y = 0$ and $y = H$ exchange heat with the overlying and underlying nanofluid-saturated tightly-packed porous media such that their temperature is $T_0 + \frac{\Delta T}{2}$ and $T_0 - \frac{\Delta T}{2}$, respectively. The general boundary condition on velocity and the third-type boundary condition on temperature used in the study are as follows:

$$v = 0,\ \frac{\partial u}{\partial y} = +\frac{{\gamma_l}^* u}{\sqrt{K_l}},\ +k_{nf}\frac{\partial T}{\partial y} = h_l\left(T - T_0 - \frac{\Delta T}{2}\right),\ at\ y = 0, \tag{8}$$

$$v = 0,\ \frac{\partial u}{\partial y} = -\frac{{\gamma_u}^* u}{\sqrt{K_u}},\ -k_{nf}\frac{\partial T}{\partial y} = h_u\left(T - T_0 + \frac{\Delta T}{2}\right),\ at\ y = H, \tag{9}$$

where ${\gamma_l}^*, {\gamma_u}^*$, are non-dimensional parameters that characterize the permeable property of horizontal walls.

Using the following scaling

$$\left(x^*, y^*\right) = \frac{1}{H}(x, y), \quad \overrightarrow{v}^* = \frac{H}{\alpha_f}\overrightarrow{v}, \quad t^* = \frac{\alpha_f}{H^2}t,$$

$$p^* = \frac{H^2}{\mu_f \alpha_f} p, \quad T^* = \frac{T - T_0}{\Delta T}, \tag{10}$$

we now proceed to non-dimensionalize the Eqs. (1)–(4) and (8)–(9) and by dropping the asterisk in the resulting equation, we obtain the dimensionless governing equations in component form as follows:

$$\frac{\partial u}{\partial x} + \frac{\partial v}{\partial y} = 0 \tag{11}$$

$$\frac{1}{Pr_{nf}}\left(\frac{\partial u}{\partial t} + u\frac{\partial u}{\partial x} + v\frac{\partial u}{\partial y}\right) = -\frac{a_1}{\Lambda}\frac{\partial p}{\partial x} + a_1\left(\frac{\partial^2 u}{\partial x^2} + \frac{\partial^2 u}{\partial y^2}\right), \tag{12}$$

$$\frac{1}{Pr_{nf}}\left(\frac{\partial v}{\partial t} + u\frac{\partial v}{\partial x} + v\frac{\partial v}{\partial y}\right) = -\frac{a_1}{\Lambda}\frac{\partial p}{\partial y} + a_1\left(\frac{\partial^2 u}{\partial x^2} + \frac{\partial^2 u}{\partial y^2}\right) - \frac{1}{Pr_{nf}}\left(\frac{H^2}{\alpha_f^2} g\right) + a_1 Ra_{nf} T, \tag{13}$$

$$\left(\frac{\partial T}{\partial t} + u\frac{\partial T}{\partial x} + v\frac{\partial T}{\partial y}\right) = a_1\left(\frac{\partial^2 T}{\partial x^2} + \frac{\partial^2 T}{\partial y^2}\right) + \left(\frac{H^2}{\alpha_f^2 \Delta T}\right)\frac{G}{s_r}, \tag{14}$$

$$v = 0, \quad \frac{\partial u}{\partial y} = +Ds_l u, \quad \frac{\partial T}{\partial y} = +b_1 Bi_l\left(T - \frac{1}{2}\right), \quad at\ y = 0, \tag{15}$$

$$v = 0, \quad \frac{\partial u}{\partial y} = -Ds_u u, \quad \frac{\partial T}{\partial y} = -b_1 Bi_u\left(T + \frac{1}{2}\right), \quad at\ y = 1, \tag{16}$$

where

$Pr_{nf} = \frac{\mu_{nf}}{\rho_{nf}\alpha_{nf}}$, $Ra_{nf} = \frac{(\rho\beta)_{nf}\Delta T H^3}{\mu_{nf}\alpha_{nf}}$, $a_1 = \frac{\alpha_{nf}}{\alpha_f}$, $b_1 = \frac{k_f}{(k_{nf})_m}$, $Ds_l = \frac{\tilde{\alpha}_l H}{\sqrt{K_l}}$,
$Ds_u = \frac{\tilde{\alpha}_u H}{\sqrt{K_u}}$, $Bi_l = \frac{Hh_l}{(k_{nf})_m}$, $Bi_u = \frac{Hh_u}{(k_{nf})_m}$.

Following the standard procedure, we now eliminate the pressure term from Eqs. (12)–(13) so as to reduce the number of dependent variables to obtain:

$$\frac{1}{Pr_{nf}}\left[\frac{\partial}{\partial t}\left(\frac{\partial v}{\partial x} - \frac{\partial u}{\partial y}\right) + u\frac{\partial}{\partial x}\left(\frac{\partial v}{\partial x} - \frac{\partial u}{\partial y}\right) + v\frac{\partial}{\partial y}\left(\frac{\partial v}{\partial x} - \frac{\partial u}{\partial y}\right)\right] = a_1\left(\frac{\partial^2}{\partial x^2} + \frac{\partial^2}{\partial y^2}\right)\left(\frac{\partial v}{\partial x} - \frac{\partial u}{\partial y}\right) + a_1^2 Ra_{nf}\frac{\partial T}{\partial x}. \tag{17}$$

Introducing the stream function, $\psi(x, y, t)$ in the form:

$$u = -\frac{\partial \psi}{\partial y}, \quad v = \frac{\partial \psi}{\partial x}, \tag{18}$$

and using this in Eqs. (14) and (17), we get:

$$\frac{1}{Pr_{nf}}\left[\frac{\partial}{\partial t}\left(\nabla^2\psi\right)+\frac{\partial\left(\psi,\nabla^2\psi\right)}{\partial(x,y)}\right]=a_1\nabla^4\psi+a_1^2Ra_{nf}\frac{\partial T}{\partial x}, \tag{19}$$

$$\frac{\partial T}{\partial t}+\frac{\partial(\psi,T)}{\partial(x,y)}=a_1\nabla^2T+\left(\frac{H^2}{\alpha_f^2\Delta T}\right)\frac{G}{s_r}. \tag{20}$$

Using Eq. (18) in the boundary condition given by Eqs. (15)–(16), we obtain:

$$\frac{\partial\psi}{\partial x}=0,\ \frac{\partial^2\psi}{\partial y^2}=+Ds_l\frac{\partial\psi}{\partial y},\ \frac{\partial T}{\partial y}=+b_1Bi_l\left(T-\frac{1}{2}\right),\ at\ y=0, \tag{21}$$

$$\frac{\partial\psi}{\partial x}=0,\ \frac{\partial^2\psi}{\partial y^2}=-Ds_u\frac{\partial\psi}{\partial y},\ \frac{\partial T}{\partial y}=-b_1Bi_u\left(T+\frac{1}{2}\right),\ at\ y=1. \tag{22}$$

Equations (19) and (20) which are in terms of ψ have the superposed solution:

$$\psi(x,y)=\Psi(x,y), \tag{23}$$

$$T=T_b(y)+\Theta(x,y) \tag{24}$$

where $T_b(y)$ satisfies the boundary conditions of the static state, while $\Psi(x,y)$ and $\Theta(x,y)$ satisfy those pertaining to the dynamic state. These are given by (refer appendix),

$$T_b(y)=-\beta y+\frac{1}{2}\left(\frac{Bi_l+Bi_u}{Bi_l-Bi_u}\right)-\frac{\beta Bi_u}{Bi_l-Bi_u}, \tag{25}$$

$$\frac{1}{Pr_{nf}}\left[\frac{\partial}{\partial t}\left(\nabla^2\Psi\right)+\frac{\partial\left(\Psi,\nabla^2\Psi\right)}{\partial(x,y)}\right]=a_1\nabla^4\Psi+a_1^2Ra_{nf}\frac{\partial\Theta}{\partial x}, \tag{26}$$

$$\frac{\partial\Theta}{\partial t}=\nabla^2\Theta-\chi\left(\delta_{k1}\frac{\tau^2}{1+\chi}\Theta-\delta_{k2}\nabla^2\Theta\right)+f(y)\frac{\partial\psi}{\partial x}, \tag{27}$$

$$\frac{\partial\Psi}{\partial x}=0,\ \frac{\partial^2\Psi}{\partial y^2}=+Ds_l\frac{\partial\Psi}{\partial y},\ \frac{\partial\Theta}{\partial y}=+b_1Bi_l\Theta,\ at\ y=0, \tag{28}$$

$$\frac{\partial\Psi}{\partial x}=0,\ \frac{\partial^2\Psi}{\partial y^2}=-Ds_u\frac{\partial\Psi}{\partial y},\ \frac{\partial\Theta}{\partial y}=-b_1Bi_u\Theta,\ at\ y=1, \tag{29}$$

where

$$\left.\begin{array}{ll}\delta_{km}=1, & if\ k=m\\ 0, & if\ k\neq m\end{array}\right\},\ (m,k=1,2), \tag{30}$$

and

$$\left.\begin{aligned} f(y) &= L_1 \mathrm{Cosh}(\tau y) + L_2, \\ L_1 &= \chi\left[\tfrac{2\chi}{\tau}\mathrm{Sinh}\left(\tfrac{\tau}{2}\right) + \sqrt{3+3\chi}\,\mathrm{Sinh}\left(\tfrac{\tau}{2}\right) + \mathrm{Cosh}\left(\tfrac{\tau}{2}\right)\right]^{-1}, \\ L_2 &= \tfrac{L_1}{\chi}\left[\sqrt{3+3\chi}\,\mathrm{Sinh}\left(\tfrac{\tau}{2}\right) + \mathrm{Cosh}\left(\tfrac{\tau}{2}\right)\right] \end{aligned}\right\}. \tag{31}$$

In Eq. (28), $k = 1, 2$ correspond to transparent approximation (optically thin medium) and opaque approximation (optically thick medium), respectively [12].

3 Linear Stability Analysis

To perform a linear stability analysis, we consider the following normal mode decomposition:

$$\left.\begin{aligned} \Psi(x, y) &= F(y)\,\mathrm{Sin}(\pi\kappa x), \\ \Theta(\mathrm{x}, \mathrm{y}) &= G(y)\,\mathrm{Cos}(\pi\kappa x) \end{aligned}\right\}. \tag{32}$$

Substituting Eq. (32) in Eqs. (26)–(29), we obtain the following two-point boundary-eigen-value-problem (BEVP):

$$\frac{d^4}{dy^4}\left[F(y)\right] - 2b^2\frac{d^2}{dy^2}\left[F(y)\right] + b^4F(y) - a_1 Ra_{nf}\, bG(y) = 0, \tag{33}$$

$$2(1+\chi\delta_{k2})\frac{d^2}{dy^2}\left[G(y)\right] - \left[b^2(1+\chi\delta_{k2}) - \frac{\chi}{1+\chi}\delta_{k1}\tau^2\right]G(y) + bf(y)F(y) = 0, \tag{34}$$

$$F(0) = 0,\ \frac{d^2}{dy^2}[F(0)] = +Ds_l\frac{d}{dy}[F(0)],\ \frac{d}{dy}[G(0)] = +b_1 Bi_l G(0), \tag{35}$$

$$F(1) = 0,\ \frac{d^2}{dy^2}[F(1)] = -Ds_u\frac{d}{dy}[F(1)],\ \frac{d}{dy}[G(1)] = -b_1 Bi_l G(1), \tag{36}$$

where Ra_{nf} is the eigen value of the problem which is to be determined as a function of $b = \pi\kappa$, the wave number, and the parameters arising in the problem. We now briefly take up the solution procedure adopted for obtaining Ra_{nf} and b.

4 Solution of the BEVP

Adopting Chebyshev pseudospectral-QZ method, the present range of y, [0, 1], is reset to $[-1, 1]$. We also use a coordinate transformation:

$$Y = 2y - 1. \tag{37}$$

Now, using the transformation given by Eq. (37) to rewrite Eqs. (33)–(34) we obtain:

$$16\frac{d^4}{dy^4}\big[F(y)\big] - 8b^2\frac{d^2}{dy^2}\big[F(y)\big] + b^4F(y) - a_1Ra_{nf}bG(y) = 0, \tag{38}$$

$$f\left(\frac{Y+1}{2}\right)bF(y) - \left[b^2(1-\chi\delta_{k2}) - \frac{\chi}{1+\chi}\delta_{k1}\tau^2\right]G(y) + (1+\chi\delta_{k2})\frac{d^2}{dy^2}\big[G(y)\big] = 0. \tag{39}$$

The transformed form of boundary condition in Eqs. (35)–(36) are obtained in the form:

$$F(-1) = 0,\ \frac{d^2}{dY^2}[F(-1)] = +Ds_l\frac{d}{dY}[F(-1)],\ \frac{d}{dY}[G(-1)] = +b_1Bi_lG(-1), \tag{40}$$

$$F(1) = 0,\ \frac{d^2}{dY^2}[F(1)] = -Ds_u\frac{d}{dY}[F(1)],\ \frac{d}{dY}[G(1)] = -b_1Bi_lG(1). \tag{41}$$

We note that in Eqs. (38)–(41), the unknown functions $F(y)$ and $G(y)$ can be decomposed in terms of Chebyshev polynomials that form an orthogonal basis in $y[-1, 1]$. Therefore, we consider the following series solution:

$$F(Y) = \sum_{n=0}^{15} c_nT_n(Y),\ G(Y) = \sum_{n=0}^{15} d_nT_n(Y), \tag{42}$$

where $T_n(Y) = \cos(n\cos^{-1}Y)$ is the Chebyshev polynomial which satisfies the orthogonality:

$$\int_{-1}^{1}\frac{T_n(Y)T_m(Y)}{\sqrt{1-Y^2}}dY = \frac{\pi}{h_n}\delta_{n,m} = \frac{\pi}{h_n}\left\{\begin{matrix}0, n\neq m\\ 1, n=1\end{matrix}\right. and h_n = \left\{\begin{matrix}1, n=0\\ 2, n\geq 1\end{matrix}\right\}. \tag{43}$$

The c_n's and d_n's in Eq. (42) are represented by the discrete version at the Chebyshev–Gauss–Lobbato collocation as:

$$c_n = \frac{2}{h_n N}\sum_{j=0}^{N}\frac{1}{h_j}F(Y_j)T_n(Y_j),\ d_n = \frac{2}{c_n N}\sum_{j=0}^{N}\frac{1}{h_j}G(Y_j)T_n(Y_j), \tag{44}$$

where $z_j = -\mathrm{Cos}\left(\frac{j\pi}{N}\right), j = 1, 2, 3, \ldots,$ are collocation points.

Using Eq. (42) in Eqs. (38)–(39), we get a system of linear algebraic equations with Ra_{nf} as the eigen value and these are solved by the QZ-algorithm for different values of b. From an array of values of $Ra_{nf}(b)$, by minimization we find Ra_{nfc} and b_c. For more details on the method, we refer to the work of Canuto et al. [37].

5 Validation of Result

The results of Goody [12] in the case of transparent and opaque media for free isothermal conditions are recovered exactly from the results of the present problem by considering the limits $Ds_l, Ds_u \to 0$ and $Bi_l, Bi_u \to \infty$.

6 Results and Discussion

The problem deals with Rayleigh-Bénard convection in a rectangular geometry bounded between two horizontal walls. The fluid under consideration is a radiating nanofluid which is either of the transparent or the opaque type. The boundaries are permeable by the assumption of densely-packed porous walls. Further, the walls permit transport of heat into the Rayleigh-Bénard system and from the Rayleigh-Bénard system to the outside environment. The fluid permeable walls permit such a transaction. In view of the above observations, it is quite clear that the boundary condition applicable at the two horizontal walls cannot be of the classical type. This calls for general boundary conditions on both velocity and temperature. Though the governing equations remain the same, the boundary condition renders it impossible to keep the problem tractable.

The Chebyshev pseudo-spectral method is adopted to obtain the Rayleigh number as a function of the wave number which is then minimized to obtain the critical values of Ra_{nf} and b. Additionally, the problem is kept realistic by considering the actual thermophysical properties of the nanofluid and the porous matrix it occupies. This influence is also captured in the critical Rayleigh and wave numbers.

6.1 Choice of Mathematical Models

6.1.1 Modeling of the Radiating Nanofluid

Radiation emitting and absorbing Newtonian nanofluids are considered. The radiation explicitly modifies the conservation of energy and implicitly influences the conservation of linear momentum. Two types of media considered are: transparent and opaque. We follow Goody [12] in noting that the equation of energy is altered differently for transport and opaque media.

The radiation effect in the two media gives rise to a non-uniform temperature gradient, which is the main reason for most of the instabilities in the fluid medium under consideration. The nanofluids chosen for investigation are water-copper and water-alumina nanofluids. For the sake of comparison of the individual effects of nanoparticle/s we consider the same volume fraction of nanoparticle/s in water. To be specific, we have considered it to be \$0.04\$. The water as a base fluid (also known as carrier fluid) along with nanaoparticle/s needs modeling for its thermophysical properties which has been done using phenomenological laws [38, 39] and mixture theory and documented in Tables 1 and 2. The modeling of nanofluid-saturated porous media is handled by adopting the Khanafer-Vafai-Lightstone model (KVL model) [40]. As a result of this, the porosity and permeability of the nanofluid-saturated porous medium come into the picture. Filter velocity is used by making use of the Dupuit's law which states that the filter velocity is porosity times the clear fluid velocity.

6.1.2 Modeling of Boundary Condition

Since the horizontal boundaries are permeable and allow heat transport between the Rayleigh-Bénard configuration and the outside environment, the velocity boundary condition cannot be that of a rigid boundary nor that of a free boundary. The Beavers-Joseph slip condition [30] can be made use of to model this interfacial condition (Siddheshwar [31]). A slip-Darcy number arises in this modeling, one each for the two boundaries. Likewise, the thermal conditions at the interface can neither be isothermal nor isoflux boundary condition and hence we would require the use of a Robin type of boundary condition (radiating boundary condition). A Biot number arises in the modeling, again one each for the two boundaries.

6.1.3 Difficulty with the Mathematical Model in Obtaining an Analytical Solution

In addition to the governing equations being coupled, one of the equations has a variable coefficient due to the presence of radiation. This makes it virtually impossible in obtaining an analytical solution for the case of general boundary condition. In view

Table 1 Thermophysical properties of nanofluids with volume fraction $\phi_{np} = 0.04$, at 300 K

Nanofluid	ρ_{nf}	k_{nf}	μ_{nf}	$(\rho C_p)_{nf} \times 10^{-6}$	$(C_p)_{nf}$	$(\rho\beta)_{nf}$	$\beta_{nf} \times 10^5$	$\alpha_{nf} \times 10^7$
Water-copper	1116.02	0.686071	0.000985625	4.12169	3693.22	0.202365	18.1328	1.6654
Water-alumina	1314.54	0.68926	0.000985625	4.13777	3147.71	0.206983	15.7457	1.66578

Table 2 Thermophysical properties of nanofluid-saturated glass balls' porous medium with volume fraction $\Phi = 0.5$, at 300 K

Nanofluid	$(k_{nf})_m$	b_1
Water-copper	0.868036	0.706192
Water-alumina	0.86963	0.704897

of this, we have chosen the versatile numerical method known as the Chebyshev pseudo-spectral method which uses the Chebyshev polynomial as the basis function in its eigen function expansion. Chebyshev function being a solution of the Chebyshev differential equation, which is a Sturm–Liouville problem, it is apparent that orthogonality of eigen functions is guaranteed. A discrete version of the Fourier–Chebyshev coefficient is used and this yields us the necessary initial values while obtaining the other coefficients which arise due to the boundary condition in the form of a recurrence relation.

6.2 Transparent Nanofluid Medium

The effects of radiation on Ra_{nfc} and b_c when the nanofluid medium is transparent are depicted in Figs. 2 and 3. The non-zero value of the conduction-radiation parameter, χ, indicates the deviation of temperature from that of the conduction state. An increase in χ results in an exponential increase in the basic temperature distribution, which further results in the convection being delayed at large values of the parameter, χ. Also, the absorption parameter, τ, which characterizes the absorption coefficient and distance between the horizontal planes, impacts as a stabilizing effect on the Rayleigh-Bènard system. It can be observed from Table 3 that when the nanofluid medium is of transparent type, the heat released for convection is slower as τ is increased.

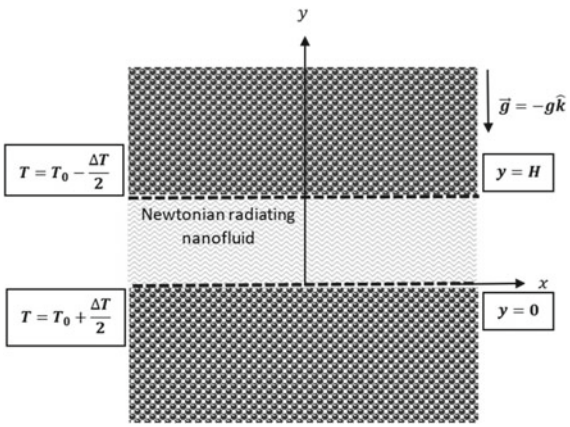

Fig. 1 Physical configuration

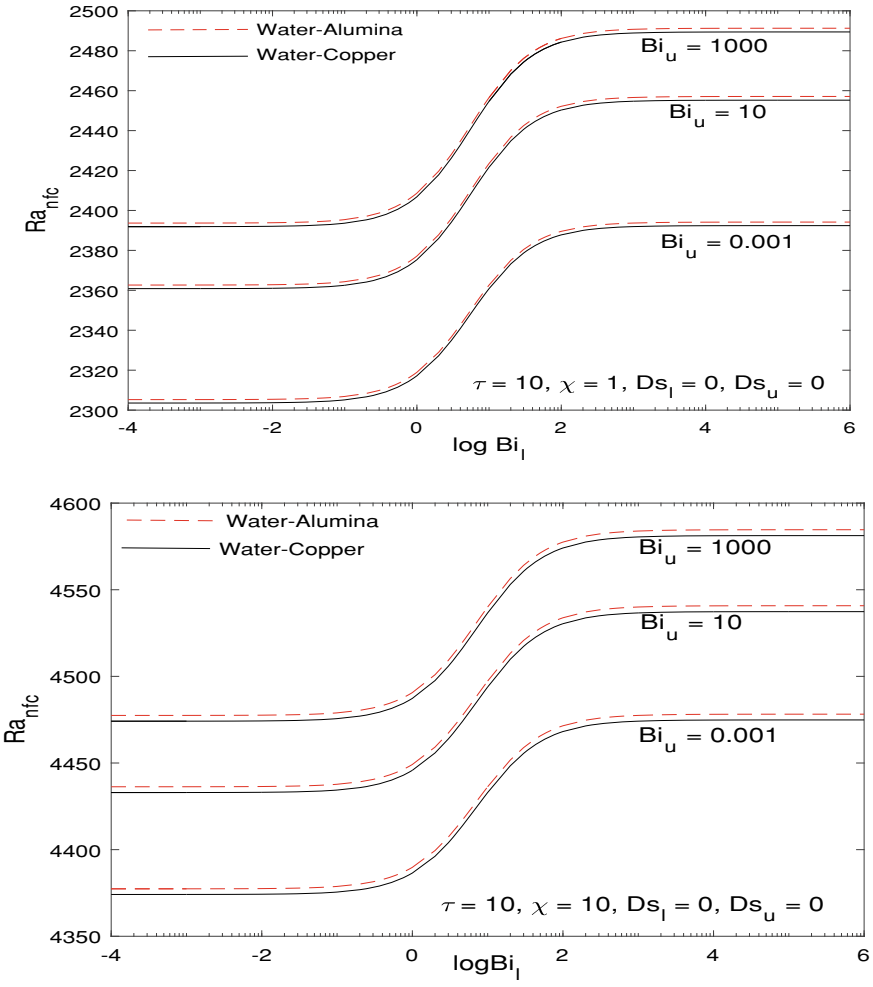

Fig. 2 Plot of Ra_{nfc} for different values of Bi_u and χ, for transparent medium

The effects of general boundary condition with respect to temperature can be analyzed from the Figs. 2 and 3, where it can be observed that the value of the Biot number which covers results of isoflux boundaries to that of isothermal boundaries, and in the presence of radiation continues to exhibit the classical behavior. Likewise, the effects of general boundary condition with respect to velocity have been depicted in Figs. 4 and 5, where the values of the slip-Darcy number allow us to bridge the gap between the results of stress free to rigid boundaries. The classical behavior of the system is seen in the presence of radiation as well.

In the results of two nanofluids considered, it is evident (from Table 3) that thermodynamically correct results have been obtained, i.e., the onset of convection is

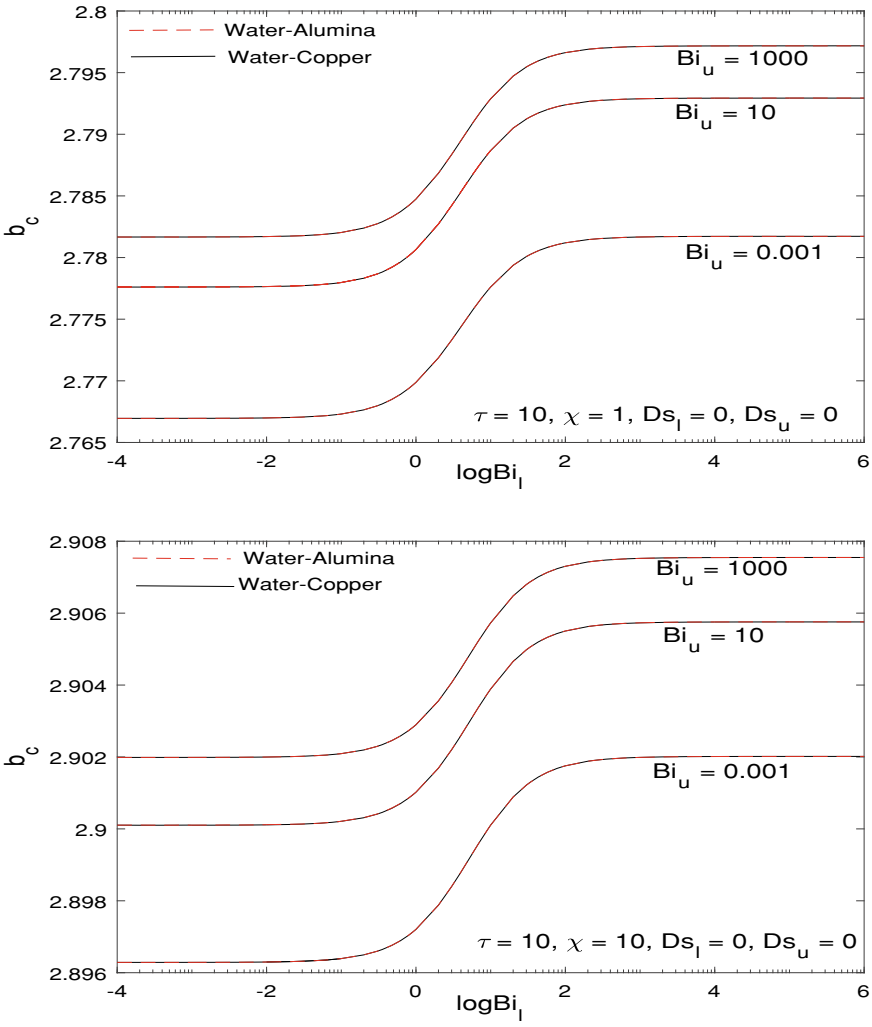

Fig. 3 Plot of b_c for different values of Bi_u and χ, for transparent medium

early in water-copper nanofluid when compared to that in water-alumina nanofluid in presence/absence of radiation.

6.3 Opaque Nanofluid Medium

The radiation effects in an opaque nanofluid medium can be observed in Figs. 6, 7, 8 and 9. When compared to its nature of influence in a transparent nanofluid medium, τ

Table 3 Critical wave number, b_c, and critical Rayleigh number, Ra_{nfc}, for different boundary combinations and for $\chi = 10$

τ	Boundary combinations	Water-alumina nanofluid				Water-copper nanofluid			
		Transparent medium		Opaque medium		Transparent medium		Opaque medium	
		b_c	Ra_{nfc}	b_c	Ra_{nfc}	b_c	Ra_{nfc}	b_c	Ra_{nfc}
10	RIRI	4.23923	9039.88525	3.11733	20,200.90841	4.23923	9033.17905	3.11733	20,185.92226
	RARI	4.23502	8965.20034	2.54390	15,134.38494	4.23502	8958.54954	2.54391	15,123.15756
	RARA	4.23084	8892.42022	0.01000	8306.97170	4.23084	8885.82341	0.01000	8300.80923
	RIFI	3.58356	6565.97797	2.68204	12,866.78163	3.58356	6561.10704	2.68204	12,857.23645
	RAFI	3.58281	6529.31527	2.21228	9482.67981	3.58281	6524.47155	2.21228	9475.64513
	RIFA	3.56714	6356.78529	2.07575	7535.96213	3.56714	6352.06953	2.07575	7530.37161
	RAFA	3.56637	6323.40889	0.01379	3600.72813	3.56637	6318.71789	0.01378	3598.05690
	FIFI	2.90757	4585.39169	2.22149	7645.75103	2.90757	4581.99004	2.22148	7640.07906
	FAFI	2.90201	4478.16676	1.75306	4349.55787	2.90201	4474.84467	1.75306	4346.33117
	FAFA	2.89629	4377.36001	0.01000	1333.80578	2.89629	4374.11271	0.01000	1332.81630
100	RIRI	4.74503	571,320.45110	4.74503	571,320.45110	4.74503	570,896.60370	4.74503	570,896.60370
	RARI	4.74503	571,320.35400	4.74503	571,320.35400	4.74503	570,896.50670	4.74503	570,896.50670
	RARA	4.74503	571,320.25770	4.74503	571,320.25770	4.74503	570,896.41040	4.74503	570,896.41040
	RIFI	3.94386	442,958.49800	3.94386	442,958.49800	3.94386	442,629.89090	3.94386	442,629.89090
	RAFI	3.94386	442,958.50140	3.94386	442,958.50140	3.94386	442,629.89430	3.94386	442,629.89430
	RIFA	3.94386	442,955.16090	3.94386	442,955.16090	3.94386	442,626.55620	3.94386	442,626.55620
	RAFA	3.94386	442,955.16480	3.94386	442,955.16480	3.94386	442,626.56010	3.94386	442,626.56010
	FIFI	3.13820	327,269.32580	3.13820	327,269.32580	3.13820	327,026.54230	3.13820	327,026.54230
	FAFI	3.13820	327,268.04050	3.13820	327,268.04050	3.13820	327,025.25790	3.13820	327,025.25790
	FAFA	3.13820	327,266.76450	3.13820	327,266.76450	3.13820	327,023.98290	3.13820	327,023.98290

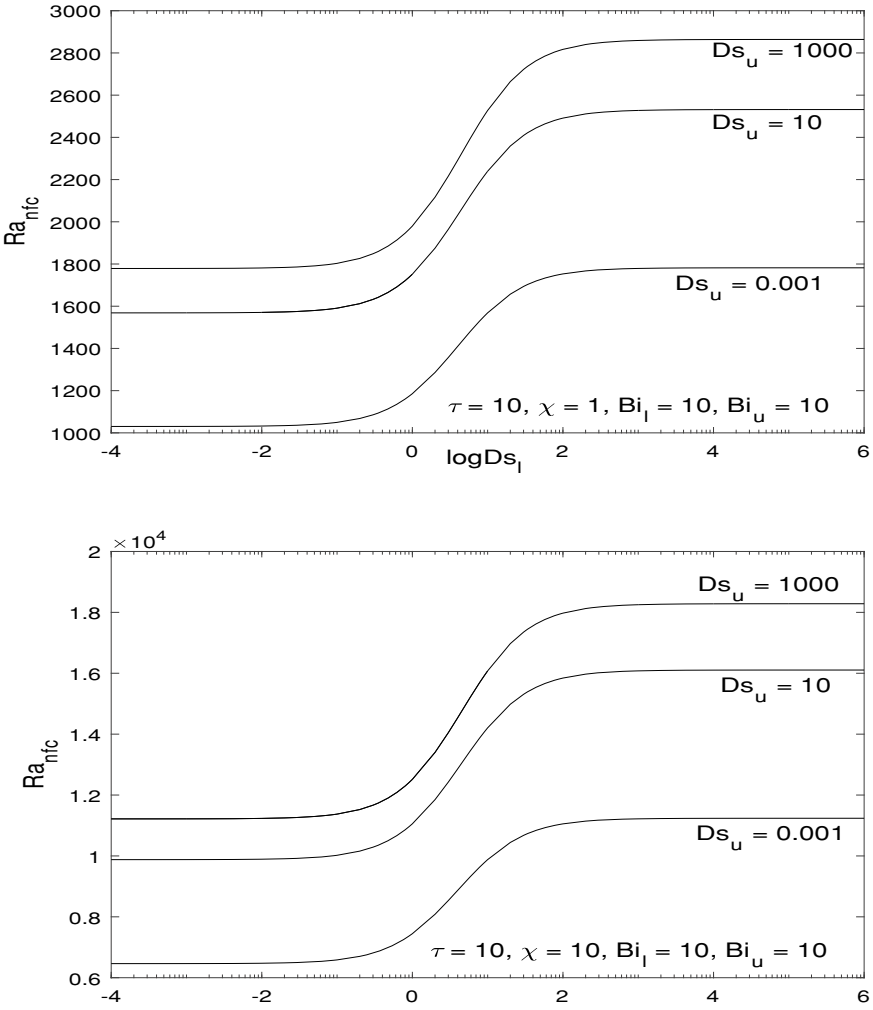

Fig. 4 Plot of Ra_{nfc} for different values of Ds_u and χ, for water-copper nanofluid, for transparent medium

presents a contradicting behavior in the case of opaque medium. This could possibly be due to the fact that when the medium is opaque, the absorption of radiation is not as evident as in a transparent medium. In view of this, the heat released for convection is delayed quite substantially in the case of an opaque medium than that in a transparent medium. Hence, τ exhibits a destabilizing effect on the Rayleigh-Bénard system and is enhanced more with an increase in the value of τ. However, the effect of χ is similar to that in the transparent medium and is thus to stabilize the system which is enhanced further with an increase in χ.

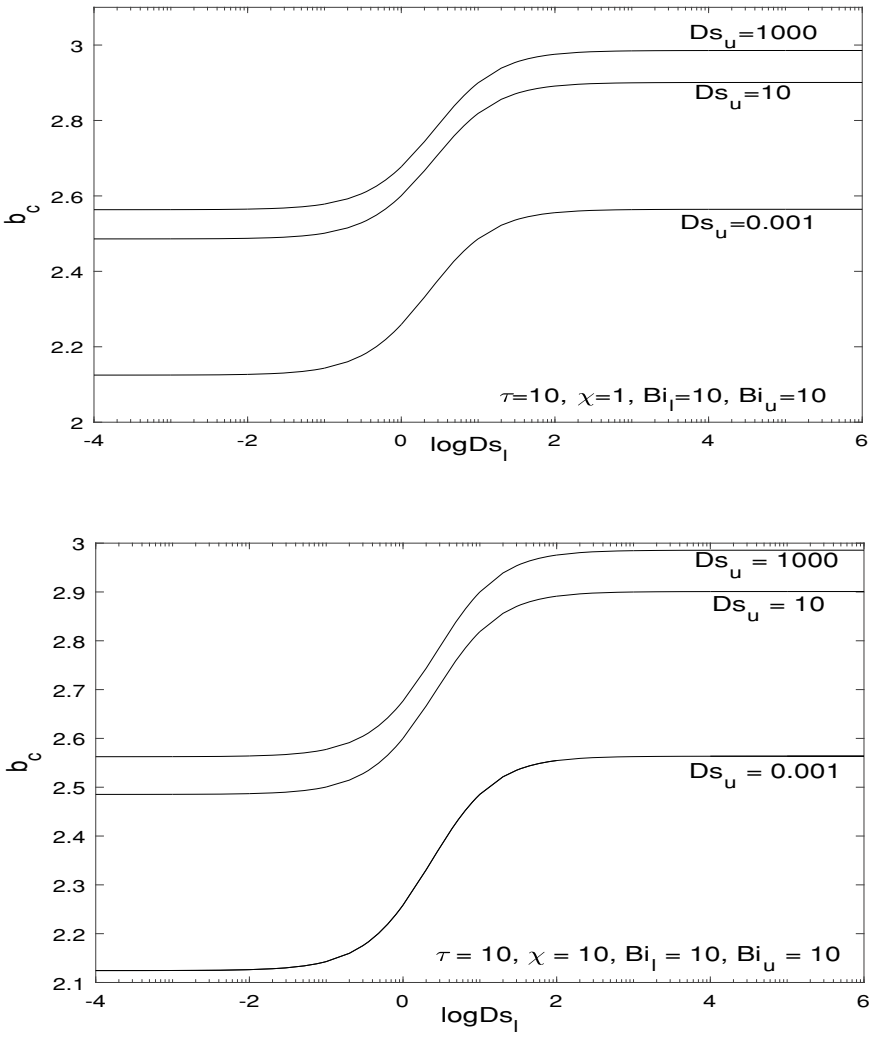

Fig. 5 Plot of b_c for different values of Ds_u and χ, for water-copper nanofluid, for transparent medium

The results pertaining to general boundary condition remain unaltered with what has been observed in the case of the transparent fluid medium, i.e., increasing values of slip-Darcy numbers and Biot numbers impart a stabilizing effect on the onset of convection.

In view of the results discussed in Sects. 6.2 and 6.3, the following mathematical inequalities are true:

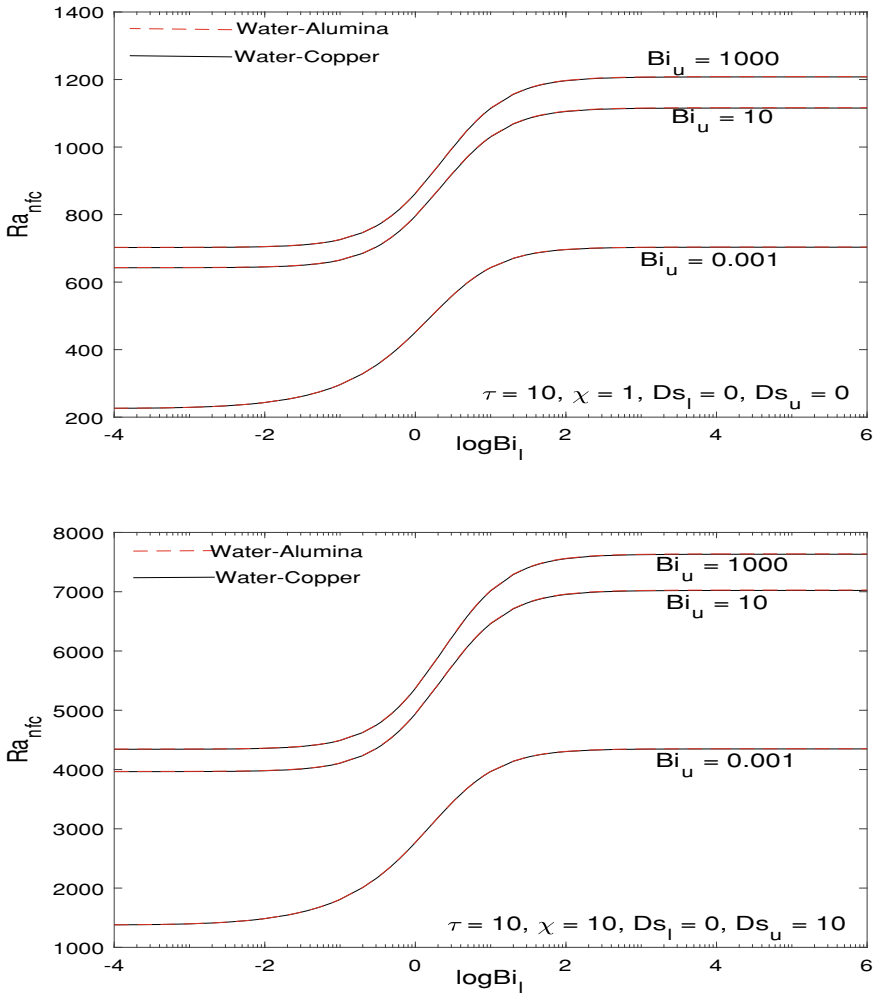

Fig. 6 Plot of Ra_{nfc} for different values of Bi_u and χ, for opaque medium

$$\left.\begin{array}{l}
\left(Ra_{nfc}\right)_{\tau=10}^{Opaque} \gg \left(Ra_{nfc}\right)_{\tau=10^2}^{Opaque}, \\
\left(Ra_{nfc}\right)_{\tau=10}^{Transparent} \ll \left(Ra_{nfc}\right)_{\tau=10^2}^{Transparent}, \\
\left(Ra_{nfc}\right)_{\chi=1} < \left(Ra_{nfc}\right)_{\chi=10}, \\
\left(Ra_{nfc}\right)_{Water-copper} < \left(Ra_{nfc}\right)_{Water-alumina}, \\
\left(Ra_{nfc}\right)_{Adiabatic\ boundaries} < \left(Ra_{nfc}\right)_{General\ rough\ boundaries} < \left(Ra_{nfc}\right)_{Isothermal\ boundaries}, \\
\left(Ra_{nfc}\right)_{Stress-free\ boundaries} < \left(Ra_{nfc}\right)_{General\ rough\ boundaries} < \left(Ra_{nfc}\right)_{Rigid\ boundaries}
\end{array}\right\}, \tag{45}$$

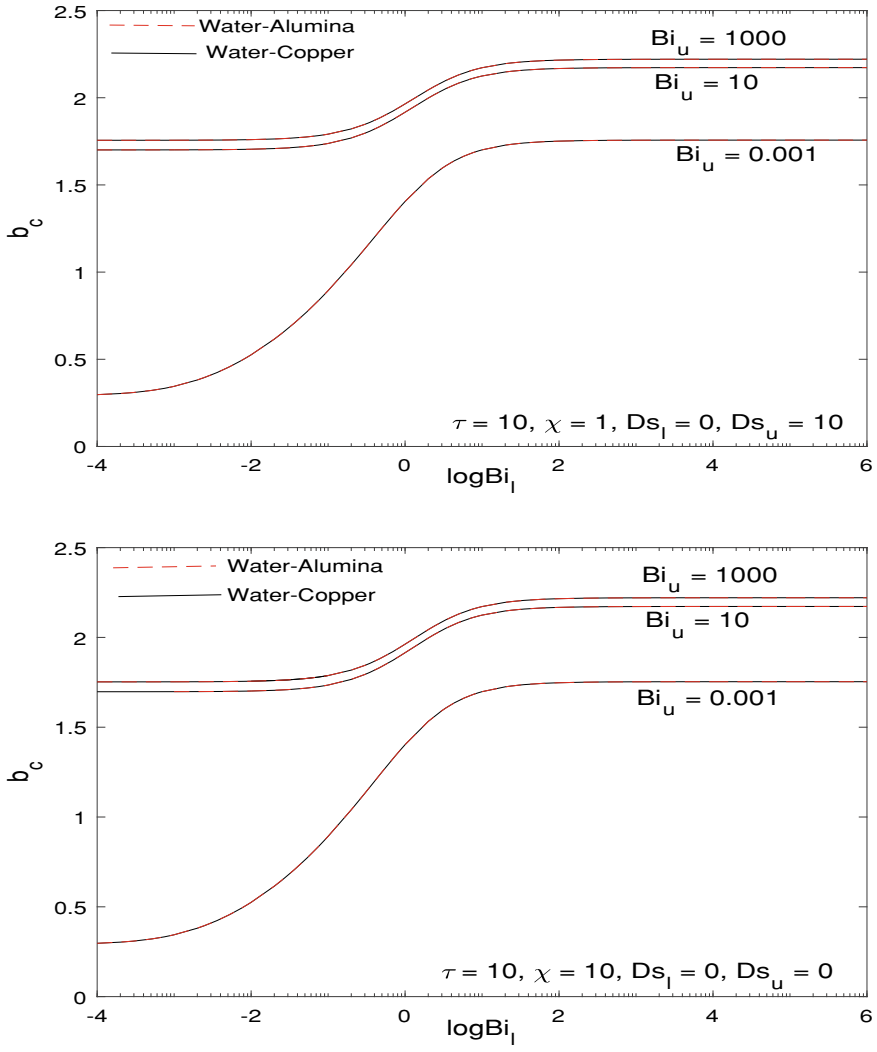

Fig. 7 Plot of b_c for different values of Bi_u and χ, for opaque medium

$$\left.\begin{array}{l}(b_c)^{Opaque}_{\tau=10} \gg (b_c)^{Opaque}_{\tau=10^2},\\ (b_c)^{Transparent}_{\tau=10} \ll (b_c)^{Transparent}_{\tau=10^2},\\ (b_c)_{\chi=1} < (b_c)_{\chi=10},\\ (b_c)_{Water-copper} < (b_c)_{Water-alumina},\\ (b_c)_{Adiabatic\ boundaries} < (b_c)_{General\ rough\ boundaries} < (b_c)_{Isothermal\ boundaries},\\ (b_c)_{Stress-free\ boundaries} < (b_c)_{General\ rough\ boundaries} < (b_c)_{Rigid\ boundaries}\end{array}\right\}. \quad (46)$$

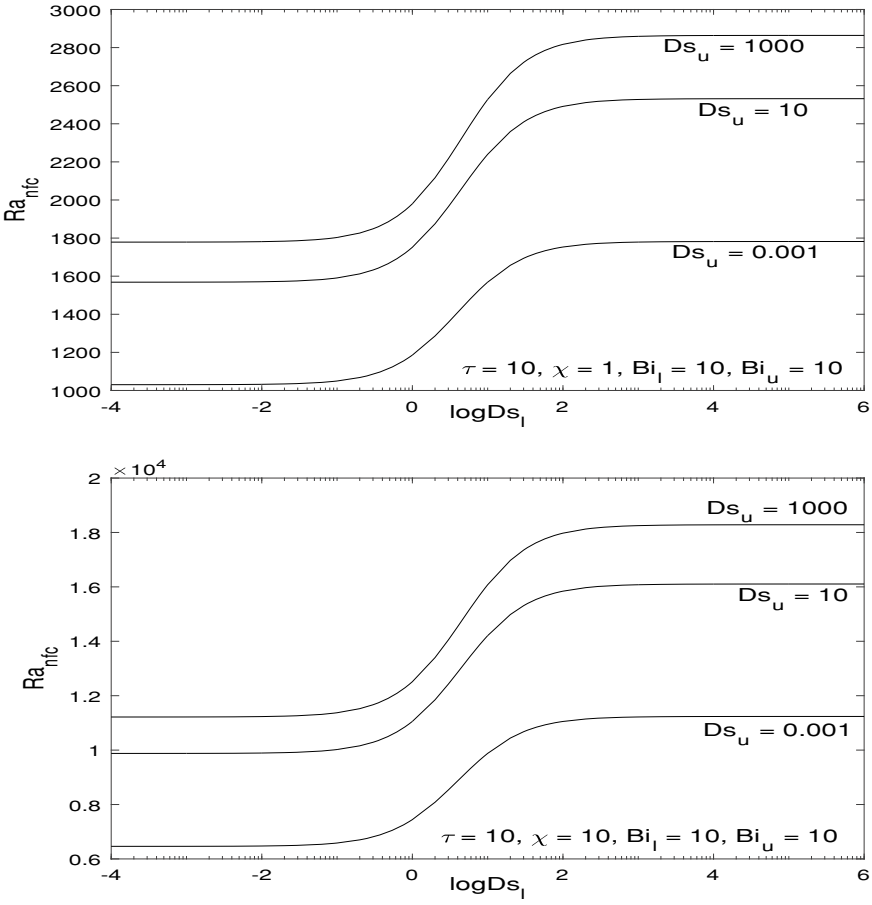

Fig. 8 Plot of Ra_{nfc} for different values of Ds_u and χ, for water-copper nanofluid and the opaque medium

In the neutral stability curve represented in Fig. 10, we can observe the effects of radiation in different fluid media. It is evident that when τ and χ are negligibly small, i.e., 10^{-4}, the radiation effects on Ra_{nfc} and b_c are obviously absent. However, when τ and χ are increased to 10, the radiation effects on Ra_{nfc} and b_c are observed to be significant in an opaque fluid medium than that in a transparent fluid medium, for finite values of Biot numbers and slip-Darcy numbers. Mathematically speaking, the following relation holds:

$$\left(Ra_{nfc}\right)_{Opaque\ medium} < \left(Ra_{nfc}\right)_{Transparent\ medium} < \left(Ra_{nfc}\right)_{No\ radiation}.$$

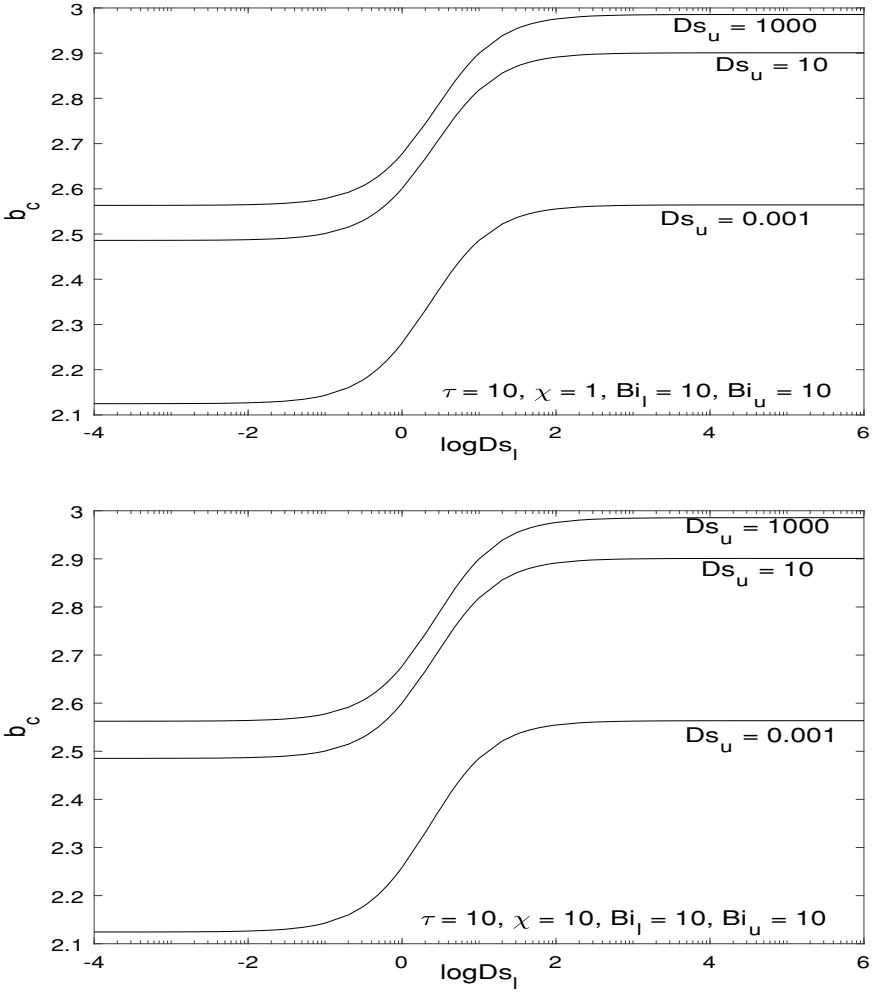

Fig. 9 Plot of b_c for different values of Ds_u and χ, for water-copper nanofluid and the opaque medium

7 Conclusion

1. The onset of convection is earlier in water-copper nanofluid as compared to that in a water-alumina nanofluid.
2. The absorption parameter, τ, and conductive-radiative parameter, χ, have a stabilizing effect on the onset of convection in a transparent fluid medium.
3. The absorption parameter, τ, has a destabilizing effect, whereas the conductive-radiative parameter, χ, has a stabilizing effect on the onset of convection in an opaque fluid medium.

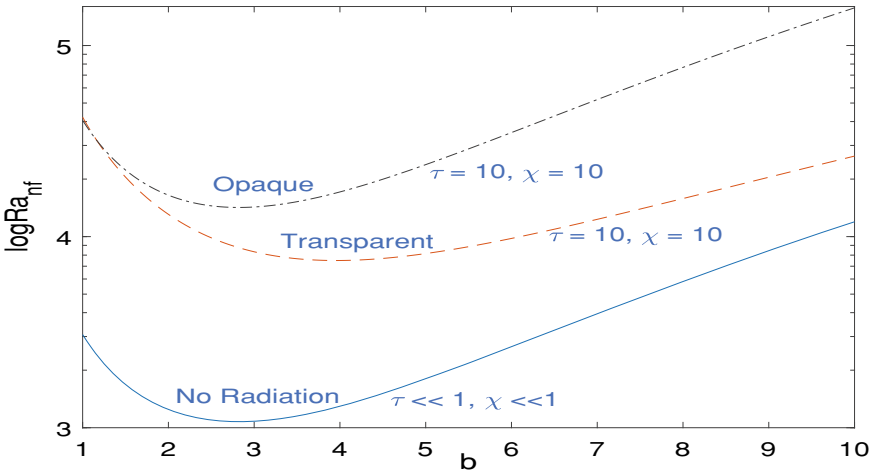

Fig. 10 Plot of Ra_{nfc} versus b for finite values of $Bi_l = 10$, $Bi_u = 10$, $Ds_l = 10$, and $Ds_u = 10$, for different media

4. The opaque fluid medium releases heat for convection slower than that in a transparent fluid medium.
5. The results of rough boundaries (using general boundary condition) bridge the gap between the results of stress-free and rigid boundaries, and that between adiabatic and isothermal boundaries.

Acknowledgements This work was supported by the IPRG project between the CHRIST (Deemed to be University) and the Universiti Malaysia Terengganu.

Appendix

The energy equation (3) in the basic state is given by,

$$\frac{G_b}{s_r} + a_1 \frac{d^2 T_b}{dy^2} = 0, \tag{47}$$

which indicates that the heat transfer takes place essentially due to conduction and radiation. Considering F_y as the y-component of the radiative heat flux, then

$$G_b = -\frac{dF_y}{dy}. \tag{48}$$

Using Eq. (48) we can write Eq. (47) as follows:

$$F_y + a_1 s_r \beta = c, \tag{49}$$

where c is the constant of integration and $\beta = \frac{dT_b}{dy}$.

Using the definition of β along with boundary conditions given by Eqs. (21)–(22) we obtain:

$$T_b(y) = -\beta y + \frac{1}{2}\left(\frac{Bi_l + Bi_u}{Bi_l - Bi_u}\right) - \frac{\beta Bi_u}{Bi_l - Bi_u}.$$

Assuming the Milne-Eddington approximation, which is defined as,

$$\left.\begin{array}{l} I(\mu_3, y) = I^+(y), for\, 0 < \mu_3 < 1, \\ I(\mu_3, y) = I^-(y), for\, -1 \le \mu_3 \le 0 \end{array}\right\}. \tag{50}$$

Using the radiative heat transfer equation in the form:

$$\mu_3 \frac{dI}{dy} = K_a[P_B - I], \tag{51}$$

where $I(\vec{r})$ is the intensity of radiation along the direction of the vector $\vec{r}$, K_a is the absorption coefficient of the fluid per unit volume, P_B is the Planck black body intensity, and μ_3 is the directional cosine in the direction of $\vec{r}$.

Substituting Eq. (51) in Eq. (49) we obtain the differential equation associated with the heat flux F_y in the form [12]

$$\frac{d^2F_y}{dy^{*2}} - \tau^2 F_y = -\tau^2 \frac{\chi}{1+\chi} c, \tag{52}$$

where $y^* = \frac{y}{H}$, $\tau^2 = 3K_a^2H^2(1+\chi)$, $\chi = \frac{4\pi Q_1}{3\alpha_f K_a s_r}$ $and Q_1 = \frac{4S_c}{\pi} T_a^3$.

Solving Eq. (52) using the following non-dimensional radiative boundary condition and dropping the asterisk for simplicity:

$$\left.\begin{array}{l} \frac{dF_y}{dy} = -2K_aF_yH \;\; at\; y = 0, \\ \frac{dF_y}{dy} = +2K_aF_yH \;\; at\; y = 1 \end{array}\right\}, \tag{53}$$

we obtain

$$\left.\begin{array}{l} f(y) = \frac{\beta}{\beta} = L_1 \mathrm{Cosh}(\tau y) + L_2, \\ L_1 = \chi\left[\frac{2\chi}{\tau}\mathrm{Sinh}\left(\frac{\tau}{2}\right) + \sqrt{3+3\chi}\mathrm{Sinh}\left(\frac{\tau}{2}\right) + \mathrm{Cosh}\left(\frac{\tau}{2}\right)\right]^{-1}, \\ L_2 = \frac{L_1}{\chi}\left[\sqrt{3+3\chi}\mathrm{Sinh}\left(\frac{\tau}{2}\right) + \mathrm{Cosh}\left(\frac{\tau}{2}\right)\right] \end{array}\right\}. \tag{54}$$

$\overline{\beta}$ in Eq. (54) is the mean value of β throughout the fluid medium. The radiative boundary condition in Eq. (53) is due to the fact that the molecular conduction ensures continuity of temperature at the two surfaces.

References

1. Bénard H (1901) Les tourbillons cellulaires dans une nappe liquide propageant de la chaleur par convection: en régime permanent. Gauthier-Villars, Paris
2. Rayleigh L (1916) LIX. On convection currents in a horizontal layer of fluid, when the higher temperature is on the under side. Lond Edinb Dublin Philos Mag J Sci 32:529–546
3. Pellew A, Southwell RV (1940) On maintained convective motion in a fluid heated from below. Proc R Soc Lond A 176:312–343
4. Bergé P, Dubois M (1984) Rayleigh-Bénard convection. Contemp Phys 25:535–582
5. Sparrow EM, Goldstein RJ, Jonsson VK (1964) Thermal instability in a horizontal fluid layer: effect of boundary conditions and non-linear temperature profile. J Fluid Mech 18:513–528
6. Tritton DJ (1998) Physical fluid dynamics. Oxford University Press Inc., New York
7. Chandrasekhar S (2013) Hydrodynamic and hydromagnetic stability. Dover Publications
8. Platten JK, Legros JC (1984) Convection in liquids. Elsevier, Berlin
9. Getling AV (1998) Rayleigh-Bénard convection: structures and dynamics, vol 11. World Scientific, Singapore
10. Nield DA, Bejan A (2006) Convection in porous media, vol 3. Springer, New York
11. Straughan B (1993) The energy method, stability, and nonlinear convection, vol 48. Springer, New York
12. Goody RM (1956) The influence of radiative transfer on cellular convection. J Fluid Mech 1:424–435
13. Spiegel EA (1960) The convective instability of a radiating fluid layer. Astrophys J 132:716–728
14. Murgai MP, Khosla PK (1962) A study of the combined effect of thermal radiative transfer and a magnetic field on the gravitational convection of an ionized fluid. J Fluid Mech 14:433–451
15. Khosla PK, Murgai MP (1963) A study of the combined effect of thermal radiative transfer and rotation on the gravitational stability of a hot fluid. J Fluid Mech 16:97–107
16. Gille J, Goody R (1964) Convection in a radiating gas. J Fluid Mech 20:47–79
17. Christophorides C, Davis SH (1970) Thermal instability with radiative transfer. Phys Fluids 13:222–226
18. Arpaci VS, Bayazitoğlu Y (1973) Thermal stability of radiating fluids: asymmetric slot problem. Phys Fluids 16:589–593
19. Lienhard JH (1990) Thermal radiation in Rayleigh-Bénard instability
20. Siegel R, Howell JR (1992) Thermal radiation heat transfer. NASA STI/Recon Tech Rep A 93:17522
21. Bdéoui F, Soufiani A (1997) The onset of Rayleigh-Bénard instability in molecular radiating gases. Phys Fluids 9:3858–3872
22. Devi SN, Nagaraju P, Hanumanthappa AR (2002) Effect of radiation on Rayleigh-Bénard convection in an anisotropic porous medium
23. Lan CH, Ezekoye OA, Howell JR, Ball KS (2003) Stability analysis for three-dimensional Rayleigh-Bénard convection with radiatively participating medium using spectral methods. Int J Heat Mass Transf 46:1371–1383
24. Ridouane EH, Hasnaoui M, Campo A (2006) Effects of surface radiation on natural convection in a Rayleigh-Bénard square enclosure: steady and unsteady conditions. Heat Mass Transf 42:214–225
25. Gad MA, Balaji C (2010) Effect of surface radiation on RBC in cavities heated from below. Int Commun Heat Mass Transf 37:1459–1464

26. Mishra SC, Akhtar A, Garg A (2014) Numerical analysis of Rayleigh-Bénard convection with and without volumetric radiation. Numer Heat Transf Part A: Appl 65:144–164
27. Chaabane R, Askri F, Jemni A, Nasrallah SB (2017) Analysis of Rayleigh-Bénard convection with thermal volumetric radiation using Lattice-Boltzmann formulation. J Therm Sci Technol 12:JTST0020–JTST0020
28. Goody RM, Yung YL (1964) Absorption by atmospheric gases. In: Atmospheric radiation. Oxford University Press
29. Goody RM, Yung YL (1989) Radiation calculations in a clear atmosphere. In: Atmospheric radiation. Oxford University Press, New York
30. Beavers GS, Joseph DD (1967) Boundary conditions at a naturally permeable wall. J Fluid Mech 30:197–207
31. Siddheshwar PG (1995) Convective instability of ferromagnetic fluids bounded by fluid-permeable, magnetic boundaries. J Magn Magn Mater 149:148–150
32. Weidman PD, Kassoy DR (1986) The influence of side wall heat transfer on convection in a confined saturated porous medium. Phys Fluids 29:349–355
33. Barletta A (1999) Analysis of combined forced and free flow in a vertical channel with viscous dissipation and isothermal-isoflux boundary conditions. Int J Heat Transf 121:349–356
34. Barletta A, Rossi di Schio E (2001) Effect of viscous dissipation on mixed convection heat transfer in a vertical tube with uniform wall heat flux. Heat Mass Transf 38:129–140
35. Barletta A, Magyari E (2006) Thermal entrance heat transfer of an adiabatically prepared fluid with viscous dissipation in a tube with isothermal wall. Int J Heat Transf 128:1185–1193
36. Barletta A, Storesletten L (2012) A three-dimensional study of the onset of convection in a horizontal, rectangular porous channel heated from below. Int J Therm Sci 55:1–15
37. Canuto VM, Christensen-Dalsgaard J (1998) Turbulence in astrophysics: stars. Annu Rev Fluid Mech 30(1):167–198
38. Brinkman HC (1952) The viscosity of concentrated suspensions and solutions. J Chem Phys 20:571–571
39. Hamilton RL, Crosser OK (1962) Thermal conductivity of heterogeneous two-component systems. Ind Eng Chem Fundam 1:187–191
40. Khanafer K, Vafai K, Lightstone M (2003) Buoyancy-driven heat transfer enhancement in a two-dimensional enclosure utilizing nanofluids. Int J Heat Mass Transf 46:3639–3653

Chapter 13
Numerical Study of Quadratic Boussinesq Non-Newtonian Viscoelastic Fluid with Quadratic Rosseland Thermal Radiation

Mahanthesh Basavarajappa

Abstract The temperature difference in many applications, such as the polymer industries and heat exchangers, is quite large; consequently, the variation in the density of working fluid due to the temperature is significant. Therefore, the nonlinear variation of density with respect to the temperature cannot be ignored as it influences the rheological behaviors of the working fluid immensely. Furthermore, there is a disparity in the modeling of Rosseland thermal radiation when quadratic (nonlinear) convection is significant. This study focuses on presenting an appropriate model of quadratic Boussinesq convection and quadratic Rosseland thermal radiation in a heat transfer problem. Therefore, a numerical study of the flow and heat transport of a non-Newtonian viscoelastic fluid over an elongated plate with transpiration cooling is carried out. The nonlinear form of the Boussinesq approximation is considered, along with an appropriate approach is proposed for modeling the Rosseland radiative heat flux. The governing equations consisting of modified Navier-Stokes momentum, conservation of mass, conservation of energy, and modified basic state equation. The nonlinear self-similar governing equations are solved by using finite difference method-based routine. The importance of the quadratic thermal convection number, quadratic thermal radiation, viscoelastic fluid parameter and suction/ injection factor on the heat transfer phenomenon is discussed. Streamlines are also drawn to study the flow pattern subject to nonlinear convection. It is established that the rate of heat transport increases with the viscoelastic behavior of the working fluid. The thickness of the momentum boundary layer enlarged due to the nonlinear variation of the density with temperature. The results of the conventional mixed convection model are obtained from the present study by setting to zero the value of the nonlinear convection parameter. Also, setting a unit value to the temperature ratio in the present problem, the results of linearized Rosseland thermal radiation problem. The present simulations are applicable in the polymer and heat exchanger industry.

M. Basavarajappa (✉)
School of Mathematical and Statistical Sciences, University of Texas Rio Grande Valley, Edinburg, TX 78539, USA
e-mail: mahanthesh.b@utrgv.edu

D. Tripathi et al. (eds.), *Advancements in Nanotechnology for Energy and Environment*, Advances in Sustainability Science and Technology,
https://doi.org/10.1007/978-981-19-5201-2_13

Keywords Viscoelastic fluid · Quadratic thermal radiation · Nonlinear Boussinesq approximation · Transpiration cooling · Rosseland radiative heat transfer

1 Introduction

Theoretical investigations describing non-Newtonian liquids are increasing in recent times due to widespread engineering applications such as polymer industries, fiber manufacturing, plastic manufacturing, crude oil extraction, and paper manufacturing. Several models of non-Newtonian materials have been suggested due to the exertion of apprehending the features of the fluid with one model, e.g., viscoelastic fluids (Walter-B fluid, Maxwell fluid, and Oldroyd B fluid), micropolar fluid, power law fluid, Eyring-Powell fluid, Casson fluid, etc. The importance of viscoelastic material can be found in plastics manufacturing, polymer industry, wire drawing, oil drilling, papermaking, etc. Therefore, there is an exponential increase in attempts relating to the study of heat transport in viscoelastic fluids subjected to various physical mechanisms. Beard and Walter [1] proposed the viscoelastic materials model and its governing equations. Therefore, additional auxiliary conditions are needed to address this equation. There, the studies related to the heat flow of viscoelastic material were mathematically challenging. Rajagopal [2] addressed the paucity of additional auxiliary conditions. Beard and Walter [1] observed an overshoot in the surface layer thickness of the velocity through the solution of the perturbation. Subsequently, Frater [3] proposed his comments on the acceleration caused by the disturbance. Ariel [4] used a hybrid numerical technique to examine the velocity near the boundary layer and encountered the same trend.

Subsequently, Rollins and Vajravelu [5] studied the influence of two distinct thermal energy boundary conditions on the flow of viscoelastic material due to the plate elongation. Siddappa and Abel [6] analyzed the transition of the viscoelastic material that obeys Walter's liquid B on an elongated sheet with transpiration. They found that factor-related viscoelastic fluid increases the fluid velocity field of Walters-B liquid. Prasad et al. [7] extended the work of Siddappa and Abel [6] with a porous medium and demonstrated that the velocity of Walter's B liquid can be controlled by a porous medium. Abel et al. [8] analyzed the importance of temperature-induced buoyancy force and concentration in the flow of viscoelastic material. They used linear Boussinesq approximation in the analysis, where the change in density with temperature is considered linearly. They showed that the buoyancy force facilitates the growth of the momentum boundary layer. Hayat et al. [9] found Homotopy series solutions for mixed convection by linear Boussinesq approximation and transport of viscoelastic material on an elongated surface with cross-diffusion effects. They also found that the buoyancy force is in favor of the thickness of the velocity layer and the consequence of the Soret mechanism on the thermal field is opposite to that of the Dufour mechanism. Recently, Li et al. [10] also used linear density temperature fluctuation to study mixed convection in viscoelastic material subjected to

Cattaneo-Christov heat flux. A widespread literature survey on linear Boussinesq approximation is presented by [11–15].

Besides, in heat exchangers, nuclear power plants, solar collectors, hot rolling, heat storage systems, etc., they involve very high temperatures. In such scenarios, the magnitude of the thermal energy difference is considerable within the systems, the density variability with thermal energy in a linear form becomes inoperative; therefore, it is imperative to use the nonlinear density temperature fluctuation (nonlinear Boussinesq approximation (NBA)) to capture the effects of buoyancy forces in the flow system with respect to the linear Boussinesq approximation (LBA). Goren [16] deliberated the fluctuation of the temperature of the quadratic density $\left(\Delta\rho = -\rho\beta(T - T_s)^2\right)$ instead of linear density temperature fluctuation $(\Delta\rho = -\rho\beta(T - T_s))$ in the term of buoyancy force. Vajravelu and Sastri [17] introduced a new dimension to it and considered the following;

$$\Rightarrow \rho(T) = \rho(T_\infty) + \left(\frac{\partial\rho}{\partial T}\right)_\infty (T - T_\infty) + \frac{1}{2!}\left(\frac{\partial^2\rho}{\partial T^2}\right)_\infty (T - T_\infty)^2 + \cdots, \quad (1)$$

By truncating the series by taking only second-order terms,

$$\Rightarrow \frac{\Delta\rho}{\rho} = -\left[\beta_0(T - T_\infty) + \beta_1(T - T_\infty)^2\right]. \quad (2)$$

where $\beta_0 = \frac{1}{\rho}\left(\frac{\partial\rho}{\partial T}\right)_\infty$ and $\beta_1 = \frac{1}{2\rho}\left(\frac{\partial^2\rho}{\partial T^2}\right)_\infty$ are thermal expansion coefficients of first and second-order. Mahanthesh et al. [18] studied the quadratic convective flow (NBA) on an elongated surface subjected to nonlinearized radiation. They found that the NBA mechanism increased the velocity field. Heat and mass transport subjected to the NBA are scrutinized by Jha et al. [19]. Mandal and Mukhopadhyay [20] examined the quadratic convection mechanism on micropolar fluid transport subjected to nonlinearized thermal energy radiation. Mahanthesh et al. [18] also inspected the combined effects on quadratic convection and nonlinear thermal radiation on Maxwell fluid with a three-dimensional flow case. Furthermore, Hayat et al. [21] considered the phenomenon of nonlinearized thermal energy radiation together with quadratic convection in their study of flow over a surface of varying thickness using the Walters-B nanomaterial.

The study of heat transport subjected to Rosseland thermal radiation is carried out in two ways. Nonlinear thermal radiation is one of two, in which the appearance of thermal energy radiation is deliberated by following the Rosseland approximation (see [22, 23]) for the radiative heat flux without simplifying it (see Mahanthesh et al. [18], Mandal and Mukhopadhyay [20], Mahanthesh et al. [18], Hayat et al. [21], Makinde and Animasaun [24], López et al. [25], Bhatti et al. [26], Muhammad et al. [27], Shaw et al. [28], and references contained therein). In the second approach, the nonlinear term involved in the radiative heat flux was linearized with the assumption that the temperature difference was small (see Cortell [29], Raza et al. [30]). The steps involved in linearization are reported in Cortell [29] and also in the next section. It is

very important to note that there is a discrepancy between the assumptions made in the modeling of NBA and the Rosseland thermal energy radiation aspects. Therefore, a new way is presented to incorporate the Rosseland thermal energy radiation to agree with the quadratic Boussinesq approximation hypothesis (see [31, 32]).

Aggravated by the literature review, the quadratic form of thermal radiation and thermal convection on the flow of viscoelastic material on an elongated vertical plate is examined. The cooling effect of transpiration is also taken into account. Surface layer approximations are implemented to govern the problem. The subsequent nonlinear differential system is treated using the finite difference method. The results are presented and analyzed through surface plots and streamlines. A direct comparison is made with the available literature for a limiting case to validate the method used.

2 Mathematical Modeling

2.1 Problem Statement

The non-transient dimensional flow of polymer solution (viscoelastic fluid) due to the elongation of a vertical permeable plate is considered. The plate is kept at an adaptable temperature $T_p(x)$ and elongates with the velocity $u_p(x)$. The plate is stretched along the x-direction. Also, T_∞ signifies the ambient temperature. Induced magnetism is ignored. As seen in Fig. 1, the x-axis is taken along the flat plate surface, and the y-axis is measured upright to the x-axis.

The buoyancy and elongation of the plate make the motive force for the movement of the polymer solution. The nonlinear (quadratic) Boussinesq approximation is adopted due to the large temperature variation of the system. The properties of the fluid are kept constant with the exception of the buoyancy force. The fluctuation in density with temperature is assumed to be quadratic. As for the energy equation of viscoelastic fluid concerned, viscous heating and deformation work are neglected.

The governing equations under boundary layer theory $\left(u \gg v, \frac{\partial}{\partial y} \gg \frac{\partial}{\partial x}, \frac{\partial^2}{\partial y} \gg \frac{\partial^2}{\partial x} \text{ and } \frac{\partial p}{\partial y} = 0\right)$ are provided below (see Abel et al. [8], Hayat et al. [9], Vajravelu and Sastri [17], Thriveni and Mahanthesh [32], Yih [33]);

Continuity Equation

$$\frac{\partial u}{\partial x} + \frac{\partial v}{\partial y} = 0, \tag{3}$$

Conservation of Momentum

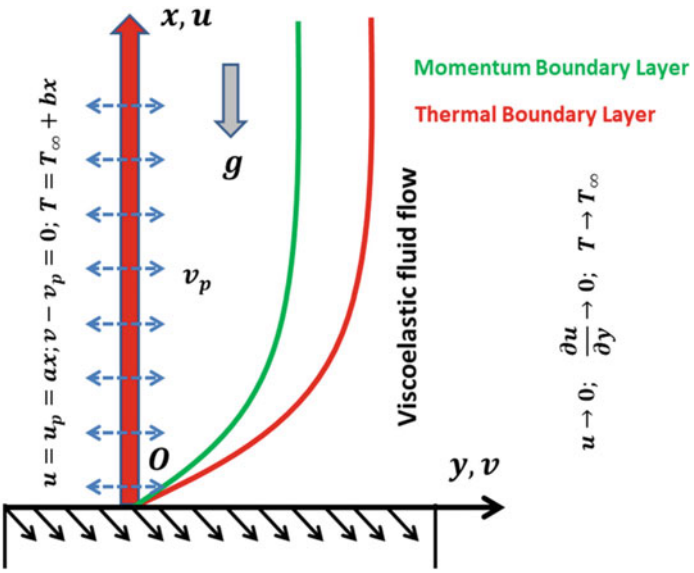

Fig. 1 Geometry of the problem

$$u\frac{\partial u}{\partial x} + v\frac{\partial u}{\partial y} = \nu\frac{\partial^2 u}{\partial y^2} - \Lambda\left(u\frac{\partial^3 u}{\partial x \partial y^2} + \frac{\partial u}{\partial x}\frac{\partial^2 u}{\partial y^2} + \frac{\partial u}{\partial y}\frac{\partial^2 v}{\partial y^2} + v\frac{\partial^3 u}{\partial y^3}\right)$$
$$+g\left[\beta_0(T - T_\infty) + \beta_1(T - T_\infty)^2\right], \tag{4}$$

Conservation of Energy

$$u\frac{\partial T}{\partial x} + v\frac{\partial T}{\partial y} = \alpha\frac{\partial^2 T}{\partial y^2} - \frac{1}{\rho C_p}\frac{\partial q_R}{\partial y}, \tag{5}$$

Boundary conditions (BC's) (see [8, 9]):

$$\text{at } y = 0 : u = u_p = ax,\ v = -v_p,\ T = T_p(x) = T_\infty + bx$$
$$\text{as } y \to \infty : u \to 0,\ \frac{\partial u}{\partial y} \to 0,\ T \to T_\infty. \tag{6}$$

The q_R (by following the Rosseland approximation [22]) is given below.

$$q_R = -\frac{4}{3k^*}\nabla(e_b) \text{ where } e_b = \sigma^* T^4. \tag{7}$$

The study of heat transport subjected to the Rosseland thermal radiation is carried out in two ways. Nonlinear thermal radiation is the first approach where the feature of thermal energy radiation is deliberated using the Rosseland approximation directly without simplifying the Eq. 7. Therefore, the energy equation becomes;

$$u\frac{\partial T}{\partial x}+v\frac{\partial T}{\partial y}=\frac{k}{\rho C_p}\frac{\partial^2 T}{\partial y^2}+\frac{\partial}{\partial y}\left[\frac{16\sigma^*}{3k^*}T^3\frac{\partial T}{\partial y}\right]. \tag{8}$$

Second approach, the nonlinear term T^4 in Eq. 7 was linearized with low-temperature difference hypothesis. That is, the temperature T is expressed by using the Taylor series about T_∞ as follows (see Cortell [29])

$$T^4=T_\infty^4+4T_\infty^3(T-T_\infty)+6T_\infty^2(T-T_\infty)^2+\cdots \tag{9}$$

By considering only a first-order term as the temperature difference is presumed to be very small then we get.

$$T^4\approx -3T_\infty^4+4T_\infty^3T. \tag{10}$$

Upon using the Eqns. (7) and (10), the temperature Eq. (5) yields

$$u\frac{\partial T}{\partial x}+v\frac{\partial T}{\partial y}=\frac{1}{\rho C_p}\left(k+\frac{16\sigma^*T_\infty^3}{3k^*}\right)\frac{\partial^2 T}{\partial y^2}. \tag{11}$$

Eq. (11) represents the energy equation subjected to linearized thermal radiation.

However, in this study, a new approach of incorporating the Rosseland thermal radiation to agree with the hypothesis (density varies quadratically with temperature) made when modeling the nonlinear Boussinesq approximation is proposed. That is, the temperature expressed about T_∞ by using Taylor series and then it is trimmed as below (see Mahanthesh and Thriveni [32])

$$T^4=T_\infty^4+4T_\infty^3(T-T_\infty)+6T_\infty^2(T-T_\infty)^2+\cdots$$

$$T^4\approx T_\infty^4+4T_\infty^3(T-T_\infty)+6T_\infty^2(T-T_\infty)^2,$$

$$T^4\approx 3T_\infty^4+6T_\infty^2T^2-8T_\infty^3T, \tag{12}$$

Using (7) and (12), the Eq. (5) yields

$$\rho C_p\left(u\frac{\partial T}{\partial x}+v\frac{\partial T}{\partial y}\right)=\left(k_{hnl}-\frac{32\sigma^*T_\infty^3}{3k^*}\right)\frac{\partial^2 T}{\partial y^2}+\frac{24\sigma^*T_\infty^3}{3k^*}\frac{\partial^2}{\partial y^2}\left(T^2\right), \tag{13}$$

Now, the friction factor and Nusselt number are defined as (see Hayat et al. [9]):

$$Sf = \frac{\tau_p}{\rho u_p^2/2}, Nu = \frac{xq_p}{k(T_w - T_\infty)}, \tag{14}$$

where,

$$\tau_p = \mu\left(\frac{\partial u}{\partial y}\right)_{y=0} + \Lambda\left(u\frac{\partial^2 u}{\partial x \partial y} + v\frac{\partial^2 u}{\partial y^2} - 2\frac{\partial v}{\partial y}\frac{\partial u}{\partial y}\right)_{y=0},$$

$$q_p = -k\left(\frac{\partial T}{\partial y}\right)_{y=0} + q_R|_{y=0}$$

where (u, v) are velocities along x- and y-directions, $\nu = \frac{\mu}{\rho}$, μ, ρ, α, are kinematic viscosity, dynamic viscosity, density and thermal diffusivity respectively, g -acceleration due to gravity, T -temperature, β_0 and β_1 -coefficients of thermal expansion, k -thermal conductivity, Λ –viscoelastic fluid parameter, ρC_p-specific heat, b and a are positive constants, σ^*, q_R, and k^* are the Stefan-Boltzmann constant, radiative heat flux, and coefficient of mean absorption respectively.

2.2 Similarity Solutions

Introduce the following similarity transformations (see Hayat et al. [9])

$$f = \frac{\psi}{\nu\sqrt{Re_x}}, \theta = (T - T_\infty)\left(T_p - T_\infty\right)^{-1}, \eta = \frac{y}{x}\sqrt{Re_x} \tag{15}$$

into Eqs. (3), (4), (6), (8), (11), (13), and (14), then Eq. (3) identically satisfied while other equations reduced to.

Linear Momentum Equation

$$\frac{d^3 f}{d\eta^3} + f\frac{d^2 f}{d\eta^2} - \left(\frac{df}{d\eta}\right)^2 - V_e\left(f\frac{d^4 f}{d\eta^4} - 2\frac{df}{d\eta}\frac{d^3 f}{d\eta^3} + \left(\frac{d^2 f}{d\eta^2}\right)^2\right) + \lambda\theta(1 + Q_c\theta) = 0, \tag{16}$$

Using Linear Thermal Radiation

$$\frac{1}{Pr}\left(1 + \frac{4R}{3}\right)\frac{d^2\theta}{d\eta^2} + f\frac{d\theta}{d\eta} - \theta\frac{df}{d\eta} = 0, \tag{17}$$

Using Nonlinear Thermal Radiation.

$$\frac{1}{Pr}\frac{d^2\theta}{d\eta^2} + f\frac{d\theta}{d\eta} - \theta\frac{df}{d\eta} + \frac{4R}{3Pr}\frac{d}{d\eta}\left[\left(1 + \left(\theta_p - 1\right)\theta\right)^3\frac{d\theta}{d\eta}\right] = 0, \tag{18}$$

Using Quadratic Thermal Radiation

$$\frac{1}{Pr}\left(1-\frac{8R}{3}\right)\frac{d^2\theta}{d\eta^2}+f\frac{d\theta}{d\eta}-\theta\frac{df}{d\eta}+\frac{2R}{Pr\left(\theta_p-1\right)}\frac{d^2}{d\eta^2}\left[(1+(\theta_w-1)\theta)^2\right]=0, \tag{19}$$

with BC's

$$f(\eta)=S,\ \frac{df}{d\eta}=1,\theta(\eta)=1 \text{ at } \eta=0$$

$$\frac{df}{d\eta}\to 0,\ \frac{d^2f}{d\eta^2}\to 0,\theta(\eta)\to 0 \text{ as } \eta\to\infty \tag{20}$$

Dimensionless quantities of engineering interest are

$$Re_x^{\frac{1}{2}}Sf=(1+3V_e)\frac{d^2f}{d\eta^2}|_{\eta=0},$$

$$Re_x^{-\frac{1}{2}}Nu=-\left(1+\frac{4}{3}R\right)\frac{d\theta}{d\eta}|_{\eta=0}, \text{(Linear thermal radiation)},$$

$$Re_x^{-\frac{1}{2}}Nu=-\left(1+\frac{4}{3}R\theta_p^3\right)\frac{d\theta}{d\eta}|_{\eta=0}, \text{(Nonlinear thermal radiation)},$$

$$Re_x^{-\frac{1}{2}}Nu=-\left(1+(4/3)R+3R(\theta_p-1)\right)\frac{d\theta}{d\eta}|_{\eta=0}, \text{(Quadratic thermal radiation)} \tag{21}$$

Where ψ, f, θ, and η are stream function, dimensionless velocity, dimensionless temperature, and similarity variable, $Pr=\frac{\nu}{\alpha}$ is the Prandtl number, $V_e=\frac{\Lambda a}{\nu}$ is the viscoelastic fluid factor, $S=\sqrt{\frac{\rho}{a\mu}}\,v_p$ suction/injection factor, $Q_c=\frac{\beta_1}{\beta_0}(T_w-T_\infty)$ is quadratic convection factor, $\lambda=\frac{g\beta_0 b}{a^2}=\frac{g\beta_0(T_w-T_\infty)x^3/\nu^2}{u_p^2x^2/\nu^2}=\frac{Gr_x}{Re_x^2}$ is the mixed convection factor, $\theta_p=\frac{T_w}{T_\infty}$ is the temperature ratio factor, and $Re_x=u_wx/_\nu$ local Reynolds number.

3 Results and Discussion

Owing to the nonlinear in nature of the 2-point boundary value problem (BVP) comprised in Eqns. 16–20, the finite difference method based bvp5c algorithm applied for the numerical solutions. Many eminent researchers have employed and described in detail the effectiveness of this method. For the numeric simulations, the

values of key parameters have been selected carefully as default parametric values $Pr = 1$, $Ve = \lambda = 0.5$, $Q_c = 0.2$, $R = 0.5$, $\theta_p = 1.5$ and $S = 0.2$ (see [9, 17, 33]). The employed method has been substantiated by comparing the values of the chosen key parameter with allied published works when $Vc = \lambda = R = S = 0$. Table 1 gives the documentation of the Nusselt number ($Re_x^{-\frac{1}{2}} Nu$) in comparison with those of [9] and [33] for $Pr = 0.72, 1, 3, 10$. The comparison shows excellent collaboration. Moreover, Table 1 depicts that the rate of heat transfer $Re_x^{-\frac{1}{2}} Nu$ increases as the Pr increases. A larger Pr correlates with a thinner temperature boundary layer thickness. The greater the thickness of the temperature boundary layer, the greater will be $Re_x^{-\frac{1}{2}} Nu$. The same result can also be found in Table 2. Table 2 presents the numeric values of $Re_x^{-\frac{1}{2}} Nu$ versus Pr to compare the consequence of Rosseland linear thermal radiation (RLTR) and Rosseland quadratic thermal radiation (RQTR) aspects. It is very clear that the values of $Re_x^{-\frac{1}{2}} Nu$ are higher in the case of RQTR than in the of RLTR. Indeed, there is a difference of more than 100% between the values of $Re_x^{-\frac{1}{2}} Nu$ with RQTR and $Re_x^{-\frac{1}{2}} Nu$ with RLTR. The slope of the data points is calculated to estimate the rate at which $Re_x^{-\frac{1}{2}} Nu$ is increased due to the change in Pr for both cases. Here, the $Re_x^{-\frac{1}{2}} Nu$ with RLTR aspect is increased with Pr at the rate of 0.4278 while $Re_x^{-\frac{1}{2}} Nu$ subjected to RQTR aspect is enhanced with Pr at the rate of 1.4933. That is, the rate of upsurge in the Nusselt number with RQTR is three times greater than the rate of upsurge in the Nusselt number with RLTR.

Figure 2 is plotted to compare the velocities with and without quadratic Boussinesq approximation (QBA). Here, the velocities ($f'(\eta)$, $f(\eta)$) and their relevant boundary layer thickness are higher in the presence of quadratic Boussinesq approximation than its absence. Physically, the effect of quadratic convection effect (quadratic Boussinesq approximation) is known to add on to the buoyancy forces and as a result the flow distribution intensifies. Compared to the two curves in Fig. 3, the temperature field $\theta(\eta)$ is higher in the presence of QBA. The quadratic Boussinesq approximation has a significant effect on the transverse velocity that it does on axial velocity

Table 1 Comparison of $Re_x^{-\frac{1}{2}} Nu$ with those of [9, 33] when $Vc = \lambda = R = S = 0$

Pr	$Re_x^{-\frac{1}{2}} Nu$		
	Yih [33] (Keller's box method)	Hayat et al. [9] (Homotopy Analysis Method)	Present results (Finite Difference Method-bvp5c)
0.72	0.8086	0.8086	0.8088
1.0	1.0000	1.0000	1.0000
3.0	1.9237	1.9237	1.9236
10.0	3.7207	3.7207	3.7206

Table 2 The $Re_x^{-\frac{1}{2}} Nu$ for RLTR and RQTR cases when $Ve = \lambda = 0.5$, $Q_c = 0.2$, $R = 0.5$, $\theta_p = 1.5$ and $S = 0.2$ for various values of Pr

Pr	$Re_x^{-\frac{1}{2}} Nu$	
	Rosseland Linear Thermal Radiation (RLTR)	Rosseland Quadratic Thermal Radiation (RQTR)
0.7	1.1696	2.4332
1.0	1.4512	3.1110
1.5	1.7282	3.7205
3.0	2.2192	5.9581
Slope	0.4278	1.4933

and temperature, as compared to Figs. 2 and 3. Figure 4 is sketched to compare the significance of Rosseland linear thermal radiation (RLTR), Rosseland quadratic thermal radiation (RQTR), Rosseland nonlinear thermal radiation (RNTR) effects on the temperature field $\theta(\eta)$. This figure is prepared by solving the Eqs. 17–19 individually along with Eq. 16. Among the three different forms of radiation effects, the impact of RNTR is more prominent than the effects of RQTR and RLTR in a order.

The role of quadratic thermal convection parameter Q_c on the velocities ($f'(\eta)$, $f(\eta)$) is illustrated in Fig. 5. The accelerated flow (both axial velocity and transverse velocity) due to quadratic thermal convection parameter Q_c as observed in Fig. 5 is occasioned by the stronger buoyancy force. It is also justifiable since this Q_c is a supplementary term to the buoyancy force. However, the temperature field $\theta(\eta)$ and its related layer thickness are diminished by increasing Q_c.

Figures 6 and 7 show the consequence of the viscoelastic material parameter (V_e) on dimensionless profiles $f'(\eta)$, $f(\eta)$ and $\theta(\eta)$ across the flow region. It is worth remembering that the negative values of V_e ($V_e < 0$) represent Walter's liquid B, the positive values of V_e ($V_e > 0$) signify the second-grade fluid and $V_e = 0$

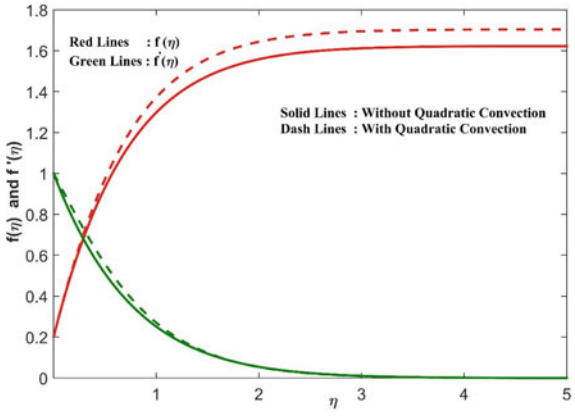

Fig. 2 Velocity profiles ($f(\eta)$, $f'(\eta)$) versus η

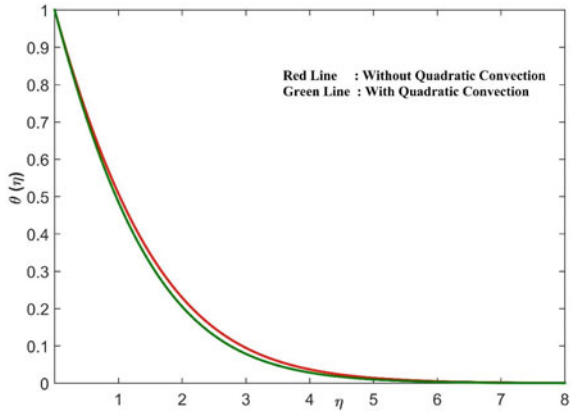

Fig. 3 Temperature profile $(\theta(\eta))$ versus η

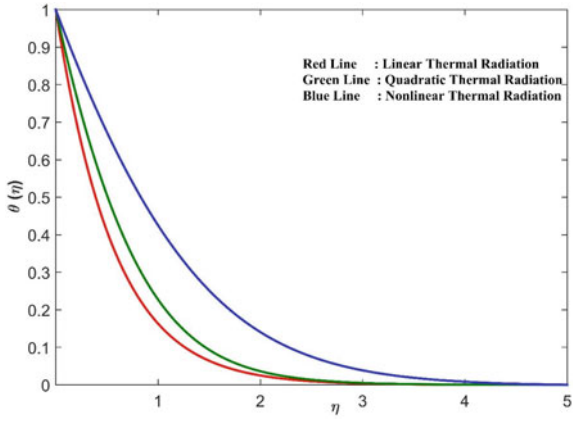

Fig. 4 Temperature profile $(\theta(\eta))$ versus η for linear, quadratic and nonlinear thermal radiation

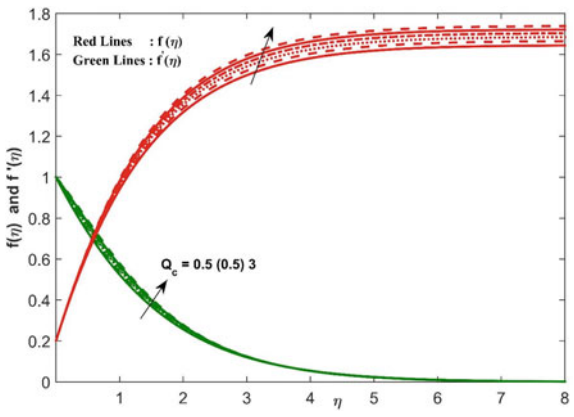

Fig. 5 Velocity profiles $(f(\eta), f'(\eta))$ versus η for various numeric values Q_c

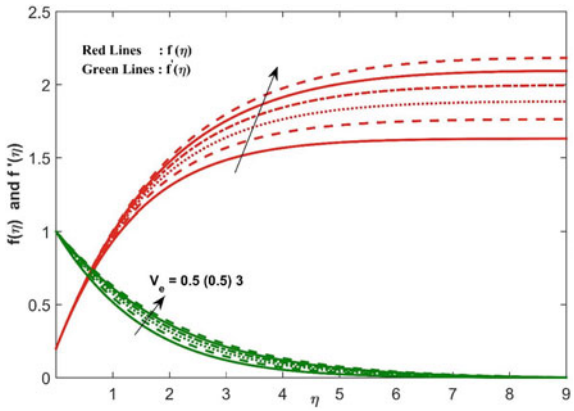

Fig. 6 Velocity profiles $(f(\eta), f'(\eta))$ versus η for various numeric values of V_e

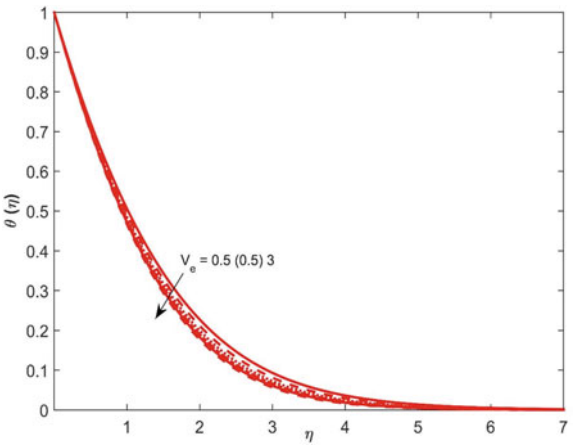

Fig. 7 Temperature profile $(\theta(\eta))$ versus η for various numeric values V_e

signifies the Newtonian fluid. It is evident from Fig. 6 that the velocities elevated with V_e whereas the layer thickness reduced for larger V_e. Due to the nonlinear form of the constitutive equations, flows of viscoelastic material facilitate instability. Normal stresses owing to the fluid elasticity cause instability. Figure 8 presents the streamlines for $Q_c = 0, 0.5, 1.0, 1.5$.

4 Concluding Remarks

Theoretical analysis was performed on the dynamics of a viscoelastic material with quadratic thermal convection on a stretchable surface with quadratic Rosseland thermal radiation. The flow is configured in a two-dimensional extensible vertical

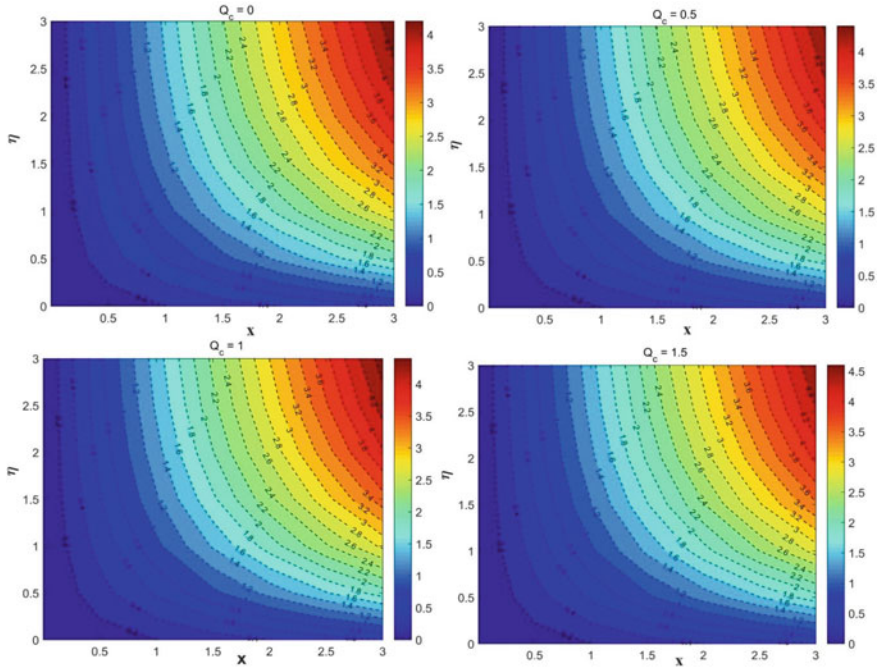

Fig. 8 Streamlines for various numerical values of Q_c

surface with transpiration cooling. The nonlinear 2-point boundary value problem has been solved numerically.

The main outcome of the present analysis are:

- An increase in the viscoelastic material parameter values strengthen the velocity field and rate of heat transport while it shrinks the thermal boundary layer structure.
- Quadratic thermal convection factor improved the thickness of the velocity boundary layer by contracting the thermal boundary layer structure.
- Among the three different forms of Rosseland thermal radiation, the thermal field is lower for Rosseland linear thermal radiation (RLTR) than for RQTR and RNTR in an order.
- The inclusion of a quadratic term in the fluctuation of the density temperature significantly affects the velocities, the temperature, and the Nusselt number.
- The growth of the mixed convection parameter increases the velocity of the viscoelastic fluid due to a lower viscous force, while the temperature field is reduced.
- The heat transfer rate improves due to the appearance of suction/injection.
- The heat transport rate advances for a higher value of quadratic convection parameter and lower value of quadratic thermal radiation parameter.

References

1. Beard DW, Ken Walters (1964) Elastico-viscous boundary-layer flows I. Two-dimensional flow near a stagnation point." In: Mathematical Proceedings of the Cambridge Philosophical Society, 60(3), pp. 667–674. Cambridge University Press
2. Rajagopal KR (1995) On boundary conditions for fluids of the differential type. In: Navier—Stokes Equations and Related Nonlinear Problems, pp. 273–278. Springer, Boston, MA
3. Frater KR (1970) On the solution of some boundary-value problems arising in elastico-viscous fluid mechanics. Z Für Angew Math Und Phys ZAMP 21(1):134–137
4. Ariel PD (1992) A hybrid method for computing the flow of viscoelastic fluids. Int J Numer Meth Fluids 14(7):757–774
5. Rollins D, Vajravelu K (1991) Heat transfer in a second-order fluid over a continuous stretching surface. Acta Mech 89(1–4):167–178
6. Siddappa B, Abel MS (1986) Visco-elastic boundary layer flow past a stretching plate with suction and heat transfer. Rheol Acta 25(3):319–320
7. Prasad KV, Subhas Abel M, Sujit Kumar Khan (2000) Momentum and heat transfer in visco-elastic fluid flow in a porous medium over a non-isothermal stretching sheet. Int J Numer Methods Heat & Fluid Flow
8. Abel M, Subhas Sujit Kumar Khan, Prasad KV (2001) Convective heat and mass transfer in a visco-elastic fluid flow through a porous medium over a stretching sheet. Int J Numer Methods Heat & Fluid Flow
9. Hayat T, Mustafa M, Pop I (2010) Heat and mass transfer for Soret and Dufour's effect on mixed convection boundary layer flow over a stretching vertical surface in a porous medium filled with a viscoelastic fluid. Commun Nonlinear Sci Numer Simul 15(5):1183–1196
10. Li J, Zheng L, Liu L (2016) MHD viscoelastic flow and heat transfer over a vertical stretching sheet with Cattaneo-Christov heat flux effects. J Mol Liq 221:19–25
11. Mebarek-Oudina F (2017) Numerical modeling of the hydrodynamic stability in vertical annulus with heat source of different lengths. Eng Sci Technol, Int J 20(4):1324–1333
12. Khan U, Zaib A, Mebarek-Oudina F (2020) Mixed convective magneto flow of SiO_2—$MoS_2/C_2H_6O_2$ hybrid nanoliquids through a vertical stretching/shrinking wedge: Stability analysis". Arab J Sci Eng
13. Mebarek-Oudina F, Aissa A, Mahanthesh B, Öztop HF (2020) Heat transport of magnetized Newtonian nanoliquids in an annular space between porous vertical cylinders with discrete heat source. Int Commun Heat Mass Transfer 117:104737
14. Zaim A, Aissa A, Mebarek-Oudina F, Mahanthesh B, Lorenzini G, Sahnoun M, El Ganoui M (2020) Galerkin finite element analysis of magneto-hydrodynamic natural convection of Cu-water nanoliquid in a baffled U-shaped enclosure. Propulsion and Power Research
15. Mebarek-Oudina F, Bessaïh R (2019) Numerical simulation of natural convection heat transfer of copper-water nanofluid in a vertical cylindrical annulus with heat sources. Thermophys Aeromech 26(3):325–334
16. Goren SL (1966) On free convection in water at 4 C. Chem Eng Sci 21(6–7):515–518
17. Vajravelu K, Sastri KS (1977) Fully developed laminar free convection flow between two parallel vertical walls—I. Int J Heat Mass Transf 20(6):655–660
18. Mahanthesh B, Gireesha BJ, Thammanna GT, Shehzad SA, Abbasi FM, Gorla RSR (2018) Nonlinear convection in nano Maxwell fluid with nonlinear thermal radiation: A three-dimensional study. Alex Eng J 57(3):1927–1935
19. Jha BK, Sarki MN (2020) Chemical reaction and Dufour effects on nonlinear free convection heat and mass transfer flow near a vertical moving porous plate. Heat Transfer 49(2):984–999
20. Mandal, Iswar Chandra, Swati Mukhopadhyay (2019) Nonlinear convection in micropolar fluid flow past an exponentially stretching sheet in an exponentially moving stream with thermal radiation. Mech Adv Mater Struct 26(24): 2040–2046
21. Hayat T, Qayyum S, Alsaedi A, Ahmad B (2017) Magnetohydrodynamic (MHD) nonlinear convective flow of Walters-B nanofluid over a nonlinear stretching sheet with variable thickness. Int J Heat Mass Transf 110:506–514

22. Rosseland S (1931) Astrophysik und atom-theoretische Grundlagen. Springer-Verlag, Berlin, pp 41–44
23. Sparrow EM, Cess RD (1978) Radiation Heat Transfer. Hemisph Publ Corp, Washington
24. Makinde OD, Animasaun IL (2016) Bioconvection in MHD nanofluid flow with nonlinear thermal radiation and quartic autocatalysis chemical reaction past an upper surface of a paraboloid of revolution. Int J Therm Sci 109:159–171
25. Lopez A, Ibanez G, Pantoja J, Moreira J, Lastres O (2017) Entropy generation analysis of MHD nanofluid flow in a porous vertical microchannel with nonlinear thermal radiation, slip flow and convective-radiative boundary conditions. Int J Heat Mass Transf 107:982–994
26. Bhatti Muhammad Mubashir, Abbas T, Rashidi MM (2016) Numerical study of entropy generation with nonlinear thermal radiation on magnetohydrodynamics non-Newtonian nanofluid through a porous shrinking sheet. J Magn 21(3): 468–475
27. Muhammad T, Waqas H, Khan SA, Ellahi R, Sait SM (2020) Significance of nonlinear thermal radiation in 3D Eyring–Powell nanofluid flow with Arrhenius activation energy. J Therm Anal Calorim, 1–16
28. Shaw S, Mabood F, Muhammad T, Nayak MK, Alghamdi M (2020) Numerical simulation for entropy optimized nonlinear radiative flow of GO-Al_2O_3 magneto nanomaterials with auto catalysis chemical reaction. Numer Methods PartL Differ EquS
29. Bataller RC (2008) Radiation effects in the Blasius flow. Appl Math Comput 198(1):333–338
30. Raza J, Mebarek-Oudina F, Ram P, Sharma S (2020) MHD flow of non-Newtonian molybdenum disulfide nanofluid in a converging/diverging channel with Rosseland radiation. Defect and Diffusion Forum 401:92–106
31. Mahanthesh B (2021). Quadratic radiation and quadratic Boussinesq approximation on hybrid nanoliquid flow. In: Mathematical Fluid Mechanics (pp. 13–54). De Gruyter
32. Thriveni K, Mahanthesh B (2020) Optimization and sensitivity analysis of heat transport of hybrid nanoliquid in an annulus with quadratic Boussinesq approximation and quadratic thermal radiation. Eur Phys J Plus 135(6):459
33. Yih KA (1999) Free convection effect on MHD coupled heat and mass transfer of a moving permeable vertical surface. Int Commun Heat Mass Transfer 26(1):95–104

Chapter 14
Composite Nanofluids Flow Driven by Electroosmosis Through Squeezing Parallel Plates in Presence of Magnetic Fields

J. Prakash, R. Balaji, Dharmendra Tripathi, Abhishek Kumar Tiwari, and R. K. Sharma

Abstract Fluid flow across parallel plates has been involved in a variety of commercial and technological applications which have continuously been attracting the interest of the researchers. This chapter presents an approach to investigate electromagnetohydrodynamics (EMHD) squeezing flow of viscous ternary composite nanofluid (Al_2O_3 (spherical), silicon dioxide (spherical), and multi-walled carbon nanotube (MWCNT) (cylindrical) with base fluid H_2O (water)) with zeta potential effects. A set of partial differential equations describing continuity and momentum equations in the mathematical framework is considered. In the present work, the electro-viscous effects caused by electric double-capacity flow field distortions are thoroughly examined over a wide range of applied plate motion intensities. The results of the model vary significantly from those obtained using a normal Poisson–Boltzmann equation model. The governing equations are then transformed into ordinary differential equations using similarity transformation and then numerically solved using MATLAB software. The numerical solutions are employed to explore the scaling phenomena of the liquid, while plates move apart and collide. The influences of numerous parameters on fluid axial velocity and skin friction coefficient have also been explored, including squeezing number, zeta potential parameter,

J. Prakash
Department of Mathematics, Avvaiyar Government College for Women, Karaikal, Puducherry-U.T. 609 602, India

R. Balaji
Department of Mathematics, Panimalar Engineering College, Chennai, Tamil Nadu 600123, India

D. Tripathi (✉)
Department of Mathematics, National Institute of Technology, Uttarakhand, Srinagar 246174, India
e-mail: dtripathi@nituk.ac.in

A. K. Tiwari
Department of Applied Mechanics, Motilal Nehru National Institute of Technology Allahabad, Prayagraj 211004, India

R. K. Sharma
Department of Mechanical Engineering, Manipal University Jaipur, Rajasthan 303007, India

D. Tripathi et al. (eds.), *Advancements in Nanotechnology for Energy and Environment*, Advances in Sustainability Science and Technology,
https://doi.org/10.1007/978-981-19-5201-2_14

electric field parameter, and electroosmosis parameter. Numerical results conveyed that prominent retardation in flow of ternary hybrid nanofluid is attained due to magnification of electroosmotic parameter at the lower plate.

Keywords Squeezing flow · Magnetic field · Electroosmotic flow · Zeta potential · Ternary hybrid nanofluids

1 Introduction

Squeezing flow explains mobility of a droplet of the material. In current science and technology, squeezing flow has a broad variety of applications, including composite material joining, food preservation, warm plate welding, cooling liquid, squeezed films, and rheological testing. Study of the momentum equation is crucial in analysing the squeezing flow [1]. Stefan et al. [1] provided an essential and breakthrough research on squeezing movement under the idea of lubricating oil. This outstanding work sets the path for additional research into the squeezing flow. Previous squeezing motion experiments depended on the Reynolds equation, as presented by Jackson [2], Usha, and Sridharan [3] which is insufficient in some situations. Reynolds [4] had spent decades studying the squeezing motion of elliptic plates, while Archibald [5] studied the same issue with rectangular plates. Mahmood et al. [6] presented the squeezed dynamic analysis for heat transfer on a porous surface. Hayat et al. [7] investigated the impact of chemical reaction and thermally conductive conditions on squeezing motion. Maintaining flow in magnetic fields has significant consequences for many areas of physics, such as nuclear reactors with geothermal extractions, magneto-hydrodynamics (MHD) generators, aeronautical, plasma research, and aerodynamic boundary layer management, among others [8–14]. Adesanya et al. [15] investigated the unstable MHD squeezing Eyring-Powell liquid motion across an infinite tube. They arrived to the conclusion that velocity profile varies with Hartmann parameter. Domairry and Aziz [16] also conducted a homotopy perturbation study for MHD squeeze movement over parallel discs. Thus, a wide literature is available on understanding of squeezing flow.

Electroosmosis is a basic electrokinetic occurrence in which a peripheral electric field implemented between the inlet and outlet induces flow of an electrolyte in a plate/channel after interaction between both the dielectric walls of the plate/channel, and the polar fluid has formed near-wall layers of counter-ions within the fluid. Electric field has the potential to modulate electric field, whereas neutral core pushes and moves like a solid body [17]. Reuss [18] demonstrated the hypothesis for the first time in an experiment using porous clay [18], whereas Helmholtz [19] published theoretical research on electric double layer (EDL) which relates the electrical and stream properties for electrokinetically powered motions. Von Smoluchowski [20] made substantial advances to the understanding of electrokinetically propelled streams, especially when the EDL thickness is much smaller than the channel height. Burgreen and Nakache [21] investigated the impact of the surface potential on liquid flow

through ultrafine slits using the Debye–Hückel linear approach to the applied electric distribution within an applied electrical field. Umavathi et al. [22] used a central difference technique based on Lobotto quadrature to describe the transient squeezing motion of magnetised nanofluid lubricant over parallel discs with heterogeneous boundary layer. They observed that a greater resistance magnetic body strength (i.e. a higher Hartmann number) dampens velocity in the intermediate zone. Prajapati [23] and Khan et al. [24] looked into magneto-hydrodynamics with squeeze film dynamics while employing variation of parameters method (VPM) to assess the load capacity of magnetic squeezing films. All of these studies discovered that magnetic lubricants improve efficiency as it regulates lubricant viscosity fluctuation under high operating conditions. Zhao et al. [25] investigated electro-viscous influence on the squeezing stream of thin electrolyte sheets restricted between two curved and flat charged surfaces using lubrication assumptions. They solved the Nernst–Planck–Poisson/Navier–Stokes equation and investigated the interaction between the conservative electric double layer (EDL) strength and the electro-viscous effect-enhanced viscous dissipation hydrodynamic force, demonstrating that the EDL's counter-ion conductivity has a significant influence on the electro-viscous impact at a given zeta potential and generates a much sharper velocity distribution. Talapatra and Chakraborty [26] examined effects of electric double layer flow field distortion on electroosmotic squeezing flow between two charged parallel plates. Several studies of MHD in electroosmotic flows are interesting to be looked into [27–33].

Choi [34] first time presented idea of nanofluids. Xuan and Roetzel [35] include thermal dispersion in motion helped to improve the heat transfer mechanism. They suggested two different approaches to determine the link between heat transport and nanofluid. Xuan and Li [36] presented a theoretical model which characterised the heat transport properties of a nanofluid flowing in a tubular area. The clustering of nanoparticles was explored in the research of Kelbinski et al. [37, 38]. Natural convection was analysed by Ghalambaz et al. [39, 40] and shown to be present in the flow of nanofluid that contained phase-change particles. Ghalambaz [41, 42] reported spontaneous convection which occurs in an unstable flow of nanofluid. According to findings investigations, nanofluids have a wide range of potential uses, including those in the fields of industrialised cooling, the production of detergent, medicinal applications, nuclear reactors, microchip technology, and other related fields.

The goal of producing nanofluid composites is to improve the thermal conductivity or rheological characteristics of individual nanoparticles. The thermal conductivity and rheological properties of the resultant nanofluid may be improved by framing a composite nanofluid. Superior thermal conductivity does not guarantee better rheological properties of a nanofluid created by adding nanoparticles. A nanofluid which is more stable and effective may be achieved by incorporating various rheological or thermal characteristics into the nanofluid. For example, Al_2O_3 has a high level of chemical inertness and stability, but it has a poor thermal conductivity as well. The thermal conductivity and chemical reactivity of metals such as aluminium, silver, and copper, on the other hand, are much lower. Hybrid nanofluids are created by combining different types of nanoparticles with various types of physical and chemical connections. They are used in nuclear safety, the pharmaceutical sector, the

cooling of electronic devices, and other areas. A large number of researchers are showing interest in hybrid nanofluids. Saeed et al. [43] reported Darcy–Forchheimer flow for hybrid nanofluids across a spinning disc. Alzahrani et al. [44] explained the mobility of hybrid nanofluid on a flat plate. Kumar [45] reported hybrid nano-liquid flow through a stretched surface using the Runge–Kutta technique. Hybrid nanofluid investigations [46–49] and the references therein provide more pertinent information.

There are three different types of nanoparticle mixtures in the ternary composite nanofluids. Ternary hybrid nanofluids have better thermophysical characteristics because of the unique features of each nanoparticle in their ternary mixing. Photovoltaic thermal collectors and solar electricity are noticeable uses of ternary nanofluids. Animasaun et al. [50] studied the flow of a nanofluid across a convective heated surface. Arif et al. [51] investigated the flow of ternary hybrid nanofluids between parallel channels. Souby et al. [52] explained ternary hybrid nanofluid in a microchannel. Nano-liquids based on ethylene glycol flow laminarly as reported by Sundar et al. [53]. Nanofluid viscosity is affected by the concentration and temperature of nanoparticles [54]. The rheological characteristics of water-based ternary hybrid nano-liquids were also investigated by Zayan et al. [55].

Based on the finding of the literature, the present study introduces a mathematical model for coupled magneto-hydrodynamics and electroosmotic squeezing stream with zeta potential effects in parallel plate lubrication geometry. To the best of the authors' knowledge, the resulting electromagnetic hydrodynamics viscous ternary hybrid nanofluid (Al_2O_3, SiO_2, MWCNT/water), with squeezing flow effects have not been explored in the available literature. There is a clear scope of mathematical investigation on the thermo-osmotic effects in squeezing flows which provided a strong motivation for the present work.

2 Mathematical Model Formulation

The numerical simulation of incompressible, viscous, squeezing ternary hybrid nanofluid (Al_2O_3, SiO_2, MWCNT/water) flow across parallel plates has been introduced in the present work (Fig. 1). The Cartesian coordinate system (X, Y) is considered. X axis is oriented along the plate, and Y axis is perpendicular to the plate. Further, the suspended particles are flowing in front of a magnetic field $B(t)\left(= \frac{B_0}{\sqrt{1-a\,t}}\right)$, and fluid electrical net charge thickness ρ_e and rest of the body forces are disregarded. The length of the parallel plates is

$$h(t) = H(1 - a\,t)^{1/2} \tag{1}$$

The preliminary position of the upper plate is H at $t = 0$, and a is a characteristic frequency parameter.

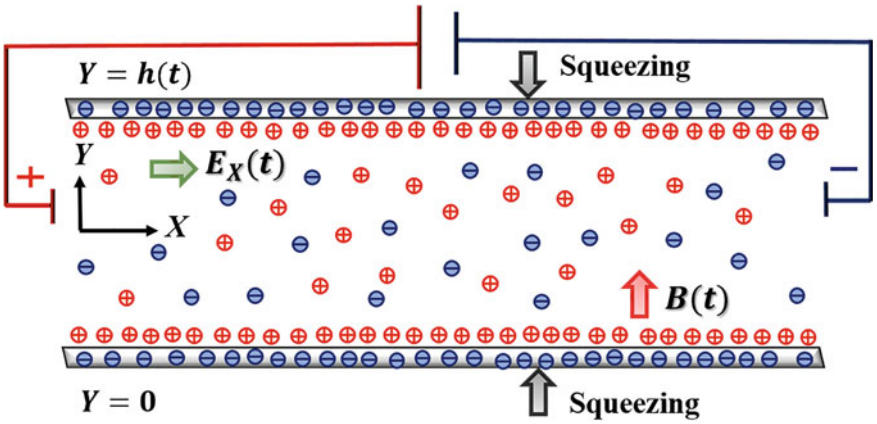

Fig. 1 Geometrical representation of squeezing flow modulated by electroosmosis in the presence of magnetic field

2.1 The Governing Equations

The fluid flow is showed by the continuity and momentum equations as:

$$\frac{\partial U}{\partial X} + \frac{\partial V}{\partial Y} = 0 \tag{2}$$

$$\rho_{\text{thnf}}\left(\frac{\partial U}{\partial t} + U\frac{\partial U}{\partial X} + V\frac{\partial U}{\partial Y}\right) = -\frac{\partial P}{\partial X} + \mu_{\text{thnf}}\left(\frac{\partial^2 U}{\partial X^2} + \frac{\partial^2 U}{\partial Y^2}\right) - \sigma_{\text{thnf}} B(t)u + \rho_e E_X(t), \tag{3}$$

$$\rho_{\text{thnf}}\left(\frac{\partial V}{\partial t} + U\frac{\partial V}{\partial X} + V\frac{\partial V}{\partial Y}\right) = -\frac{\partial P}{\partial Y} + \mu_{\text{thnf}}\left(\frac{\partial^2 V}{\partial X^2} + \frac{\partial^2 V}{\partial Y^2}\right), \tag{4}$$

where the velocity components (U, V) represent along (X, Y) direction, respectively, ρ_{thnf} density of ternary hybrid fluid, P pressure, μ_{thnf} dynamics viscosity of ternary hybrid. It is assumed that the applied electric field $E_X(t)$ of parallel plates can be defined as

$$E_X(t) = \frac{E_x}{1 - a\,t} \tag{5}$$

2.2 Thermophysical Properties of Ternary Hybrid Nanofluid

2.2.1 Density

Nanofluids with a ternary hybrid structure have a density that is defined [50–55] as:

$$\rho_{\text{thnf}} = \rho_1\phi_1 + \rho_2\phi_2 + \rho_3\phi_3 + (1 - \phi_1 - \phi_2 - \phi_3)\rho_f \tag{6}$$

where ϕ_1, ϕ_2, ϕ_3 are the volume fractions and ρ_1, ρ_2, ρ_3 are the densities of nanoparticle-1, nanoparticle-2, and nanoparticle-3, respectively, and ternary hybrid nanofluid (THN) of total volume faction is $\phi = \phi_1 + \phi_2 + \phi_3$. The base density fluid is ρ_f.

Al_2O_3 (spherical) is considered as nanoparticle-1, nanoparticle-2 is silicon dioxide (spherical), multi-walled carbon nanotube (MWCNT) (cylindrical) is considered as nanoparticle-3, and base fluid is H_2O(water).

2.2.2 Viscosity

Nanofluids with a ternary hybrid structure have a dynamic viscosity that is defined [50–55] as

$$\mu_{hnf} = \left(\mu_{nf,1}\phi_1 + \mu_{nf,2}\phi_2 + \mu_{nf,3}\phi_3\right)/\phi \tag{7}$$

where $\mu_{nf,i} = \mu_f\left(1 + B_i\phi + C_i\phi^2\right)$ is the dynamic viscosity of *i*th-type nanoparticle (with given shape) suspension and the base fluid of dynamic viscosity is μ_f.

2.2.3 Electrical Conductivity

The electrical conductivity of ternary hybrid nanofluid [50] is defined as

$$\frac{\sigma_{\text{thnf}}}{\sigma_{\text{hnf}}} = \frac{(1 + 2\phi_1)\sigma_1 + (1 - 2\phi_1)\sigma_{\text{hnf}}}{(1 - \phi_1)\sigma_1 + (1 + \phi_1)\sigma_{\text{hnf}}} \tag{8}$$

where $\frac{\sigma_{\text{hnf}}}{\sigma_{\text{nf}}} = \frac{(1+2\phi_2)\sigma_2+(1-2\phi_2)\sigma_{\text{nf}}}{(1-\phi_2)\sigma_2+(1+\phi_2)\sigma_{\text{nf}}}$ and $\frac{\sigma_{\text{nf}}}{\sigma_f} = \frac{(1+2\phi_3)\sigma_3+(1-2\phi_3)\sigma_f}{(1-\phi_3)\sigma_3+(1+\phi_3)\sigma_f}$.

Here, $\sigma_1, \sigma_2, \sigma_3$ are the electrical conductivity of nanoparticle-1, nanoparticle-2, and nanoparticle-3, respectively; the base electrical conductivity is σ_f. Tables 1 and 2 contain information on the thermophysical constants with regard to the nanoparticles and the base fluid.

Table 1 Parameters for defining shape and properties of nanoparticles

Nanoparticle shape	B	C
Platelets	37.1	612.6
Cylindrical	13.5	904.4
Spherical	2.5	6.2

Table 2 Thermophysical aspects of water, Al_2O_3, SiO_2, MWCNT

Properties	Pure water	Al_2O_3	SiO_2	MWCNT
Density ρ $\left(\mathrm{Kgm}^{-3}\right)$	997.1	3970	2270	2600
Electric conductivity $\sigma\,(\mathrm{Sm}^{-1})$	5.5×10^{-6}	5.96×10^{7}	3.5×10^{6}	1.9×10^{-4}

2.3 Electrical Potential

The electrical potential as a result of the EDL is given by the Boltzmann–Poisson equation moulded in parallel plates.

$$\nabla^2 \overline{\Phi} = -\frac{\rho_e}{\varepsilon_{ef}} \tag{9}$$

where ε_{ef} is the permittivity or the dielectric constant of the solution. The count of the ions of type-i, referred to as n_i, in a symmetric electrolyte solution, should be assumed to be the equilibrium Boltzmann distribution equation applicable:

$$\tilde{n}_i = \tilde{n}_{i0} \exp\left(-\frac{\tilde{z}_i e\,\overline{\Phi}}{k_B \tilde{T}_{\tilde{H}}}\right) \tag{10}$$

where $\tilde{T}_{\tilde{H}}$, e, k_B, $\tilde{n}_{i0}$, and $\tilde{z}_i$ are the absolute temperature, charge of an electron, Boltzmann constant, bulk ionic concentration, and the valence of type-i ions, respectively.

The net volume charging density (ρ_e) is linked to the overall concentration and the difference between anions and cations for a symmetric electrolyte of value $\tilde{z}$ as:

$$\tilde{\rho}_e = \tilde{z}e(\tilde{n}_+ - \tilde{n}_-) \tag{11}$$

Substituting Eq. (10) in Eq. (11), the equation modifies as:

$$\rho_e = -2\tilde{z}e\tilde{n}_0 \sinh\left(\frac{\tilde{z}e\overline{\Phi}}{k_B \tilde{T}_{\tilde{H}}}\right) \tag{12}$$

Substituting the value of charged density (Eq. (12)) in the Poisson equation (Eq. (9)) results in:

$$\frac{\partial^2 \overline{\Phi}}{\partial Y^2} = \frac{2\tilde{z}e\tilde{n}_0}{\varepsilon_{ef}} \sinh\left(\frac{\tilde{z}e\overline{\Phi}}{k_B \tilde{T}_{\tilde{H}}}\right), \tag{13}$$

2.4 Dimensional Boundary Conditions

The inflicted boundary conditions for the proposed problem are defined by

$$\begin{aligned} &U = 0, \;\; V = V_H = \frac{dh}{dt}, \;\; \overline{\Phi} = \tilde{\xi} \;\; at \;\;\; Y = h(t) \\ &\frac{\partial U}{\partial Y} = 0, \;\; V = 0, \;\; \frac{\partial \overline{\Phi}}{\partial Y} = 0 \; at \;\;\; Y = 0 \end{aligned} \tag{14}$$

3 Scaling Analysis

Defining the similarity transformations which are transformed from the governing equations [1–5] into the non-dimensional form:

$$\left.\begin{aligned} U &= \frac{aX}{2(1-at)} f'(\eta), \;\; V = \frac{-aH}{2\sqrt{1-at}} f(\eta), \\ \Phi &= \frac{\tilde{z}e\overline{\Phi}}{k_B \tilde{T}_{\tilde{H}}}, \quad \eta = \frac{Y}{H\sqrt{1-at}}. \end{aligned}\right\} \tag{15}$$

The non-dimensional form of momentum equations is:

$$\begin{aligned} &\rho_{\text{hnf}}\left[\frac{a^2 X}{4\left(1-a\tilde{t}\right)^2}\left(2f'(\eta) + \eta f''(\eta) + (f'(\eta))^2 - f(\eta) f''(\eta)\right)\right] \\ &= -\frac{\partial P}{\partial X} + \frac{\mu_{\text{hnf}} aX}{2H^2(1-at)^2} f'''(\eta) - \frac{\sigma_{\text{hnf}} B_0^2 aX}{2(1-at)^2} f'(\eta) + \frac{\rho_e E_x}{(1-at)}, \end{aligned} \tag{16}$$

$$\begin{aligned} &\rho_{hnf}\left[\frac{-a^2 H}{4(1-at)^{3/2}}\left(f(\eta) + \eta f'(\eta) - f(\eta) f'(\eta)\right)\right] \\ &= -\frac{\partial P}{\partial Y} - \frac{\mu_{hnf} a}{2H(1-at)^{3/2}} f''(\eta) \end{aligned} \tag{17}$$

Now, differentiating Eq. (16) w.r.t 'X' and Eq. (17) w.r.t 'Y', then Eq. (17) becomes,

$$\frac{\partial^2 P}{\partial X \partial Y} = 0 \tag{18}$$

and Eq. (16) as,

$$f'''' - \frac{SA_\rho}{A_\mu}\left(3f''(\eta) + \eta f'''(\eta) - f(\eta)f'''(\eta) + f''(\eta)f'(\eta)\right) - \frac{A_\sigma}{A_\mu}M^2 f'' + \frac{2Ue}{A_\mu}m^2\Phi' = 0, \tag{19}$$

The zeta potential established throughout a large range of PH ionic solutions does not exceed 25 mV in all electric double layers, and we obtain:

$$\Phi'' - m^2 \sinh(\Phi) = 0. \tag{20}$$

The associated dimensionless boundary conditions

$$f(0) = 0,\ \ f''(0) = 0,\ \ \Phi'(0) = 0,\ f(1) = 1,\ \ f'(1) = 0,\ \ \Phi(1) = \xi \tag{21}$$

in which $S = \frac{a\rho_f H^2}{2\mu_f}$ is the squeezing number, $M = HB_0\sqrt{\frac{\sigma_f}{\mu_f}}$ is the Hartmann number, $\xi = \frac{\tilde{z}e\tilde{\xi}}{k_B\tilde{T}_{\tilde{H}}}$ is the zeta potential parameter, $Ue = \frac{1}{a\tilde{X}}U_{hs}$ is electric field parameter, where $U_{hs} = -\frac{k_B\tilde{T}_{\tilde{H}}\varepsilon_{ef}E_x}{\mu_f\tilde{z}e}$ is the Helmholtz–Smoluchowski velocity and $m^2 = K^2H^2(1-at)$ is electroosmosis parameter, where $K^2 = -\frac{2\tilde{z}^2e^2\tilde{n}_0}{\varepsilon_{ef}k_B\tilde{T}_{\tilde{H}}}$ is the Debye–Hückel parameter.

3.1 Coefficient of Skin Friction

The dimensional form of coefficient of skin friction is presented as follows:

$$C_f = \frac{\mu_{\text{thnf}}}{\rho_{\text{thnf}}V_{\tilde{H}}^2}\left(\frac{\partial U}{\partial Y}\right)_{Y=h(t)}, \tag{22}$$

Using (12) in Eq. (19), we obtain the dimensionless form of coefficient of skin friction as follows:

$$\frac{A_\rho H^2}{A_\mu X^2}(1-at)R_x C_f = f''(1)\,. \tag{23}$$

where $R_x = \frac{2\rho_f V_H^2 X\sqrt{1-at}}{aH\mu_f}$ is the local Reynolds numbers.

$$A_\mu = \left[\left(1 + B_1\phi + C_1\phi^2\right)\phi_1 + \left(1 + B_2\phi + C_2\phi^2\right)\phi_2 + \left(1 + B_3\phi + C_3\phi^2\right)\phi_3\right]/\phi,$$

$A_\sigma = A_{hnf}\left(\frac{(1+2\phi_1)\sigma_1+(1-2\phi_1)A_{hnf}}{(1-\phi_1)\sigma_1+(1+\phi_1)A_{hnf}}\right)$, $A_{hnf} = A_{nf}\left(\frac{(1+2\phi_2)\sigma_2+(1-2\phi_2)A_{nf}}{(1-\phi_2)\sigma_2+(1+\phi_2)A_{nf}}\right)$ and $A_{nf} = \sigma_f\left(\frac{(1+2\phi_3)\sigma_3+(1-2\phi_3)\sigma_f}{(1-\phi_3)\sigma_3+(1+\phi_3)\sigma_f}\right)$.

4 Numerical Solution

Nonlinear system of differential Eqs. (19–20) with boundary condition (Eq. 21) has been solved using with shooting method. Converting higher order differential Eqs. (19–20) into first-order equations as follows:

$$\left.\begin{aligned}
y_1 &= f;\\
y_2 &= f'\\
y_3 &= f''\\
y_4 &= f'''\\
y_5 &= \frac{A_\rho S}{A_\mu}(3y_3 + \eta y_4 - y_1 y_4 + y_3 y_2) + \frac{A_\sigma}{A_\mu}M^2 y_3 - \frac{2Ue}{A_\mu}m^2 y_2\\
y_6 &= \Phi\\
y_7 &= \Phi'\\
y_8 &= m^2\sinh(y_6)
\end{aligned}\right\} \tag{24}$$

Boundary conditions (18) and the corresponding initial conditions are introduced as:

$$\left.\begin{aligned}
&y_1(0) = 0,\ \ y_3(0) = 0,\ \ y_6(0) = 0,\\
&y_2(0) = a_1,\ \ y_4(0) = a_2,\ \ y_7(0) = a_3\,.
\end{aligned}\right\} \tag{25}$$

In this, a_1, a_2, and a_3 at the beginning point $\eta = 0$ are assumed in order to integrate Eq. (24), then problem will convert into initial value problem. This concept is applied to create a programme with the help of MATLAB software.

The MATLAB bvp4c function is used to solve the numerical aspect of the issue. Both for small and high values of S, the strong agreement is easily apparent. Table 3 is also presented to investigate the current results of the skin friction coefficient for S with numerical solution Wang [57], VPM solution [58], and Keller-box scheme solution [59] in the absence of ternary hybrid nanofluid (Al_2O_3, SiO_2, MWCNT/water), electric and magnetic fields. It is clear from Table 3 that this study's results are far more encouraging than the previous one. Because of this, there is a high degree of

Table 3 Numerical values for velocity $f''(1)$ for absence of electric filed parameter, Hartmann number, and ternary hybrid nanofluid (Al_2O_3, SiO_2, MWCNT/water)

S	Wang [57]	Khan et al. [58]	Mat Noor et al. [59]	Present result
−0.9780	2.235	2.1915	2.1917	2.191502244
0.09998	2.9279	2.9277	2.9277	2.927684329
0	3	3	3	3.000000001
0.09403	3.0665	3.0663	3.0664	3.066378685
1.1224	3.714	3.708	3.708	3.708000172

confidence in MATLAB replies. In the absence of an electromagnetic hydrodynamic and ternary hybrid nanofluid influences, these effects may be of low importance, but they may be of enormous importance when paired with an electromagnetic field and ternary hybrid nanofluids.

5 Results and Discussion

There are many astounding characteristics that might affect the velocity and local skin friction of ternary hybrid nanofluid (Al_2O_3, SiO_2, MWCNT/water), which are discussed in this section (Figs. 2, 3, 4, 5, 6, 7, 8, 9, 10, 11). The incorporation of three nanoparticles into base fluids has the potential to significantly enhance the density as well as the viscosity properties of the fluids. The kind of nanoparticles used in the mixture, as well as their dimensions and proportions, has a significant impact on the effectiveness of the ternary nanofluid (Al_2O_3, SiO_2, MWCNT/water).

5.1 Flow Field Analysis

This section's primary goal is to explore the numerical findings offered by the graphical representation. For the important parameters such as electroosmosis, electric field, squeezing, Hartmann number, zeta potential parameter, and nanoparticle volume fraction, numerical simulations are performed, and the influence of these variables on velocity is investigated in Figs. 2, 3, 4, 5, 6, 7. Figure 2 depicts the effect of the electroosmosis parameter on fluid velocity. The fluid velocity is seen to decrease in the range of (about) and to increase in the region of. This is due to an increase in collisions between particles near parallel plates when the electroosmotic parameter (m) is lowered. As a result, the fluid velocity accumulates at the right border and rises towards the left boundary.

Figure 3 depicts dimensionless velocity distributions for both positive and negative values of the electric field parameter. The electric field component is very important in managing the squeezing flow. Electrical field parameter value is negative when the

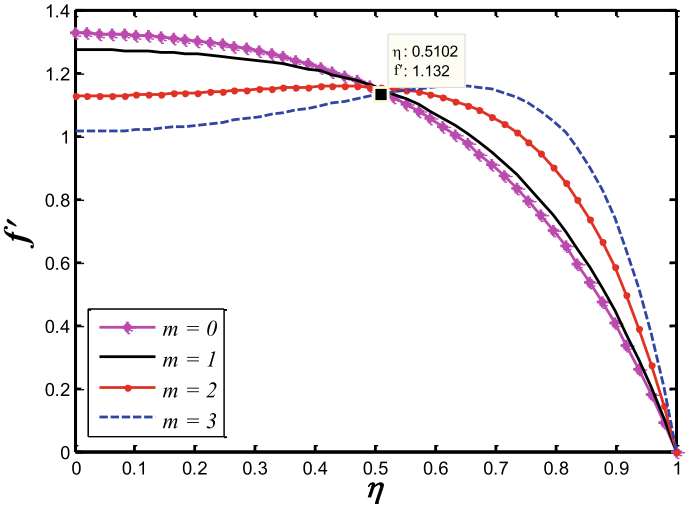

Fig. 2 Impact of m on $f'(\eta)$ for $S = 2$; $M = 2$,$\phi_1 = 0.03$, $\phi_2 = 0.02$, $\phi_1 = 0.01$, $\xi = 0.5$, and $Ue = 2$

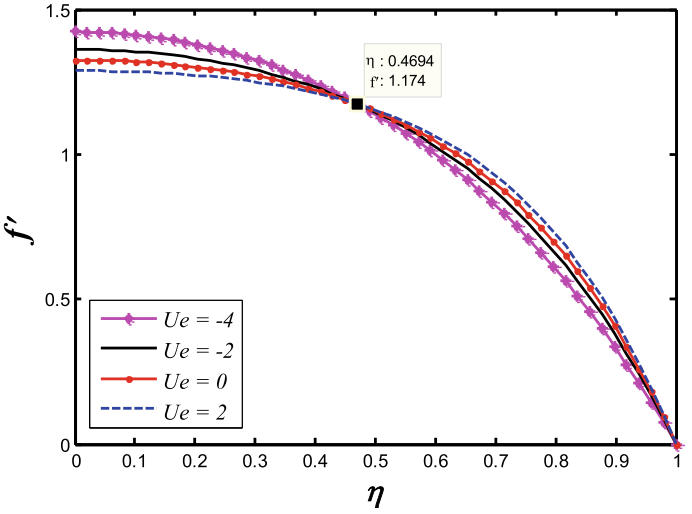

Fig. 3 Impact of Ue on $f'(\eta)$ for $S = 2$; $M = 2$, $\phi_1 = 0.03$, $\phi_2 = 0.02$, $\phi_1 = 0.01$, $\xi = 0.5$, and $m = 1.5$

electrical field direction is reversed and oriented in the positive axial direction (left to right in Fig. 1), but positive when oriented in the negative axial direction (right to left). It is observed that when the value of U_e increases, the velocity distribution decreases. However, there is an enhancement in the velocity distribution f' for $\eta > 0.4698$.

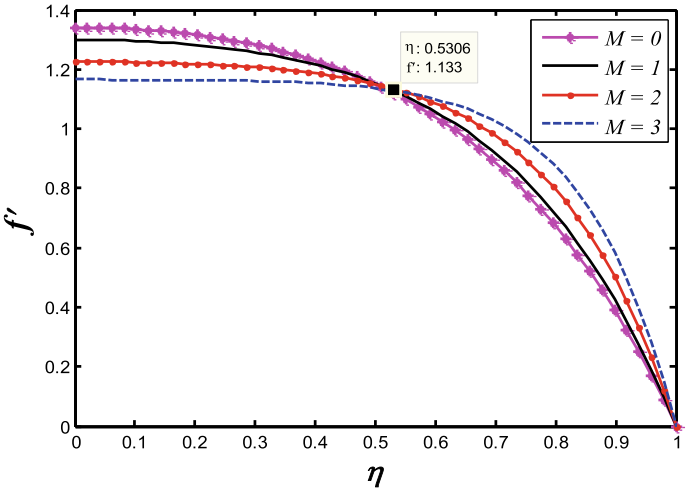

Fig. 4 Impact of M on $f'(\eta)$ for $S = 2$; $Ue = 2$,$\phi_1 = 0.03$, $\phi_2 = 0.02$, $\phi_1 = 0.01$, $\xi = 0.5$, and $m = 1.5$

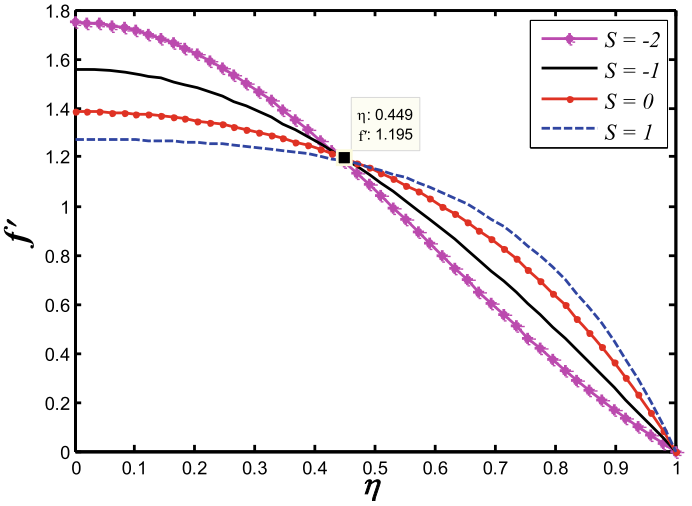

Fig. 5 Impact of S on $f'(\eta)$ for $M = 2$; $Ue = 2$, $\phi_1 = 0.03$, $\phi_2 = 0.02$, $\phi_1 = 0.01$, $\xi = 0.5$, and $m = 1.5$

Figure 4 depicts the effects of the Hartmann number on the distribution of fluid velocity. Increasing the Hartmann number, or the intensity of the magnetic field, reduces velocity in the bottom half of the body while increasing it in the upper half of the body as a result of velocity re-distribution, magnetic (Lorentz) body force contributes to viscous hydrodynamic force through Hartmann number. The magneto-hydrodynamics impact is null when $Ha = 0$. Cramer and Pai [56] observed that when

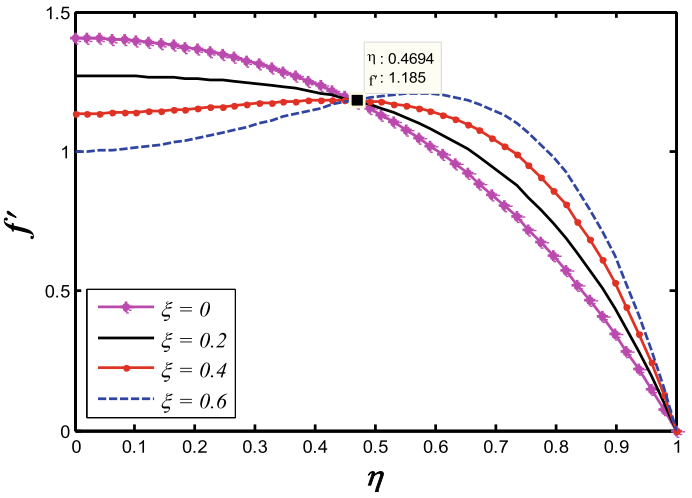

Fig. 6 Impact of ξ on $f'(\eta)$ for $M = 2$; $S = 2$; $\phi_1 = 0.03$, $\phi_2 = 0.02$, $\phi_1 = 0.01$, $Ue = 2$, and $m = 1.5$

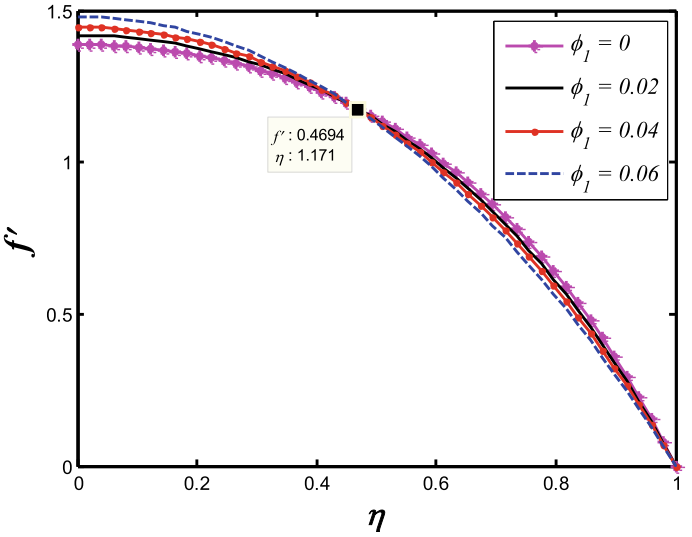

Fig. 7 Impact of ϕ_1 on $f'(\eta)$ for $M = 2$; $S = 2$; $\xi = 0.5$, $\phi_2 = 0.02$, $\phi_1 = 0.01$, $Ue = 2$, and $m = 1.5$

$Ha = 1$, both magnetic drag and viscous forces directly contribute. The magnetic force surpasses the viscous force at $Ha > 1$, which results in significant damping in the bottom half space.

Figure 5 presents the effect of S on the velocity distribution. Figure 5 explains two scenarios in respect of the squeeze number: when the plates are sliding away,

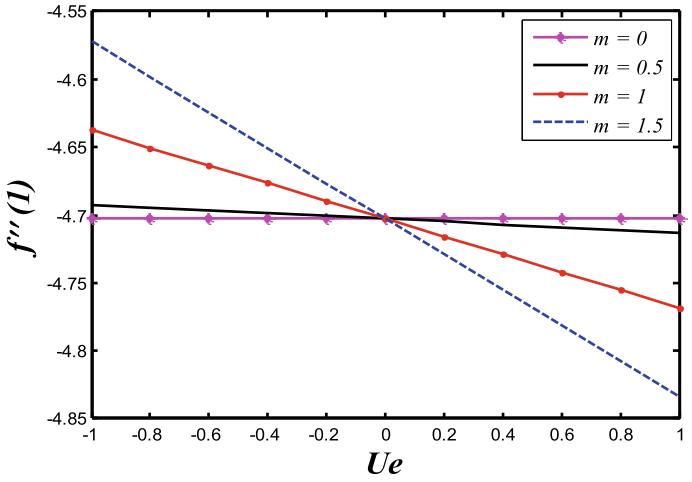

Fig. 8 Impact of m on $f''(1)$ for $M = 2$; $\phi_1 = 0.03$, $\phi_2 = 0.02$, $\phi_1 = 0.01$, $S = 2$, and $\xi = 0.5$

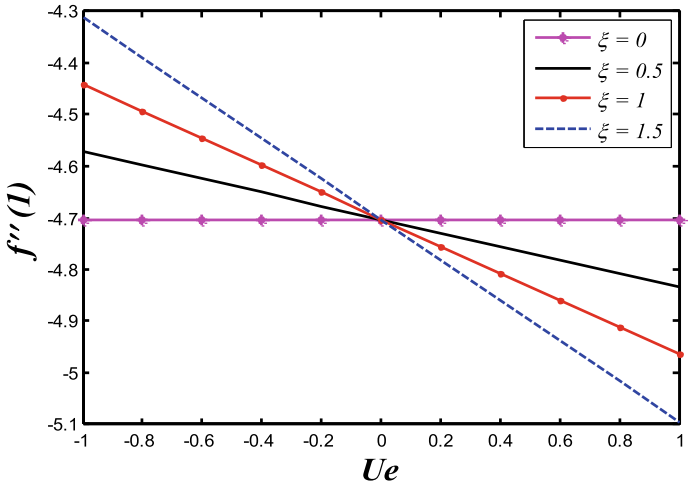

Fig. 9 Impact of ξ on $f''(1)$ for $m = 1.5$; $\phi_1 = 0.03$, $\phi_2 = 0.02$, $\phi_1 = 0.01$, $M = 2$, and $S = 2$

i.e. separating ($S > 0$), and once the plates are closing, i.e. squeezing ($S < 0$). It is observed that the fluid velocity reduces in left half plate by augmenting the value of squeezing parameter, but reverse nature is occurred in the rest of the plate.

Figure 6 visualises the influence of zeta potential parameter ξ for the velocity distribution. In the top plate boundary condition, $\Phi(1) = \xi$, the zeta potential parameter $\xi = \frac{\tilde{z}e\tilde{\xi}}{k_B \tilde{T}_{\tilde{H}}}$ appears. This parameter causes a visible speeding in the bottom half space and a noticeable slowdown in the top half space when the value of this parameter is raised. It is also important in the removal of polluted water from nuclear

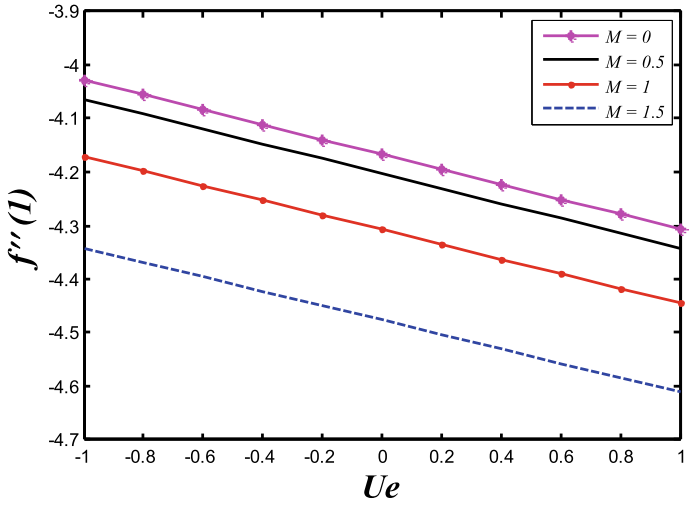

Fig. 10 Impact of M on $f''(1)$ for $m = 1.5$; $\phi_1 = 0.03$, $\phi_2 = 0.02$, $\phi_1 = 0.01$, $S = 2$, and $\xi = 0.5$

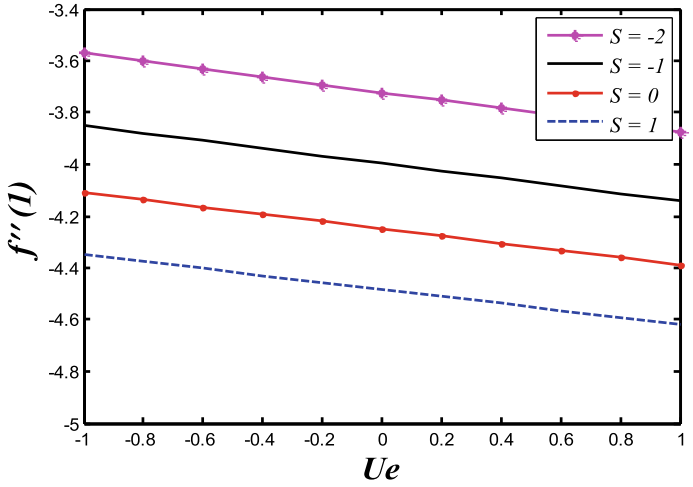

Fig. 11 Impact of S on $f''(1)$ for $m = 1.5$; $\phi_1 = 0.03$, $\phi_2 = 0.02$, $\phi_1 = 0.01$, $M = 2$, and $\xi = 0.5$

power plants because surface strain (electrical potential fluctuation across inner and external surfaces) plays an important role.

Figure 7 shows the variation of the nanoparticle volume fraction of Al_2O_3 (ϕ_1) on the axial velocity $f'(\eta)$ profile. In the main flow regime, there are two variational trends that may be noticed in the axial velocity. These tendencies are as follows: the axial velocity is disadvantageous (drawn down) in the bottom half of the wall and beneficial (pulled up) in the top half of the wall in the lower half of the wall. The

bottom half of the wall has an unfavourable axial velocity, whereas the top half of the wall has a favourable axial velocity. It is also concluded that the fluid velocity oscillation behaviour is noticed in the parallel wall, when the Al_2O_3 nanoparticle is enhanced in Fig. 7.

5.2 Skin Friction Coefficient: Surface Viscous Drag Analysis

Figures 8, 9 depicts the influence of electroosmosis parameter (m) and zeta potential parameter (ξ) on skin friction coefficient, $f''(1)$ at the upper plate against electric field parameter (Ue), for the dual cases of $Ue < 0$ and $Ue \geq 0$ again. The zeta potential and electroosmosis characteristics can be used on parallel plates to determine the charge constancy of a distributed system. It has been used to calculate the electrical charge of a lipid bilayer. An electric charge is supplied across the two plates of a folded capillary flow cell. The skin friction coefficient increases at $Ue < 0$, but opposite characteristics are noticed at $Ue \geq 0$ when electroosmosis parameter (m) and zeta potential parameter (ξ) are increased.

Figures 10, 11 illustrate the effects of Hartmann number and squeezing parameter on the numerical results of skin friction coefficient vs. electric field parameter. Figure 10 indicates a rise in the Hartmann number results with a reduction in the skin fraction coefficient at both ends (lower and upper) of the parallel plates. The fluid near the parallel plate has a stronger Lorentz force than the fluid in the central sections. This is because the Lorentz force offers resistance in fluid motion. As a consequence, high Lorentz pressures cause skin friction coefficients in the core region of plates to lose momentum. The skin friction coefficient is lowered in both the squeezing and separating plate scenarios, $S < 0$ and $S > 0$ (see Fig. 11). Additionally, these techniques may be employed to enhance the charge stability of a distributed electromagnetic ionic lubrication mechanism.

6 Conclusions

Two-dimensional squeezing motion of viscous ternary hybrid nanofluid contained between two infinite parallel plates was studied in the presence of magnetic and electric forces in this chapter. The THNF consists of a combination of nanoparticles (Al_2O_3, SiO_2, MWCNT) with base fluid as water. The findings of present analysis can be summarised as follows:

- For negative electric field, the fluid velocity and skin friction coefficient in the parallel plates are significantly enhanced at the beginning of the experiment owing to a rise in the electroosmosis parameter, while the reverse trend is seen for positive electric field.

- As the magnitude of the electroosmosis parameter and the zeta potential parameter are increased, the fluid velocity increases proportionally.
- With a higher value of zeta potential, skin friction becomes more significant, causing acceleration to occur first at the top plate for $Ue < 0$ and then lowering skin friction for $Ue \geq 0$.

Several novel elements of electromagnetic ionic squeeze film thermodynamics have been discovered in this study. Nonetheless, only the behaviour of viscous fluids has been studied. Subsequent study will focus on non-viscous characteristics (e.g. viscoplastic, microstructural, viscoelastic, etc.) and will be published as soon as feasible.

References

1. Stefan MJ (1874) Versuch uber die scheinbare adhesion, Akademie der Wissenschaften in Wien. Mathematik-Naturwissen 230(69):713–721
2. Jackson J (1963) A study of squeezing flow. Appl Sci Res Sect A 11(1):148–152
3. Usha R, Sridharan R (1996) Arbitrary squeezing of a viscous fluid between elliptic plates. Fluid Dyn Res 18(1):35–51
4. Reynolds O (1886) IV On the theory of lubrication and its application to Mr. Beauchamp towers experiments, including an experimental determination of the viscosity of olive oil. Philos Trans Roy Soc Lond 177:157–234
5. Archibald F (1965) Load capacity and time relations for squeeze films. Trans Am Soc Mech Eng 78:A231–A245
6. Mahmood M, Asghar S, Hossain M (2007) Squeezed ow and heat transfer over a porous surface for viscous fluid. Int J Heat Mass Transf 44(2):165–173
7. Hayat T, Khan M, Imtiaz M, Alsaedi A (2017) Squeezing ow past a riga plate with chemical reaction and convective conditions. J Mol Liq 225:569–576
8. Sheikholeslami M, Ganji D, Rashidi M (2016) Magnetic field effect on unsteady nanofluid flow and heat transfer using Buongiorno model. J Magn Magn Mater 416:164–173
9. Rudraswamy N, Gireesha B, Krishnamurthy M (2016) Effect of internal heat generation/absorption and viscous dissipation on MHD flow and heat transfer of nanofluid with particle suspension over a stretching surface. J Nanofluids 5(6):1000–1010
10. Bharathi V, Vijayaragavan R, Prakash J (2021) A study of electro-osmotic and magnetohybrid nanoliquid flow via radiative heat transfer past an exponentially accelerated plate. Heat Transf 50(5):4937–4960
11. Ravikumar R, Arul FreedaVinodhini G, Prakash J (2019) Heat transfer and slip effects on the Mhd peristaltic flow of viscous fluid in a tapered microvessels: application of blood flow research. Int J Eng Adv Technol (IJEAT) 9(1):5384–5390
12. Prakash J, Balaji N, Siva EP, Chanrasekaran AD (2012) Non-linear blood flow analysis on MHD peristaltic motion of a Williamson fluid in a micro channel. AIP Conference Proceedings, p 20048
13. Govindarajan A, Vidhya M, Siva EP, Prakash J (2018) MHD peristaltic transport of a dusty couple stress fluid through a symmetric porous channel. Int J Eng Technol 7 (4.10):306–309
14. Kothandapani M, Pushparaj V, Prakash J (2016) Effects of slip and heat transfer on the MHD peristaltic flow of a Jeffery fluid through a vertical tapered asymmetric channel. Global J Pure Appl Math (GJPAM) 12(1):205–212
15. Adesanya SO, Ogunseye HA, Jangili S (2018) Unsteady squeezing flow of a radiative Eyring Powell fluid channel flow with chemical reactions. Int J Therm Sci 125:440–447

16. Domairry G, Aziz A (2009) Approximate analysis of MHD Squeeze flow between two parallel disks with suction or injection by homotopy perturbation method. Math Probl Eng. https://doi.org/10.1155/2009/603916
17. Bruus H (2008) Theoretical microfluidics, oxford master series in condensed matter physics. Oxford University Press, Oxford, UK
18. Reuss FF (1809) Sur un nouvel effet de l'electricite galvanique. Memoires de la Societe Imperiale des Naturalistes de Moscou 2:327–337
19. Helmholtz H (1879) Uber den Einflus der elektrischen Grenzschichten bei galvanischer Spannung und der durch Wasserstromung erzeugten Potentialdifferenz. Ann 7:337
20. von Smoluchowski M (1917) Versuch einer mathematischen Theorie der Koagulationskinetic kolloid Losungen. Z Phys Chem 92:129–135
21. Burgreen D, Nakache FR (1964) Electrokinetic flow in ultrafine capillary slits. J Phys Chem 68:1084–1091
22. Umavathi JC, Patil SL, Mahanthesh B, Anwar Bég O (2021) Unsteady squeezing flow of magnetized nano-lubricant between parallel disks with Robin boundary condition. Proc IMechE J Nanomater Nanoeng Nanosyst 15. https://doi.org/10.1177/23977914211036562
23. Prajapati BL (1995) Magnetic-fluid-based porous squeeze films. J Magn Magn Mater 149:97–100
24. Khan U, Ahmed N, Zaidi ZA, Asadullah M, Mohyud-Din ST (2014) MHD squeezing flow between two infinite plates. Ain Shams Eng J 5(1):187–192
25. Zhao C et al (2020) Electroviscous effects on the squeezing flow of thin electrolyte solution films. J Fluid Mech 888:A29
26. Talapatra S, Chakraborty S (2009) Squeeze-flow electroosmotic pumping between charged parallel plates. Intl J Fluid Mech Res 36:460–472
27. Prakash J, Tripathi D (2020) Study of EDL phenomenon in Peristaltic pumping of a Phan-Thien-Tanner Fluid through asymmetric channel. Korea-Aust Rheol J 32(4):271–285
28. Ramesh K, Prakash J (2020) Heat transfer enhancement in radiative peristaltic propulsion of nanofluid in the presence of induced magnetic field. Numer Heat Transf Part A: Appl 79(2):83–110
29. Prakash J, Yadav A, Tripathi D, Tiwari AK (2019) Computer modelling of peristalsis-driven intrauterine fluid flow in the presence of electromagnetohydrodynamics. Eur Phys J Plus 134(2):81
30. Prakash J, Tripathi D, Beg OA, Tiwari AK, Kumar R (2021) Thermo-electrokinetic rotating non-Newtonian hybrid nanofluid flow from an accelerating vertical surface. Heat Transf. https://doi.org/10.1002/htj.22373
31. Tripathi D, Prakash J, Gnaneswara Reddy M, Kumar R (2021) Numerical study of electroosmosis induced alterations in peristaltic pumping of couple stress hbrid nanofluids through microchannel. Indian J Phys 95(11):2411–2421
32. Vijayaragavan R, Bharathi V, Prakash J (2021) Influence of electroosmosis mechanism and chemical reaction on convective flow over an exponentially accelerated plate. Int J Appl Comput Math 7(4):1–26
33. Rajaram V, Varadharaj B, Prakash J (2021) A study of electro-osmotic and magnetohybrid nanoliquid flow via radiative heat transfer past an exponentially accelerated plate. Heat Transf 50(5):4937–4960
34. Choi SUS, Eastman JA (1995) Enhancing the thermal conductivity of fluids with nanoparticles. Argonne National Lab 43 (ANL/MSD/CP-84938 CONF-951135–29), pp 99–105
35. Xuan Y, Roetzel W (2000) Conceptions for heat transfer correlation of nanofluids. Int J Heat Mass Transf 43(19):3701–3707
36. Xuan Y, Li Q (2004) Heat transfer enhancement of nanofluids. Int J Heat Fluid Flow 21(1):58–64
37. Keblinskia P, Phillpot S, Choi SUS, Eastman JA (2002) Mechanisms of heat flow in suspensions of nano-sized particles (nanofluids). Int J Heat Mass Transf 45(4):36–44
38. Keblinskia P, Eastman JA, Cahill DG (2005) Nanofluids for thermal transport. Mater Today 8(6):36–44

39. Mehryan SAM, Ghalambaz M, Gargari LS, Hajjar A, Sheremet M (2020) Natural convection flow of a suspension containing nano-encapsulated phase change particles in an eccentric annulus. J Energy Storage 28:101236
40. Ghalambaz M, Groşan T, Pop I (2019) Mixed convection boundary layer flow and heat transfer over a vertical plate embedded in a porous medium filled with a suspension of nano-encapsulated phase change materials. J Mol Liq 293:111432
41. Ghalambaz M, Mehryan SAM, Hajjar A, Veismoradi A (2020) Unsteady natural convection flow of a suspension comprising Nano-Encapsulated Phase Change Materials (NEPCMs) in a porous medium. Adv Powder Technol 31(3):954–966
42. Hajjar A, Mehryan SAM, Ghalambaz M (2020) Time periodic natural convection heat transfer in a nano-encapsulated phase-change suspension. Int J Mech Sci 166:105243
43. Saeed A, Jawad M, Alghamdi W, Nasir S, Gul T, Kumam P (2021) Hybrid nanofluid flow through a spinning Darcy-Forchheimer porous space with thermal radiation. Sci Rep 11(1):1–15
44. Alzahrani AK, Ullah MZ, Alshomrani AS, Gul T (2021) Hybrid nanofluid flow in a Darcy-Forchheimer permeable medium over a flat plate due to solar radiation. Case Stud Therm Eng 26:100955
45. Kumar TS (2021) Hybrid nanofluid slip flow and heat transfer over a stretching surface. Partial Differ Equ Appl Math 4:100070
46. Tripathi D, Prakash J, Anwar Bég O, Kumar R (2021) Thermal analysis of $\gamma Al_2O_3/H_2O$ and $\gamma Al_2O_3/C_2H_6O_2$ elastico-viscous nanofluid flow driven by peristaltic wave propagation with electroosmotic and magnetohydrodynamic effects: applications in nanotechnological energy systems. Energy Syst Nanotechnol Adv Sustain Sci Technol 223–259. https://doi.org/10.1007/978-981-16-1256-5_13
47. Bharathi V, Vijayaragavan R, Prakash J (2020) Comparative analysis of Cu/blood and Cu–CuO/blood nanofluids on a peristaltic flow governed by an asymmetric channel. Heat Transf 49(8):4923–4944
48. Prakash J, Tripathi D, Beg OA, Tiwari AK, Kumar R (2022) Thermo-electrokinetic rotating non-Newtonian hybrid nanofluid flow from an accelerating vertical surface. Heat Transf 51(2):1746–1777
49. Prakash J, Reddy MG, Tripathi D, Tiwari AK (2020) A model for electro-osmotic flow of pseudoplastic nanofluids in presence of peristaltic pumping: an application to smart pumping in energy systems. In: Ledwani L, Sangwai J (eds) Nanotechnology for energy and environmental engineering. Green energy and technology. Springer, Cham. https://doi.org/10.1007/978-3-030-33774-2_8
50. Animasaun IL, Yook SJ, Muhammad T, Mathew A (2022) Dynamics of ternary-hybrid nanofluid subject to magnetic flux density and heat source or sink on a convectively heated surface. Surf Interfaces 28:101654
51. Arif M, Kumam P, Kumam W, Mostafa Z (2022) Heat transfer analysis of radiator using different shaped nanoparticles water-based ternary hybrid nanofluid with applications: a fractional model. Case Stud Therm Eng 31:101837
52. Souby MM, Bargal MH, Wang Y (2021) Thermohydraulic performance improvement and entropy generation characteristics of a microchannel heat sink cooled with new hybrid nanofluids containing ternary/binary hybrid nanocomposites. Energy Sci Eng 9(12):2493–2513
53. Sundar LS, Chandra Mouli KV, Said Z, Sousa A (2021) Heat transfer and second law analysis of ethylene glycol-based ternary hybrid nanofluid under laminar flow. J Therm Sci Eng Appl 13(5):051021
54. Sahoo RR, Kumar V (2020) Development of a new correlation to determine the viscosity of ternary hybrid nanofluid. Int Commun Heat Mass Transfer 111:104451
55. Zayan MJ, Rasheed AK, John A, Khalid M, Ismail AF, Aabid A, Baig M (2021) Investigation on rheological properties of water-based novel ternary hybrid nanofluids using experimental and Taguchi method. Materials 15(1):28
56. Cramer KC, Pai SI (1973) Magnetofluid dynamics for engineers and applied physicists. MacGraw-Hill, New York, USA
57. Wang CY (1976) The squeezing of a fluid between two plates. J Appl Mech 43:579–583

58. Khan U, Ahmed N, Khan SI, Zaidi ZA, Xiao-Jun Y, Mohyud-Din ST (2014) On unsteady two-dimensional and axisymmetric squeezing flow between parallel plates. Alex Eng J 53:463–468
59. Mat Noor NA, Shafie S, Admon MA (2021) Slip effects on MHD squeezing flow of Jeffrey nanofluid in horizontal channel with chemical reaction. Mathematics 9:1215